

# Diplomarbeit

zur Erlangung des akademischen Grades  
Diplom-Physiker

## Measurement of the Cross Section for the Process $pp \rightarrow \gamma^*/Z \rightarrow \tau^+\tau^-$ and a Search for Neutral MSSM Higgs Bosons with the ATLAS Detector

Christian Gumpert

geboren am 06.09.1985 in Berlin

TECHNISCHE UNIVERSITÄT DRESDEN

INSTITUT FÜR KERN- UND TEILCHENPHYSIK

FACHRICHTUNG PHYSIK

FAKULTÄT MATHEMATIK UND NATURWISSENSCHAFTEN

16. Dezember 2011





Eingereicht am 16.12.2011

1. Gutachter: Prof. M. Kobel
2. Gutachter: Prof. D. Stöckinger





# Kurzdarstellung

Die Suche nach Higgs Bosonen ist eines der Hauptziele des ATLAS Experiments. Die minimale supersymmetrische Erweiterung des Standard Modells der Teilchenphysik enthält drei neutrale Higgs Bosonen, welche sich durch den Zerfall in Paare von Tau Leptonen nachweisen lassen. Ein wesentlicher Untergrund für diesen Entdeckungskanal ist im niedrigen Massenbereich  $M_A = 100 - 150$  GeV durch den Prozess  $\gamma^*/Z \rightarrow \tau^+\tau^-$  gegeben.

In dieser Arbeit wird die Erzeugungshäufigkeit von Tau Lepton Paaren über den Prozess  $pp \rightarrow \gamma^*/Z \rightarrow \tau^+\tau^-$  durch die Analyse des voll leptonischen Endzustandes bestimmt. Dazu werden  $L = 35.5 \text{ pb}^{-1}$  an Daten des ATLAS Detektors aus Proton-Proton Kollisionen bei einer Schwerpunktsenergie von 7 TeV ausgewertet. Das ermittelte Ergebnis von  $\sigma(pp \rightarrow \gamma^*/Z \rightarrow \tau^+\tau^-) = 1.05 \pm 0.13 \text{ (stat.)} \pm 0.10 \text{ (syst.)} \pm 0.04 \text{ (lumi.) nb}$  stimmt mit der theoretischen Vorhersage überein.

Weiterhin wird eine Untersuchung des Entdeckungskanals  $pp \rightarrow h/H/A \rightarrow \tau^+\tau^-$  für den Massenbereich  $M_A = 100 - 150$  GeV im rein leptonischen Endzustand durchgeführt. Dazu wird die Ereignisselektion durch den Einsatz multivariater Methoden optimiert. Die Auswertung von  $L = 1.06 \text{ fb}^{-1}$  Daten des ATLAS Detektors basiert auf der optimierten Selektion. Die statistische Auswertung der gemessenen Daten liefert keine signifikante Abweichung von der Standard Modell Vorhersage. Daher werden Ausschlussgrenzen im  $M_A \times \tan \beta$  Parameterraum des MSSMs abgeleitet. Im Rahmen des  $m_h^{\text{max}}$  Szenarios kommt diese Arbeit zu dem Schluss, dass Werte  $\tan \beta > 32 - 51$  abhängig vom Parameter  $M_A$  mit einer Wahrscheinlichkeit von 95% ausgeschlossen sind.

## Abstract

The search for Higgs bosons is among the primary goals of the ATLAS experiment. The minimal supersymmetric extension to the Standard Model contains three neutral Higgs bosons which are detectable through their decays into pairs of tau leptons. A major background for this discovery channel in the low mass region  $M_A = 100 - 150$  GeV arises from  $\gamma^*/Z \rightarrow \tau^+\tau^-$  events.

In this thesis, the cross section of the process  $pp \rightarrow \gamma^*/Z \rightarrow \tau^+\tau^-$  is measured by investigating the fully leptonic final state. Therefore,  $L = 35.5 \text{ pb}^{-1}$  of data from proton-proton collisions recorded by the ATLAS detector at a centre-of-mass energy of 7 TeV are analysed. The result obtained is  $\sigma(pp \rightarrow \gamma^*/Z \rightarrow \tau^+\tau^-) = 1.05 \pm 0.13 \text{ (stat.)} \pm 0.10 \text{ (syst.)} \pm 0.04 \text{ (lumi.) nb}$  and is in agreement with the theoretical prediction.

Furthermore, the discovery channel  $pp \rightarrow h/H/A \rightarrow \tau^+\tau^-$  is analysed in the purely leptonic final state for the low mass region  $M_A = 100 - 150$  GeV. An optimisation of the event selection by the usage of multivariate techniques is investigated. The optimal selection strategy is applied on  $L = 1.06 \text{ fb}^{-1}$  of data recorded by the ATLAS detector. As the statistical analysis does not yield a significant deviation from the Standard Model expectation, exclusion limits in the  $M_A \times \tan \beta$  parameter space of the MSSM are derived. In the context of the  $m_h^{\text{max}}$  scenario, this thesis concludes that values of  $\tan \beta > 32 - 51$  depending on the parameter  $M_A$  are excluded at a 95% confidence level.



# Table of Contents

<b>List of Figures</b>	<b>xi</b>
<b>List of Tables</b>	<b>xiii</b>
<b>1 Introduction</b>	<b>1</b>
<b>2 Theoretical Foundations</b>	<b>3</b>
2.1 The Standard Model of Particle Physics . . . . .	3
2.1.1 Electroweak Gauge Theory . . . . .	4
2.1.2 Higgs Mechanism . . . . .	6
2.1.3 Quantum Chromodynamics . . . . .	9
2.2 Supersymmetry . . . . .	10
2.2.1 Motivation . . . . .	10
2.2.2 Minimal Supersymmetric Standard Model . . . . .	11
<b>3 The ATLAS Experiment</b>	<b>15</b>
3.1 The Large Hadron Collider . . . . .	15
3.2 The ATLAS Detector . . . . .	17
3.2.1 ATLAS Coordinate System . . . . .	18
3.2.2 The Inner Detector . . . . .	19
3.2.3 The Calorimetry System . . . . .	21
3.2.4 The Muon Spectrometer . . . . .	23
3.2.5 The ATLAS Trigger and Data Acquisition System . . . . .	24
3.2.6 Luminosity Measurement . . . . .	25
3.3 Event Generation . . . . .	26
3.3.1 Monte Carlo Generators and Simulated Data Sets . . . . .	28
3.4 Object Reconstruction and Identification . . . . .	29
3.4.1 Electrons . . . . .	30
3.4.2 Muons . . . . .	31
3.4.3 Jets . . . . .	32
3.4.4 Missing Transverse Energy . . . . .	33
<b>4 Event Topology</b>	<b>35</b>
4.1 The Process $pp \rightarrow \gamma^*/Z \rightarrow \tau^+\tau^-$ . . . . .	35
4.2 The Process $pp \rightarrow h/H/A \rightarrow \tau^+\tau^-$ . . . . .	36
4.3 Decay of Tau Leptons . . . . .	39
4.4 Event Topology . . . . .	40

4.5	Background Processes	43
4.6	Mass Reconstruction Techniques	45
<b>5</b>	<b>Measurement of the <math>pp \rightarrow \gamma^*/Z \rightarrow \tau^+\tau^-</math> Cross Section</b>	<b>47</b>
5.1	Data and Simulated Samples	47
5.2	Event Preselection	48
5.2.1	Vertex Requirement	48
5.2.2	Detector Status	48
5.2.3	Trigger Selection	48
5.2.4	Jet Cleaning	49
5.3	Object Definitions	49
5.4	Corrections to the Simulated Samples	51
5.4.1	Trigger Efficiency Correction	51
5.4.2	Corrections Related to Lepton Candidates	51
5.4.3	Pile-up Related Corrections	52
5.5	Event Selection	53
5.5.1	Event Preselection	54
5.5.2	Selection of the $e\mu$ Final State	54
5.5.3	Lepton Isolation	54
5.5.4	Suppression of $W \rightarrow \ell\nu$ Backgrounds	55
5.5.5	Suppression of the $t\bar{t}$ Background	57
5.5.6	Definition of the Visible Mass Window	58
5.6	Estimation of Background Contributions	58
5.6.1	Estimation of the Multijet Background	58
5.6.2	Normalisation of the Simulation of $W$ Decays	62
5.6.3	Normalisation of the Simulation of $t\bar{t}$ Processes	64
5.7	Methodology of the Cross Section Measurement	64
5.7.1	Determination of the Acceptance and Correction Factors	66
5.8	Evaluation of Systematic Uncertainties	67
5.8.1	Theoretical Uncertainties	67
5.8.2	Uncertainty on the Luminosity Measurement	68
5.8.3	Uncertainties Related to the Corrections Applied	68
5.8.4	Jet Energy Scale and $E_{T,\text{miss}}$ Uncertainty	68
5.8.5	Uncertainty on the Estimate of the Multijet Background	69
5.8.6	Uncertainties Related to the Detector Status	73
5.8.7	Uncertainties on the Acceptance Factor	73
5.8.8	Summary of Systematic Uncertainties	73
5.9	Summary	74
5.9.1	Results	74
5.9.2	Discussion and Outlook	75
<b>6</b>	<b>A Search for Neutral MSSM Higgs Bosons in the <math>\tau^+\tau^-</math> Channel</b>	<b>79</b>
6.1	Data and Simulated Samples	79
6.2	Event Preselection	79

6.2.1	Trigger Selection	80
6.2.2	Readout Problems in the Calorimeter System	80
6.3	Object Definitions	81
6.4	Corrections to the Simulated Samples	82
6.4.1	Trigger Efficiency Correction	82
6.4.2	Corrections Related to Lepton Candidates	82
6.4.3	Pile-up Related Corrections	83
6.4.4	Correction for Problematic Calorimeter Regions	83
6.5	Baseline Selection	85
6.5.1	Event Preselection	85
6.5.2	Selection of the $e\mu$ Final State	85
6.5.3	Raised $p_T$ Thresholds for the Trigger Candidate	85
6.5.4	Lepton Isolation	85
6.5.5	Summary of the Baseline Selection	86
6.6	Optimisation of the Event Selection	87
6.6.1	Definition of Discriminating Variables	87
6.6.2	Validation of Simulated Samples	89
6.6.3	Description of Investigated Methods	93
6.6.4	Performance Evaluation of Multivariate Analysis Tools	96
6.7	Background Estimation	102
6.7.1	Estimation of the Multijet Background	104
6.7.2	Estimation of the Top Quark and Di-boson Background	104
6.8	Statistical Procedure	105
6.8.1	Review of the Profile Likelihood Method	106
6.8.2	Event Counting Analysis	109
6.8.3	Template Fit of the Visible Mass Spectrum	111
6.9	Evaluation of Systematic Uncertainties	115
6.9.1	Theoretical Uncertainties	115
6.9.2	Experimental Uncertainties	117
6.9.3	Summary of Systematic Uncertainties	118
6.10	Summary	119
6.10.1	Results	119
6.10.2	Discussion and Outlook	120
<b>7</b>	<b>Conclusion</b>	<b>123</b>
<b>A</b>	<b>Theoretical Considerations</b>	<b>125</b>
A.1	Conventions	125
A.1.1	Units	125
A.1.2	Four-vector Notation	125
A.1.3	PAULI and $\gamma$ Matrices	125
A.2	LAGRANGE Formalism and DIRAC equation	126
A.3	YANG–MILLS Theory	127
A.4	Derivation of the Electroweak Lagrangian	129

<b>B</b>	<b>Coordinate Transformations</b>	<b>133</b>
<b>C</b>	<b>Measurement of the <math>pp \rightarrow \gamma^*/Z \rightarrow \tau^+\tau^-</math> Cross Section</b>	<b>135</b>
C.1	Simulated Data Sets . . . . .	135
C.2	Jet Cleaning Procedure . . . . .	135
C.3	Detailed Object Definitions . . . . .	136
C.4	Correction Factors for the Simulated Samples . . . . .	136
C.5	Cutflows for the Individual Regions . . . . .	137
C.6	Systematic Uncertainty on the QCD Background Estimate . . . . .	137
<b>D</b>	<b>A Search for Neutral MSSM Higgs Bosons in the <math>\tau^+\tau^-</math> Channel</b>	<b>143</b>
D.1	Simulated Data Sets . . . . .	143
D.2	Readout Problems in the EM Calorimeter . . . . .	143
D.3	Detailed Object Definitions . . . . .	144
D.4	Corrections for the Simulated MC Samples . . . . .	144
D.5	Optimisation of the Event Selection . . . . .	144
D.6	Template Fit of the Visible Mass Spectrum . . . . .	147
D.7	Systematic Uncertainty on the QCD Estimate . . . . .	150
	<b>Bibliography</b>	<b>157</b>

# List of Figures

2.1	Exclusion limits for the SM Higgs boson mass by ATLAS . . . . .	9
2.2	MSSM Higgs boson masses . . . . .	13
3.1	LHC accelerator complex . . . . .	16
3.2	Event rates . . . . .	17
3.3	The ATLAS detector . . . . .	18
3.4	The ATLAS coordinate system . . . . .	19
3.5	The Inner Detector . . . . .	20
3.6	The ATLAS calorimetry system . . . . .	22
3.7	The electromagnetic calorimeter . . . . .	23
3.8	Sketch of the muon spectrometer . . . . .	24
4.1	Feynman diagrams for $\gamma^*/Z$ boson production . . . . .	36
4.2	Feynman diagrams for neutral MSSM Higgs boson production . . . . .	37
4.3	Production cross section for neutral MSSM Higgs bosons . . . . .	37
4.4	Branching ratio of neutral MSSM Higgs bosons into tau lepton pairs . . . . .	38
4.5	Total production cross section for neutral MSSM Higgs bosons . . . . .	38
4.6	Feynman diagrams for signal processes . . . . .	40
4.7	Distribution of kinematic variables at event generation level . . . . .	41
4.8	Feynman diagrams for top quark production at the LHC . . . . .	43
4.9	Collinear mass approximation . . . . .	46
5.1	Vertex multiplicity distribution . . . . .	53
5.2	Lepton isolation variables . . . . .	56
5.3	Angular correlation between lepton candidates and $\vec{E}_{T,\text{miss}}$ . . . . .	57
5.4	Distribution of important kinematic variables . . . . .	59
5.5	Visible mass spectrum . . . . .	60
5.6	Idea of the ABCD method . . . . .	61
5.7	Dependence of $R_{\text{OS/SS}}$ on the lepton isolation . . . . .	70
5.8	Event display for selected data event . . . . .	77
6.1	Pile-up emulation . . . . .	84
6.2	Distributions of discriminating variables . . . . .	90
6.3	Validation of simulated samples for $t\bar{t}$ processes . . . . .	92
6.4	Validation of simulated samples for di-boson production . . . . .	94
6.5	Performance dependence on variable transformations . . . . .	98
6.6	Performances of final variable sets . . . . .	98

6.7	Classifier response functions . . . . .	100
6.8	Mass resolution with the visible mass definition . . . . .	103
6.9	Visible mass distribution for different background components . . . . .	112
6.10	Templates for the visible mass distribution . . . . .	114
6.11	Validation of the template fit . . . . .	116
6.12	Sampling distributions . . . . .	120
6.13	Expected discovery significance and observed exclusion limit . . . . .	121
6.14	Visible mass distribution in the signal region . . . . .	122
B.1	Plot of $\eta$ as function of $\vartheta$ . . . . .	133
C.1	Dependence of $\varepsilon_{\text{QCD}}$ on the lepton isolation . . . . .	137
D.1	Electron trigger efficiency correction factors . . . . .	145
D.2	Muon trigger efficiency correction factors . . . . .	145
D.3	Distributions of discriminating variables . . . . .	146
D.4	Overtraining check for the BDT classifier . . . . .	147
D.5	Reference PDFs for the projective likelihood approach . . . . .	148
D.6	Templates for the visible mass distribution . . . . .	149
D.7	Dependence of $R_{\text{OS/SS}}$ on the lepton isolation . . . . .	150



# List of Tables

2.1	Fermions in the SM . . . . .	3
2.2	Gauge bosons in the SM . . . . .	4
2.3	Quantum numbers of the fermions . . . . .	5
2.4	Limits on the SM Higgs boson mass . . . . .	8
2.5	Particle Content of the MSSM . . . . .	12
2.6	Modified Higgs couplings in the MSSM . . . . .	14
3.1	Performance of lepton identification and reconstruction algorithms . . . . .	30
4.1	Branching ratios for the decay of the $Z$ boson and the $\tau$ lepton . . . . .	39
5.1	Trigger efficiency correction factors . . . . .	51
5.2	Event yields in the signal region . . . . .	58
5.3	QCD multijet estimation with the ABCD method . . . . .	63
5.4	Control regions for $W$ decays . . . . .	64
5.5	Control region for $t\bar{t}$ events . . . . .	65
5.6	Fiducial phase space region . . . . .	66
5.7	Systematic uncertainty on the ratio $R_{\text{OS/SS}}$ . . . . .	71
5.8	Systematic uncertainty on the selection efficiency $\varepsilon_{\text{QCD}}$ . . . . .	72
5.9	Systematic uncertainties on the acceptance factor $A_Z$ . . . . .	74
5.10	Systematic uncertainties on the correction factor $C_Z$ . . . . .	74
5.11	Systematic uncertainties on the background estimates . . . . .	75
5.12	Final input for the cross section calculation . . . . .	76
6.1	Event yields expected after the baseline selection . . . . .	86
6.2	Event yields in control regions for $t\bar{t}$ and di-boson processes . . . . .	91
6.3	Variable sets with optimal performance . . . . .	99
6.4	Achieved performance for optimal variable sets . . . . .	99
6.5	Cut values on the classifier response functions . . . . .	101
6.6	Comparison of event yields for different selection strategies . . . . .	102
6.7	Final event yields in the signal region . . . . .	103
6.8	Numbers for multijet background estimation . . . . .	104
6.9	Event yields in the control region for $t\bar{t}$ , single top and di-boson events . . . . .	105
6.10	Relative systematic uncertainties . . . . .	118
6.11	Parameters for the event counting analysis . . . . .	119
C.1	Simulated data sets used . . . . .	138

C.2	Jet cleaning cuts . . . . .	139
C.3	Object definitions . . . . .	140
C.4	Electron identification efficiency correction factors . . . . .	141
C.5	Lepton isolation efficiency correction factors . . . . .	141
C.6	Pile-up correction factors . . . . .	141
C.7	Event yields in the signal and the three control regions . . . . .	142
D.1	Simulated data sets used . . . . .	151
D.2	Object definitions . . . . .	152
D.3	Muon trigger efficiency correction factors . . . . .	153
D.4	Electron reconstruction efficiency correction factors . . . . .	153
D.5	Electron identification efficiency correction factors . . . . .	154
D.6	TMVA configuration options . . . . .	154
D.7	Variable sets under investigation . . . . .	155
D.8	Performance of variable sets . . . . .	155

# Chapter 1

## Introduction

The era of modern particle physics started with the discovery of the electron by THOMSON in 1897 [1]. Shortly after, experiments by EINSTEIN and COMPTON revealed particle properties of light which contradict MAXWELL's theory of electromagnetic waves. This ambiguity is explained by the theory of Quantum Electrodynamics (QED) founded by DIRAC in the 1920's which interprets the photon as light quantum. In 1934, FERMI gave the first theoretical description for  $\beta$ -decays of nuclei by adopting the idea of neutrinos from PAULI and by postulating a four-fermion interaction [2]. During the 1960's, contributions from GLASHOW, SALAM and WEINBERG led to a joint description of electromagnetic and weak interactions by the electroweak theory [3–5]. The four-fermion contact interaction of the FERMI theory is replaced by the exchange of  $W$  and  $Z$  bosons which were discovered by experiments at CERN<sup>1</sup> in 1983 [6–9]. The formulation of Quantum Chromodynamics (QCD) as the theory of strong interactions was proved by the discovery of the gluon at DESY in 1979 [10]. In 1964, HIGGS and others proposed a mechanism for spontaneous symmetry breaking in the electroweak sector in order to allow for massive particles [11, 12]. This mechanism introduces a further scalar field, the *Higgs* field, whose vacuum expectation value gives rise to the gauge boson masses. The Standard Model of Particle Physics (SM) describes all known elementary particles and their interactions except for gravity. Its predictions have been tested in a vast number of experiments to very high precision. Solely, an experimental observation of the postulated Higgs boson is missing to complete the list of SM particles.

Notwithstanding the thorough experimental verification of the SM, it is expected to be an effective theory for energies at and below the electroweak scale<sup>2</sup>  $v \approx 246$  GeV which is embedded in a more fundamental theory. Moreover, there are theoretical motivations and experimental indications that the SM does not provide a complete description of nature and needs to be extended. As symmetries play an important role in various fields of physics, the idea of Supersymmetry (SUSY) is considered as promising candidate for *Beyond Standard Model* (BSM) theories. Supersymmetric theories exhibit a fermion-boson symmetry which doubles the number of particles by introducing super-partners. Theoretical arguments suggest that the masses of new particles are at the TeV scale.

In order to identify the mechanism of electroweak symmetry breaking and to explore the parameter space of BSM theories, the Large Hadron Collider (LHC) has been installed

---

<sup>1</sup>Conseil Européen pour la Recherche Nucléaire

<sup>2</sup>In this thesis natural units, which are explained in Appendix A.1.1, are used.

---

at CERN. It will be able to produce proton-proton collisions at a centre-of-mass energy up to  $\sqrt{s} = 14$  TeV with a very high rate. This unprecedented energy scale and the huge amount of data expected allow for probing the parameter space of BSM theories. To this end, two multi-purpose particle detectors, ATLAS<sup>3</sup> and CMS<sup>4</sup>, are installed at the LHC which are capable of detecting and analysing a wide range of physics processes.

The LHC started operation in November 2009 and since the 30<sup>th</sup> of March 2010 proton-proton collision at a centre-of-mass energy of  $\sqrt{s} = 7$  TeV have been taking place. In this thesis, experimental data from proton-proton collisions recorded by the ATLAS detector during 2010 and the first half of 2011 is analysed. The goal of this thesis is the evaluation of the recorded data with regard to the Higgs sector of the Minimal Supersymmetric Standard Model (MSSM) in the context of the  $m_h^{\text{max}}$  scenario. The Higgs sector of the MSSM contains two Higgs doublets which yield three neutral  $h/H/A$  and two charged  $H^\pm$  Higgs bosons. A search for the neutral MSSM Higgs bosons in the channel  $h/H/A \rightarrow \tau^+\tau^- \rightarrow e\mu + 4\nu$  is performed.

Before the data can be analysed, the detector and its performance needs to be understood. The well-known SM processes are of great help for testing and improving reconstruction techniques and analysis strategies. Since  $pp \rightarrow \gamma^*/Z \rightarrow \tau^+\tau^-$  events constitute the largest background for the MSSM Higgs boson search, a deep understanding of this process and its properties is an essential precondition. Therefore, the first part of this thesis is devoted to the cross section measurement of the process  $pp \rightarrow \gamma^*/Z \rightarrow \tau^+\tau^-$  with the 2010 data set corresponding to an integrated luminosity of  $L = 35.5 \text{ pb}^{-1}$ . Thereby, the focus is put on a data-driven estimation of the background contribution arising from QCD processes and its uncertainty.

In the second part of this thesis, a search for neutral MSSM Higgs bosons in the parameter range<sup>5</sup>  $M_A = 100 - 150 \text{ GeV}$  and  $\tan\beta = 5 - 50$  is performed. For this purpose, the data taken during the first half of 2011 which amounts to an integrated luminosity of  $L = 1.06 \text{ fb}^{-1}$  is used. The event selection is optimised and different multivariate methods are investigated with respect to their rejection power against reducible background components. Furthermore, the interpretation of the data observed requires advanced statistical methods for deriving solid statements on the parameter space of the MSSM. This work reviews two methods based on the profile likelihood method, an *event counting* approach and a *shape analysis*, and evaluates their feasibility.

The theoretical framework of the SM and the phenomenology of the Higgs sector in the MSSM are outlined in Chapter 2. The experimental setup with focus on particle detection and identification with the ATLAS detector is described in Chapter 3. Chapter 4 reviews briefly the event topology of the signal processes and lists the background processes considered. In Chapter 5 the measurement of the cross section for the process  $pp \rightarrow \gamma^*/Z \rightarrow \tau^+\tau^-$  in the  $e\mu + 4\nu$  final state is presented. The search for neutral MSSM Higgs bosons in the the channel  $h/H/A \rightarrow \tau^+\tau^- \rightarrow e\mu + 4\nu$  is detailed in Chapter 6. Finally, the results are summarised and discussed in Chapter 7.

---

<sup>3</sup>A Toroidal LHC ApparatuS

<sup>4</sup>Compact Muon Solenoid

<sup>5</sup>For an explanation of these parameters, please refer to Section 2.2.2.

# Chapter 2

## Theoretical Foundations

In order to explain the occurring processes at the LHC, a theory, capable of describing high energy interactions at microscopic scales, is needed. The combination of Quantum Mechanics (QM) and the theory of relativity leads to the formulation of Quantum Field Theories (QFT). A popular example of a quantum field theory is the SM which is currently the best tested theory for elementary particles and their interactions. A brief description of the SM with emphasis on phenomenological implications is given in Section 2.1.

Although the Standard Model is extensively tested and no significant deviations from its predictions were found so far, many BSM theories have been suggested to solve the experimental and theoretical shortcomings of the SM. In the context of this work, the Higgs sector of the MSSM is investigated. A brief motivation for SUSY and the MSSM is given in Section 2.2.

### 2.1 The Standard Model of Particle Physics

The particles, which are currently believed to be elementary, can be categorised according to their spin  $S$  into fermions with half-integer spin, and bosons with integer spin values. Fermions are further divided into leptons which do not interact via the strong force and quarks which undergo strong interactions. Furthermore, the fermions come in three different generations which behave identically under the symmetry transformation explained below and differ only in the masses of the contained particles. There are always two different flavours of leptons and quarks per generation which yields in total 12 fermions as shown in Table 2.1. The SM is a quantum field theory which incorporates the

type	first generation		second generation		third generation	
	flavour	mass	flavour	mass	flavour	mass
lepton	$\nu_e$	$< 2 \text{ eV}$	$\nu_\mu$	$< 2 \text{ eV}$	$\nu_\tau$	$< 2 \text{ eV}$
	$e$	512 keV	$\mu$	105.6 MeV	$\tau$	1.777 GeV
quark	$u$	$\approx 2.5 \text{ MeV}$	$c$	1.27 GeV	$t$	172 GeV
	$d$	$\approx 5 \text{ MeV}$	$s$	101 MeV	$b$	4.2 GeV

**Table 2.1:** Fermionic particle content of the Standard Model [13].

boson	mass	electric charge	symmetry group
$\gamma$	$< 10^{-18}$ eV	0	$U(1)_Y \otimes SU(2)_L$
$Z$	91.188 GeV	0	$U(1)_Y \otimes SU(2)_L$
$W^\pm$	80.40 GeV	$\pm 1$	$U(1)_Y \otimes SU(2)_L$
$g$	0 eV <sup>1</sup>	0	$SU(3)_C$

**Table 2.2:** Gauge bosons in the Standard Model [13].

concept of local gauge invariance. Particles which are charged under a certain symmetry group can interact with each other. This interaction is mediated by the gauge bosons associated to this symmetry group. The symmetry group of the SM is given by

$$U(1)_Y \otimes SU(2)_L \otimes SU(3)_C \quad (2.1)$$

and gives rise to the gauge bosons outlined in Table 2.2. In the next sections the electroweak (EW) sector of the SM and the Higgs mechanism are discussed in more detail followed by a brief description of strong interactions and their experimental implications.

### 2.1.1 Electroweak Gauge Theory

Local gauge symmetries can be described by YANG–MILLS theories [14] whose general concept is reviewed in Appendix A.3. The electroweak sector of the SM corresponds to a YANG–MILLS theory with a  $U(1)_Y \otimes SU(2)_L$  symmetry group.

#### The $U(1)_Y \otimes SU(2)_L$ symmetry group

The choice of the  $U(1)_Y \otimes SU(2)_L$  symmetry group for the electroweak sector of the SM is motivated by the following experimental observations:

- Electromagnetic interactions of fermions are proportional to their electric charge  $Q$  and do not change the particle flavour.
- Neutrinos do not interact electromagnetically ( $\Rightarrow Q_\nu = 0$ ).
- Weak interactions can change the flavour of particles and violates the parity symmetry<sup>2</sup>.
- No right chiral<sup>3</sup> neutrinos have been observed.

---

<sup>1</sup>This is the theoretical value.

<sup>2</sup>Parity transformation affects all spatial coordinates:  $\vec{x} \rightarrow \vec{x}' = -\vec{x}$ .

<sup>3</sup>A spinor  $\psi$  can be decomposed in its left chiral  $\psi_L$  and right chiral component  $\psi_R$  using the projection operators  $\hat{P}_L = \frac{1}{2}(\mathbb{1} - \gamma_5)$  and  $\hat{P}_R = \frac{1}{2}(\mathbb{1} + \gamma_5)$ . See also Appendix A.2 for more details.

particles			$Y_L$	$T_3$	$Q$
$\begin{pmatrix} \nu_e \\ e \end{pmatrix}_L$	$\begin{pmatrix} \nu_\mu \\ \mu \end{pmatrix}_L$	$\begin{pmatrix} \nu_\tau \\ \tau \end{pmatrix}_L$	$-\frac{1}{2}$	$\frac{1}{2}$	0
$\begin{pmatrix} u \\ d \end{pmatrix}_L$	$\begin{pmatrix} c \\ s \end{pmatrix}_L$	$\begin{pmatrix} t \\ b \end{pmatrix}_L$	$-\frac{1}{2}$	$-\frac{1}{2}$	-1
			$\frac{1}{6}$	$\frac{1}{2}$	$\frac{2}{3}$
			$\frac{1}{6}$	$-\frac{1}{2}$	$-\frac{1}{3}$
$e_R$	$\mu_R$	$\tau_R$	-1	0	-1
$u_R$	$c_R$	$t_R$	$\frac{2}{3}$	0	$\frac{2}{3}$
$d_R$	$s_R$	$b_R$	$-\frac{1}{3}$	0	$-\frac{1}{3}$

**Table 2.3:** Quantum numbers of all fermions<sup>6</sup> for the  $U(1)_Y \otimes SU(2)_L$  symmetry.

The corresponding charges are called *Hypercharge*  $Y_L$  for the  $U(1)_Y$  symmetry group and *weak isospin*  $\vec{T} = (T_1, T_2, T_3)$  for the  $SU(2)_L$  symmetry group. While the former symmetry applies to all fermions, only the left chiral components are affected by  $SU(2)_L$  symmetry transformations. All transformations<sup>4</sup> for the left chiral  $SU(2)_L$  doublets and right chiral  $SU(2)_L$  singlets are given by

$$L = \begin{pmatrix} \nu_{e,L} \\ e_L \end{pmatrix} \rightarrow L' = e^{iY_L\alpha(x)} e^{i\sum_a \vartheta_a(x)T_a} L, \quad (2.2)$$

$$Q = \begin{pmatrix} u_L \\ d_L \end{pmatrix} \rightarrow Q' = e^{iY_L\alpha(x)} e^{i\sum_a \vartheta_a(x)T_a} Q, \quad (2.3)$$

$$e_R \rightarrow e'_R = e^{iY_L\alpha(x)} e_R, \quad (2.4)$$

$$u_R \rightarrow u'_R = e^{iY_L\alpha(x)} u_R, \quad (2.5)$$

$$d_R \rightarrow d'_R = e^{iY_L\alpha(x)} d_R \quad (2.6)$$

with  $T_a = \sigma_a/2$  being half of the PAULI matrices and  $\alpha, \vartheta_a$  being real, continuous transformation parameters.

Table 2.3 summarises the charges of all fermions with the electric charge<sup>5</sup>  $Q$  defined as  $Q = Y_L + T_3$ . The covariant derivative for this particular symmetry group is given as

$$D_\mu = \partial_\mu + ig_W W_\mu^a T_a + ig_Y Y_L B_\mu \quad (2.7)$$

with the gauge boson fields  $W_\mu^a$  and  $B_\mu$ . Possible mass terms for fermions and bosons whose general forms are given by

$$\mathcal{L}_{\text{mass,fermion}} \propto m \bar{\psi} \psi = m (\bar{\psi}_L \psi_R + \bar{\psi}_R \psi_L), \quad (2.8)$$

$$\mathcal{L}_{\text{mass,boson}} \propto M^2 W^\mu W_\mu \quad (2.9)$$

<sup>4</sup>For simplicity, the notation is restricted to fermions of the first generation.

<sup>5</sup>The electric charge  $Q$  is given in multiples of the elementary charge  $e = 1.6 \cdot 10^{-19}$  As.

<sup>6</sup>Antiparticles carry opposite charges.

were omitted so far as they would break the invariance of the Lagrangian under local symmetry transformations.

Unfortunately, the assumption of mass less particles contradicts the experimental observation of massive fermions and bosons whose masses differ from 512 keV for the electron up to 172 GeV for the top quark. Therefore, a mechanism is needed to describe massive fields and introduce mass terms in a way that is compatible with the requirement of local gauge invariance.

### 2.1.2 Higgs Mechanism

The Higgs<sup>7</sup> mechanism [11, 12, 15] postulates an additional doublet  $\Phi$  of complex scalar fields with the potential

$$V(\Phi) = -\mu^2 \Phi^\dagger \Phi + \lambda (\Phi^\dagger \Phi)^2, \quad \lambda > 0. \quad (2.10)$$

The hypercharge is chosen to be  $Y_\Phi = \frac{1}{2}$  such that the lower component of the doublet does not carry any electric charge,

$$\Phi = \begin{pmatrix} \phi^+ \\ \phi^0 \end{pmatrix}. \quad (2.11)$$

Analogously to a complex scalar field, the Lagrangian for the Higgs sector is given by

$$\mathcal{L}_{\text{Higgs}} = (D^\mu \Phi)^\dagger (D_\mu \Phi) - V(\Phi) \quad (2.12)$$

which is invariant under  $U(1)_Y \otimes SU(2)_L$  symmetry transformations. Depending on the sign of  $\mu^2$ , the minimum of the potential is found to be:

$$\mu^2 \leq 0 : \frac{\partial V}{\partial \Phi} = 0 \rightarrow |\Phi_{\min}| = 0, \quad (2.13)$$

$$\mu^2 > 0 : \frac{\partial V}{\partial \Phi} = 0 \rightarrow |\Phi_{\min}| = \sqrt{\frac{\mu^2}{2\lambda}} \equiv \frac{v}{\sqrt{2}}. \quad (2.14)$$

The vacuum expectation value  $\langle 0|\Phi|0\rangle$  vanishes in the first case and the ground state of the Higgs field is symmetric under  $U(1)_Y \otimes SU(2)_L$ . However, if  $\mu^2 > 0$ , a non-zero vacuum expectation value exists. Since no positive charged permanent background field is observed, the ground state must take the form

$$\Phi_0 = \begin{pmatrix} 0 \\ \frac{v}{\sqrt{2}} \end{pmatrix} \quad (2.15)$$

which obviously violates the  $U(1)_Y \otimes SU(2)_L$  symmetry. Considering measurements of the muon decay width, the vacuum expectation value can be constrained to  $v \approx 246$  GeV. The fact that the ground state does not exhibit the full symmetry of the Lagrangian in Equation (2.12) is called *spontaneous symmetry breaking*.

---

<sup>7</sup>named after Peter W. Higgs



Expanding the Higgs doublet around its minimum introduces four real scalar fields which correspond to excitations of the ground state,

$$\Phi_{\text{full}} = \begin{pmatrix} \xi_1(x) + i\xi_2(x) \\ \frac{1}{\sqrt{2}}(v + h(x)) + i\eta(x) \end{pmatrix}. \quad (2.16)$$

Since an infinitesimal  $U(1)_Y \otimes SU(2)_L$  symmetry transformation takes the form

$$e^{i\beta(x)Y_\Phi} e^{i\alpha_a(x)T_a} \Phi_0 = [\mathbb{1}_2 + i\alpha_a(x)T_a + i\beta(x)Y_\Phi] \Phi_0 + \mathcal{O}(\alpha_a^2, \beta^2) \quad (2.17)$$

$$= \Phi_0 + \frac{v}{2\sqrt{2}} \begin{pmatrix} \alpha_2(x) + i\alpha_1(x) \\ i(\beta(x) - \alpha_3(x)) \end{pmatrix} + \mathcal{O}(\alpha_a^2, \beta^2), \quad (2.18)$$

the fields  $\xi_1$ ,  $\xi_2$  and  $\eta$  can be eliminated by applying a gauge transformation. Hence, these fields have no physical meaning and correspond to the mass less GOLDSTONE bosons which occur when a continuous symmetry is spontaneously broken. The remaining field  $h(x)$  is called the Higgs field and is linked to the Higgs boson. Using the *unitary gauge*, the Higgs doublet becomes

$$\Phi = \frac{1}{\sqrt{2}} \begin{pmatrix} 0 \\ v + h(x) \end{pmatrix} \quad (2.19)$$

and can be employed for evaluating the covariant derivative in Equation (2.12).

It turns out that the mass eigenstates of the gauge bosons are linear combinations of the four gauge boson fields  $W_\mu^a, B_\mu$  with  $\theta_W$  being the weak mixing angle,

$$W_\mu^\pm = \frac{1}{\sqrt{2}} (W_\mu^1 \mp iW_\mu^2), \quad (2.20)$$

$$\begin{pmatrix} A_\mu \\ Z_\mu \end{pmatrix} = \begin{pmatrix} \cos \theta_W & \sin \theta_W \\ -\sin \theta_W & \cos \theta_W \end{pmatrix} \begin{pmatrix} B_\mu \\ W_\mu^3 \end{pmatrix}. \quad (2.21)$$

The resulting linear combinations are also eigenstates to the operator  $Q = Y_L + T_3$  which can be identified with the electric charge. As the Higgs ground state is electrical neutral, the remaining symmetry group is the  $U(1)_Q$ .

Finally, one finds

$$(D^\mu \Phi)^\dagger (D_\mu \Phi) = \frac{g_W^2 v^2}{4} \left[ W^{+\mu} W_\mu^- + \frac{1}{2 \cos^2 \theta_W} Z^\mu Z_\mu \right] \left( 1 + \frac{h}{v} \right)^2 + \frac{1}{2} (\partial^\mu h) (\partial_\mu h) \quad (2.22)$$

from which one can identify the gauge boson masses

$$M_W = \frac{g_W v}{2}, \quad (2.23)$$

$$M_Z = \frac{g_W v}{2 \cos \theta_W} = \frac{M_W}{\cos \theta_W}, \quad (2.24)$$

$$M_A = 0. \quad (2.25)$$

scattering amplitude of gauge bosons	$M_H \leq 850 \text{ GeV}$
validity of the SM up to $\Lambda \approx 1 \text{ TeV}$	$M_H \leq 750 \text{ GeV}$
vacuum stability of the Higgs potential for $\Lambda \approx 1 \text{ TeV}$	$M_H \geq 60 \text{ GeV}$
electroweak precision measurements	$M_H = 76^{+33}_{-24} \text{ GeV}$
LEP (95% confidence level)	$M_H \geq 114.1 \text{ GeV}$
ATLAS (95% confidence level)	$M_H \notin [131 \text{ GeV}, 237 \text{ GeV}]$ $M_H \notin [251 \text{ GeV}, 453 \text{ GeV}]$

**Table 2.4:** Theoretical bounds on the SM Higgs boson mass and experimentally observed exclusion limits [16–18].

Furthermore, the coupling of the gauge bosons to the Higgs field are proportional to the square of the gauge boson mass.

Expanding the term for the Higgs potential, the mass of the Higgs boson is found to be

$$M_H^2 = 2\lambda v^2, \quad (2.26)$$

which is a free parameter of the theory. Limits on the Higgs mass can be derived from theoretical considerations and are given in Table 2.4 together with observed exclusion limits from direct Higgs searches at LEP<sup>8</sup> and ATLAS (cf. Figure 2.1). To account for non-zero fermion masses, YUKAWA terms can be added to the Lagrangian “by hand”. The corresponding part for the first fermion generation is<sup>9</sup>

$$\mathcal{L}_{\text{Yukawa}} = y_e \bar{L} \Phi e_R + y_d \bar{Q} \Phi d_R + y_u \bar{Q} \Phi^C u_R + \text{h.c.} \quad (2.27)$$

$$= \left[ \frac{y_e v}{\sqrt{2}} \bar{e} e + \frac{y_d v}{\sqrt{2}} \bar{d} d + \frac{y_u v}{\sqrt{2}} \bar{u} u \right] \left( 1 + \frac{h}{v} \right). \quad (2.28)$$

The fermion masses are given by  $M_f = y_f v / \sqrt{2}$  and the couplings to the Higgs field are proportional to the fermion masses.

The complete electroweak Lagrangian and its derivation can be found in Appendix A.4. Since the interactions of the  $Z$  boson are of major interest, the relevant part of the Lagrangian is stated below:

$$\mathcal{L}_{\text{EW}|Z_\mu} = -\frac{g_W}{2 \cos \theta_W} \bar{\psi} (c_V \gamma^\mu - c_A \gamma^\mu \gamma^5) \psi Z_\mu \quad (2.29)$$

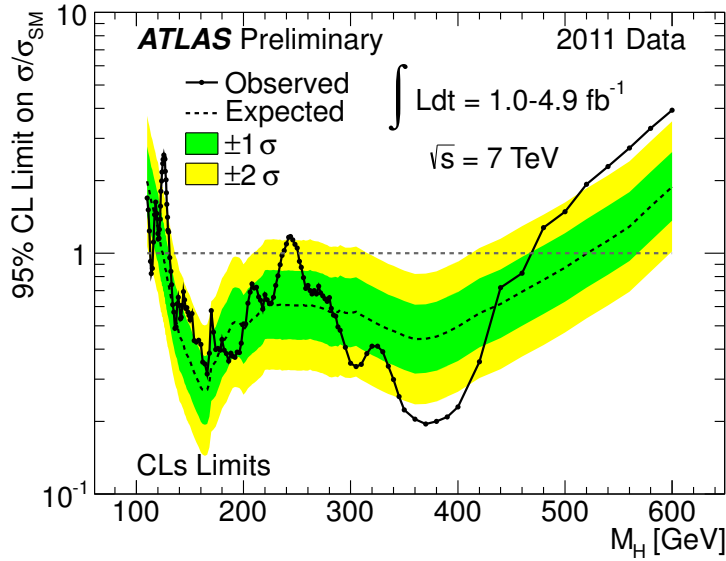
$$\text{with } c_V = T_3 - 2 \sin^2 \theta_W Q \quad (2.30)$$

$$\text{and } c_A = T_3. \quad (2.31)$$

---

<sup>8</sup>Large Electron Positron Collider

<sup>9</sup> $\Phi^C = i\sigma_2 \Phi$



**Figure 2.1:** The combined upper limit on the SM Higgs boson production cross section divided by the SM expectation as a function of  $M_H$  is indicated by the solid line. This is a 95% confidence level limit using the  $CL_s$  method [19]. The dotted line shows the median expected limit in the absence of a signal and the green and yellow bands indicate the corresponding 68% and 95% expected regions [18].

### 2.1.3 Quantum Chromodynamics

Strong interactions are generated by a local  $SU(3)_C$  gauge invariance which gives rise to eight massless vector bosons, the *gluons*. The corresponding charge is called *colour* and can describe three different states labelled red, green and blue. Among the fermions only the quarks are charged under  $SU(3)_C$  whereas the leptons do not participate in strong interactions.

An important property of QCD is the fact that no free, coloured particles have been observed so far which leads to the conclusion that all free particles must be in a colour singlet state. This effect is called *colour confinement*. In particular, individual partons<sup>10</sup> which might be produced in hadron-hadron collisions, must undergo further strong interactions to reach a colour singlet state. Thereby, other hadrons are necessarily produced. Thus, a parton manifests itself as a shower of hadrons at the macroscopic scale. The transition from coloured partons produced in a collision to a set of colourless hadrons is referred to as *hadronisation*.

Furthermore, the strong coupling  $\alpha_S = g_S/(4\pi)$ , as all coupling constants, is a function of the renormalisation<sup>11</sup> scale but exhibits an opposed scale dependence compared to

<sup>10</sup>Parton refers to any possible constituent of a proton and comprises the particle classes of quarks and gluons.

<sup>11</sup>The concept of renormalisation is not discussed in the context of this work but the idea can be summarised as follows: Higher order calculations can depend on an arbitrary scale  $\mu_R$  which is introduced to regularise occurring loop integrals. Parameters of the Lagrangian can be redefined

QED. While the electromagnetic coupling increases with increasing energy, the behaviour is reversed for the strong coupling leading to *asymptotic freedom* at high energies (or equivalently, at short distances). On the other hand, the coupling strength becomes large at low energies causing a breakdown of the perturbation principle. Therefore, empirical models must be used to treat hadron decays in the low energy regime.

## 2.2 Supersymmetry

There is a consensus among physicists that the SM can not be a complete description of nature. It has shortcomings on both the experimental and the theoretical side which can be overcome by possible extensions. The choice of Supersymmetry as a promising candidate is motivated in the next section, followed by a brief description of the Higgs sector in the MSSM and its phenomenology.

### 2.2.1 Motivation

The SM shows an excellent agreement between its prediction of many observables and the corresponding precision measurements [20]. However, it can not explain all experimental observations and does not answer all theoretical questions. Three representative deficits are:

#### Dark matter

Astrophysical data indicates the existence of non-baryonic, weakly interacting and neutral matter of unknown composition, so-called *Dark Matter*. Supersymmetry increases the number of particles and contains weakly interacting massive particles (WIMPs) which are favourite dark matter candidates.

#### Grand unification

Embedding the SM in a more fundamental framework, is theoretically very appealing. The unification of the symmetry structure of the SM into a larger symmetry group leads to the formulation of *Grand Unified Theories* (GUT). Below some energy scale the generic theory could be broken into the symmetry group of the SM which is then interpreted as low energy limit. An indication for this is given by the running couplings which *almost* meet at a scale of  $\approx 10^{15}$  GeV. The scale dependence is affected by the possible existence of SUSY particles. For masses of SUSY particles in the range of 1 – 10 TeV an unification of all three coupling constants at  $\mu \approx 10^{16}$  GeV is achieved [21].

#### Hierarchy problem

Higher order loop corrections to the Higgs mass take the form  $\delta M_H^2 \propto \Lambda^2$  where  $\Lambda$

---

to absorb divergences and thereby become functions of the renormalisation scale. It can be shown that higher order corrections scale  $\propto \log \frac{E}{\mu_R}$  with  $E$  being a typical energy in the process under consideration. Choosing an appropriate scale  $\mu_R \approx E$  can therefore decrease the impact of higher order terms. Hence, the coupling constant  $g(\mu_R)$  can be interpreted as *effective* coupling constant for processes at the energy scale of  $\mu_R$ .

is the energy scale up to which the SM is expected to be valid [22]. Putting in the GUT scale  $\Lambda \approx 10^{15}$  GeV where new physics is expected to show up, would require a severe *fine-tuning* of the order of  $(v/10^{15} \text{ GeV})^2 = \mathcal{O}(10^{-26})$  which seems unnatural. Supersymmetry could solve this problem as each fermion has a bosonic partner yielding the same correction but with opposite sign. Therefore, the cancellation of higher order correction terms would be exact and automatic<sup>12</sup>.

### 2.2.2 Minimal Supersymmetric Standard Model

In a SUSY theory, the symmetry of the SM is extended by a further symmetry between fermionic and bosonic states which are linked by an operator  $Q$  and arranged in super-multiplets. More precisely,  $Q$  is a spinor operator which commutes with the four-momentum operator  $P^\mu$  and all generators of the  $U(1)_Y \otimes SU(2)_L \otimes SU(3)_C$  symmetry but changes the spin. The partners of the leptons and quarks are called *sleptons* and *squarks* respectively while the partners of the gauge and Higgs bosons are named *gauginos* and *higgsinos*.

$$Q |\text{Fermion}\rangle \propto |\text{Boson}\rangle \quad (2.32)$$

$$[Q, P^\mu] = 0 \quad (2.33)$$

$$[Q, T_a] = [Q, Y_L] = [Q, \lambda_i] = 0 \quad (2.34)$$

It follows from Equation (2.33) that  $Q$  also commutes with  $P^\mu P_\mu$  and, thus, particles in the same super-multiplet have the same mass. Since no light SUSY particles have been observed so far (for instance, no scalar particle with a mass of 512 keV which could be interpreted as *selectron* has been discovered), Supersymmetry must be broken at a higher mass scale  $M_{\text{SUSY}}$ . As the details of the responsible mechanism are unknown, explicitly SUSY breaking terms are added to the MSSM Lagrangian in a way which avoids the re-occurrence of the fine-tuning problem (*soft Supersymmetry breaking*) [23].

In general, Supersymmetry allows terms in the Lagrangian which violates the conservation of the total lepton or baryon number. These terms are not included in the MSSM as the stability of the proton imposes severe constraints on possible baryon number violating effects. Instead of formulating an explicit lepton and baryon number symmetry in the MSSM, one rather introduces the *R-parity* defined as

$$P_R = (-1)^{3(B-L)+2s} \quad (2.35)$$

which is a multiplicative and conserved quantum number. As the angular momentum conservation is ensured at every vertex, the product of  $(-1)^{2s}$  is always equal to +1 for all involved particles and, therefore,  $B - L$  is conserved as well. Furthermore, SM particles have  $P_R = +1$  while their super-partners have odd parity  $P_R = -1$ . As important

<sup>12</sup>This statement is only true for an exact Supersymmetry which implies that all SM particles and their supersymmetric partners have the same mass. As no SUSY particles at the electroweak energy scale have been observed, SUSY must be broken at a scale  $M_{\text{SUSY}}$  and the corrections remain of the order  $\delta M_H^2 \propto \alpha_{\text{EM}} \cdot M_{\text{SUSY}}^2$  which leads to the requirement of  $M_{\text{SUSY}} = \mathcal{O}(1 \text{ TeV})$  in order to avoid a precise fine-tuning.

## 2.2 Supersymmetry

SM particles					super partners				
leptons ( $S = \frac{1}{2}$ )	$\nu_{e,L}$	$\nu_{\mu,L}$	$\nu_{\tau,L}$		$\tilde{\nu}_{e,L}$	$\tilde{\nu}_{\mu,L}$	$\tilde{\nu}_{\tau,L}$	sleptons ( $S = 0$ )	
	$e_L$	$\mu_L$	$\tau_L$		$\tilde{e}_L$	$\tilde{\mu}_L$	$\tilde{\tau}_L$		
	$e_R$	$\mu_R$	$\tau_R$		$\tilde{e}_R$	$\tilde{\mu}_R$	$\tilde{\tau}_R$		
quarks ( $S = \frac{1}{2}$ )		$u_L$	$c_L$	$t_L$		$\tilde{u}_L$	$\tilde{c}_L$	$\tilde{t}_L$	squarks ( $S = 0$ )
		$u_R$	$c_R$	$t_R$		$\tilde{u}_R$	$\tilde{c}_R$	$\tilde{t}_R$	
		$d_L$	$s_L$	$b_L$		$\tilde{d}_L$	$\tilde{s}_L$	$\tilde{b}_L$	
		$d_R$	$s_R$	$b_R$		$\tilde{d}_R$	$\tilde{s}_R$	$\tilde{b}_R$	
gauge bosons ( $S = 1$ )	$W^{1,2,3}$	$B$	$g^{1\dots 8}$		$\tilde{W}^{1,2,3}$	$\tilde{B}$	$\tilde{g}^{1\dots 8}$		gauginos ( $S = \frac{1}{2}$ )
Higgs bosons ( $S = 0$ )	$H_u^+$	$H_u^0$	$H_d^-$	$H_d^0$	$\tilde{H}_u^+$	$\tilde{H}_u^0$	$\tilde{H}_d^-$	$\tilde{H}_d^0$	higgsinos ( $S = \frac{1}{2}$ )

**Table 2.5:** Particle content of the MSSM.

implications, SUSY particles must always be produced in pairs and the lightest supersymmetric particle (LSP) can not decay further and, therefore, provides an attractive candidate for the non-baryonic dark matter observed in cosmology.

The simplest supersymmetric extension of the SM has the same symmetry group but requires two Higgs doublets to generate masses for up-type and down-type fermions. The whole particle content of the MSSM is listed in Table 2.5.

As already stated, the MSSM Higgs sector contains two complex doublets  $H_u$  and  $H_d$  with hypercharges  $Y_u = -\frac{1}{2}$  and  $Y_d = \frac{1}{2}$  respectively. Similarly to the SM case, the MSSM Higgs potential has a stable minimum which breaks the local symmetry. The expansion around this minimum leads to the parametrisation of the Higgs doublets as given in Equation (2.36) and yields eight mixed fields:

$$H_u = \frac{1}{\sqrt{2}} \begin{pmatrix} v_u + H_u^0 + iP_u^0 \\ H_u^- \end{pmatrix}, \quad H_d = \frac{1}{\sqrt{2}} \begin{pmatrix} H_d^+ \\ v_d + H_d^0 + iP_d^0 \end{pmatrix}, \quad (2.36)$$

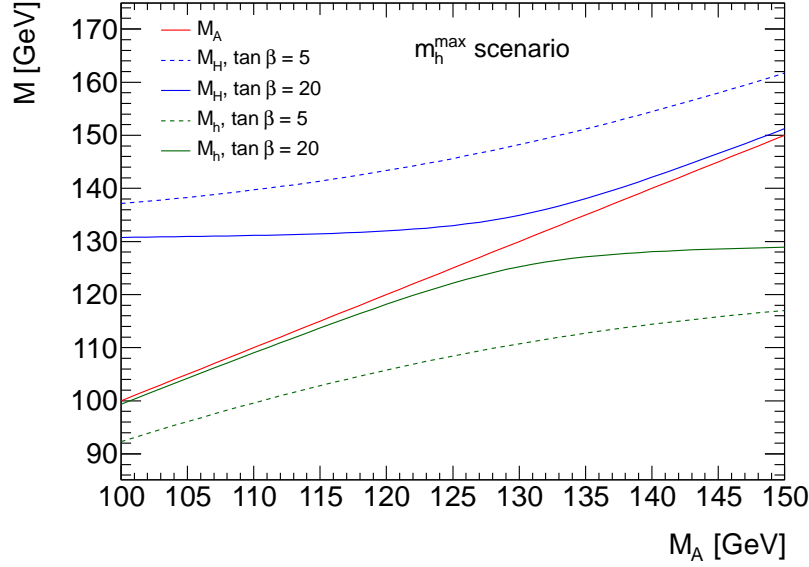
$$\begin{pmatrix} G^0 \\ A^0 \end{pmatrix} = \begin{pmatrix} \cos \beta & \sin \beta \\ -\sin \beta & \cos \beta \end{pmatrix} \begin{pmatrix} P_u^0 \\ P_d^0 \end{pmatrix}, \quad (2.37)$$

$$\begin{pmatrix} G^\pm \\ H^\pm \end{pmatrix} = \begin{pmatrix} \cos \beta & \sin \beta \\ -\sin \beta & \cos \beta \end{pmatrix} \begin{pmatrix} H_u^\pm \\ H_d^\pm \end{pmatrix}, \quad (2.38)$$

$$\begin{pmatrix} H^0 \\ h^0 \end{pmatrix} = \begin{pmatrix} \cos \alpha & \sin \alpha \\ -\sin \alpha & \cos \alpha \end{pmatrix} \begin{pmatrix} H_u^0 \\ H_d^0 \end{pmatrix}. \quad (2.39)$$

Breaking the continuous  $U(1)_Y \otimes SU(2)_L$  symmetry generates three mass less Goldstone bosons which can be identified with  $G^0$  and  $G^\pm$ . Thus, two charged Higgs bosons  $H^\pm$  remain as well as three neutral<sup>13</sup> Higgs bosons  $\phi = h, H, A$  of which  $A$  is odd under

<sup>13</sup>For the rest of this work  $\phi$  always refers to any of the neutral MSSM Higgs bosons if not stated otherwise.



**Figure 2.2:** The masses of the neutral MSSM Higgs bosons  $h$  (green),  $H$  (blue) and  $A$  (red) are shown as function of  $M_A$  for  $\tan \beta = 5$  (dashed) and  $\tan \beta = 20$  (solid).

CP transformation<sup>14</sup> while  $h$  and  $H$  are even. At tree level, the properties of the MSSM Higgs bosons can be described by two parameters: the mass of the pseudo-scalar Higgs boson  $M_A$  and the ratio of the vacuum expectation values  $\tan \beta = v_u/v_d$ . The masses of the other Higgs bosons at tree-level are then given as

$$M_{\pm}^2 = M_A^2 + M_W^2, \quad (2.40)$$

$$M_{h,H}^2 = \frac{1}{2} \left[ M_A^2 + M_Z^2 \mp \sqrt{(M_A^2 + M_Z^2)^2 - 4M_A^2 M_Z^2 \cos^2 2\beta} \right], \quad (2.41)$$

$$\Rightarrow M_h < M_Z, \quad (2.42)$$

where the last statement contradicts with the results of direct Higgs searches performed by the LEP experiments. It turns out that the upper bound on  $M_h$  can be shifted to  $M_h \lesssim 135$  GeV by including higher order corrections coming from the top quark. The mass splitting for the three neutral MSSM Higgs bosons is shown in Figure 2.2.

The couplings with the SM particles are modified by functions of the mixing angles  $\alpha$  and  $\beta$ . A summary is given in Table 2.6 which lists the couplings between the MSSM Higgs bosons and SM particles normalised to the corresponding couplings in the SM. One observes that the coupling to gauge bosons, which are dominant in the SM due to the large gauge boson masses, is suppressed in the MSSM or even absent in the case of the CP odd Higgs boson. On the other hand, the coupling to down-type fermions is enhanced for large values of  $\tan \beta$  which opens  $\phi \rightarrow b\bar{b}$  and  $\phi \rightarrow \tau^+\tau^-$  as interesting search channels for MSSM Higgs bosons.

<sup>14</sup>CP stands for a combined charge and parity transformation of a process/state.

coupling to	up-type fermion	down-type fermion	gauge boson
$h$	$\cos \alpha / \sin \beta$	$-\sin \alpha / \cos \beta$	$\sin (\beta - \alpha)$
$H$	$\sin \alpha / \sin \beta$	$\cos \alpha / \cos \beta$	$\cos (\beta - \alpha)$
$A$	$\cot \beta$	$\tan \beta$	0

**Table 2.6:** Higgs couplings in the MSSM relative to the SM couplings [16].

In order to describe the MSSM Higgs sector beyond tree level the energy scale of SUSY breaking  $M_{\text{SUSY}}$ , the gaugino masses at the electroweak scale  $M_2$ , the strength of the supersymmetric Higgs mixing  $\mu$ , the gluino mass  $M_{\tilde{g}}$  and the stop mixing parameter  $X_t$  are need in addition. A set of benchmark scenarios is defined to simplify the comparison of results between different groups and experiments [24]. In the context of this thesis the  $m_h^{\text{max}}$  scenario is used which is defined by

$$M_{\text{SUSY}} = 1 \text{ TeV} , \quad (2.43)$$

$$M_2 = 200 \text{ GeV} , \quad (2.44)$$

$$\mu = 200 \text{ GeV} , \quad (2.45)$$

$$M_{\tilde{g}} = 800 \text{ GeV} , \quad (2.46)$$

$$X_t = 2 \text{ TeV} \quad (2.47)$$

and maximises the upper bound on mass of the lightest, CP even MSSM Higgs boson to  $M_h \leq 135 \text{ GeV}$ .



# Chapter 3

## The ATLAS Experiment

ATLAS is a particle physics experiment conducted by about 3000 scientists from 38 countries. The ATLAS detector, installed at the LHC, is designed as a general-purpose detector for high energy particle collisions. The goals of the ATLAS collaboration are numerous, ranging from testing the SM predictions at high energies over the search for Higgs bosons to the discovery of New Physics like Supersymmetry, dark matter or additional dimensions.

In order to meet the requirements for these ambitious aims, a profound understanding of the detector performance is necessary as well as an extensive knowledge about the hadron collider itself.

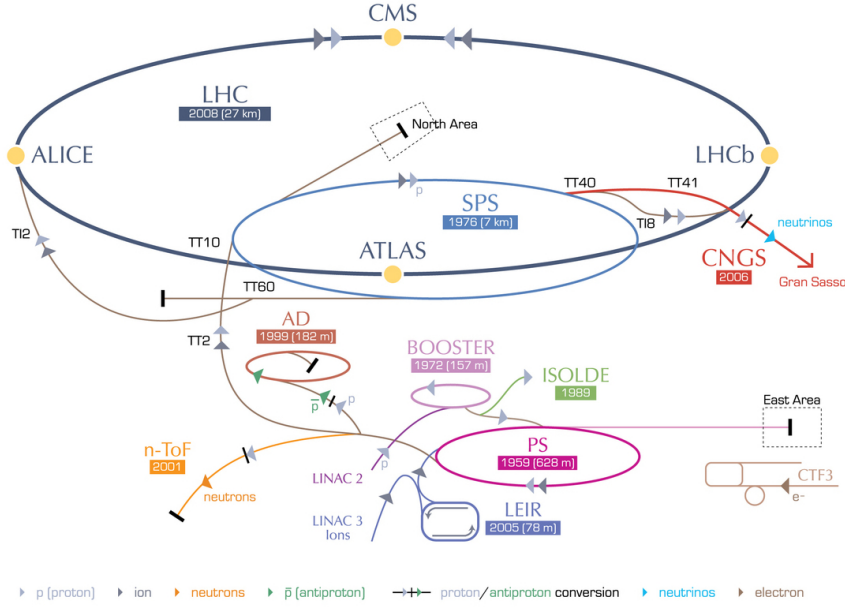
### 3.1 The Large Hadron Collider

The LHC [25] is currently the world's largest particle collider located at the border between France and Switzerland near Geneva. It is installed in a tunnel 100 m underground which is 27 km in circumference and was formerly used by the LEP collider. Using the synchrotron principle the LHC can accelerate either proton or lead ion beams to very high energies.

The protons are obtained from a hydrogen source and pre-accelerated by the existing infrastructure of former experiments [26]. The whole accelerator complex is shown in Figure 3.1. As a first step, protons of 50 MeV are generated by the linear accelerator LINAC 2 and then fed in the Proton Synchrotron Booster (PSB) which passes them to the Proton Synchrotron (PS). After being accelerated to an energy of 26 GeV the protons are forwarded to the Super Proton Synchrotron (SPS) which finally injects the beam into the main accelerator at an energy of 450 GeV. In the LHC ring, the energy of the protons is ramped up to a maximum of 7 TeV per beam which results in a centre-of-mass energy of  $\sqrt{s} = 14$  TeV.

In order to bend the counter-rotating beams around the ring, 1232 superconducting dipole magnets cooled by super-fluid helium are installed in the tunnel. While operating at a temperature of 1.9 K, they produce a magnetic field of 0.5 – 8.3 T depending on the beam energy.

The two beams can be brought to collision at the interaction points where the four LHC experiments ATLAS [27], CMS [28], ALICE [29] and LHCb [30] are located. ATLAS and CMS are multi-purpose detectors which look for hints of New Physics of various



**Figure 3.1:** The LHC accelerator complex [31].

kinds whereas ALICE and LHCb have more specialised detector concepts to investigate specific phenomena. The LHCb experiment intends to measure B meson decays and CP violation parameters with very high precision searching for answers to the imbalance between matter and antimatter. The ALICE collaboration focuses on heavy-ion collisions to examine the quark-gluon-plasma and addresses open questions in QCD like the source of hadron masses or the confinement of quarks.

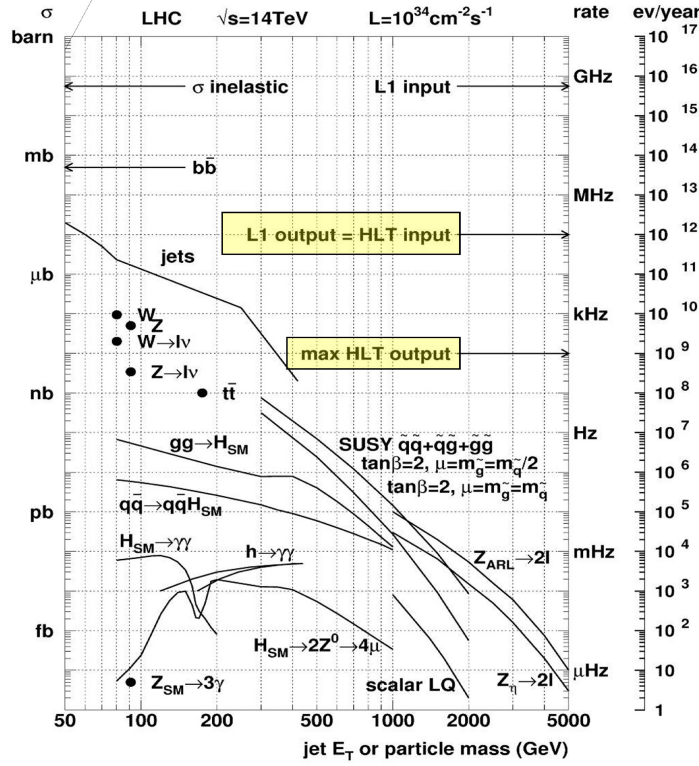
Since the protons are accelerated in cavities by a 400.8 MHz radio frequency, it is not possible to sustain a continuous proton beam. Therefore, the protons are grouped in bunches with up to  $1.15 \cdot 10^{11}$  protons per bunch and 2808 bunches per beam with a separation in time of 25 ns. The rate  $\dot{N}$  at which a certain process occurs, can be derived from the cross section  $\sigma$  of the studied process and the instantaneous luminosity  $\mathcal{L}$  as

$$\dot{N} \equiv \frac{dN}{dt} = \sigma \cdot \mathcal{L}. \quad (3.1)$$

In contrast to the cross section, the instantaneous luminosity depends on machine parameters and can be adjusted according to the needs of the experiments. New Physics processes predominantly have cross sections orders of magnitudes smaller compared to ordinary SM processes. Hence, a high luminosity is needed to reach sensitivity for these processes. Assuming a Gaussian beam distribution the instantaneous luminosity can be written in terms of beam parameters as

$$\mathcal{L} = \frac{n_b^2 n_p f \gamma_r}{4\pi \varepsilon_n \beta^*} F \quad (3.2)$$

where  $n_b$  is the number of bunches per beam,  $n_p$  the number of protons per bunch,  $f$  the



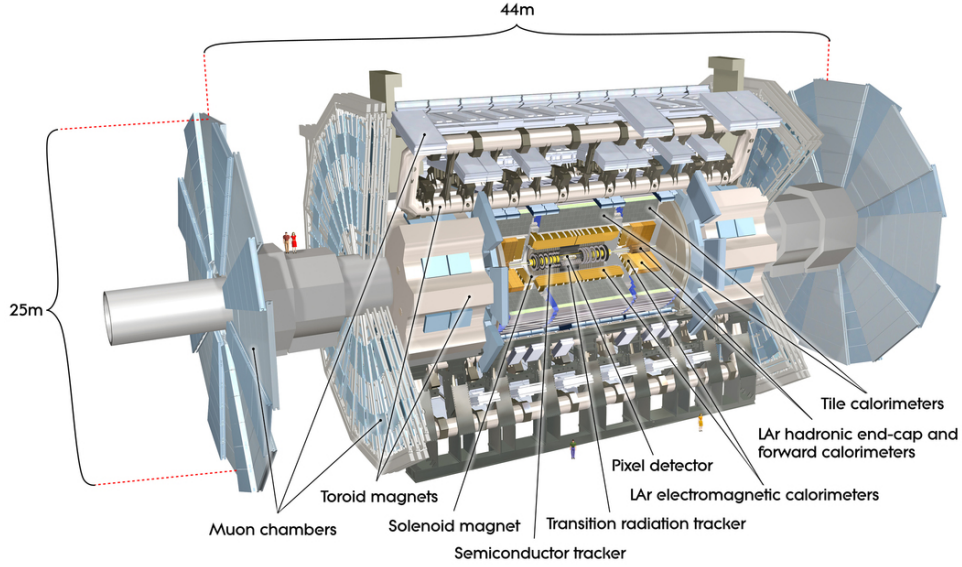
**Figure 3.2:** Cross sections and expected event rates for several processes [32].

revolution frequency,  $\gamma_r$  the relativistic gamma factor,  $\varepsilon_n$  the normalised transverse beam emittance,  $\beta^*$  the beta parameter and  $F$  describes the geometric reduction due to the crossing angle of both beams at the interaction point. The LHC has been designed for peak luminosities of  $\mathcal{L} = 10^{34} \text{ cm}^{-2} \cdot \text{s}^{-1}$ . In Figure 3.2 the expected cross sections for a variety of processes and the corresponding event rates are shown for the design value of  $\sqrt{s} = 14 \text{ TeV}$ . Also, the possible acceptance rates of different trigger levels are indicated illustrating the challenges for the trigger and data acquisition system which is explained further in Section 3.2.5.

The LHC started operating in November 2009 and on November the 23rd first proton-proton collisions at a centre-of-mass energy of 900 GeV were recorded. After a short period of further testing and commissioning the beam energy has been increased to 3.5 TeV and first proton-proton collisions at  $\sqrt{s} = 7 \text{ TeV}$  were achieved on March the 30<sup>th</sup>, 2010. By the end of the 2011 data taking period,  $L = 5.25 \text{ fb}^{-1}$  of data for proton-proton collisions at  $\sqrt{s} = 7 \text{ TeV}$  with instantaneous luminosities up to  $\mathcal{L} = 3.6 \cdot 10^{33} \text{ cm}^{-2} \text{s}^{-1}$  were recorded by the ATLAS detector.

## 3.2 The ATLAS Detector

The ATLAS detector [27] is a multi-purpose detector which follows a hermetic detector design. In order to cover the broad physics programme of the ATLAS collaboration, it



**Figure 3.3:** The ATLAS detector [27].

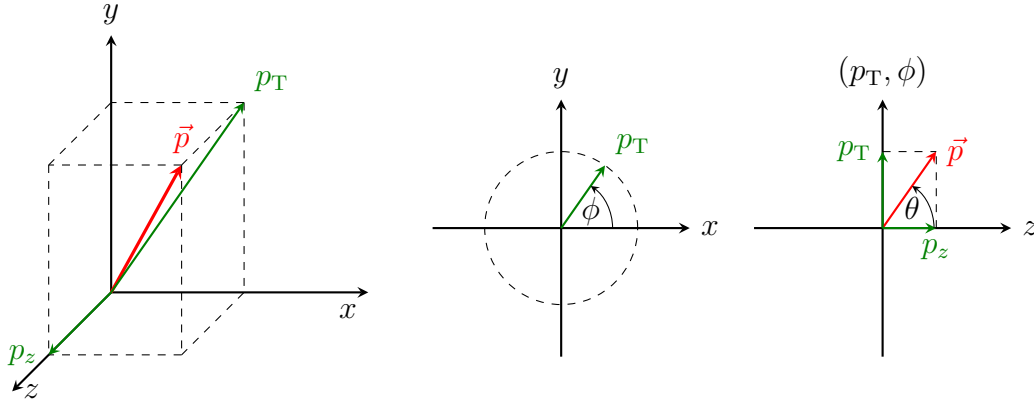
needs an outstanding performance in terms of neutral and charged particle identification as well as an excellent energy resolution. The unprecedented energy and collision rate at the LHC impose further restrictions on the technical design of the detector. A sketch of the ATLAS detector is displayed in Figure 3.3. Tracks of charged particles are reconstructed using information from the Inner Detector (ID) which is placed in the centre of the detector. It is surrounded by a superconducting solenoid providing a 2 T magnetic field. The Electromagnetic Calorimeter (ECAL) is responsible for measuring the energy of electrons and photons whereas hadrons deposit most of their energy in the Hadronic Calorimeter (HCAL). The Muon Spectrometer (MS) is the outermost sub-detector containing an air-core toroid magnet system with a strong bending power for measuring the momenta of muons with high precision.

The next section introduces the ATLAS coordinate system and some nomenclature which is useful for describing the kinematics of particles. Afterwards the various detector subsystems are described in more detail.

### 3.2.1 ATLAS Coordinate System

A right-handed coordinate system is used with the  $z$ -axis coinciding with the beam pipe where  $z = 0$  is the nominal interaction point, the  $x$ -axis pointing from the interaction point to the centre of the LHC ring and the positive  $y$ -axis is pointing upwards. The azimuthal angle  $\phi$  is measured in the  $x$ - $y$ -plane which is perpendicular to the beam axis. The polar angle  $\theta$  is defined with respect to the beam axis (cf. Figure 3.4). In hadron colliders the pseudorapidity  $\eta$  defined as

$$\eta = -\ln \tan \frac{\theta}{2} \quad (3.3)$$



**Figure 3.4:** The ATLAS coordinate system.

is a widespread variable because it provides a more natural description of QCD processes. The angular separation between two objects is given by the quantity

$$\Delta R = \sqrt{(\Delta\eta)^2 + (\Delta\phi)^2}. \quad (3.4)$$

The projection of quantities on the transverse plane is denoted by a subscript  $_T$ . Since the magnetic field in the Inner Detector is parallel to the beam direction, the track of a charged particle is a helix whose radius is related to the transverse momentum  $p_T$  of the particle and is approximately given by

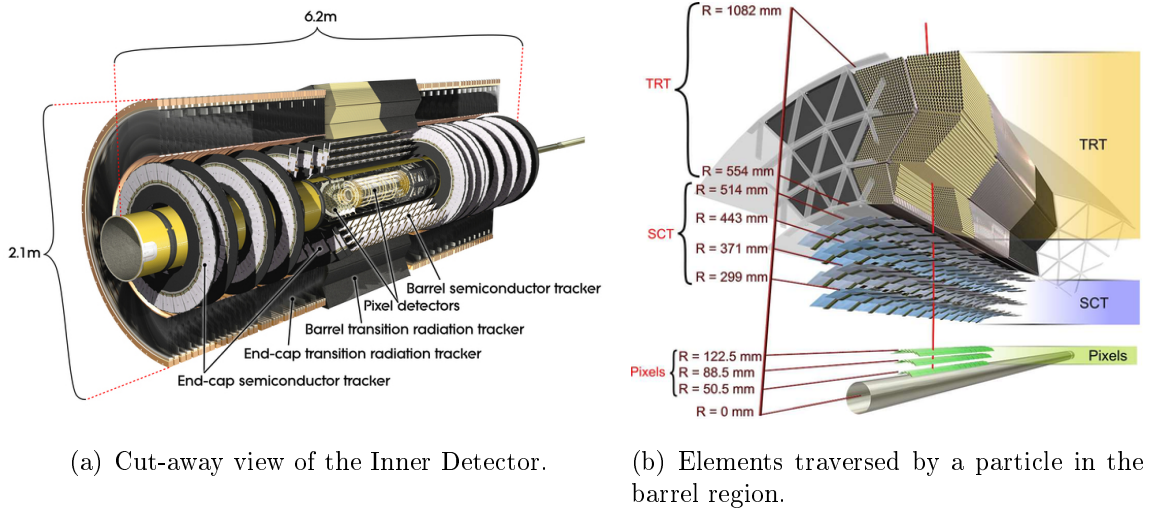
$$r = \frac{p_T}{B \cdot q} \quad (3.5)$$

where  $B$  is the nominal value of the magnetic field and  $q$  the absolute value of the particle's charge. The kinematics of a particle can be described by the three quantities  $p_T$ ,  $\eta$  and  $\phi$ . Some useful relations and conversions can be found in Appendix B.

### 3.2.2 The Inner Detector

The cylindrical inner detector with a length of 7 m and a diameter of 2.3 m is the innermost part of the ATLAS detector covering pseudorapidities up to  $|\eta| \leq 2.5$ . It is within a solenoidal magnetic field of 2 T and is able to reconstruct tracks of charged particles above a  $p_T$  threshold of 100 MeV.

Consisting of three independent and complementary subsystems it has robust pattern recognition capabilities and provides essential information for track reconstruction. A precise description of particle tracks is crucial for an accurate momentum measurement and a good vertex identification. Especially, the analyses of processes involving  $b$ -quarks profit from the ability to resolve secondary vertices which are caused by decays of long-lived  $B$ -mesons. These needs ask for high-granular precision detectors like semiconducting pixel or strip detectors. However, this solution contradicts the requirement of having a minimal amount of material in front of the calorimeters to minimise



**Figure 3.5:** The Inner Detector [27].

the distortion of the energy measurement. Therefore, a compromise is chosen and the semiconducting technology is complemented by transition radiation trackers which have much less material per point, a lower cost and provide additional information for electron identification in the range  $|\eta| < 2.0$ . The less precise measurement in the Transition Radiation Trackers (TRT) is compensated by the larger number of hits expected per track. The relative precision of the different components are matched such that no single sub-detector dominates the momentum resolution. Figure 3.5 shows the layout of the Inner Detector.

### The Pixel Detector

The pixel detector consists of 3 layers in the barrel region and 5 disks in both end-cap regions. The detector part closest to the interaction point is the *B*-layer at a radius of  $\approx 5$  cm covering a range in pseudorapidity up to  $|\eta| \leq 2.5$ . Due to its exposure to high ionising radiation, it suffers from radiation damage and may need to be replaced to sustain a high tracking performance over the whole lifetime of the experiment. The remaining two layers are located at radii of 9 cm and 13 cm and span a range of  $|\eta| \leq 1.7$ . Each end-cap module hosts 5 disks with pixel detectors providing additional space points in the range  $1.7 \leq |\eta| \leq 2.5$ . The intrinsic spatial resolution achieved by the barrel layers is  $115 \mu\text{m}$  in  $z$ -direction and  $10 \mu\text{m}$  in the transverse plane.

### The Semiconductor Tracker

The semiconducting tracking (SCT) system comprises four layers, made out of two silicon strip layers with a stereo angle of 40 mrad, in the barrel and nine detector wheels in the end-cap regions. The layers in the barrel are placed at intermediate radii between 30 cm and 52 cm covering the  $\eta$  range up to  $\pm 1.4$ . In the barrel region four space points per track are expected, each one with a resolution of  $17 \mu\text{m}$  in  $R\phi$  and  $580 \mu\text{m}$  in  $z$ . The

same precision is achieved by the SCT modules in the end-cap regions which cover the pseudorapidities between  $1.4 \leq |\eta| \leq 2.5$ . The rather large uncertainty on the  $z$ -position is caused by the small stereo angle between adjacent strip layers. The mechanic design and the positioning of the read-out electronics inhibit larger stereo angles and, hence, a better resolution in  $z$  direction.

### The Transition Radiation Tracker

The TRT system consists of straw tubes filled with a gas-mixture containing Xenon and is interleaved with radiator components. A charged particle crossing a straw tube creates ionised atoms along its track which are accelerated by a high voltage and collected at the electrodes. Photons arising from transition radiation are absorbed by the Xenon gas and yield a typically larger signal. By supporting two different thresholds the readout electronic can distinguish between both signals. Therefore, it contributes to the track reconstruction as well as to the electron identification.

The tubes have a diameter of 4 mm resulting in total active detector volume of  $3 \text{ m}^3$ . They are each equipped with a  $30 \text{ }\mu\text{m}$  thick gold sense wire which is divided in the middle to limit the occupancy at high instantaneous luminosities.

In the barrel region  $|\eta| \leq 0.7$  the straws are aligned in parallel to the beam axis at radii between 56 cm and 107 cm with readout electronics at both ends while in the end-cap region the tubes are oriented axially with only one readout chip at the outer radius. The end-cap modules extend the coverage up to  $|\eta| \leq 2.0$ . The resolution of the drift-time measurement is about  $130 \text{ }\mu\text{m}$  in  $R\phi$  per straw and on average 36 hits per track are expected which results in an expected total uncertainty of about  $25 \text{ }\mu\text{m}$  in  $R\phi$ . The spacing of the straw tubes has been optimised for tracking at the expense of electron identification which would benefit from bigger radiator components. However, the TRT system provides a good pattern recognition by its continuous tracking measurements at larger radii and allows a discrimination between electron and hadron signatures.

### 3.2.3 The Calorimetry System

The calorimetry system is designed to provide an accurate energy measurement for electrons, photons and hadrons. A close to full coverage is desirable for a good missing transverse energy (MET) performance but due to technical limitations (e.g. a hole for the beam pipe is needed) a hermetic energy measurement can not be achieved. However, the calorimeters cover a large fraction of the solid angle and a good MET resolution is expected. In order to use information from shower shapes to distinguish between different particle types, a high granularity of the calorimeters is beneficial.

The calorimetry system is divided into two subsystems: the electromagnetic calorimeter and the hadronic calorimeter. The overall layout of the calorimetry system is shown in Figure 3.6 and the two different detector components are explained further in the following paragraphs.

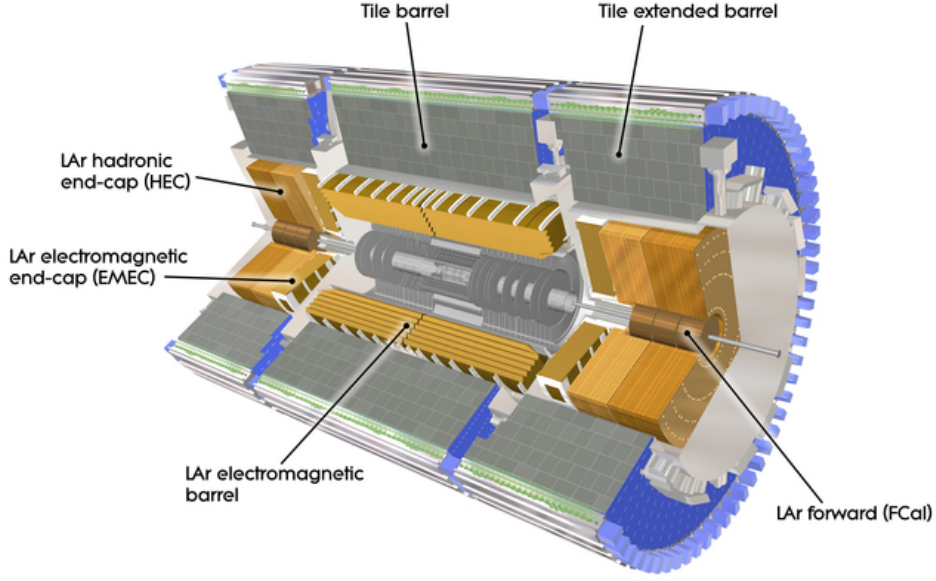


Figure 3.6: The ATLAS calorimetry system [27].

### The Electromagnetic Calorimeter

The electromagnetic (EM) calorimetry consists of three parts: the barrel calorimeter covering  $|\eta| < 1.475$  and two end-cap calorimeters extending the coverage to  $1.35 < |\eta| < 3.2$ . An accordion shaped sampling geometry with lead as absorber and liquid argon as sensitive component is used to detect electromagnetically interacting particles and provides a full coverage in  $\phi$ . Due to the special accordion geometry, information about the longitudinal evolution of electromagnetic showers can be assessed. In the region  $|\eta| < 1.8$ , a presampler detector is set up to correct for energy losses upstream the calorimeter.

Over the central region ( $|\eta| < 2.5$ ) the EM calorimeter is segmented into three longitudinal samplings as shown in Figure 3.7(a). The first sampling has a thickness of  $\approx 6$  radiation lengths and serves as preshower detector enhancing the particle identification. In addition, its narrow strips provide a good resolution of  $\Delta\eta = 0.003$  and contribute to a precise position measurement. The middle section consists of square towers with a granularity of  $\Delta\eta \times \Delta\phi = 0.025 \times 0.025$  whereas the third sampling has a slightly worse resolution of  $\Delta\eta = 0.05$ . The inner wheel in the end-cap calorimeter consists of only two samplings with a coarser granularity of  $\Delta\eta \times \Delta\phi = 0.1 \times 0.1$  which is sufficient to satisfy the physics requirements in terms of jet reconstruction and missing transverse energy measurement. The total thickness of the electromagnetic calorimeter in terms of radiation lengths  $X_0$  is at least 24 in the barrel section and 26 in the end-cap regions. The transition region from the barrel to the end-cap section at  $1.37 \leq |\eta| \leq 1.52$  is excluded from physics measurements due to the large amount of material equivalent to  $7X_0$  in front of the electromagnetic calorimeters (cf. Figure 3.7(b)).



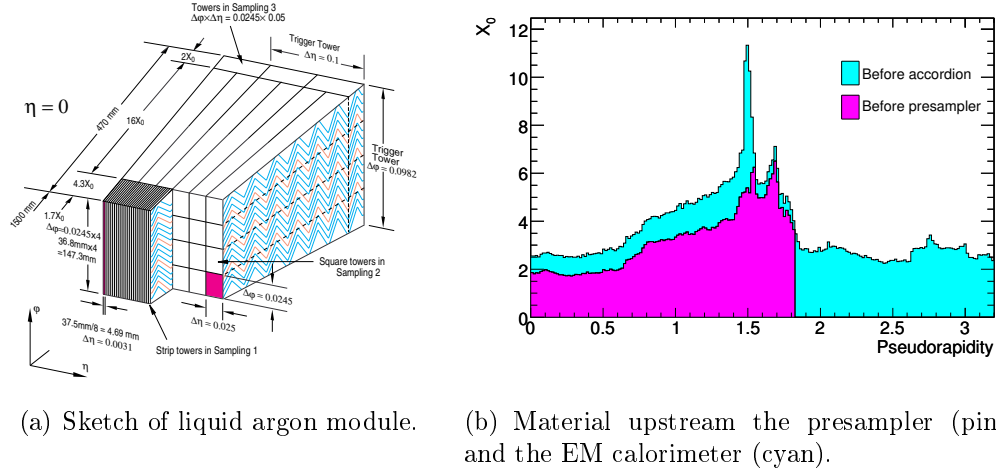


Figure 3.7: The electromagnetic calorimeter [27].

### The Hadronic Calorimeter

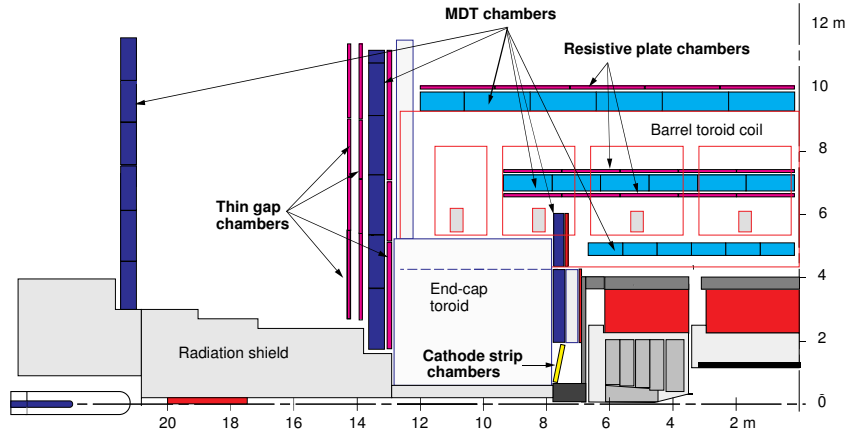
The hadronic calorimetry system covers pseudorapidities up to  $|\eta| < 4.9$ . The varying radiation conditions over the  $\eta$ -range are taken into account by the usage of different detector technologies. In the region  $|\eta| < 1.7$ , which comprises the barrel and extended barrel components, a sampling concept with steel as absorber and scintillating tiles as active medium is used. The hadronic end-cap (HEC) and the forward calorimeter (FCAL), covering the range  $1.5 < |\eta| < 3.2$  and  $3.1 < |\eta| < 4.9$  respectively, suffer from a much higher radiation flux. Therefore, the intrinsically radiation hard liquid argon (LAr) technology is employed. The hadronic calorimeters are segmented longitudinally into three samplings except for the HEC which has four samplings. The granularity is  $\Delta\eta \times \Delta\phi = 0.1 \times 0.1$  in the region  $|\eta| < 2.5$  and  $\Delta\eta \times \Delta\phi = 0.2 \times 0.2$  in the region beyond the tracking acceptance.

An important aspect in the design of the hadronic calorimetry is a sufficiently large thickness to minimise the punch-through of high energetic particles into the muon system. With a thickness corresponding to 10 interaction lengths  $\lambda$ , a good containment of hadronic showers is ensured and the rate of punch-through events is reduced well below the irreducible level of prompt muons or muons originating from decays in flight.

#### 3.2.4 The Muon Spectrometer

The muon spectrometer is the outermost part of the ATLAS detector and is designed to provide an efficient muon identification combined with a precise momentum measurement. Whereas electron, photons and hadrons are absorbed by the calorimetry system, muons with a  $p_T > 3$  GeV can penetrate the detector and reach the muon spectrometer. This behaviour is based on the long lifetime of  $\tau_\mu = 2.2 \mu\text{s}$  [13], a higher mass of  $m_\mu = 105.6$  MeV, which reduces the energy loss due to bremsstrahlung, and the minimum ionising characteristics.

The muon spectrometer covers the pseudorapidity range up to  $|\eta| < 2.7$  and uses a



**Figure 3.8:** Layout of the ATLAS muon spectrometer in the  $R - z$  plane [27].

toroidal magnetic field for momentum measurements. The magnetic field is provided by large barrel toroids in the range  $|\eta| < 1.4$  and two end-cap magnets for  $1.6 < |\eta| < 2.7$ . In the transition region of  $1.4 < |\eta| < 1.6$  charged particles are deflected by a combination of both fields.

The spectrometer is instrumented with different types of chambers for precision tracking and triggering. These chambers are arranged in three cylindrical layers around the beam axis in the barrel section as shown in Figure 3.8. In the transition and end-cap region the chambers are installed in planes perpendicular to the beam axis.

Since muons with a high  $p_T$  are of special interest for the ATLAS physics programme, information from the muon spectrometer is used for triggering events. This role imposes further restriction on the design of the chambers because a very short response time is crucial for an efficient trigger. Therefore, different kinds of chambers are used: Monitored Drift Tubes (MDT) and Cathode Strip Chambers (CSC) measure precisely track variables whereas Resistive Plate Chambers (RPC) and Thin Gas Chambers (TGC) with intrinsic high time resolution provide information for the trigger system.

The desired accuracy for the momentum measurement up to  $p_T \approx 1$  TeV requires an alignment of the muon chambers with a precision of about  $30 \mu\text{m}$  as well as an accurate knowledge of the magnetic field. Therefore, information from 12000 optical precision sensors and 1800 HALL sensors is used for the correction of the momentum and track measurement.

### 3.2.5 The ATLAS Trigger and Data Acquisition System

The bunch spacing of 25 ns corresponds to a nominal collision rate of 40 MHz which has to be reduced by more than five orders of magnitude to reach the possible storage rate of 200 Hz. As the ATLAS physics goals comprise the search for Higgs bosons and BSM processes whose typical cross sections are many orders of magnitude smaller than those of QCD processes (cf. Figure 3.2), an extremely efficient trigger system is needed for

selecting those interesting events<sup>1</sup>. The trigger system is highly configurable in terms of combinations of different requirements and algorithms at all levels which are referred to as trigger chains. In addition, prescale factors<sup>2</sup> can be introduced to limit the rate of trigger chains with a very high occurrence.

In order to cope with the high rates, the ATLAS trigger consists of three consecutive levels, each one refining the decision made by the previous level and applying additional selection criteria if needed. Furthermore, an “early abort” approach is chosen which means that one event is rejected as soon as all active trigger chains stopped.

The first trigger level (L1 trigger) accepts events with a rate of 75 kHz and relies solely on information from the calorimeters and the muon spectrometer with a reduced granularity. The L1 trigger looks for signatures from interesting objects like electrons, photons, jets or large missing transverse or total energy and defines regions of interest (RoI) which contain the  $\eta$  and  $\phi$  coordinates of the detected feature as well as a threshold (e.g. energy or  $p_T$ ). In order to avoid a large dead time fraction, the readout channels are equipped with circular buffers retaining the information long enough to accommodate the L1 trigger latency of 2.5  $\mu$ s. In case an event is accepted by the L1 trigger, the event data is transferred to Readout Buffers (ROBs) where it is temporarily stored and available for the next stages of the trigger system.

The level 2 (L2) trigger is seeded by the RoI information and makes use of the full granularity and precision of the data inside the RoI. The required detector information, which has to be readout, corresponds to about 2% of the total event data. This reduced data transfer allows an average L2 processing time of 40 ms. L2 selection criteria further reduce the event rate to 3.5 kHz at which events are passed to the final event filter (EF). During the transition from the L2 stage to the event filter the event builder is invoked which collects the data from the Readout System (ROS) and assembles a formatted single event data structure.

The event filter benefits from offline analysis algorithms, the latest calibrations, alignment measurements and the current magnetic field map to improve its selection efficiency. After an average processing time of 4 s the data is transferred to a permanent storage and the final event acceptance rate is roughly 200 Hz which is limited by the available bandwidth of 300 MB/s.

### 3.2.6 Luminosity Measurement

In addition to the main ATLAS detector, three additional detector systems are installed in the forward region. Two of them, LUCID (Luminosity measurement using Cerenkov Integrating Detector) and ALFA (Absolute Luminosity For ATLAS), are devoted to luminosity measurements whereas the Zero-Degree-Calorimeter (ZDC) is used to determine the centrality in heavy ion collisions. As it can be seen from Equation (3.1), the luminos-

<sup>1</sup>Even though it would be highly desirable, it is not possible to disentangle different proton-proton interactions taking place in one bunch crossing. Therefore, the term *event* always refers to total information read out from the detector after a positive trigger decision.

<sup>2</sup>A prescale factor is a positive integer number  $N$  which specifies that only 1 out of  $N$  events accepted by the trigger is actually kept.

ity is a crucial ingredient for relating the number of observed events to a cross section. Therefore, a precise measurement of the luminosity is essential and the two dedicated detectors are explained in the following two paragraphs.

#### LUCID

The two LUCID detectors are located at  $z = \pm 17$  m with respect to the nominal interaction point and use a Cerenkov light based technology to perform relative luminosity measurements. During the initial phase luminosity calculations from the LHC beam parameters gave a relative uncertainty of  $\approx 25\%$ . Dedicated calibration measurements with the ALFA detector as well as the measurement of physics processes, such as  $W$  and  $Z$  boson decays, will improve the measurement to an accuracy of about 5%.

The major task of LUCID is the detection of inelastic proton-proton collision to measure the integrated luminosity and provide an online luminosity monitoring. At the LHC design luminosity multiple proton-proton interactions per bunch crossing will occur and the exact number is necessary to calculate the luminosity. LUCID is based on the concept that the number of detected particles is proportional to the number of proton-proton interactions.

#### ALFA

The ALFA detectors use scintillating fibres in Roman pots<sup>3</sup> at  $z = \pm 240$  m to detect protons. The optical theorem relates the elastic scattering amplitude in forward direction with the total cross section and, therefore, can be used in a direct luminosity measurement. Measuring the number of protons at extremely small angles requires special beam conditions which are established in calibration runs. Furthermore, the location far away from the interaction point in combination with the Roman pot technique allows to measure protons at scattering angles of  $3 \mu\text{rad}$ .

## 3.3 Event Generation

Simulated pseudo-data is vital for assessing the discovery potential of new physics processes. Additionally, the detector performance can be evaluated by comparing the measurement of well-known SM processes to their expectation. The generation of pseudo-data can be divided into the following steps:

#### Event generation

A variety of event generators based on Monte Carlo (MC) techniques is available. These generators are able to model particle interactions and produce pseudo-data samples with sufficiently large statistics. This modelling includes:

---

<sup>3</sup>*Roman pots* are cylindrical devices attached directly to the beam pipe. A thin window separates the detector inside the pot from the vacuum system of the beam pipe. Therefore, it is possible to perform measurements very close to the actual beam.

- description of the partons in the initial state protons by parton density functions (PDF),
- definition of the hard<sup>4</sup> interaction between one parton from each proton which is the interaction of interest and can be calculated to a fixed order of the coupling constants in perturbation theory,
- decays of short-living resonances,
- corrections due to bremsstrahlung radiation in the initial and final state,
- interactions of the other partons at lower energy scales<sup>5</sup>,
- description of beam remnants,
- phenomenological models for the hadronisation process.

The generators implement different methods to accomplish this complex task. The output of an event generator is a list of all produced particles with their properties as charge, spin and Lorentz vector<sup>6</sup>.

### Detector simulation

The final state particles are handed to the detector simulation which uses GEANT4 to simulate the detector response [33]. Therefore, the whole geometry of the ATLAS detector including all material properties has to be known and constant efforts for improving the detector description are ongoing. Due to the huge number of interactions between final state or secondary particles with the detector material, this step takes most of the time during the event simulation work flow.

### Pile-up

The effect of overlaying detector signals which are not coming from the same proton-proton interaction is called pile-up. This effect can occur due to more than one proton-proton interaction during one bunch crossing (in-time pile-up) or proton-proton interactions in subsequent bunch crossings (out-of-time pile-up). The former is mainly driven by the instantaneous luminosity whereas the latter also depends on the bunch train structure<sup>7</sup>. In order to simulate these effects, several generated events can be superimposed.

### Digitalisation

The expected output from the readout electronics, corresponding to the detector response of the merged pile-up and signal events, is simulated. The result is equivalent to the expected output of a real data event.

### Object reconstruction

Using the digital detector response, reconstruction algorithms condense information

---

<sup>4</sup>The hard interaction is used to describe the process with the largest momentum transfer.

<sup>5</sup>Parton interactions at lower energy scales than the hard interaction are called *underlying event*.

<sup>6</sup>The output from the event generator is sometimes called *MC truth* information.

<sup>7</sup>The proton bunches are grouped into trains of a certain length followed by empty, meaning not filled, bunch positions. This structure is given by the LHC operation and evolves over time.

and create analysis-oriented data structures. During this step energy deposits in adjacent calorimeter cells are grouped into clusters, hits in the tracking system are associated to tracks and physics object candidates are formed. This step is equal for data and simulated events and the object reconstruction is described in more detail in Section 3.4.

In order to enrich the statistics of simulated MC samples<sup>8</sup> in certain regions of the phase space, cuts on kinematic variables are applied at generator level which leads to a generator filter efficiency  $\varepsilon$ . The number  $N_{\text{MC}}$  of simulated events of a process with a cross section  $\sigma$  corresponds to an equivalent integrated luminosity

$$L_{\text{MC}} = \frac{N_{\text{MC}}}{\sigma \cdot \varepsilon}. \quad (3.6)$$

To compare these events with real data corresponding to an integrated luminosity  $L$ , the simulation has to be scaled by a factor

$$w = \frac{L}{L_{\text{MC}}} = \frac{L \cdot \sigma \cdot \varepsilon}{N_{\text{MC}}}. \quad (3.7)$$

#### 3.3.1 Monte Carlo Generators and Simulated Data Sets

A large variety of different MC generators exist ranging from multi-purpose generators to specialised tools for individual processes. In the following, the generators used for this study are briefly mentioned. For details on the various MC generators, please refer to the given references because the discussion of technical details is beyond the scope of this work.

Electroweak processes have either been simulated with the PYTHIA v6.423 [34] or the ALPGEN v2.13 [35] generator while processes including top quarks have been generated with MC@NLO v3.3 [36, 37]. HERWIG v6.510 [38] have been used to simulate di-boson processes. The production of neutral MSSM Higgs bosons have been generated by POWHEG [39] for the gluon-fusion process and by SHERPA v1.2.3 [40] for the  $b$ -associated production<sup>9</sup>. In the case of the POWHEG generator, a SM like Higgs boson is generated with its width set to the MSSM expectation. Therefore, the CP properties of the neutral MSSM Higgs boson  $A$  are not reflected in these samples. This is a valid approach since the CP properties are expected to play a subordinate role for the discovery of the Higgs bosons.

ALPGEN, MC@NLO, HERWIG and POWHEG do not include a parton shower model. Therefore, the produced samples have been interfaced to HERWIG and JIMMY v4.31 [41], a generator for multi-parton interactions, except for the POWHEG samples which use the parton shower algorithm of PYTHIA.

The ALPGEN samples employ the CTEQ6L1 [42] set of PDFs, SHERPA, MC@NLO and POWHEG use the CTEQ6.6 [43] PDFs while PYTHIA and HERWIG samples rely on

---

<sup>8</sup>The term *MC samples* refers to a collection of simulated events and is derived from the fact that most generators rely on MC techniques during the event generation step.

<sup>9</sup>The different production mechanisms are explained in more detail in Section 4.2.

the MRST2007LO\* [44] set of PDFs. JIMMY uses the AUET1 [45] set of parameters to simulate the underlying event while PYTHIA deploys the AMBT1 [46] set of tuned parameters.

Finally, the decays of tau leptons are modelled by TAUOLA [47].

### 3.4 Object Reconstruction and Identification

The purpose of the ATLAS detector is the recognition and identification of particles and the measurement of their kinematic properties. A priori, particles can not be measured directly but manifest themselves through interactions with the detector material. Depending on the scope of the experiment and the particles of interest, an appropriate detector concept has to be chosen to extract a maximum amount of information.

The ATLAS detector design, as outlined in Section 3.2, ensures good object reconstruction and identification capabilities. Considering the different lifetimes, only a few species of the particles produced in the collision will reach the sensitive detector components. These are electrons, muons and photons as well as long-living or stable hadrons like charged pions, kaons, protons or neutrons. Therefore, the reconstruction and identification algorithms have been optimised for a limited number of particle flavours. Only particles which do not interact via the strong or electromagnetic force, can pass the detector without leaving a signature. In the SM this applies only to neutrinos but possible extensions contain other particles with a similar behaviour and, therefore, need inductive methods to infer the presence of those particles.

The object reconstruction and identification is performed in two steps. First, information from basic detector units like calorimeter cells or pixels in the tracking system are gathered and evaluated. Adjacent calorimeter cells are grouped into energy clusters using clustering algorithms and hits in the tracking system are combined to tracks by advanced fitting procedures. Then, identification algorithms make use of the condensed information to perform hypothesis tests and classify the object under investigation. Given a signature in the detector, the identification algorithms can only state a probability that this signature is caused by a certain particle type<sup>10</sup>. In order to meet the needs of various physics analyses which may benefit from different background rejection rates and identification efficiencies, a couple of working points for object identifications are supported<sup>11</sup>. To avoid confusion between real physics objects and objects classified by an identification algorithm to be of a certain kind, the latter are referred to as candidates.

For this study the charged leptons play an important role and their reconstruction and identification algorithms are briefly reviewed in the next paragraphs. The reconstruction of hadronic showers as jets is of further interest as well as the concept of missing transverse energy. Both topics are also explained in the remainder of this chapter.

<sup>10</sup>The probability of an object being classified correctly by an identification algorithm is called *identification efficiency* and is always connected to a *fake rate* which is the probability of mistakenly accepting an object of wrong type.

<sup>11</sup>These working points are usually labelled as `loose`, `medium` and `tight` and correspond (in this order) to decreasing fake rates and identification efficiencies.

	electrons	muons
reconstruction efficiency	$\approx 99\%$	$\approx 94\%$ (STACO combined)
identification efficiency	71.6% ( <b>tight</b> )	87.1%
background rejection	$1.4 \cdot 10^5$ ( <b>tight</b> )	250
energy/momentum resolution	$0.56\% \oplus \frac{9.3\%}{\sqrt{E}} \oplus \frac{1\%}{E}$	$3.75\% \oplus \frac{23\%}{p_T} \oplus 0.024\% \cdot p_T$

**Table 3.1:** Examples for reconstruction and identification efficiencies with corresponding background rejections for electron and muon reconstruction/identification algorithms together with obtained relative precision of the energy/momentum measurement ( $E$  and  $p_T$  always in GeV) [49–51].

### 3.4.1 Electrons

The signature of an electron in the detector is characterised by a track pointing to an energy deposit in the electromagnetic calorimeter<sup>12</sup>. A “sliding-window” algorithm [48], which uses a window size of  $3 \times 5$  cells in  $\eta$  and  $\phi$ , finds electromagnetic energy clusters in the second compartment of the EM calorimeter containing a local energy maximum [49]. Only clusters with energies above 2.5 GeV are kept and considered in the track matching step. Reconstructed tracks are extrapolated to the second layer of the EM calorimeter taking into account the effect of energy losses due to bremsstrahlung. The matching is based on the  $\Delta R$  between the extrapolated track and the cluster position which is required to be below a certain threshold<sup>13</sup>. An electron candidate is built if at least one track is matched to the cluster. Finally, several corrections to the reconstructed cluster energy are applied and the four-momentum vector is built using additional information from the best matched track.

Electron identification algorithms rely on calorimeter, tracking and combined calorimeter/tracking variables to classify the electron candidates. The standard algorithm uses simple cuts on these variables which have been optimised for three different background rejection rates. As an example, the electron identification efficiency along with the background rejection<sup>14</sup> for the **tight** selection is given in Table 3.1.

The **loose** identification imposes cuts on the energy leakage into the hadronic calorimeter and on the shape of the electromagnetic shower. It provides excellent electron identification efficiencies but low background rejections.

The **medium** selection additionally requires better track quality and utilises information from the first layer of the EM calorimeter. Requiring the track to be reconstructed from at least one hit in the pixel detector and at least seven hits in pixel and SCT tracking system allows for tightening the matching criteria to the cluster. Furthermore, electron

---

<sup>12</sup>There are dedicated identification algorithms for electrons outside the tracking acceptance ( $|\eta| > 2.47$ ) which are not discussed here.

<sup>13</sup>For tracks without any hits in silicon tracker, only a comparison of the  $\phi$  coordinates is done due to the limited accuracy of the measured  $\eta$  coordinate in the TRT system.

<sup>14</sup>A background rejection of  $R$  means that one out of  $R$  background objects is mistakenly identified as electron candidate.



candidates coming from photon conversions are efficiently rejected as they usually have no hits in the pixel system. In order to reduce the background originating from energy depositions of  $\pi^0$  particles one can benefit from the higher granularity in the first compartment of the EM calorimeter.  $\pi^0 \rightarrow \gamma\gamma$  decays produce two close-by energy maxima and, therefore, can be vetoed by looking for a second local energy maximum in the vicinity of the original cluster.

The highest rejection power is achieved by the **tight** selection criteria which have even stricter requirements on the track quality and the matching itself. Additionally, particle identification information from the TRT system is used to reject charged hadrons and electron candidates assigned to a photon conversion vertex are discarded. The ratio of the cluster energy to the track momentum is tested for the hypothesis of being an electron.

### 3.4.2 Muons

ATLAS has two competitive families of muon reconstruction algorithms called STACO and MuID. For this study the STACO family is used and the associated algorithms are explained in the remainder of this section.

The reconstruction and identification of muon candidates is mainly based on tracking information. The **MuonBoy** algorithm is used for pattern recognition and track reconstruction in the muon spectrometer and performs the following steps:

1. identification of regions of activity (ROA),
2. reconstruction of local segments in each muon station within the ROA,
3. forming muon track candidates by combining segments of different stations which requires at least two segments in different muon stations,
4. performing a global track fit on all muon track candidates in the muon spectrometer using the individual hit information.

For the reconstruction of muon candidates multiple strategies are pursued:

**Standalone:** Tracks reconstructed in the muon spectrometer are extrapolated to the beam pipe accounting for multiple scattering and energy losses in the upstream material. Standalone muons have the advantage of a larger coverage of  $|\eta| < 2.7$  compared to combined muons. However, they suffer from efficiency degradation in poorly equipped regions at  $\eta \approx 0$  and  $|\eta| \approx 1.2$  where no independent momentum measurement is possible. In addition, very low momentum muons with  $p_T \leq 3$  GeV are difficult to reconstruct because they do not reach the outermost part of the detector. Muons produced in the calorimeter by pion or kaon decays are considered as background by most physics analyses but are likely to be reconstructed as standalone muon candidates.

**Combined:** Combined muon candidates are found by matching standalone muon candidates to nearby tracks in the inner detector. The  $\chi^2_{\text{match}}$  describes the quality of

the match and is used to decide which combinations of inner detector tracks and standalone muons are kept. Both measurements are statistically combined using their covariance matrices. Combined muon candidates have the highest purity but they are restricted to the tracking acceptance and are subject to the same efficiency degradation as the standalone muons.

**Segment tagged:** To resolve the efficiency losses of the standalone algorithm and to increase the reconstruction efficiency for low  $p_T$  muons, the segment tagging algorithm starts from inner detector tracks and looks for a matching segment in the innermost stations of the muon spectrometer. If the segment is sufficiently close to the predicted track position, the inner detector track is interpreted as segment tagged muon candidate.

**Calorimeter tagged:** Dedicated algorithms can infer the presence of a muon from its minimum ionising signature in the calorimeter. This approach is not considered in this study.

Similarly to the electron case, various quality levels are defined to provide different working points for the physics analyses. Of major interest for this study are **tight** muon candidates which are either combined muon candidates or segment tagged muon candidates with at least 2 segments in the muon spectrometer. The reconstruction and identification efficiency for this working point are given in Table 3.1.

#### 3.4.3 Jets

Proton-proton collision may produce one or more quarks or gluons in the final state. Due to the colour confinement in QCD which is explained in Section 2.1.3, these particles hadronise and create a multitude of neutral and charged hadrons. These ensembles of particles are collimated in space and referred to as hadronic jets. Close-by tracks and focused energy depositions in the calorimeter system with a significant fraction in the hadronic calorimeter are characteristic features of jets. Gathering the signatures of all hadrons coming from the same outgoing parton and combining this information in a reconstructed jet object is the primary goal of jet reconstruction algorithms. These are either seeded by tracking information or energy deposits patterns. The former is insensitive to the neutral components of a jet and not considered in this analysis. Reconstruction algorithms starting from calorimeter information differ in their strategy of finding energy clusters associated to a jet and the energy calibration scheme. In this study, **AntiKt4TopoEM** jets are used and the related algorithm is outlined in the remainder of this paragraph.

Energy depositions in calorimeter cells are grouped into topological clusters by starting from a cell with a signal to noise ratio  $\Gamma$  above a threshold of  $\Gamma > 4$ . All adjacent cells are collected in the cluster and neighbours of those are only included if they fulfil another signal to noise criteria of  $\Gamma > 2$ . Finally, a ring of guard cells with  $\Gamma > 0$  is added to the cluster. A negative signal is possible due to noise and pile-up corrections. These initial clusters are analysed for local maxima by splitting algorithms and further divided

if maxima are found. The prepared clusters are interpreted as mass less pseudo-particles whose four-momenta are reconstructed from the cluster energies and the direction given by the energy weighted barycentre of the clusters. Afterwards, they are handed over to jet finding algorithms which implement different prescriptions how these objects are combined into jets.

The **AntiKt4** algorithm [52, 53] uses an ordering parameter  $R$  in the inverse momentum space to merge energy clusters into jets. The ordering parameter  $R$  is the only free parameter of the algorithm and allows for controlling the cone size of reconstructed jets. In the default configuration, the value  $R = 0.4$  is chosen. The **AntiKt** algorithm ensures that all input objects end up in exactly one jet and that the theoretical requirements of infrared and collinear safety<sup>15</sup> are met.

Another experimentally important point is the energy calibration of the jets reconstructed. Interactions of hadrons with the calorimeter can either be of electromagnetic or hadronic nature. As the detector response is different for both kind of interactions, dedicated calibration schemes are needed. By default, the signal of calorimeter cells is interpreted with the electromagnetic calibration. Corrections can be applied on the level of reconstructed cluster objects before these are given to the jet finding algorithms or at the level of already reconstructed jets. The latter method modifies the energies of all cells associated to a jet by correction factors which depend on the position of the cell and the cell signal density. This approach is applied in the **AntiKt4TopoEM** algorithm. An overall Jet Energy Scale (JES) correction accounting for pile-up effects, noise in the calorimeter and algorithm effects is applied on top of that.

### 3.4.4 Missing Transverse Energy

At hadron colliders, the longitudinal momentum fractions carried by the colliding partons are unknown and so is the total momentum of the centre-of-mass system. Therefore, the conservation of momentum can not be employed for constraining momenta of undetectable particles. However, the transverse momenta of the incoming partons can be neglected and thus a momentum conservation in the transverse plane can be formulated leading to the following definition of the missing transverse momentum:

$$p_{x,\text{miss}} = - \sum_i p_{x,i}, \quad (3.8)$$

$$p_{y,\text{miss}} = - \sum_i p_{y,i} \quad (3.9)$$

where the sums go over all produced visible particles. The momentum of a particle and its transverse component can only be measured by the tracking system in ATLAS which has a limited coverage up to  $|\eta| < 2.5$ . Because a close to full coverage is desirable for

<sup>15</sup>A light quark with energy  $E_q$  can radiate a gluon with an energy  $E_g$  at an angle  $\theta$  corresponding to the interaction  $q \rightarrow qg$ . The propagator of the outgoing light quark is proportional to  $(E_q E_g (1 - \cos \theta))^{-1}$  which is divergent for  $E_g \rightarrow 0$  (infrared divergence) and  $\theta \rightarrow 0$  (collinear divergence). Therefore, the radiation of a soft and/or collinear gluon should not spoil the performance of the jet reconstruction algorithms.

a good performance of the missing transverse momentum measurement, ATLAS uses its calorimeter systems which have a larger coverage in  $\eta$  to measure the *Missing Transverse Energy*. Even though energy is a scalar quantity, a transverse energy together with its components can be defined according to

$$E_T = \frac{E}{\cosh \eta}, \quad (3.10)$$

$$E_x = E_T \cos \phi, \quad (3.11)$$

$$E_y = E_T \sin \phi. \quad (3.12)$$

The  $\vec{E}_{T,\text{miss}}$  is then defined as

$$\vec{E}_{T,\text{miss}} = - \sum_i \vec{E}_{T,i} \quad (3.13)$$

where the sum goes over all produced particles.

In the large energy limit, when the masses of individual particles are negligible compared to their energies, the  $\vec{E}_{T,\text{miss}}$  becomes equivalent to the missing transverse momentum. ATLAS considers an object-based and a cell-based approach for reconstructing the missing transverse energy. The former benefits from a correct energy calibration of all reconstructed and classified objects. As the object-based approach was still under investigation at the beginning of this study, the cell-based  $\vec{E}_{T,\text{miss}}$  reconstruction algorithm is used which calculates  $\vec{E}_{T,\text{miss}}$  according to

$$\vec{E}_{T,\text{miss}} = \vec{E}_{T,\text{miss}}^{\text{calo}} + \vec{E}_{T,\text{miss}}^{\text{cryo}} + \vec{E}_{T,\text{miss}}^{\text{Muon}}. \quad (3.14)$$

The first term describes the energy contributions from all reconstructed and calibrated<sup>16</sup> topological clusters in the calorimeters. Due to the thickness of the cryostat between the electromagnetic and hadronic calorimeter in the barrel section which corresponds to half an interaction length, hadronic showers can lose part of their energy. The second term in (3.14) accounts for these losses by comparing the energy depositions in the last layer of the electromagnetic calorimeter with those in the first layer of the hadronic calorimeter. Contributions from muons are treated separately as they deposit only a small fraction of their energy in the calorimeters. The transverse energy of reconstructed muon candidates is calculated from its measured momentum. In order to avoid a double counting of muon contributions, the energy deposits along the direction of a track associated to a reconstructed muon candidate are subtracted as these are already included in the calorimeter term.

---

<sup>16</sup>The calibration depends once more on the cell signal density and information about the shower shape to distinguish energy deposits from electromagnetic and hadronic interactions.

# Chapter 4

## Event Topology

As the event topology is very similar for  $pp \rightarrow \gamma^*/Z \rightarrow \tau^+\tau^-$  and  $pp \rightarrow \phi \rightarrow \tau^+\tau^-$  processes<sup>1</sup>, the common kinematic properties are discussed in this chapter. Other processes, which yield the same signature, are also mentioned as they constitute the background for both signal processes. In addition, the decay of tau leptons is briefly reviewed together with possible methods for retrieving information about the invariant mass of the di-tau system.

### 4.1 The Process $pp \rightarrow \gamma^*/Z \rightarrow \tau^+\tau^-$

Since the gauge fields  $A^\mu$  and  $Z^\mu$  have the same quantum numbers, the related gauge bosons, the photon  $\gamma$  and the  $Z$  boson, differ only in their rest mass and their coupling structure to fermions. This analysis is not sensitive to the latter and can therefore, only rely on the different masses to distinguish the processes  $pp \rightarrow Z \rightarrow \tau^+\tau^-$  and  $pp \rightarrow \gamma^* \rightarrow \tau^+\tau^-$ . However, either gauge boson is an intermediate particle which does not need to be on-shell<sup>2</sup>. Consequently, it is not possible to disentangle the contributions coming from an off-shell photon, labelled  $\gamma^*$ , and the  $Z$  boson itself. To make a well-defined statement, the cross section for the inclusive process  $pp \rightarrow \gamma^*/Z \rightarrow \tau^+\tau^-$  restricted to the mass range of the intermediate vector boson<sup>3</sup> of  $66 \text{ GeV} \leq m_{\tau\tau} \leq 116 \text{ GeV}$  is measured. In the following sections, this ambiguity is only stated explicitly in Feynman diagrams and where otherwise confusion may occur.

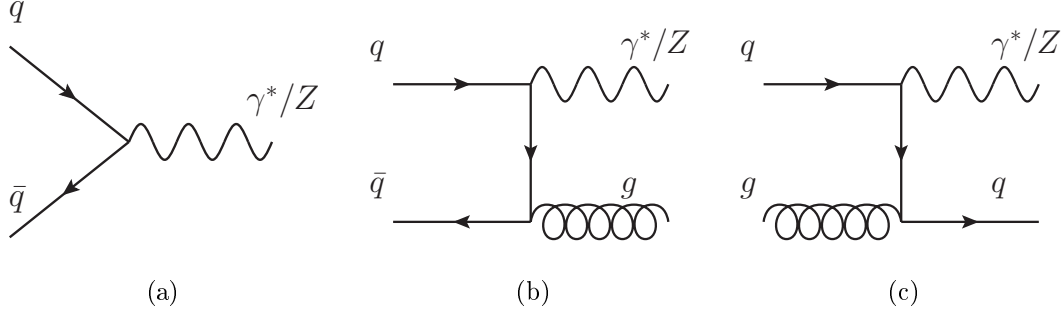
Possible tree-level and next-to-leading order production processes for the  $Z$  boson are shown in Figure 4.1. Since the transverse momenta of the incoming partons are negligible, the  $p_T$  of the  $Z$  boson, produced by  $q\bar{q} \rightarrow Z$  (cf. Figure 4.1(a)), is also extremely small. The process in Figure 4.1(b) is a higher order correction to the first one (initial state radiation) and causes a non-zero  $p_T$  of the  $Z$  boson. However, the collinear radiation of a soft gluon is preferred (see also footnote 15 on page 33) which leads to a diminished influence on the  $p_T$  of the  $Z$  boson. The last diagram 4.1(c) is a  $u$ -channel process whose cross section is proportional to  $(1 + \cos\theta)^{-1}$  with the scattering angle between the incoming and outgoing quark in the centre-of-mass frame labelled  $\theta$ . Therefore, the

---

<sup>1</sup>In the following, both processes are referred to as “signal processes”.

<sup>2</sup>On-shell means that the invariant mass of a particle is equal to its rest mass. The opposite is called off-shell.

<sup>3</sup>The mass of the intermediate gauge boson is given by the invariant mass of the di-tau system.



**Figure 4.1:** Tree-level and next-to-leading order production processes for the  $Z$  boson.

dominant contribution comes from  $\theta \approx \pi$  which corresponds to a backward scattering of the quark and, thus, the  $p_T$  of the  $Z$  boson is again small. To conclude, the  $Z$  boson is predominantly produced with a low transverse momentum.

As it can be seen from Equations (2.29) and (A.57), the coupling of the  $Z$  and  $\gamma^*$  does not depend on the generation index of the fermions. Therefore, the branching ratio<sup>4</sup> into charged leptons is the same<sup>5</sup> for all three generations (cf. Table 4.1).

As a consequence of the low transverse momentum of the produced gauge boson, the two tau leptons exhibit a back-to-back topology in the transverse plane. In the limit  $p_{T,Z} \rightarrow 0$ , the opening angle in the  $x$ - $y$ -plane approaches  $\Delta\phi(\tau^+, \tau^-) \rightarrow \pi$ .

The theoretical cross section [54, 55] for the process  $pp \rightarrow \gamma^*/Z \rightarrow \tau^+\tau^-$  at a centre-of-mass energy of  $\sqrt{s} = 7$  TeV including NNLO<sup>6</sup> QCD and EW corrections is given by

$$\sigma_{\text{Theory}}(pp \rightarrow \gamma^*/Z \rightarrow \tau^+\tau^-) |_{66 \text{ GeV} \leq m_{\tau\tau} \leq 116 \text{ GeV}} = 964 \pm 48 \text{ pb}. \quad (4.1)$$

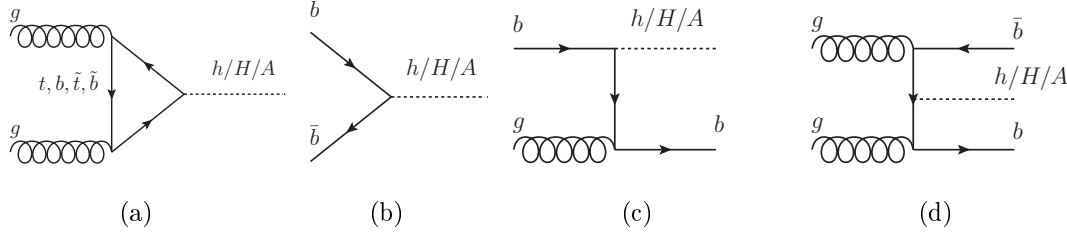
## 4.2 The Process $pp \rightarrow h/H/A \rightarrow \tau^+\tau^-$

Because the couplings between the vector bosons and neutral MSSM Higgs bosons are suppressed or even absent (cf. Table 2.6), the contributions of vector boson fusion or Higgs strahlung processes to the total production cross section are diminished in the MSSM. Therefore, the production of neutral MSSM Higgs bosons is driven by the gluon-fusion process depicted in Figure 4.2(a) and the  $b$ -associated production shown in Figures 4.2(b) to 4.2(d). Sizeable loop contributions in the gluon-fusion process arises from top and bottom quarks where the latter is enhanced for large values of  $\tan\beta$ . Also, effects of stop and sbottom squarks have to be considered if the squarks are light [56]. Owing to the relatively large Yukawa coupling, the Higgs radiation off bottom quarks amounts to a

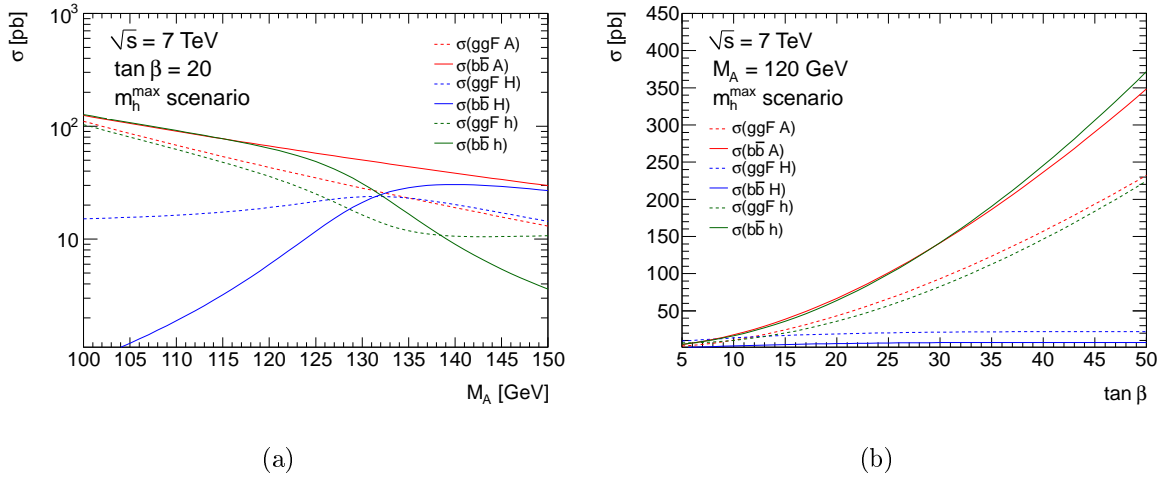
<sup>4</sup>The branching ratio  $\mathcal{BR}$  is the decay width for one specific decay channel divided by the total width of the decaying particle.

<sup>5</sup>To be more precise, this statement holds only if the influence of the phase space integral is neglected. As the  $Z$  mass is much larger than the masses of all charged leptons, the effect of the phase space integral is indeed negligible.

<sup>6</sup>next-to-next-to-leading order



**Figure 4.2:** Production processes for neutral MSSM Higgs bosons.



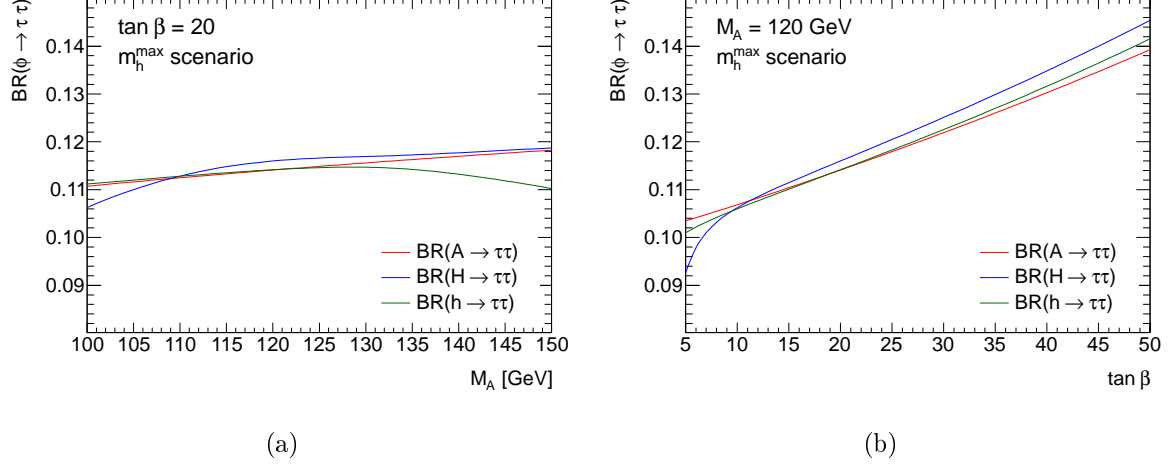
**Figure 4.3:** Production cross sections for the neutral MSSM Higgs bosons  $A$  (red),  $H$  (blue) and  $h$  (green) via gluon-fusion process (dashed) and in association with  $b$ -quarks (solid) as a function of  $M_A$  (left) and  $\tan\beta$  (right).

considerable contribution which is again enhanced for larger values of  $\tan\beta$ . The masses of the neutral CP even MSSM Higgs bosons, the couplings and the branching ratios are calculated with the programme Feynhiggs 2.7.4 [57–60]. The cross sections for the gluon-fusion process are based on HIGLU [61] and ggh@nnlo [62, 63] while the cross section for the  $b$ -associated production is derived in the Santander matching scheme [64] from 4- and 5-flavour calculations [65, 66]. Figure 4.3 displays the contributions of the different production processes for all three Higgs bosons as a function of the two parameters  $M_A$  and  $\tan\beta$ .

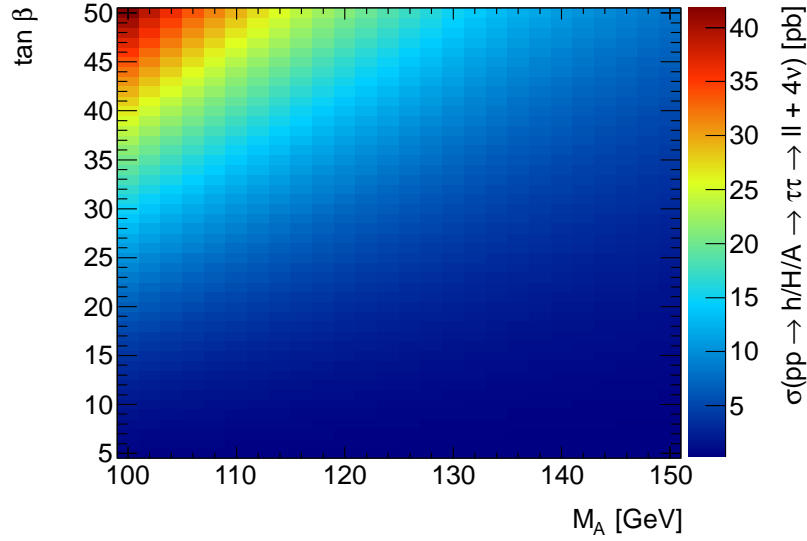
Similarly to the case of  $Z$  boson production, the Higgs bosons are mostly produced with a small transverse momentum leading again to a back-to-back topology of the two tau leptons in the transverse plane. In the case of  $b$ -quark associated Higgs boson production, the presence of one or two additional  $b$ -jets<sup>7</sup> can be used for a more exclusive event selection. This feature is not exploited in this study.

In the low mass regime of  $M_A = 100 - 150$  GeV, which is addressed in this thesis, the

<sup>7</sup>The term  $b$ -jet refers to a hadronic shower initiated by a  $b$  quark. Sophisticated  $b$ -tagging algorithms employ the properties of long-living  $B$  mesons to classify a jet as originating from a  $b$  quark or not.



**Figure 4.4:** Branching ratio  $\mathcal{BR}(\phi \rightarrow \tau^+\tau^-)$  of the neutral MSSM Higgs bosons  $A$  (red),  $H$  (blue) and  $h$  (green) as a function of  $M_A$  (left) and  $\tan \beta$  (right).



**Figure 4.5:** Total cross section in pb for the production of neutral MSSM Higgs bosons in proton-proton collisions at  $\sqrt{s} = 7$  TeV including gluon-fusion and  $b$ -quark associated production mechanisms.



$Z$ boson decay		Tau lepton decay	
decay channel	branching ratio	decay channel	branching ratio
$Z \rightarrow e^+e^-$	3.363%	$\tau \rightarrow e\nu_e\nu_\tau$	17.85%
$Z \rightarrow \mu^+\mu^-$	3.366%	$\tau \rightarrow \mu\nu_\mu\nu_\tau$	17.36%
$Z \rightarrow \tau^+\tau^-$	3.367%	$\tau \rightarrow q\bar{q}'\nu_\tau$	64.79%
$Z \rightarrow \nu\bar{\nu}$	20.00%		
$Z \rightarrow q\bar{q}$	69.91%		

**Table 4.1:** Decay channels of the  $Z$  boson and  $\tau$  lepton with branching ratios [13].

neutral Higgs bosons decay almost exclusively into  $b\bar{b}$  and  $\tau^+\tau^-$  pairs. Due to the low Higgs boson masses and the reduced coupling to vector bosons, Higgs boson decays into pairs of  $W$  or  $Z$  bosons, which play a dominant role in the SM, are comparably rare. The exact branching ratio  $\mathcal{BR}(\phi \rightarrow \tau^+\tau^-)$  depends on the parameters  $M_A$  and  $\tan\beta$  and is of the order of 10 – 12% as shown in Figure 4.4.

The total cross section for the process  $pp \rightarrow \phi \rightarrow \tau^+\tau^- \rightarrow \ell^+\ell^- + 4\nu$  is shown in Figure 4.5 as a function of  $M_A$  and  $\tan\beta$ . Thereby, the contributions of both production processes and all three neutral MSSM Higgs bosons<sup>8</sup> are summed. Additionally, the branching ratios for the tau lepton decays, as explained in Section 4.3, are included.

For simplicity it is assumed that the event kinematics for the decay of the neutral Higgs boson are determined by the mass of the Higgs boson and do not depend on the value of  $\tan\beta$ . This is a valid approximation as  $\tan\beta$  mostly influences the total cross section and the branching ratios.

## 4.3 Decay of Tau Leptons

So far, the signal processes are discussed up to the  $\tau^+\tau^-$  final state but the tau lepton  $\tau$  is not a stable particle. Due to its short lifetime  $\tau_\tau$  corresponding to  $c\tau_\tau = 87.11 \mu\text{m}$  [13], it decays before any interaction with the sensitive detector material takes place. Therefore, the signature of a tau lepton is given by the signature of its decay products together with the presence of a neutrino which contributes to the  $\vec{E}_{\text{T,miss}}$  measurement. Depending on the final states products, the decay modes of tau leptons can be classified as follows:

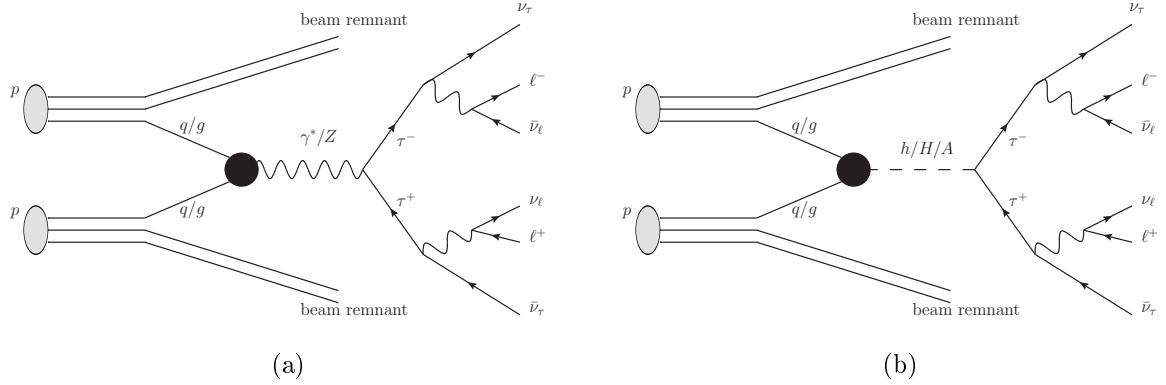
**hadronic decays:**  $\tau \rightarrow \nu_\tau q\bar{q}'$ ,

**leptonic decays**<sup>9</sup>:  $\tau \rightarrow \ell\nu_\tau\nu_\ell$ .

The branching ratios for the different tau lepton decay modes are summarised in Table 4.1. Although this analysis focuses only on the leptonic tau decays, it should be

<sup>8</sup>It is essential to notice that, in general, the masses of the three neutral Higgs bosons are different (cf. Figure 2.2). Therefore, it must be ensured that the analysis is sensitive to the masses of all three Higgs bosons if one uses the stated cross sections.

<sup>9</sup>In the scope of this work, the symbol  $\ell$  represents a light charged lepton,  $\ell = e, \mu$ .



**Figure 4.6:** Production of tau lepton pairs via  $\gamma^*/Z$  gauge bosons (left) or neutral MSSM Higgs bosons (right).

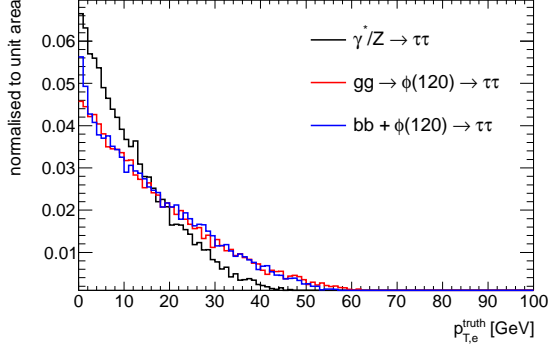
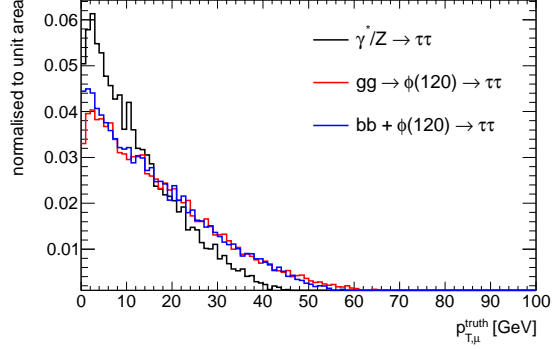
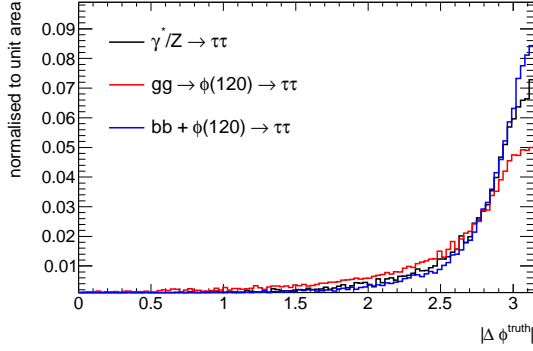
mentioned that dedicated reconstruction and identification algorithms for hadronically decaying tau leptons exist [67]. Even though the leptonic decays suffer from a significantly smaller branching ratio, they play an important role due to their clear signature in the detector. Especially at hadron colliders like the LHC, the reconstruction and identification of hadronically decaying tau leptons is a challenging task and strongly affected by the large amount of QCD processes leading to a sizeable background contamination. In contrast, the leptonic final state benefits from large reconstruction and identification efficiencies with a comparably small background contamination.

## 4.4 Event Topology

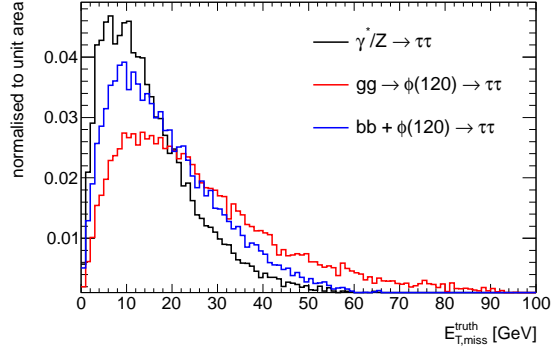
Examples of Feynman diagrams for both signal processes are given in Figure 4.6. Summarising the remarks of the previous sections, events from the two signal processes are characterised by two oppositely charged leptons, either two muons, two electrons or one electron and one muon. This work concentrates on the  $e\mu + 4\nu$  final states which reduces dramatically the background contributions arising from  $\gamma^*/Z \rightarrow e^+e^-$  and  $\gamma^*/Z \rightarrow \mu^+\mu^-$  events.

According to the remarks in Section 4.1 and 4.2, the  $Z$  and Higgs bosons are mostly produced with a small  $p_T$  resulting in a maximum transverse momentum of the tau lepton about  $p_{T,\tau} \approx m/2$  with  $m$  being the mass of the decaying resonance. Despite the fact that the decaying resonances have high masses of  $m \gtrsim 90$  GeV, the charged leptons in the final state have rather low transverse momenta because the four neutrinos in the event carry away a noticeable amount of energy. Figures 4.7(a) and 4.7(b) show the expected  $p_T$  distributions of the produced leptons for the different signal processes. These distributions are retrieved at event generation level before any detector simulation is applied.

Due to the momentum of the tau lepton of  $p_\tau = m/2 \approx 45 - 75$  GeV, which is much greater than its rest mass, its decay products are strongly boosted. Therefore, the direc-


 (a) Electron  $p_T$  distribution.

 (b) Muon  $p_T$  distribution.


(c) Opening angle between the two leptons in the transverse plane.


 (d)  $E_{T,miss}$  distribution.

**Figure 4.7:** Normalised distributions of important kinematic variables after event generation (no detector simulation is applied) for the three signal processes:  $pp \rightarrow \gamma^*/Z \rightarrow \tau^+\tau^-$  (black) and the two production processes for a neutral Higgs boson with a mass of 120 GeV, gluon-fusion process (red) and  $b$ -quark associated production (blue).

tion of flight of the produced leptons is approximately the direction of the tau lepton. Hence, the back-to-back topology of the tau leptons is transferred to the charged leptons as it is shown in Figure 4.7(c). Even though there are four neutrinos in the event, two from each tau lepton decay, only a small to moderate  $E_{T,\text{miss}}$  is expected because the back-to-back topology in the transverse plane leads to large cancellations. The expected  $E_{T,\text{miss}}$  distribution is depicted in Figure 4.7(d).

Furthermore, no more detector activity in the vicinity of the two charged leptons is expected since the only close-by produced particles are neutrinos whose interactions with the detector are negligible. The *isolation* of lepton candidates can be measured by two criteria. On the one hand, further tracks close to the lepton candidate can be considered. On the other hand, energy deposits in the proximity of the reconstructed lepton candidate can be used to define an isolation criteria. The former is a *track-based* isolation criteria which is insensitive to neutral particles while the latter is a *calorimeter-based* isolation criteria.

Track-based isolation criteria are calculated by summing the  $p_T$  of all reconstructed tracks which are inside a cone with an opening angle defined as  $\Delta R$  around the lepton candidate and obey  $p_{T,\text{track}} \geq 1$  GeV. The track of the candidate itself is thereby omitted. They are labelled **ptconeXX** where **XX** defines the cone size as  $\Delta R = 0.\text{XX}$ .

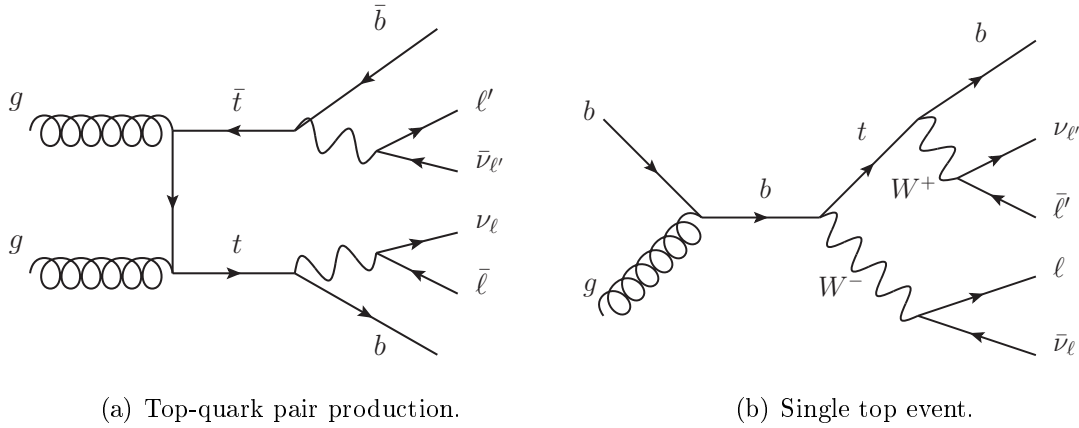
Calorimeter-based isolation variables are derived similarly. Again, a cone around the momentum axis of the lepton candidate is spanned. All energy clusters inside this cone are considered to calculate the total transverse energy where the transverse energy of one cluster is given by Equation (3.10). The most central part of the cone is assumed to belong to the reconstructed lepton candidate and is omitted. The meaning of *most central* is different for muon and electron candidates. For the muons the central cone with an opening angle of  $\Delta R = 0.05$  is ignored while for the electrons the central  $5 \times 7$  calorimeter cells in  $\eta \times \phi$  are removed. The calorimeter-based criteria are labelled **etconeXX** with **XX** defining again the cone size as  $\Delta R = 0.\text{XX}$ .

To summarise the discussion, both signal processes are characterised by

- exactly one geometrically isolated electron candidate,
- exactly one geometrically isolated muon candidate,
- both lepton candidates must carry opposite electric charge.

In order to suppress background processes and enrich the selected data sample with signal events, the following kinematic properties can be exploited:

- both lepton candidates have a moderate  $p_T$ ,
- the angle  $\Delta\phi(e, \mu)$  between both lepton candidates in  $x$ - $y$ -plane is close to  $\pi$ ,
- the missing transverse energy is expected to be small.



**Figure 4.8:** Feynman diagrams for processes involving top quarks at the LHC.

## 4.5 Background Processes

Background processes are defined as all processes which can mimic the signature of the signal processes. Background events arise either from other physics processes whose signatures fulfil the criteria given in Section 4.4, from mis-reconstruction and -identification of lepton candidates or a combination of both. The main sources of background events are listed below.

**multijet events**<sup>10</sup>: Physical processes, which produce quarks or gluons, are characterised by the presence of jets in the finale state. These jets can either contain leptons coming from decays of heavy flavour quarks, or be mis-identified as lepton candidates. As a result, pairs of oppositely charged lepton candidates can be produced which fake the signal signature. Despite the mis-identification rate for jets being interpreted as lepton candidates is low, the overwhelmingly large cross section for QCD processes results in such events being an important background.

**$t\bar{t}$  events**: A possible Feynman diagram for top-quark pair production is shown in Figure 4.8(a). In the case that both  $W$  bosons decay leptonically, the final state contains two isolated and oppositely charged leptons and, therefore, constitutes a background to the signal processes. Nevertheless,  $t\bar{t}$  events can be distinguished from signal events by the higher transverse momentum of the charged leptons and by a significant amount of missing transverse energy.

It is also possible that one or both  $W$  bosons decay hadronically and the lepton candidates are faked by jets analogously to the case of multijet events. However, this is a minor effect due to the good background rejection of the lepton identification algorithms.

<sup>10</sup>The background coming from multijet events is referred to as QCD in tables and figures as it arises from QCD processes.

The total cross section for top pair production at the LHC with  $\sqrt{s} = 7$  TeV is calculated to [68]

$$\sigma_{t\bar{t}} = 162.6 \pm 17.1 \text{ pb} . \quad (4.2)$$

$\gamma^*/Z \rightarrow e^+e^-/\mu^+\mu^-$  : These processes produce two isolated lepton candidates of same flavour and opposite charge in the final state. Although the restriction to the  $e\mu + 4\nu$  final state reduces the background contributions of Drell-Yan and  $Z$  boson production considerably, it is still possible that one of the leptons is outside the detector acceptance or fails the reconstruction but instead an additional jet mimics another lepton candidate. Due to lepton universality in the electroweak sector,  $pp \rightarrow \gamma^*/Z \rightarrow e^+e^-/\mu^+\mu^-$  processes occur as often as the signal process  $pp \rightarrow \gamma^*/Z \rightarrow \tau^+\tau^-$  and, thus, must be considered as potential background source.

$W \rightarrow \ell\nu$  : Decays of  $W$  bosons manifest themselves through an isolated lepton candidate and a large amount of missing transverse energy. Again, the second lepton candidate may arise from any other jet in the event. The theoretical cross section for  $W$  boson production and its leptonic decay is given by [54, 55]

$$\sigma(pp \rightarrow W \rightarrow \ell\nu) = 10.5 \pm 0.5 \text{ nb} . \quad (4.3)$$

**Di-boson production:** The simultaneous production of two gauge bosons has a small cross section which results in being a minor effect for the  $\gamma^*/Z \rightarrow \tau^+\tau^-$  signal. Nevertheless, it is well suited to mimic the signature of two isolated lepton candidates with opposite charge. As a consequence, it has to be considered as background for MSSM Higgs boson searches whose cross sections are of the same order of magnitude. The total production cross sections for di-boson processes at the LHC and  $\sqrt{s} = 7$  TeV are given by [54, 55]

$$\sigma_{WW} = 44.9 \pm 2.2 \text{ pb} , \quad (4.4)$$

$$\sigma_{WZ} = 18.0 \pm 1.3 \text{ pb} , \quad (4.5)$$

$$\sigma_{ZZ} = 5.64 \pm 0.28 \text{ pb} . \quad (4.6)$$

**Single Top production:** Single top events are rather rare at the LHC. The total cross section for the production of a single (anti) top quark at  $\sqrt{s} = 7$  TeV is<sup>11</sup> [69–71]

$$\sigma_{\text{single top}} = 84.4 \pm 2.3 \text{ pb} . \quad (4.7)$$

The signature of a possible single top event is shown in Figure 4.8(b). The top quark decay involves at least one  $W$  boson which can decay leptonically. Depending on the production process of the top quark, another  $W$  boson might be present which potentially causes another lepton in the final state. Otherwise, the second lepton candidate can be produced by additional jets in the event.

---

<sup>11</sup>The given number is the sum of the  $s$ -,  $t$  and  $Wt$ -channel production cross section for top and anti-top quarks and does not yet include any branching ratio to leptonic final states.

$\gamma^*/Z \rightarrow \tau^+\tau^-$  : Of course, this process is a severe background to the search for neutral MSSM Higgs bosons in the  $\tau^+\tau^-$  channel. As already outlined, both processes exhibit the same event topology and have similar kinematic properties. Thus,  $pp \rightarrow \gamma^*/Z \rightarrow \tau^+\tau^-$  events constitute an irreducible background.

## 4.6 Mass Reconstruction Techniques

The mass is the best usable property to distinguish between a  $Z$  boson and the neutral Higgs bosons. Other differences like the spin or the coupling structure manifest themselves in different angular distributions of the decay products. Unfortunately, these effects are blurred by the limited detector resolution and the decay of the tau leptons.

Owing to the four neutrinos in the final state, it is not possible to reconstruct the complete four-momentum of the  $\tau^+\tau^-$  system. Therefore, either partial reconstruction methods or approximations are used to infer information about the invariant mass of the resonance. Three possible mass definitions are explained in the remainder of this section.

The **visible mass** is defined as the invariant mass of the visible tau lepton decay products. For the  $e\mu + 4\nu$  final state this corresponds to the invariant mass

$$m_{e\mu} = \sqrt{(p_e^\nu + p_\mu^\nu)^2}. \quad (4.8)$$

The advantage of this simple definition is the precise reconstruction of both lepton four-vectors  $p_e^\nu$  and  $p_\mu^\nu$ . However, the visible mass provides no direct link to the invariant mass of the resonance as the contributions of the neutrino momenta are ignored.

The **effective mass** incorporates information from the  $\vec{E}_{T,\text{miss}}$  measurement. It is defined as

$$m_{\text{eff}} = \sqrt{(p_e^\nu + p_\mu^\nu + p_{\text{MET}}^\nu)^2} \quad (4.9)$$

with

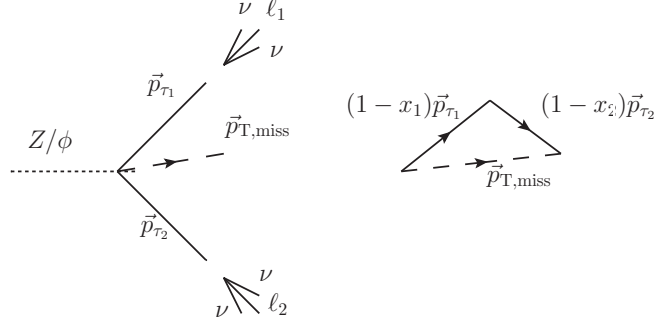
$$p_{\text{MET}}^\nu = \left( \sqrt{p_{x,\text{miss}}^2 + p_{y,\text{miss}}^2}, p_{x,\text{miss}}, p_{y,\text{miss}}, 0 \right)^T \quad (4.10)$$

and extends the visible mass with information on the neutrino momenta. Nevertheless, it can only provide an approximation since the  $\vec{E}_{T,\text{miss}}$  measurement is only sensitive to the sum of all transverse neutrino momenta which contains large cancellations (cf. Section 4.4). Additionally, it is based on the assumption that the measured  $\vec{E}_{T,\text{miss}}$  is only due to the neutrinos from the two tau lepton decays. This hypothesis ignores possible contributions from detector effects and further, simultaneous proton-proton interactions.

The **collinear approximation** [72] makes use of the large boost of the tau leptons with a typical Lorentz factor<sup>12</sup> of  $\gamma = E/m_\tau \approx 25$ . Hence, the tau lepton decay

---

<sup>12</sup> $\gamma = (1 - \beta^2)^{-\frac{1}{2}}$  with  $\beta$  being the velocity



**Figure 4.9:** Sketch of tau lepton decay topology for the collinear mass approximation.

products are approximately collinear to the initial tau leptons and one can introduce the fractions  $x_{1/2}$  of the tau lepton momenta carried by the charged leptons (cf. Figure 4.9),

$$\vec{p}_{\ell_i} = x_i \cdot \vec{p}_{\tau_i}, \quad i = 1, 2. \quad (4.11)$$

Applying the conservation of transverse momenta and assuming that the  $\vec{E}_{T,\text{miss}}$  arises only from neutrinos produced in the tau lepton decays, one obtains

$$\vec{p}_{\tau_1} + \vec{p}_{\tau_2} = \vec{p}_{\ell_1} + \vec{p}_{\ell_2} + \vec{p}_{T,\text{miss}}. \quad (4.12)$$

Combining Equations (4.11) and (4.12) and neglecting the lepton masses, the invariant mass of the  $\tau^+\tau^-$  system can be written as

$$m_{\tau\tau} = \frac{m_{\ell\ell}}{\sqrt{x_1 x_2}}, \quad (4.13)$$

$$\text{with } x_1 = \frac{p_{x,\ell_1} \cdot p_{y,\ell_2} - p_{y,\ell_1} \cdot p_{x,\ell_2}}{p_{y,\ell_2} \cdot p_{x,\text{miss}} - p_{x,\ell_2} \cdot p_{y,\text{miss}} + p_{x,\ell_1} \cdot p_{y,\ell_2} - p_{y,\ell_1} \cdot p_{x,\ell_2}}, \quad (4.14)$$

$$x_2 = \frac{p_{x,\ell_1} \cdot p_{y,\ell_2} - p_{y,\ell_1} \cdot p_{x,\ell_2}}{p_{x,\ell_1} \cdot p_{y,\text{miss}} - p_{y,\ell_1} \cdot p_{x,\text{miss}} + p_{x,\ell_1} \cdot p_{y,\ell_2} - p_{y,\ell_1} \cdot p_{x,\ell_2}} \quad (4.15)$$

and  $m_{\ell\ell}$  being the visible mass. In contrast to the other two methods, the collinear mass allows a full reconstruction of the mass of the decaying resonance. Similarly to the effective mass, this method relies on a correct measurement of the  $\vec{E}_{T,\text{miss}}$  and is very sensitive to further neutrinos in the event. In addition, the approximation breaks down for  $\Delta\phi(\ell_1, \ell_2) = \pi$  because no unique solution for  $x_{1/2}$  can be found anymore. The mass resolution already deteriorates for  $\Delta\phi(\ell_1, \ell_2) \approx \pi$  [32] leading to a large portion of signal events which can not be treated with the collinear approximation.



# Chapter 5

## Measurement of the Cross section of the Process $pp \rightarrow \gamma^*/Z \rightarrow \tau^+\tau^-$ in the $e\mu + 4\nu$ Final State

In this chapter the first measurement of the process  $pp \rightarrow \gamma^*/Z \rightarrow \tau^+\tau^- \rightarrow e\mu + 4\nu$  with the ATLAS detector [73] is presented. For this purpose  $35.5 \text{ pb}^{-1}$  of data obtained from proton-proton collisions at a centre-of-mass energy of  $\sqrt{s} = 7 \text{ TeV}$  are analysed.

The first part of this thesis is performed in the context of this cross section measurement. In the following sections, the whole analysis is described with emphasis on parts where significant contributions are made.

First, the data sets used for this measurement are mentioned in Section 5.1, followed by a brief description of the event preselection in Section 5.2. The definitions for reconstructed and identified objects are given in Section 5.3. In Section 5.4 corrections, which have to be applied on the simulated data samples, are outlined. Explanations of the final event selection and the background estimation are given in Sections 5.5 and 5.6, respectively. The methodology for the derivation of the cross section and a discussion of systematic uncertainties can be found in Sections 5.7 and 5.8. Finally, the results are summarised and discussed in Section 5.9.

### 5.1 Data and Simulated Samples

For this cross section measurement the data recorded by the ATLAS experiment in the autumn of 2010, corresponding to the data taking periods E4 - I, is analysed. The total integrated luminosity, after the requirement of a good detector status as explained in Section 5.2, is calculated to be  $L = 35.5 \text{ pb}^{-1}$  with a relative uncertainty of 3.4% [74]. Earlier periods are not included due to the rapidly changing pile-up and trigger conditions which result in a loss of only 0.2% of the total delivered luminosity. The highest instantaneous luminosity reached during this time was  $2 \cdot 10^{32} \text{ cm}^{-2}\text{s}^{-1}$ .

Samples for the different background processes are simulated with the MC generators mentioned in Section 3.3.1. The expectations obtained from these simulations are normalised to the integrated luminosity of the data sample using Equation (3.7). A complete list of all simulated samples with their corresponding cross sections and filter efficiencies can be found in Table C.1.

Pile-up effects are emulated in the simulated data sets by the so-called bunch train setup. The following timing structure for the proton bunches is chosen: individual bunches are separated by 150 ns and contained in trains of eight bunches. The average number of interactions per bunch crossing is assumed to be Poisson distributed with an expectation value of 2.2.

## 5.2 Event Preselection

The event preselection imposes requirements on the recorded data events to ensure a high quality sample of proton-proton collisions events. In the following, the cuts applied and their motivation are explained.

### 5.2.1 Vertex Requirement

The event is required to have at least one reconstructed vertex with  $\geq 3$  associated tracks. Vertices are found by extrapolating reconstructed tracks to the beam pipe and looking for regions with high track densities. Requiring a vertex with at least three associated tracks rejects events triggered by a cosmic muon traversing the detector. Those events are characterised by one track with a large transverse momentum going through the whole detector. During the vertex reconstruction step, this track is interpreted as two tracks originating from the same vertex which fails the criterion given above.

### 5.2.2 Detector Status

The state of the individual detector components is continuously monitored and stored in a data base. Additionally, the quality of the two proton beams is under constant surveillance. Events are only considered for this analysis if they were recorded when all parts of the detector, which are necessary for this study, were fully operational and the proton beams were stable.

### 5.2.3 Trigger Selection

The trigger choice is motivated by the topology of the signal events. As outlined in Section 4.4, the final state is characterised by one electron and one muon. The expected  $p_T$  distributions of both leptons without any detector effects are shown in Figures 4.7(a) and 4.7(b) and ask for low  $p_T$  threshold in order to keep the signal selection efficiency high. The efficiencies of triggers looking for muon signatures are intrinsically lower due to the limited geometrical coverage of the muon trigger system.

Therefore, an event filter trigger looking for at least one electron candidate, which passes the medium electron identification and fulfils  $p_T \geq 15$  GeV, is used for this analysis. It is labelled `EF_e15_medium`. The threshold of 15 GeV is dictated by the fact that electron triggers with lower thresholds were prescaled (cf. Section 3.2.5) over a

large fraction of the data taking periods resulting in a significantly decreased effective luminosity.

### 5.2.4 Jet Cleaning

The jet reconstruction and  $\vec{E}_{T,\text{miss}}$  measurement are very sensitive to energy deposits in the calorimeter which do not originate from proton-proton collisions. As a consequence, additional jet candidates may be reconstructed and the  $\vec{E}_{T,\text{miss}}$  measurement is distorted. Possible sources for disturbing energy deposits are hardware problems, cosmic ray showers and abnormal beam conditions. To ensure a correct  $\vec{E}_{T,\text{miss}}$  measurement, events affected by those problems, have to be rejected. The various sources and how they can be eliminated are explained in more detail in Appendix C.2.

## 5.3 Object Definitions

As explained in Section 3.4, the reconstruction and identification algorithms provide various definitions of reconstructed objects. A quality level expresses a certain confidence that the reconstructed object is classified correctly. The most appropriate definition is analysis specific and depends on the background composition as well as on the expected signal to background ratio. For the measurement of the  $pp \rightarrow \gamma^*/Z \rightarrow \tau^+\tau^- \rightarrow e\mu + 4\nu$  cross section, the following object definitions are found to be optimal. A more detailed and technical summary can be found in Table C.3.

**Electron Candidates** Electron candidates are considered if they are reconstructed and identified by either the standard algorithm or an algorithm optimised for the reconstruction of low- $p_T$  electrons. They have to pass the **medium** identification and refined track matching criteria. The latter is introduced to correct for alignment differences between the inner detector and the EM calorimeter which are observed in data. In order to ensure that the electron candidates are in a region where the reconstruction, identification, and trigger efficiencies are well understood, a transverse momentum of  $p_T \geq 16$  GeV is required. Furthermore, the candidate has to be reconstructed within  $|\eta| < 2.47$  but outside  $1.37 < |\eta| < 1.52$ . The first requirement is motivated by the tracking acceptance of the ATLAS detector while the second removes candidates reconstructed in the transition region between the barrel and the end-cap calorimeters. Regions in the calorimeters which are affected by readout problems or non-nominal high voltage conditions are flagged and stored as  $\eta \times \phi$  maps. The map corresponding to the data taking period with the highest integrated luminosity is used and the electron candidates are required to be outside of these problematic regions.

The electron four-vector is constructed from the energy measurement in the calorimeter while the direction is taken from the associated track. However, all cuts motivated by calorimeter related issues (e.g.  $\eta$  cut, problematic calorimeter regions) are applied on the position of the electron energy cluster.

**Muon Candidates** For this analysis, combined muon candidates reconstructed with the STACO algorithm are used. The required transverse momentum is  $p_T \geq 10$  GeV and candidates with pseudorapidities up to  $|\eta| \leq 2.4$  are considered. The combined track extrapolated back to the beam pipe has to match the  $z$  position of the primary vertex within 10 mm. This requirement further reduces background coming from cosmic muons. Additional constraints are imposed on the associated inner detector track to enhance the quality of the muon momentum measurement and to suppress muon signatures arising from in-flight decays of hadrons. The latter is important as interactions of hadrons in the hadronic calorimeter are likely to produce secondary muons. These secondary muons lack a track in the inner detector. Tightening the requirements on the associated inner detector track reduces the chance that a secondary muon is linked erroneously to a track produced by a charged hadron. The exact requirements are stated in Table C.3 but can be summarised as follows: it is ensured that several hits in the various layers of the inner detector are found while taking into account that the muon may pass dead detector components or poorly instrumented regions.

**Jet Candidates** Jet candidates are reconstructed using the Anti- $k_T$  algorithm with a cone parameter of  $R = 0.4$ . Their energies are calibrated to the electromagnetic energy scale with a further correction applied on top of that (cf. Section 3.4.3). To ensure that all candidates are in a region where the jet energy scale calibration is reasonably well understood, they are required to have a transverse momentum of  $p_T \geq 20$  GeV and have pseudorapidities of  $|\eta| \leq 4.5$ .

**Missing Transverse Energy** The  $\vec{E}_{T,\text{miss}}$  is reconstructed as outlined in Section 3.4.4. Topological energy clusters in the calorimeter are calibrated according to their classification as electromagnetic or hadronic interaction. Furthermore, contributions of isolated<sup>1</sup> muon candidates are added. To avoid a double counting, the energy contributions in calorimeter cells which are crossed by a track of an isolated muon candidate are subtracted,

$$\vec{E}_{T,\text{miss}} = \vec{E}_{T,\text{miss,calo}} + \vec{E}_{T,\text{miss},\mu} - \vec{E}_{T,\text{miss},\mu \text{ track}}. \quad (5.1)$$

**Resolving Ambiguities** A common problem is the classification of one and the same detector signature as reconstructed objects of different types. To resolve this ambiguity, reconstructed objects are ranked according to the complexity of their signature with the more complex signature getting a higher priority. Objects, which are close to other reconstructed objects with a higher priority, are discarded. Sometimes two close-by objects of the same type are reconstructed. In this case, the object with the higher  $p_T$  is kept. The distance between two objects is measured in  $\Delta R$  as defined in Equation (3.4).

For this analysis the following ranking is applied

$$\text{muons} > \text{electrons} > \text{jets} \quad (5.2)$$

---

<sup>1</sup>A muon candidate is defined as isolated if the  $\Delta R$  to the closest reconstructed jet is greater than 0.3.

$p_T$ range in GeV	correction factor
$16 \leq p_T \leq 18$	$1.004 \pm 0.025$
$18 \leq p_T \leq 20$	$0.987 \pm 0.023$
$20 \leq p_T$	$0.995 \pm 0.005$

**Table 5.1:** Correction factors with total uncertainty for the trigger efficiency.

with lepton candidates being removed if  $\Delta R(\ell_1, \ell_2) \leq 0.2$  and jet candidates being removed if the  $\Delta R$  to the closest object is less than 0.4.

## 5.4 Corrections to the Simulated Samples

Even though the ATLAS detector simulation contains a very complex description of the geometry together with the properties of the detector materials used, it remains an approximate model which is, for practical reasons, limited in detail and accuracy. Furthermore, detector defects, which occur during operation, can only be included in reprocessed simulations. Also, the pile-up scenario used for generating the simulations is fixed while the actual pile-up conditions vary over time. Consequently, the simulated samples have to be corrected for such effects. The corrections applied are explained in the next sections.

### 5.4.1 Trigger Efficiency Correction

This analysis uses the `EF_e15_medium` trigger and reconstructed electron candidates with  $p_T \geq 16$  GeV. The corresponding trigger efficiency  $\varepsilon_{\text{trig}}$  is measured in data and in simulated samples as a function of the  $p_T$  of the electron candidates by studying  $Z \rightarrow e^+e^-$  and  $W \rightarrow e\nu_e$  processes [75]. Thereof,  $p_T$ -dependent corrections factors  $w_{\text{trig}}$  are derived according to

$$w_{\text{trig}}(p_{T,e}) = \frac{\varepsilon_{\text{trig,data}}(p_{T,e})}{\varepsilon_{\text{trig,MC}}(p_{T,e})} \quad (5.3)$$

which are summarised in Table 5.1. The total uncertainty given includes statistical uncertainties due to the limited number of data events and effects of systematic uncertainties.

### 5.4.2 Corrections Related to Lepton Candidates

**Efficiency Corrections** Reconstruction and identification efficiencies for electron and muon candidates are determined in dedicated studies by other groups. These groups provide sets of derived correction factors which are used in this analysis.

The reconstruction efficiencies of electron candidates are found to agree between data and simulation within a relative systematic uncertainty of 1.5% [75]. Correction factors for the electron identification efficiency, which correspond to the object definition used

in this analysis, are given in Table C.4. They depend significantly on the  $\eta$  position of the associated electromagnetic energy cluster. Additionally, a shift depending on the  $p_T$  of the reconstructed electron candidate is observed. Due to the limited statistics, the correction factors are not provided as a two-dimensional map. Instead, the overall correction factor  $w_{e,\text{ID}}$  is given by

$$w_{e,\text{ID}}(p_{T,e}, \eta_e) = w_{e,\text{ID}}(p_{T,e}) \times w_{e,\text{ID}}(\eta_e). \quad (5.4)$$

The uncertainties on the individual terms are added in quadrature to yield the uncertainty on the final correction.

Similarly, correction factors for the muon reconstruction and identification efficiencies are provided [76]. Since the instrumentation of the muon spectrometer is not as uniform in  $\phi$  as the inner detector and the electromagnetic calorimeter are, these correction factors are given as a two-dimensional map in order to better reflect the poorly equipped regions due to the design of the ATLAS detector. The correction weights  $w_\mu$  are in the range 0.98 – 1.01 with uncertainties of the order of 0.01.

By studying the processes  $Z \rightarrow e^+e^-$  and  $Z \rightarrow \mu^+\mu^-$ , which are expected to yield isolated lepton candidates in the final state, one can estimate the efficiency of a lepton candidate being considered as isolated according the definition given in Section 5.5.3. The resulting correction factors  $w_{e,\text{iso}}$  and  $w_{\mu,\text{iso}}$  are summarised in Table C.5. Although the isolation efficiencies for muon candidates agree between data and the simulation within their uncertainties, it is decided to apply them on the simulation in order to be consistent with other ATLAS analyses. The correction factor for the electron isolation efficiency is the product of a  $p_T$  dependent and a  $\eta$  dependent correction.

**Energy and Momentum Corrections** By studying the SM processes  $Z \rightarrow e^+e^-$  and  $Z \rightarrow \mu^+\mu^-$ , one can compare the expected energy and momentum resolutions with the ones obtained in data. For this purpose, the invariant  $m_{ee}$  and  $m_{\mu\mu}$  mass distributions are investigated [51]. Dedicated tools are provided to the analysis teams which smear the energy/momentum of the reconstructed lepton candidates to reproduce the resolution observed in data. The resulting shift in the transverse momenta of the lepton candidates is propagated back to the  $\vec{E}_{T,\text{miss}}$  such that

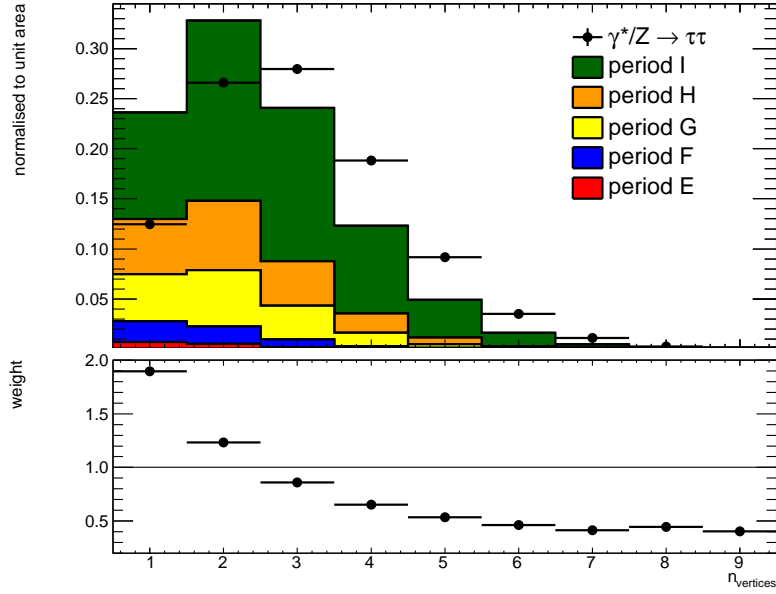
$$\vec{p}_{T,e} + \vec{p}_{T,\mu} + \vec{E}_{T,\text{miss}} = \vec{p}'_{T,e} + \vec{p}'_{T,\mu} + \vec{E}'_{T,\text{miss}} \quad (5.5)$$

where the primed quantities represent the  $\vec{p}_T$  values after the correction.

For the reconstructed muon candidates the transverse momentum is smeared while for the electron candidates the energy is modified. The correction is applied before the object selection is performed.

### 5.4.3 Pile-up Related Corrections

The MC samples are simulated with the pile-up scenario described in Section 5.1. However, the changing beam conditions cause varying instantaneous luminosities and, thus,



**Figure 5.1:** top) normalised vertex multiplicity distributions for the signal MC sample (black dots) and data (stacked); the different data periods are weighted according to their integrated luminosity fraction; bottom) derived correction weights as ratio of the stacked data histogram and the simulation.

affect the number of simultaneous proton-proton interactions. In 2010, the individual proton bunches were separated in time by 150 ns resulting in negligible out-of-time pile-up effects. A measure for the in-time pile-up activity is the number of reconstructed vertices which is assumed to be proportional to the number of simultaneous proton-proton interactions. In Figure 5.1 the normalised distribution of the number of vertices with at least three associated tracks is shown for the collected data, after all event preselection cuts, and for the signal simulation. The simulated samples are re-weighted to match the vertex multiplicity distribution observed in data. Table C.6 states the derived correction factors  $w_{\text{vertex}}$ .

## 5.5 Event Selection

This section outlines the selection for the complete  $pp \rightarrow \gamma^*/Z \rightarrow \tau^+\tau^- \rightarrow e\mu + 4\nu$  analysis. The distributions of important kinematic variables used during the event selection are shown in Figure 5.4. The shapes and normalisations of all background components are taken from simulated samples except for the multijet component which is derived from data as explained in Section 5.6.1. These plots show the data distributions only for comparison reasons. The definition of the following cuts is based purely on information obtained from simulated samples.

The goal of the event selection is to guarantee a high quality of the selected data sample and to minimise the expected relative statistical uncertainty on the signal yield. Let  $S$  denote the expected number of selected signal events and  $B$  the expected number of all

selected background events, the relative statistical uncertainty of the final measurement of  $S$ , assuming that the number of observed events follows a Poisson distribution, is given by

$$\frac{\sqrt{S+B}}{S}. \quad (5.6)$$

Therefore, the expected relative statistical uncertainty can be minimised by maximising the signal purity  $S/\sqrt{S+B}$ .

The event yields for the individual processes after several selection steps are summarised in Table 5.2 which also illustrates the enhanced purity in the signal region. Figure 5.8 shows the event display for data event passing all the selection criteria.

### 5.5.1 Event Preselection

The event selection starts with the event preselection as explained in Section 5.2. The requirement of a good detector status and the jet cleaning procedure are only applied on data. After the vertex requirement, all simulated events are weighted with the pile-up correction factor  $w_{\text{vertex}}$  depending on the number of reconstructed vertices with at least three associated tracks. The correction factor for the trigger efficiency  $w_{\text{trig}}$  is applied after the trigger requirement and depends on the  $p_T$  of the electron candidate which activated the trigger.

### 5.5.2 Selection of the $e\mu$ Final State

Afterwards, cuts motivated by the event topology for the  $e\mu$  final state are applied. Therefore, exactly one selected electron candidate and exactly one selected muon candidate are required with the lepton candidates being defined by the criteria given in Section 5.3. At this point, the simulated events are weighted with the product of the electron and muon reconstruction/identification efficiency corrections  $w_{e,\text{ID}} \times w_{\mu}$ . Both lepton candidates must carry opposite electric charges.

### 5.5.3 Lepton Isolation

As mentioned in Section 4.4, little detector activity in the vicinity of the lepton candidates is expected which can be described by track- and calorimeter-based isolation variables. In contrast, lepton candidates arising from mis-identified jets or decays of heavy quarks are characterised by nearby detector activity and can be suppressed by tightening the isolation requirements. The choice of the most appropriate cone size for the isolation variables is driven by two conflicting issues. A larger cone improves the sensitivity of the isolation variables to background events and provides a better background rejection. In contrast, a smaller cone size diminishes the chance of finding further tracks/energy clusters by accident. Additionally, it reduces effects arising from electronic noise in the calorimeter and pile-up. Another problem for the calorimeter-based isolation is the possible energy leakage of the reconstructed object outside the central cone. The higher the energy of the object, the larger the energy leakage. This problem can be resolved



by using isolation criteria normalised to the transverse momentum of the reconstructed object.

For this study, the following combination of track- and calorimeter-based isolation criteria is found to be optimal:

- An electron candidate is considered isolated if

$$\text{ptcone40}/p_T < 0.06 \quad (5.7)$$

$$\text{and etcone30}/p_T < 0.10. \quad (5.8)$$

- A muon candidate is considered isolated if

$$\text{ptcone40}/p_T < 0.06 \quad (5.9)$$

$$\text{and etcone40}/p_T < 0.06. \quad (5.10)$$

The distributions of all four isolation criteria can be found in Figure 5.2. For the analysis, both selected lepton candidates are required to be isolated. The simulated events are weighted after this step with the lepton isolation corrections  $w_{e,\text{iso}} \times w_{\mu,\text{iso}}$ .

#### 5.5.4 Suppression of $W \rightarrow \ell\nu$ Backgrounds

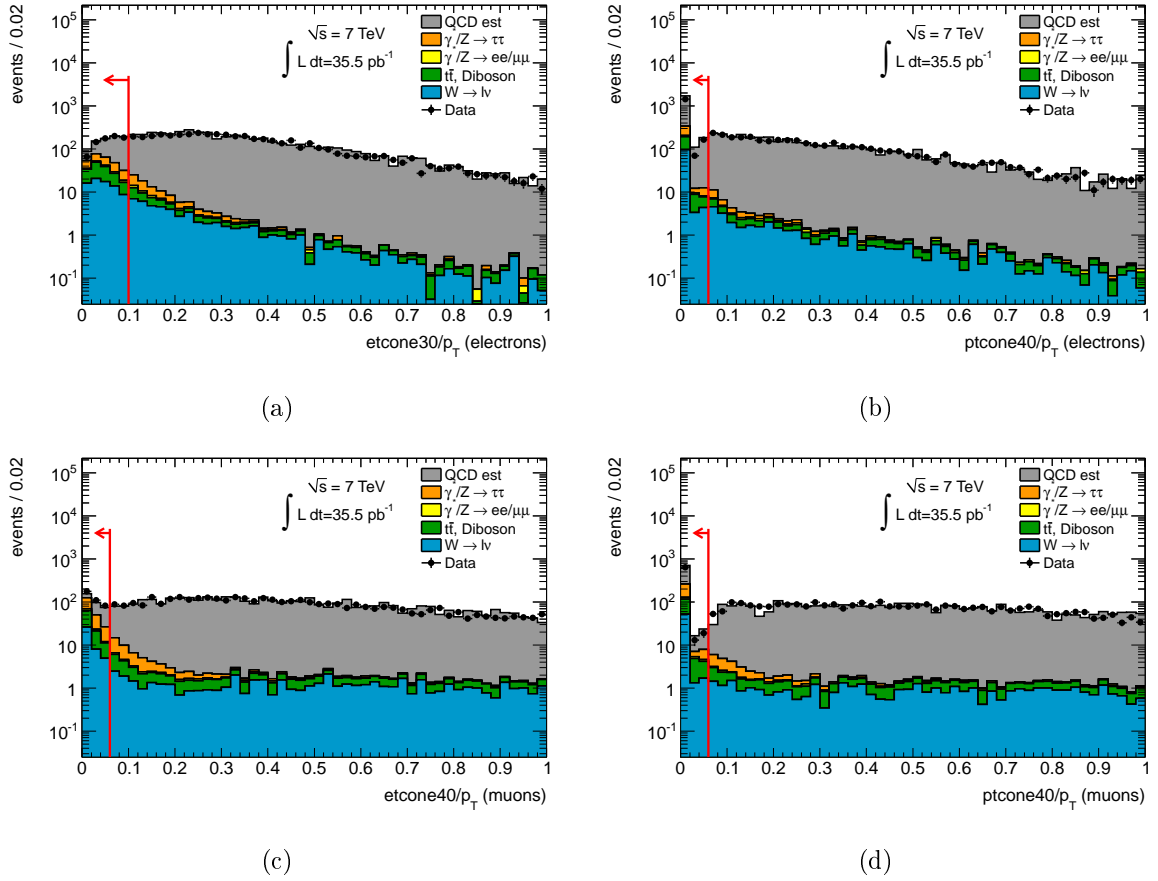
In order to suppress background contributions coming from leptonic  $W$  decays, one uses angular correlations between the reconstructed lepton candidates and the direction of the missing transverse energy. Hereby, it is always assumed that the  $\vec{E}_{T,\text{miss}}$  measurement is dominated by the neutrinos originating from the process under investigation.

Because the  $W$  decay produces only one lepton, the second lepton candidates arises mostly from an additional jet in the event. It follows from the conservation of transverse momentum that the  $\vec{p}_T$  of the lepton candidate originating from the  $W$  decay, the produced neutrino and the fake lepton candidate must balance. Hence, the  $\vec{E}_{T,\text{miss}}$  vector lies outside the opening angle between the two lepton candidates.

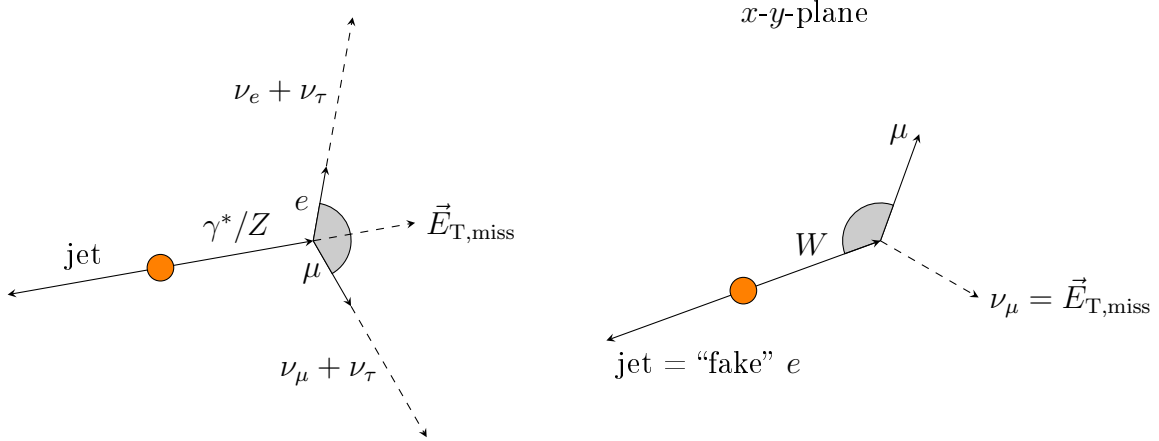
As already discussed in Section 4.6, the tau leptons in the process  $Z \rightarrow \tau^+\tau^- \rightarrow e\mu + 4\nu$  are highly boosted due to the high mass of the  $Z$  boson compared the rest mass of the tau lepton. Therefore, the decay products can be assumed to be collinear to the tau momentum axis. In the case of a very low  $p_T$  of the  $Z$  boson, the two tau leptons are back-to-back in the transverse plane leading to a  $\vec{E}_{T,\text{miss}}$  which is aligned with one of the lepton candidates. If the  $Z$  boson is produced in association with one or more additional jets, it recoils against those. The resulting  $p_T$  of the  $Z$  boson causes the tau leptons to have a smaller opening angle in the  $x$ - $y$ -plane. Then, the  $\vec{E}_{T,\text{miss}}$  vector is no longer aligned with one of the lepton candidates but lies in between. The two different topologies are sketched in Figure 5.3.

The following variable exploits this angular correlation:

$$\sum \cos \Delta\phi = \cos(\phi_e - \phi_{\text{MET}}) + \cos(\phi_\mu - \phi_{\text{MET}}). \quad (5.11)$$



**Figure 5.2:** Distribution of calorimeter-based (left) and track-based (right) isolation variables for electron (top) and muon (bottom) candidates. The individual simulated processes are normalised to the stated integrated luminosity and stacked. The multijet component is estimated from data (cf. Section 5.6.1). The red arrows indicate the applied cuts.



**Figure 5.3:** Event topology for a boosted  $\gamma^*/Z \rightarrow \tau^+\tau^- \rightarrow e\mu + 4\nu$  event (left) and a  $W + \text{jet} \rightarrow \mu\nu_\mu + \text{"fake } e\text{"}$  event (right) in the transverse plane.

This variable is positive if the  $\vec{E}_{T,\text{miss}}$  vector is in between the transverse lepton momenta, and it is negative if the  $\vec{E}_{T,\text{miss}}$  vector is outside the lepton-lepton opening angle. The value  $\sum \cos \Delta\phi = 0$  corresponds to the topology where both lepton candidates are back-to-back in the transverse plane. The distribution of this variable is shown in Figure 5.4(e). In this analysis, the events are required to fulfil

$$\sum \cos \Delta\phi > -0.15. \quad (5.12)$$

### 5.5.5 Suppression of the $t\bar{t}$ Background

Background contributions arising from top-quark pair events can be reduced by employing the different event kinematics (cf. Figure 4.8(a)). Due to the higher top quark mass, the leptons tend to have larger transverse momenta. In addition, the  $\vec{p}_T$  of the neutrinos do not necessarily cancel as it happens for signal events. Therefore,  $t\bar{t}$  events exhibit a significant  $E_{T,\text{miss}}$ . Also, the top quark decays produce at least two  $b$ -quarks which manifest themselves as jets in the detector whereas  $pp \rightarrow \gamma^*/Z \rightarrow \tau^+\tau^- \rightarrow e\mu + 4\nu$  events have no jets at leading order. All this information is condensed in the variable

$$\sum p_T + E_{T,\text{miss}} = p_{T,e} + p_{T,\mu} + \sum_{\text{jets}} p_{T,\text{jet}} + E_{T,\text{miss}} \quad (5.13)$$

which is the scalar sum of the transverse momenta of the two lepton candidates, all reconstructed jets, which have to pass the selection criteria mentioned in 5.3, and the  $E_{T,\text{miss}}$ . Its distribution is shown in Figure 5.4(f). Events are selected if

$$\sum p_T + E_{T,\text{miss}} < 150 \text{ GeV}. \quad (5.14)$$

cut	$\gamma^*/Z \rightarrow \tau^+\tau^-$	$\gamma^*/Z \rightarrow \ell^+\ell^-$	$W \rightarrow \ell\nu$	$t\bar{t}$ , di-boson	QCD	$S/\sqrt{S+B}$
di-lepton cut	$167 \pm 2$	$22 \pm 0.6$	$147 \pm 10$	$138 \pm 0.9$	—	—
lepton isolation	$87 \pm 1$	$5.5 \pm 0.2$	$10 \pm 0.7$	$58 \pm 0.5$	$12.4 \pm 7.3$	6.6
$W$ suppression	$82 \pm 1$	$3.8 \pm 0.2$	$1.9 \pm 0.4$	$24 \pm 0.3$	$9.4 \pm 5.5$	7.5
$t\bar{t}$ suppression	$75 \pm 1$	$3.5 \pm 0.2$	$1.3 \pm 0.3$	$1.3 \pm 0.1$	$8.1 \pm 4.8$	7.9
mass window	$73 \pm 1$	$1.9 \pm 0.1$	$0.6 \pm 0.2$	$0.7 \pm 0.1$	$6.9 \pm 4.1$	8.0

**Table 5.2:** Expected event yields for the different processes. The multijet contribution is estimated from data only after the isolation requirement (cf. Section 5.6.1). Other contributions are scaled to an integrated luminosity of  $L = 35.5 \text{ pb}^{-1}$ . Only statistical uncertainties are given.

### 5.5.6 Definition of the Visible Mass Window

Finally, a mass window is defined using the visible mass definition as given in Equation (4.8). From Figure 5.5 one infers that the remaining background contributions are small and almost uniformly distributed. Motivated by the limited mass resolution, a large mass window of

$$25 \text{ GeV} \leq m_{e\mu} \leq 80 \text{ GeV} \quad (5.15)$$

is defined for the final selection.

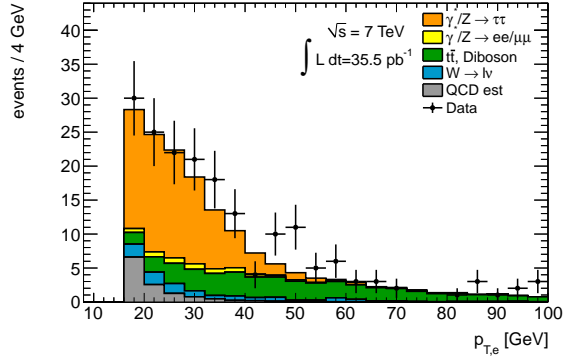
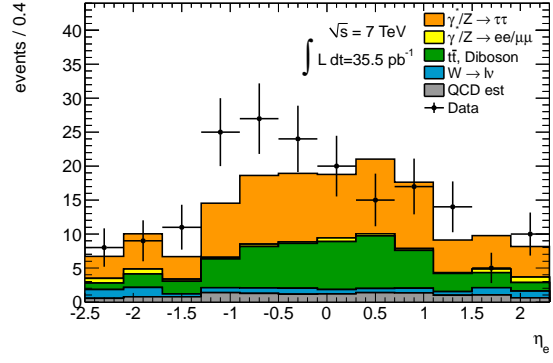
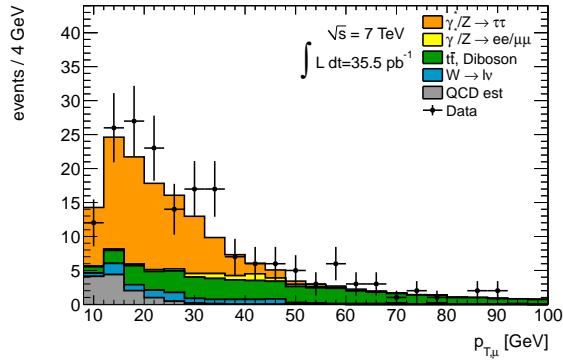
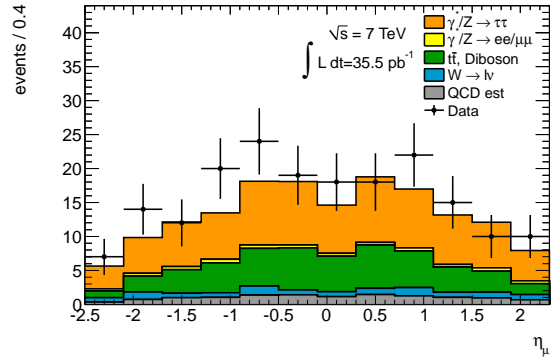
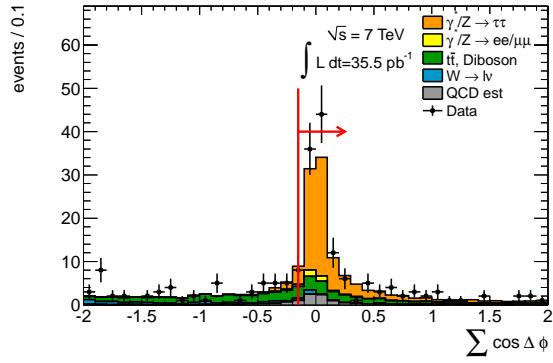
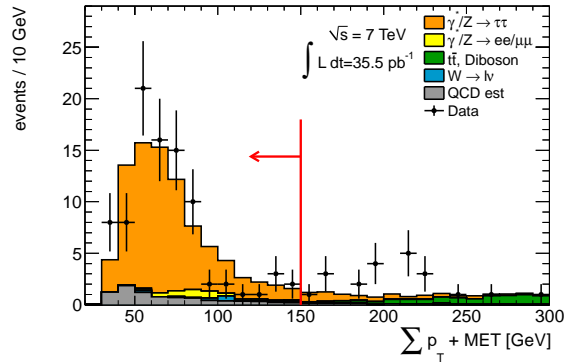
## 5.6 Estimation of Background Contributions

The important background processes for this analysis are already discussed in Section 4.5. In the scope of this work, the shape and normalisation of all background contributions, except that of the multijet background, are determined from simulations. However, the normalisation of the most important background processes are validated in dedicated control regions which is described in the following paragraphs. Also the data-driven multijet estimation is explained in the remainder of this section.

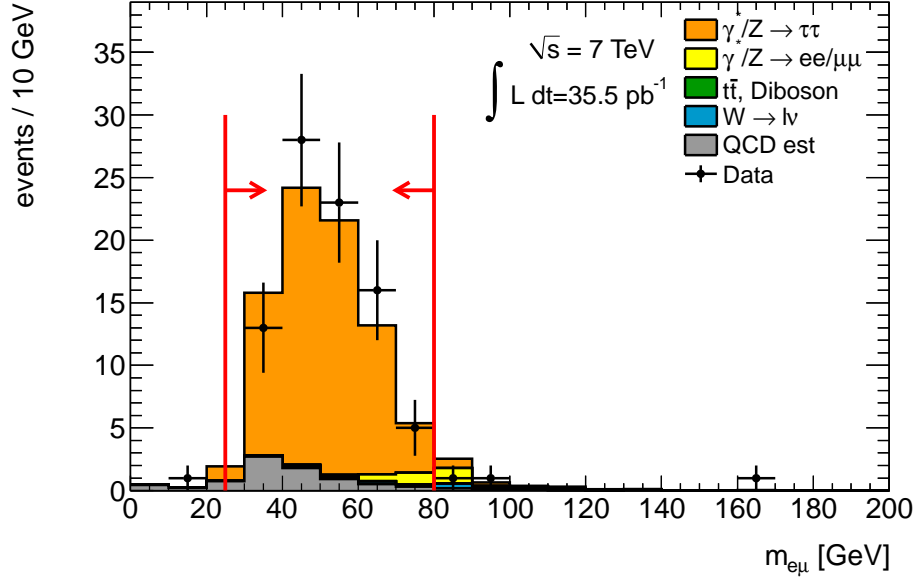
### 5.6.1 Estimation of the Multijet Background

The determination of the multijet background from simulation is unsuited for the following reasons.

1. The large cross sections for the production of jets demand for simulated samples of very high statistics in order to provide a reasonable equivalent luminosity (cf. Equation (3.6)).
2. The good background rejection of the electron and muon identification algorithms results in a very small phase space of the simulated multijet processes which is accepted. Therefore, the modelling of those processes has to be understood in minute detail.


 (a) Electron  $p_T$  distribution after the lepton isolation requirements.

 (b) Electron  $\eta$  distribution after the lepton isolation requirements.

 (c) Muon  $p_T$  distribution after the lepton isolation requirements.

 (d) Muon  $\eta$  distribution after the lepton isolation requirements.

 (e) Distribution of  $\sum \cos \Delta\phi$  after the lepton isolation requirements.

 (f) Distribution of  $\sum p_T + E_{T,\text{miss}}$  after the  $W$  suppression cut.

**Figure 5.4:** Distribution of important kinematic variables at different points in the selection (see captions). The individual simulated processes are normalised to the stated integrated luminosity and stacked. The multijet component is estimated from data (cf. Section 5.6.1). The red arrows indicate the applied cuts.



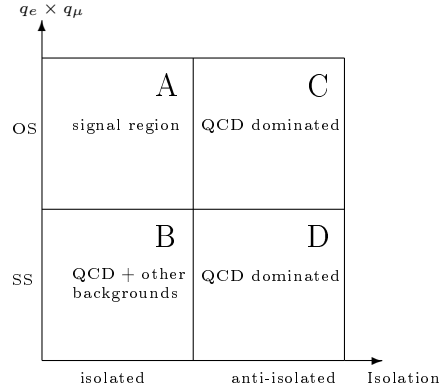
**Figure 5.5:** Visible mass spectrum before applying the final mass window cut. The individual simulated processes are normalised to the stated integrated luminosity and stacked. The multijet component is estimated from data (cf. Section 5.6.1). The red arrows indicate the applied cuts.

3. Theoretical predictions for jet production at hadron colliders are challenging as they rely on the running of the strong coupling constant and on a correct model for the colliding protons by using parton density functions. Furthermore, the hadronisation process and the simulation of additional overlaid events at lower energy scales include non-perturbative effects which are described by empirical and approximate models.

Therefore, it is essential to derive this important background in a data-driven way. For this purpose, the ABCD method is used.

### Explanation of the ABCD Method

Two variables, which are assumed to be uncorrelated and provide a reasonable discrimination power between the signal and multijet processes, are employed to span a two-dimensional phase space. This plane is divided into four disjoint regions by imposing a cut on each variable in a way that the signal process is concentrated in one region. For this analysis the charge product of the two lepton candidates and their isolation are chosen. The plane is split according to the electric charges of the reconstructed lepton candidates in an opposite sign (OS) and a same sign (SS) region. Depending on the isolation of both lepton candidates, the plane is divided in an isolated (both lepton candidates are isolated) and an anti-isolated region (both lepton candidates fail the track- and the calorimeter-based isolation criteria). The resulting two-dimensional plane with its four regions is displayed in Figure 5.6. Region A is the signal region for which the



**Figure 5.6:** Two-dimensional plane for the ABCD method.

contribution coming from multijet events is unknown. The other three control regions are dominated by background processes. Supposing that for the multijet background the charge product of the two reconstructed leptons is uncorrelated with their isolation, one obtains

$$\frac{N_A^{\text{QCD}}}{N_B^{\text{QCD}}} = \frac{N_C^{\text{QCD}}}{N_D^{\text{QCD}}} \quad (5.16)$$

$$\Rightarrow N_A^{\text{QCD}} = N_B^{\text{QCD}} \cdot \frac{N_C^{\text{QCD}}}{N_D^{\text{QCD}}} \quad (5.17)$$

$$= N_B^{\text{QCD}} \cdot R_{\text{OS/SS}} \quad (5.18)$$

where  $N_i^{\text{QCD}}$  is the number of multijet events in region  $i$ . While the regions  $C$  and  $D$  are dominated by multijet events and contributions from other background or signal processes are tiny (cf. the numbers in Table 5.3), region  $B$  contains sizeable contributions from other electroweak processes. Therefore, the number of multijet events in the individual control regions is determined from the number of observed data events in the corresponding regions according to

$$N_C^{\text{QCD}} = N_C^{\text{data}}, \quad (5.19)$$

$$N_D^{\text{QCD}} = N_D^{\text{data}}, \quad (5.20)$$

$$N_B^{\text{QCD}} = N_B^{\text{data}} - N_B^{\text{EW}} \quad (5.21)$$

with  $N_B^{\text{EW}}$  being the expected number of other electroweak background contributions in region  $B$  estimated from simulations. Possible contributions from the signal process are excluded explicitly from the correction since the normalisation of the signal process is to be measured.

Ideally, this procedure is applied after the full selection in order to derive the final number of multijet events in the signal region. However, the limited data statistics, especially in region  $B$  where only three events are observed, reduce the validity of this

estimate. Therefore, the number of multijet events in the signal region A is estimated with the ABCD method after the selection of exactly one electron and one muon candidate. The result is propagated to the end of the selection by applying an efficiency  $\varepsilon_{\text{QCD}}$  for the subsequent selection steps. This selection efficiency for the multijet background is estimated from region  $D$  as

$$\varepsilon_{\text{QCD}} = \frac{N_{D,\text{final}}^{\text{data}}}{N_{D,\text{dilepton}}^{\text{data}}} . \quad (5.22)$$

Hereby, it is assumed that the selection efficiency is neither correlated with the charge product nor with the isolation variables. This assumption is investigated in Section 5.8.5. The final estimation of multijet events in the signal region is given by

$$N_{A,\text{final}}^{\text{QCD}} = (N_{B,\text{dilepton}}^{\text{data}} - N_{B,\text{dilepton}}^{\text{EW}}) \cdot R_{\text{OS/SS}} \cdot \varepsilon_{\text{QCD}} . \quad (5.23)$$

Table 5.3 summarises<sup>2</sup> all numbers which are needed to perform the calculation. The expected number of signal events is shown only for comparison because the normalisation of this process is to be measured. The signal contribution in control region  $B$  is about 10% and is not corrected for but it is considered as a systematic uncertainty on the method. In the other control regions, the expected signal yields are small compared to other background contributions and are within the statistical uncertainty of the observed number of data events. Finally, one obtains

$$R_{\text{OS/SS}} = \frac{N_{C,\text{dilepton}}^{\text{data}}}{N_{D,\text{dilepton}}^{\text{data}}} = 1.55 \pm 0.04 \text{ (stat.)} , \quad (5.24)$$

$$\varepsilon_{\text{QCD}} = \frac{N_{D,\text{final}}^{\text{data}}}{N_{D,\text{dilepton}}^{\text{data}}} = 0.56 \pm 0.02 \text{ (stat.)} , \quad (5.25)$$

$$\Rightarrow N_{A,\text{final}}^{\text{QCD}} = 6.9 \pm 4.1 \text{ (stat.)} . \quad (5.26)$$

Figure 5.4 shows the distribution of important variables. The distribution displayed for the multijet background is derived in the following way. First, the normalisation at this point in the selection is calculated using the ABCD method described with a modified selection efficiency. The nominator in Equation (5.25) has to be adapted according to the selection step at which the distribution is shown. The shape for the distribution is then taken from data in the corresponding same-sign and anti-isolated region which is dominated by multijet events. As these shapes are only needed for illustrative purposes and do neither influence the final result nor the selection strategy, the cross checks performed are documented elsewhere [77].

The basic assumptions of the whole method are considered as sources of systematic uncertainties on the method itself and are investigated in more detail in Section 5.8.5.

### 5.6.2 Normalisation of the Simulation of $W$ Decays

Leptonic decays of  $W$  bosons constitute a major background to this measurement and, thus, their normalisation needs a careful validation. Among the three possible processes

---

<sup>2</sup>The complete cut flows for the individual control regions can be found in Appendix C.5.



region $B$ after the di-lepton requirement	$N_{B,\text{dilepton}}^{\text{signal}} = 1.4 \pm 0.2$
	$N_{B,\text{dilepton}}^{\text{EW}} = 14.0 \pm 0.8$
	$N_{B,\text{dilepton}}^{\text{data}} = 22$
region $C$ after the di-lepton requirement	$N_{C,\text{dilepton}}^{\text{signal}} = 0.6 \pm 0.1$
	$N_{C,\text{dilepton}}^{\text{EW}} = 12.0 \pm 0.7$
	$N_{C,\text{dilepton}}^{\text{data}} = 3771$
region $D$ after the di-lepton requirement	$N_{D,\text{dilepton}}^{\text{signal}} = 0.5 \pm 0.1$
	$N_{D,\text{dilepton}}^{\text{EW}} = 9.0 \pm 0.6$
	$N_{D,\text{dilepton}}^{\text{data}} = 2432$
region $D$ after the full selection	$N_{D,\text{final}}^{\text{signal}} = 0.2 \pm 0.1$
	$N_{D,\text{final}}^{\text{EW}} = 0.2 \pm 0.1$
	$N_{D,\text{final}}^{\text{data}} = 1367$

**Table 5.3:** Summary of numbers needed for the multijet estimation. Only statistical uncertainties are given.

$W \rightarrow \tau\nu_\tau$  plays a minor role due to the small branching ratio for leptonic decays of the tau lepton. As the probability for a jet being interpreted as an electron candidate is much higher than the mis-interpretation rate of jets as muon candidates, it is expected that  $W \rightarrow \mu\nu_\mu$  is a more severe background than  $W \rightarrow e\nu_e$ . That is because both processes need a second lepton candidate which usually originates from additional jets in the event.

The control regions are defined by the data preselection cuts and the presence of exactly one electron and one muon candidate. This time both leptons are required to have the same electric charge in order to reduce the migration of signal events into these control regions. Furthermore, the events have to pass the  $t\bar{t}$  suppression cut  $\sum p_T + E_{T,\text{miss}} < 150$  GeV. For the  $W \rightarrow \mu\nu_\mu$  control region the muon isolation cuts are applied while for the  $W \rightarrow e\nu_e$  control region only the electron candidate needs to be isolated. Finally, the transverse mass defined as

$$m_T = \sqrt{2 \cdot p_{T,\ell} \cdot E_{T,\text{miss}} (1 - \cos(\phi_\ell - \phi_{\text{MET}}))} \quad (5.27)$$

is employed to enrich the contribution of the  $W$  decay processes. Both control regions require a transverse mass in the range of  $60 \text{ GeV} \leq m_T \leq 100 \text{ GeV}$ . For the  $W \rightarrow \mu\nu_\mu$  control region, the transverse mass is calculated from the muon candidate and the  $\vec{E}_{T,\text{miss}}$  while for the  $W \rightarrow e\nu_e$  cross check the electron candidate is used.

In Table 5.4 the expected number of events in both control regions are shown together with the observed number of data events. In both cases, the observed number of data events agrees well with the expectation considering the limited statistics. The control region for the  $W \rightarrow \mu\nu_\mu$  events is dominated by this process and the normalisation of the  $W \rightarrow \mu\nu_\mu$  simulation is considered adequate. In the  $W \rightarrow e\nu_e$  control region, the dominant contribution arises from multijet events because of the larger mis-identification

process	events	process	events
$\gamma^*/Z \rightarrow e^+e^-$	$\leq 0.1$	$\gamma^*/Z \rightarrow e^+e^-$	$0.34 \pm 0.06$
$\gamma^*/Z \rightarrow \mu^+\mu^-$	$0.59 \pm 0.06$	$\gamma^*/Z \rightarrow \mu^+\mu^-$	$0.10 \pm 0.02$
$\gamma^*/Z \rightarrow \tau^+\tau^-$	$0.11 \pm 0.05$	$\gamma^*/Z \rightarrow \tau^+\tau^-$	$0.18 \pm 0.06$
$W \rightarrow e\nu_e$	$\leq 0.1$	$W \rightarrow e\nu_e$	$5.24 \pm 0.62$
$W \rightarrow \mu\nu_\mu$	$10.69 \pm 0.78$	$W \rightarrow \mu\nu_\mu$	$2.81 \pm 0.39$
$W \rightarrow \tau\nu_\tau$	$0.62 \pm 0.35$	$W \rightarrow \tau\nu_\tau$	$0.40 \pm 0.32$
$t\bar{t}$	$\leq 0.1$	$t\bar{t}$	$0.12 \pm 0.03$
QCD estimation	$5.17 \pm 1.04$	multijet estimation	$17.32 \pm 1.45$
$\sum$ expectations	$17.18 \pm 1.35$	$\sum$ expectations	$26.51 \pm 1.66$
data	18	data	29

(a)  $W \rightarrow \mu\nu_\mu$  control region.

(b)  $W \rightarrow e\nu_e$  control region.

**Table 5.4:** Expected and observed number of events in the control regions for  $W$  decays. The background components are normalised to an integrated luminosity of  $L = 35.5 \text{ pb}^{-1}$  except for the multijet background which is estimated from data. Only statistical uncertainties are given.

rate of jets as electron candidates. However, the normalisation of the  $W \rightarrow e\nu_e$  simulation is regarded as acceptable for this analysis.

### 5.6.3 Normalisation of the Simulation of $t\bar{t}$ Processes

Another important background is the production of  $t\bar{t}$  pairs which constitute a physical background to the signal process. Additionally, the theoretical cross section for this process is less precise, compared to that of  $Z$  and  $W$  boson production, and a cross check of the normalisation is essential. A control region is defined by requiring a successful data preselection and exactly one electron candidate and one muon candidate with opposite charge which passes the corresponding isolation criteria. Contributions of the signal process are reduced by inverting the cuts on  $\sum \cos \Delta\phi$  and  $\sum p_T + E_{T,\text{miss}}$ . The resulting numbers of expected and observed events are given in Table 5.5. It is concluded from the good agreement that the normalisation for the simulation of  $t\bar{t}$  events is correct.

## 5.7 Methodology of the Cross Section Measurement

In order to calculate a cross section of a certain signal process, the number of signal events  $N_{\text{signal}}$  and the integrated luminosity  $L$  is needed. While the latter is measured directly, the number of signal events is estimated from the observed number of data events  $N_{\text{data}}$  in the signal region and the estimated background contribution  $N_{\text{bkg}}$ . The

process	events
$\gamma^*/Z \rightarrow e^+e^-$	$\leq 0.1$
$\gamma^*/Z \rightarrow \mu^+\mu^-$	$0.19 \pm 0.04$
$\gamma^*/Z \rightarrow \tau^+\tau^-$	$0.31 \pm 0.07$
$W \rightarrow e\nu_e$	$\leq 0.1$
$W \rightarrow \mu\nu_\mu$	$1.29 \pm 0.26$
$W \rightarrow \tau\nu_\tau$	$0.33 \pm 0.25$
$t\bar{t}$	$26.96 \pm 0.38$
QCD estimation	$2.30 \pm 2.75$
$\sum$ expectations	$31.38 \pm 2.80$
data	31

**Table 5.5:** Expected and observed number of events in the control region for the  $t\bar{t}$  process. The background components are normalised to an integrated luminosity of  $L = 35.5 \text{ pb}^{-1}$  except for the multijet background which is estimated from data. Only statistical uncertainties are given.

cross section of the process can then be calculated according to

$$\sigma = \frac{N_{\text{signal}}}{L} = \frac{N_{\text{data}} - N_{\text{bkg}}}{L}. \quad (5.28)$$

However, this number is difficult to compare among different experiments as it includes the definition of the chosen signal region. By applying cuts to define the signal region, only events in a very specific part of the available phase space are selected. Therefore, the cross section calculated above is the differential cross section of the process of interest integrated over the selected, and usually highly complicated, phase space regions. For the sake of comparability, the measured cross section is corrected for effects coming from a restricted phase space. Let  $\sigma_{\text{incl}}$  denote the fully inclusive cross section for the process considered, then the correction factor  $\epsilon$  can be split into two parts,

$$\sigma = \sigma_{\text{incl}} \cdot \epsilon = \sigma_{\text{incl}} \cdot A_Z \cdot C_Z. \quad (5.29)$$

The correction factor  $A_Z$  describes the probability that the process generates a final state which is within a certain geometrical and kinematic region, the *fiducial* phase space region. Given that a signal event is within the fiducial region,  $C_Z$  represents the efficiency that this event is correctly reconstructed and selected in the signal region. Both numbers can be calculated from a simulated signal sample which contains  $N_{\text{gen}}$  events of which  $N_{\text{acc}}$  are within the fiducial phase space and  $N_{\text{sel}}$  are finally reconstructed and selected in the signal region. One obtains the following relations

$$\epsilon = \frac{N_{\text{sel}}}{N_{\text{gen}}} = \underbrace{\frac{N_{\text{acc}}}{N_{\text{gen}}}}_{A_Z} \underbrace{\frac{N_{\text{sel}}}{N_{\text{acc}}}}_{C_Z}. \quad (5.30)$$

cuts	
electrons	$p_T \geq 16 \text{ GeV}$ $ \eta  \leq 2.47$ but outside $1.37 \leq  \eta  \leq 1.52$
muons	$p_T \geq 10 \text{ GeV}$ $ \eta  \leq 2.4$
event	$\sum \cos \Delta\phi(\ell, \text{MET}) > -0.15$ $25 \text{ GeV} < m_{e\mu} < 80 \text{ GeV}$

**Table 5.6:** Definition of the fiducial phase space region.

It is important here to notice that  $N_{\text{gen}}$  and  $N_{\text{acc}}$  rely only on the simulated process and are fixed already after the event generation step (cf. Section 3.3). In contrast,  $N_{\text{sel}}$  is based on final reconstructed objects and is affected by the detector simulation and reconstructions/identification algorithms.

One can then state the fully inclusive cross section

$$\sigma_{\text{incl}} = \frac{\sigma}{A_Z \cdot C_Z} \quad (5.31)$$

and the fiducial cross section

$$\sigma_{\text{fid}} = \frac{\sigma}{C_Z}. \quad (5.32)$$

Let  $\sigma^{\gamma^*/Z}$  denote the production cross section of  $pp \rightarrow \gamma^*/Z$  with the invariant mass of the gauge boson within  $66 \text{ GeV} \leq m_{\gamma^*/Z} \leq 116 \text{ GeV}$ . Taking into account the branching ratios of the  $\gamma^*/Z$  boson and the tau lepton decays, one obtains

$$\sigma_{\text{fid}}^{\gamma^*/Z} \times \mathcal{BR}(\gamma^*/Z \rightarrow \tau^+\tau^-) \times \mathcal{BR}(\tau^+\tau^- \rightarrow e\mu + 4\nu) = \frac{N_{\text{data}} - N_{\text{bkg}}}{C_Z \cdot L}, \quad (5.33)$$

$$\sigma_{\text{incl}}^{\gamma^*/Z} \times \mathcal{BR}(\gamma^*/Z \rightarrow \tau^+\tau^-) \times \mathcal{BR}(\tau^+\tau^- \rightarrow e\mu + 4\nu) = \frac{N_{\text{data}} - N_{\text{bkg}}}{A_Z \cdot C_Z \cdot L}. \quad (5.34)$$

Since the fiducial cross section does not require an extrapolation of the measured cross section to the full phase space, it is less affected by theoretical uncertainties on the modelling of the gauge boson production and the subsequent decays.

### 5.7.1 Determination of the Acceptance and Correction Factors

The fiducial phase space in this analysis is defined by the cuts given in Table 5.6. The constraint to  $66 \text{ GeV} \leq m_{\gamma^*/Z} \leq 116 \text{ GeV}$  has to be taken into account when the correction factors  $A_Z$  and  $C_Z$  are calculated using simulated signal events. The invariant mass of the gauge boson is given by the invariant mass of the di-tau system  $m_{\tau\tau}$ . Thereby, the four-momenta of the tau leptons are given by the summed four-momenta of their decay products (one charged lepton and two neutrinos). Additionally, momenta of photons are added if these are radiated either off the tau lepton itself or off the charged lepton within

in a cone of  $\Delta R = 0.1$ . This procedure allows for partial correction of the QED final state radiation back to the tree-level process.

The correction factor  $A_Z$  is finally given by

$$A_Z = \frac{N_{\text{acc}}}{N_{\text{gen, mass window}}} = 0.1139 \pm 0.0004 \quad (5.35)$$

where both numbers are determined before any detector simulation is applied but include a correction for possible radiation of photons. Then,  $N_{\text{gen, mass window}}$  is the number of generated events which fall inside the mass window  $m_{\tau\tau} \in [66 \text{ GeV}, 116 \text{ GeV}]$  and  $N_{\text{acc}}$  is the number of events fulfilling the criteria given in Table 5.6. By construction,  $N_{\text{acc}}$  is not a strict sub-sample of  $N_{\text{gen, mass window}}$  and, hence,  $A_Z$  includes a correction for events that migrate from outside the invariant mass window into the fiducial phase space region.

The corrections factor  $C_Z$ , accounting for detector and analysis efficiencies like the reconstruction, identification and trigger efficiencies but also event selection efficiencies, is calculated according to

$$C_Z = \frac{N_{\text{sel}}^{\text{reco}}}{N_{\text{acc}}} = 0.286 \pm 0.006 \quad (5.36)$$

with  $N_{\text{sel}}^{\text{reco}}$  being the number of events passing all analysis cuts, including the corrections described in Section 5.4, after the full detector simulation is applied. Again,  $C_Z$  includes by construction a correction for events migrating from outside the fiducial phase space into the final signal region.

Both numbers are determined using a signal sample simulated with the PYTHIA generator and the PDF set and underlying event model as given in Section 3.3.1. The uncertainties stated are the statistical uncertainties arising from the limited number of simulated events.

## 5.8 Evaluation of Systematic Uncertainties

The estimation of background contributions is subject to systematic uncertainties as well as the acceptance correction factors  $A_Z$  and  $C_Z$ . In this section, different sources of systematic uncertainties are investigated and their effects are quantified. The effects of all systematic variations considered are summarised in Tables 5.9, 5.10 and 5.11.

### 5.8.1 Theoretical Uncertainties

Theoretical uncertainties on the normalisation of  $\gamma^*/Z \rightarrow \ell^+\ell^-$  and  $W \rightarrow \ell\nu_\ell$  simulations were studied in the context of the  $Z$  and  $W$  boson cross section measurements by the ATLAS collaboration [78]. The programme FEWZ [55] is used to calculate the cross sections at NNLO accuracy in electroweak and strong corrections. Systematic uncertainties are evaluated by varying the renormalisation and factorisation scales and by considering uncertainties on the strong coupling constant as well as on the PDF sets used. An overall uncertainty of 5% for the normalisation of  $\gamma^*/Z \rightarrow \ell^+\ell^-$  and  $W \rightarrow \ell\nu_\ell$  simulations is

found. Regarding the top-pair production, an uncertainty on the normalisation of  $^{+7\%}_{-9.5\%}$  is used following the strategy of the top-pair production cross section measurement by ATLAS [79].

### 5.8.2 Uncertainty on the Luminosity Measurement

The relative uncertainty on the luminosity is derived from measurements with dedicated beam conditions and is found to be 3.4% [74].

### 5.8.3 Uncertainties Related to the Corrections Applied

#### Correction Factors

All correction factors are obtained from simulation and data samples with limited statistics. In some cases, additional systematic variations are considered when deriving those correction factors. The resulting total uncertainties are given in Table 5.1, C.4, C.5 and C.6.

In general, the correction factors and their uncertainty are given in bins of some quantity (e.g.  $p_T$ ,  $\eta$  or  $n_{\text{vertex}}$ ). The impact of these uncertainties on the cross section measurement is estimated by shifting the correction factors in all bins coherently by  $\pm 1\sigma$  and evaluating the relative change in the background estimation and  $C_Z$ . This procedure leads to a conservative estimate of the systematic uncertainties as the correction factors in different bins are treated fully correlated. Indeed, a large portion of the total uncertainties on the correction factors arises from limited statistics and, therefore, is uncorrelated between different bins. A future analysis might disentangle the different contributions of the total uncertainty to perform a refined estimation of the systematic uncertainties.

This prescription is applied separately for the trigger efficiency and pile-up corrections as well as for the isolation scale factors and the muon reconstruction efficiency correction. For the electron related corrections an additional relative uncertainty of 1.5% coming from the reconstruction efficiencies (cf. Section 5.4.2) is added in quadrature.

#### Lepton Energy/Momentum Corrections

As described in Section 5.4.2, the transverse momenta/energies of reconstructed lepton candidates undergo an additional correction. The tools used for the smearing allow to shift the correction by its uncertainty. The arising systematic uncertainty is quantified by comparing the results for the background estimation and  $C_Z$  obtained with the shifted corrections to those obtained with the nominal correction.

### 5.8.4 Jet Energy Scale and $E_{T,\text{miss}}$ Uncertainty

The calibration of jet energies is subject to rather large uncertainties, especially in the low  $p_T$  regime [80]. To evaluate the consequences for this analysis, the jet energies are altered using a dedicated tool.

The missing transverse energy is calculated from reconstructed topological energy clusters and reconstructed muon candidates. Since the shift in the muon  $p_T$  due to the correction is propagated back to the  $\vec{E}_{T,\text{miss}}$  vector, the uncertainty on  $\vec{E}_{T,\text{miss}}$  coming from reconstructed muons is already accounted for. The energy of the topological clusters is modified according to a  $p_T$  dependent scaling factor [81]

$$1.03 \pm \frac{1.2 \text{ GeV}}{p_T} \quad \text{for } |\eta| < 3.2, \quad (5.37)$$

$$1.10 \pm \frac{1.2 \text{ GeV}}{p_T} \quad \text{for } |\eta| \geq 3.2. \quad (5.38)$$

Because the jet energy scale, the electron energy and the  $\vec{E}_{T,\text{miss}}$  measurement depend on calorimeter information, the corresponding systematic variations are shifted coherently.

The whole analysis is re-run to determine the relative changes in the background estimation and the calculation of  $C_Z$ .

### 5.8.5 Uncertainty on the Estimate of the Multijet Background

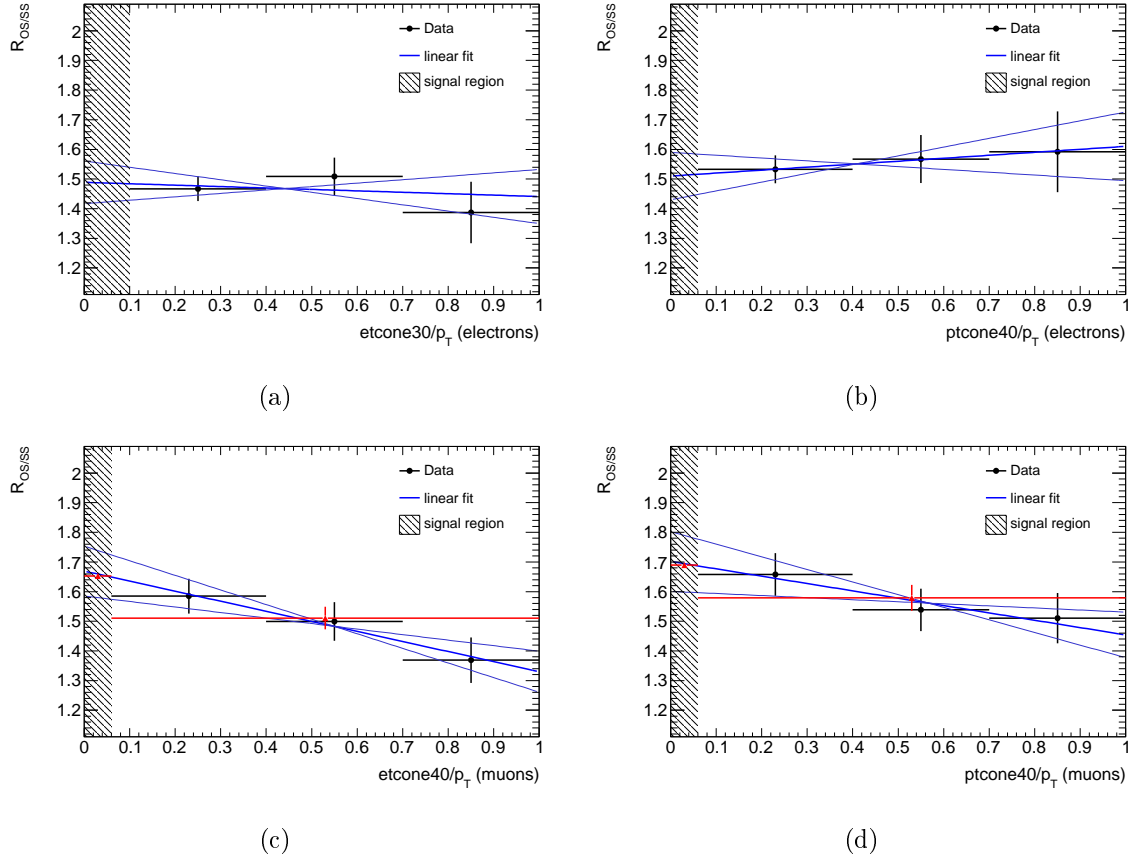
The ABCD method relies on the following vital assumptions for the multijet background estimation:

1. The ratio  $R_{\text{OS/SS}}$  is independent of the isolation of the two reconstructed lepton candidates.
2. The ratio  $R_{\text{OS/SS}}$  is not affected by selection steps after the di-lepton requirement.
3. The selection efficiency  $\varepsilon_{\text{QCD}}$  is independent of the charge product and the isolation of both lepton candidates.

#### Cross Checks for $R_{\text{OS/SS}}$

In order to evaluate the dependence of  $R_{\text{OS/SS}}$  on the isolation criteria of the two lepton candidates, the following check is performed. After the di-lepton selection criteria  $R_{\text{OS/SS}}$  is calculated analogously to (5.24) as a function of the four variables which are used to define the isolation of the electron and muon candidates. The resulting distributions are shown in Figure 5.7. The first bin is always chosen such that it covers the range used to define an isolated electron or muon candidate while the last three bins represent the anti-isolated region. Therefore, the first bin is dominated by electroweak and signal contributions and the calculation of  $R_{\text{OS/SS}}$  for multijet events would require a correction for all electroweak processes including the signal process. That is not possible as the normalisation of the latter should be measured in this analysis and, thus, the ratio  $R_{\text{OS/SS}}$  is not calculated for the first bin.

The assumption, that  $R_{\text{OS/SS}}$  is independent of the isolation, is checked by fitting the last three bins with a linear function. If the slope of this function is not compatible with 0 within the errors of the fit, a systematic uncertainty is derived in the following way:



**Figure 5.7:** Dependence of  $R_{OS/SS}$  on the calorimeter-based (left) and track-based (right) isolation variables for electron (top) and muon (bottom) candidates. The linear fit with its uncertainty on the slope parameter is displayed as blue lines. The red triangles represent the values used for determining the relative systematic uncertainty.



isolation variable	slope parameter	$R_{\text{OS/SS}}^{\text{ex}}$	$R'_{\text{OS/SS}}$	$\Delta_{\text{syst.}} R_{\text{OS/SS}}$
etcone30/ $p_{\text{T}}$ (electrons)	$-0.05 \pm 0.16$	—	—	—
ptcone40/ $p_{\text{T}}$ (electrons)	$0.10 \pm 0.20$	—	—	—
etcone40/ $p_{\text{T}}$ (muons)	$-0.34 \pm 0.15$	1.652	1.511	9.4%
ptcone40/ $p_{\text{T}}$ (muons)	$-0.25 \pm 0.18$	1.689	1.579	7.0%

**Table 5.7:** Parameters for the estimation of the systematic uncertainty on  $R_{\text{OS/SS}}$ .

1. The linear function is extrapolated to the centre of the first bin yielding an hypothetical value  $R_{\text{OS/SS}}^{\text{ex}}$ .
2. The last three bins are merged into one anti-isolated bin.
3. The ratio of opposite sign to same sign events in data is recalculated in the anti-isolated bin resulting in a value  $R'_{\text{OS/SS}}$ .
4. A relative systematic uncertainty of

$$\frac{R_{\text{OS/SS}}^{\text{ex}} - R'_{\text{OS/SS}}}{R'_{\text{OS/SS}}} \quad (5.39)$$

is stated.

The procedure leads to the relative systematic uncertainties given in Table 5.7. No significant dependence on the isolation of the electron candidate is observed. The relative uncertainties related to the isolation of the reconstructed muon candidates are assumed to be fully correlated. Therefore, the average deviation of 8.2% is quoted as systematic uncertainty on  $R_{\text{OS/SS}}$ .

One might notice that this prescription is a simplification since the actual definition of “being isolated” is two-dimensional. Therefore, one should include the exact correlation between calorimeter-based and track-based isolation variables. Additionally, if a non-negligible dependence of  $R_{\text{OS/SS}}$  on the isolation variables is observed, one should correct for this and quote the uncertainty on the correction as systematic uncertainty rather than taking the total observed discrepancy as systematic uncertainty as it is done in this analysis. However, as the uncertainty on the multijet estimate is dominated by the limited data statistics, it is decided to pursue the conservative and simplified approach described above. Nevertheless, further analyses may benefit from larger statistics and consider a more thorough treatment of this systematic uncertainty.

The second assumption is checked by calculating the ratio  $R_{\text{OS/SS}}$  from the anti-isolated region after different selection steps analogously to Equation (5.24). The values obtained are stated in Table 5.8 and are constant throughout the full selection. Hence, assumption 2) is justified.

selection step	$N_{\text{OS}}^{\text{data}}$	$N_{\text{SS}}^{\text{data}}$	$R_{\text{OS/SS}}$
di-lepton requirement	3771	2432	$1.55 \pm 0.04$
$\sum \cos \Delta\phi > -0.15$	2841	1835	$1.55 \pm 0.05$
$\sum p_{\text{T}} + E_{\text{T,miss}} < 150 \text{ GeV}$	2475	1583	$1.56 \pm 0.05$
$25 \text{ GeV} \leq m_{e\mu} \leq 80 \text{ GeV}$	2101	1367	$1.54 \pm 0.05$

**Table 5.8:** Ratio between events with oppositely charged (OS) and equally charged (SS) lepton candidates in the anti-isolated region with its statistical uncertainty at different points in the selection.

### Cross Checks for $\varepsilon_{\text{QCD}}$

For the selection efficiency  $\varepsilon_{\text{QCD}}$  a similar study is performed. After the di-lepton requirement the selection efficiency for multijet events is calculated in the same-sign region as function of the four isolation variables according to Equation (5.22). Again, the first bin contains sizeable electroweak contributions and, therefore, is not shown. The systematic uncertainty on the selection efficiency is derived in the same way as for the ratio  $R_{\text{OS/SS}}$  and the results can be found in Appendix C.6 (Figure C.1). It is found that the selection efficiency of multijet events does not depend on the isolation variables of both lepton candidates.

In order to check that  $\varepsilon_{\text{QCD}}$  does not depend on the charge product of both lepton candidates, the selection efficiency is also calculated from the anti-isolated opposite-sign region (region *C*). The result is

$$\varepsilon_{\text{QCD}}^C = \frac{N_{C,\text{final}}^{\text{data}}}{N_{C,\text{dilepton}}^{\text{data}}} = \frac{2101}{3771} = 0.56 \pm 0.02 \text{ (stat.)} \quad (5.40)$$

and is in perfect agreement with the result obtained from region *D* (cf. Equation (5.25)).

### Summary

While no significant systematic uncertainty on the selection efficiency  $\varepsilon_{\text{QCD}}$  is observed, the relative systematic uncertainty on the ratio of opposite-sign to same-sign multijet events is found to be 8.2%. According to Equation (5.23), the estimate of the number of multijet events in the signal region involves a correction for electroweak processes in the same-sign isolated region. This contribution is derived from simulated samples and are subject to the systematic uncertainties given in Table 5.11. In addition, a relative uncertainty of 10% is added in quadrature to account for the non-negligible amount of signal events in control region *B*, which is not corrected for, leading to a relative systematic uncertainty on the electroweak correction of 17.4%. The resulting systematic uncertainty on the multijet background estimate is

$$\sqrt{\left(\frac{\Delta_{\text{syst.}} R_{\text{OS/SS}}}{R_{\text{OS/SS}}}\right)^2 + \left(\frac{\Delta_{\text{syst.}} N_{B,\text{dilepton}}^{\text{EW}}}{N_{B,\text{dilepton}}^{\text{data}} - N_{B,\text{dilepton}}^{\text{EW}}}\right)^2} = 31.5\%. \quad (5.41)$$

### 5.8.6 Uncertainties Related to the Detector Status

#### Effect on Electron Candidates in Problematic Calorimeter Regions

As explained in Section 5.3, reconstructed electron candidates are rejected if they are within a calorimeter region which is flagged as problematic. Since the detector conditions evolve over time, there are several maps of problematic regions for different data taking periods. While for the data selection always the correct quality map is used, the selection on the simulated samples is based on the quality map corresponding to the last data taking period which has the largest integrated luminosity. Due to the slight degradation of the detector performance over time, quality maps for earlier periods contain fewer problematic regions. To estimate the loss in selection efficiency on the simulated samples due to the usage of the quality map with the most detector defects, the analysis is re-run with the earliest quality map containing the least problematic regions. The difference in the background estimate and the calculation of  $C_Z$  is of the order of 0.4%.

#### Effect of Jet Cleaning Procedure

The jet cleaning procedure is only applied on data events and has a selection efficiency of 99.6%. It could be considered as additional “good event requirement” which reduces the effective integrated luminosity of the data sample by 0.4%. Instead of doing so, an additional systematic uncertainty of 0.4% is assigned to the simulated samples. Efforts are on-going to emulate the jet cleaning procedure also on simulated samples which would allow a more thorough treatment of this uncertainty.

### 5.8.7 Uncertainties on the Acceptance Factor

The model dependence of the geometric and kinematic acceptance factor  $A_Z$  is determined by comparing different parametrisation for the parton density functions and the parton shower model.

The PDF sets CTEQ6.6 and HERA-PDF1.0 [82] are compared to standard PDF set of the PYTHIA generator which is MRST2007LO\*. Uncertainties of the PDF sets are evaluated as well.

The default PYTHIA parton shower model is compared with the one of the HERWIG generator to infer a possible model dependence. The results are summarised in Table 5.9.

### 5.8.8 Summary of Systematic Uncertainties

The systematic uncertainties on the acceptance factor  $A_Z$  are given in Table 5.9. The effect of individual systematic variations on the correction factor  $C_Z$  are stated in Table 5.10 while Table 5.11 shows the impact of the different systematic uncertainties on the individual background processes. The individual systematic uncertainties are added in quadrature to obtain the total systematic uncertainty.

source	$\delta A_Z/A_Z$ in %
uncertainty on CTEQ6.6 PDF	1.3
different PDF sets	1.8
different parton shower models	1.8
total uncertainty	2.9

**Table 5.9:** Relative systematic uncertainties on the acceptance factor  $A_Z$ .

source	$\delta C_Z/C_Z$ in %
trigger efficiency	2.3
pile-up correction	0.6
electron related efficiencies	5.6
muon related efficiencies	2.6
electron energy resolution	0.1
muon momentum resolution	0.1
jet energy scale and MET systematic	1.7
problematic calorimeter regions	0.4
total uncertainty	6.8

**Table 5.10:** Relative systematic uncertainties on the correction factor  $C_Z$ .

The systematic uncertainty on  $C_Z$  is dominated by the uncertainties related to lepton and trigger efficiency corrections. Also the uncertainty on the jet energy scale contributes significantly.

The systematic uncertainty on the final background estimate is dominated by the large uncertainty on the multijet estimation assigned to the method itself. Other important contributions come from the electron related efficiency corrections and from the jet energy scale uncertainty.

## 5.9 Summary

### 5.9.1 Results

The numbers needed for the final calculation of the cross section measurement are summarised in Table 5.12. One corrects for the branching ratio  $\mathcal{BR}(\tau^+\tau^- \rightarrow e\mu + 4\nu)$  in order to be able to compare with  $pp \rightarrow \gamma^*/Z \rightarrow e^+e^-/\mu^+\mu^-$  cross section measurements. According to Table 4.1 one obtains

$$\mathcal{BR}(\tau^+\tau^- \rightarrow e\mu + 4\nu) = 2 \cdot \mathcal{BR}(\tau \rightarrow e + 2\nu) \cdot \mathcal{BR}(\tau \rightarrow e + 2\nu) \quad (5.42)$$

$$= 0.062. \quad (5.43)$$

source	Relative uncertainty in %			QCD
	$\gamma^*/Z \rightarrow \ell^+\ell^-$	$W \rightarrow \ell\nu_\ell$	$t\bar{t}$ , di-boson	
theory uncertainty	5.0	5.0	10.0	–
luminosity	3.4	3.4	3.4	–
trigger efficiency	0.7	0.8	0.4	1.1
pile-up correction	0.6	0.6	0.6	0.6
electron related efficiencies	5.4	6.4	5.9	4.7
muon related efficiencies	1.2	1.8	1.7	4.9
electron energy resolution	0.1	$\leq 0.1$	0.3	0.1
muon momentum resolution	0.1	$\leq 0.1$	0.4	0.1
jet energy scale, MET systematic	7.5	11.9	9.3	2.6
problematic calorimeter regions	0.4	0.4	0.4	0.3
jet cleaning	0.4	0.4	0.4	0.4
QCD estimation	–	–	–	31.5
total uncertainty	11.2	15.0	15.4	32.4

**Table 5.11:** Relative systematic uncertainties on the background estimates.

Finally, one calculates the cross section of the process  $pp \rightarrow \gamma^*/Z \rightarrow \tau^+\tau^-$  at  $\sqrt{s} = 7$  TeV with  $66 \text{ GeV} \leq m_{\tau\tau} \leq 116 \text{ GeV}$  by using Equations (5.33) and (5.34) to

$$\sigma_{\text{fid}}^{\gamma^*/Z} \times \mathcal{BR}(\gamma^*/Z \rightarrow \tau^+\tau^-) = 119 \pm 15(\text{stat.}) \pm 7(\text{bkg.}) \pm 4(\text{lumi.}) \pm 8(\delta C_Z) \text{ pb} \quad (5.44)$$

$$= 119 \pm 15(\text{stat.}) \pm 11(\text{syst.}) \pm 4(\text{lumi.}) \text{ pb}, \quad (5.45)$$

$$\sigma_{\text{incl}}^{\gamma^*/Z} \times \mathcal{BR}(\gamma^*/Z \rightarrow \tau^+\tau^-) = 1045 \pm 129(\text{stat.}) \pm 66(\text{bkg.}) \pm 36(\text{lumi.}) \pm 73(\delta C_Z) \pm 31(\delta A_Z) \text{ pb} \quad (5.46)$$

$$= 1045 \pm 129(\text{stat.}) \pm 103(\text{syst.}) \pm 36(\text{lumi.}) \text{ pb}. \quad (5.47)$$

The statistical uncertainties quoted arise from the number of observed data events in signal region only while the systematic uncertainties stated comprise the systematic variations studied as well as effects of limited statistics for the background estimation.

## 5.9.2 Discussion and Outlook

The measured cross section is in agreement with the theoretical prediction of

$$\sigma_{\text{Theory}}(pp \rightarrow \gamma^*/Z \rightarrow \tau^+\tau^-) = 964 \pm 48 \text{ pb} \quad (5.48)$$

and the measurement of the  $\gamma^*/Z$  boson production cross section in other decay channels by the ATLAS experiment [83],

$$\sigma_{\text{incl}}^{\gamma^*/Z} \times \mathcal{BR}(\gamma^*/Z \rightarrow e^+e^-) = 750 \pm 90(\text{stat.}) \pm 80(\text{syst.}) \pm 80(\text{lumi.}) \text{ pb}, \quad (5.49)$$

$$\sigma_{\text{incl}}^{\gamma^*/Z} \times \mathcal{BR}(\gamma^*/Z \rightarrow \mu^+\mu^-) = 870 \pm 80(\text{stat.}) \pm 60(\text{syst.}) \pm 100(\text{lumi.}) \text{ pb}. \quad (5.50)$$

background contributions	multijets	$6.9 \pm 4.1 \text{ (stat.)} + 2.2 \text{ (syst.)}$
	$\gamma^*/Z \rightarrow \mu^+\mu^-$	$1.9 \pm 0.1 \text{ (stat.)} \pm 0.2 \text{ (syst.)}$
	$W \rightarrow \mu\nu_\mu$	$0.6 \pm 0.2 \text{ (stat.)} \pm 0.1 \text{ (syst.)}$
	di-boson	$0.5 \pm 0.1 \text{ (stat.)} \pm 0.1 \text{ (syst.)}$
	$t\bar{t}$	$0.2 \pm 0.1 \text{ (stat.)} \pm 0.1 \text{ (syst.)}$
	other	$\leq 0.1$
total background estimation	$N_{\text{bkg}}$	$10.1 \pm 4.1 \text{ (stat.)} \pm 2.3 \text{ (syst.)}$
expected signal events	$N_{\text{signal}}$	$72.9 \pm 1.1 \text{ (stat.)}$
observed data events	$N_{\text{data}}$	85
acceptance corrections	$A_Z$	$0.1139 \pm 0.0004 \text{ (stat.)} \pm 0.0033 \text{ (syst.)}$
	$C_Z$	$0.286 \pm 0.006 \text{ (stat.)} \pm 0.019 \text{ (syst.)}$
integrated luminosity	$L$	$35.5 \pm 1.2 \text{ (syst.) pb}^{-1}$

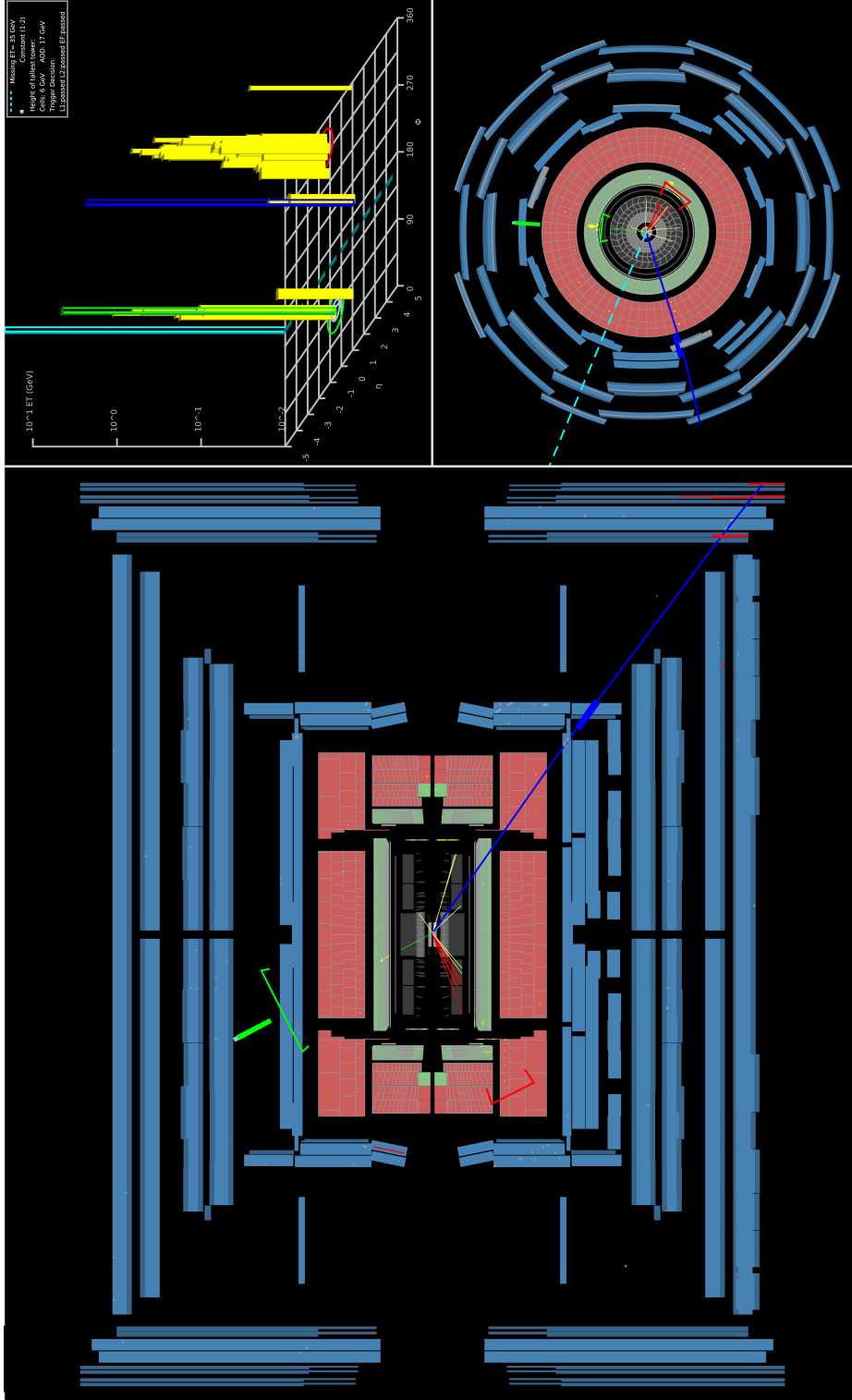
**Table 5.12:** Final numbers needed for cross section calculation.

The total uncertainty on the measurement is dominated by the limited statistics. However, contributions from systematic uncertainties are of the same order of magnitude while the uncertainty on the luminosity measurement plays a minor role. A future analysis may benefit from larger statistics to reduce both the statistical and the systematic uncertainty. The latter is dominated by low statistics in the control regions for the multijet background estimation. This situation is expected to improve with more data. Moreover, additional data will allow for a more precise determination of the lepton efficiency correction factors which, in return, reduces the corresponding systematic uncertainties. Currently, a study of the 2011 data set corresponding to  $1.5 \text{ fb}^{-1}$  is on-going and an update on the cross section measurement is going to be published soon.

The final numbers given here differ slightly from those in [73] where

$$\sigma_{\text{incl}}^{\gamma^*/Z} \times \mathcal{BR}(\gamma^*/Z \rightarrow \tau^+\tau^-) = 1060 \pm 140(\text{stat.}) \pm 80(\text{syst.}) \pm 40(\text{lumi.}) \text{ pb} \quad (5.51)$$

is stated for the  $e\mu + 4\nu$  final state. This difference arises from the way the contribution from signal events in the same-sign isolated region is handled during the multijet estimation. While this contribution is not corrected for but treated as systematic uncertainty in this thesis, the official ATLAS analysis uses the theoretical cross section to normalise the signal contribution in control region  $B$  and corrects for it. This approach leads to a slightly smaller estimate of the multijet background and, thus, results in a larger cross section. In contrast, the result, presented in the context of this work, states a smaller cross section but a larger systematic uncertainty. Both results are compatible within the uncertainties given.



**Figure 5.8:** Event display of a selected data event (run: 166786, event number: 42081853):  $\rho - \phi$  view (left),  $x - y$ -plane (bottom right) and lego plot displaying energy deposits in the calorimeter in  $\eta$  and  $\phi$  (top right). Reconstructed electron candidate (green):  $p_T = 17.3$  GeV,  $\eta = -0.51$ ,  $\phi = 85.9^\circ$ ; reconstructed muon candidate (blue):  $p_T = 15.0$  GeV,  $\eta = 1.15$ ,  $\phi = 195.3^\circ$ ; MET (cyan, dashed):  $p_T = 96.1$  GeV,  $\phi = 157.4^\circ$ ; reconstructed jet (red):  $p_T = 51.9$  GeV,  $\eta = -1.47$ ,  $\phi = 322.1^\circ$ . This event fulfills completely the criteria for the topology of a  $\gamma^*/Z$  boson produced in association with a jet and then decaying via  $\gamma^*/Z \rightarrow \tau^+\tau^- \rightarrow e\mu + 4\nu$ .





# Chapter 6

## A Search for Neutral MSSM Higgs Bosons in the $\tau^+\tau^-$ Channel

The second part of this thesis is devoted to a search for neutral MSSM Higgs bosons in the channel  $pp \rightarrow \phi \rightarrow \tau^+\tau^- \rightarrow e\mu + 4\nu$ . First, simulated samples are used to investigate different selection strategies which discriminate efficiently against background processes while retaining most of the signal events. Secondly, possible approaches for the final interpretation of the observed data are discussed. Finally, the data sample, which was recorded by the ATLAS detector in the first half of 2011 and corresponds to  $1.06 \text{ fb}^{-1}$  of proton-proton collisions at a centre-of-mass energy of  $\sqrt{s} = 7 \text{ TeV}$ , is analysed and an exclusion limit in the  $M_A \times \tan\beta$  parameter space of the MSSM is derived.

### 6.1 Data and Simulated Samples

The data taking periods B-H of the 2011 LHC proton run are considered in this study resulting in a total integrated luminosity of  $1.06 \text{ fb}^{-1}$  of good quality data events. Instantaneous luminosities up to  $1.3 \cdot 10^{33} \text{ cm}^{-2}\text{s}^{-1}$  were reached during these periods. Different beam conditions and higher instantaneous luminosities lead to different pile-up conditions in 2011 compared to the 2010 data set. Due to the small fraction of integrated luminosity, the latter is not included in this study.

In order to benefit from the insights gained by the analysis of the 2010 data set, the simulated samples are reprocessed with improved reconstruction/identification algorithms and an updated detector simulation. The exact list of simulated samples used for evaluating and optimising the different selection strategies can be found in Appendix D.1. Again, the expectations obtained from these simulations are scaled to the integrated luminosity according to Equation (3.7). Pile-up conditions are simulated in these samples by assuming that the proton bunches are grouped into bunch trains of 36 bunches where the individual bunches are separated in time by 50 ns.

### 6.2 Event Preselection

Events have to pass data preselection cuts which resemble those of the  $\gamma^*/Z \rightarrow \tau^+\tau^-$  cross section measurement outlined in Section 5.2. The requirement of at least one recon-

structed vertex with  $\geq 3$  associated tracks, the jet cleaning procedure and the requirement of a good detector status are identical. Only the trigger selection is changed and an additional criterion is introduced to remove events affected by calorimeter problems.

### 6.2.1 Trigger Selection

Motivated by the event topology triggers looking for electron or muon signatures are appropriate to select signal events. Due to the increased instantaneous luminosities in 2011, the  $p_T$  thresholds for all triggers are raised in order to keep the trigger acceptance rate at a sensible level. Therefore, an event filter trigger looking for an electron signature, which passes the `medium`<sup>1</sup> identification criteria and has a transverse momentum of  $p_T \geq 20$  GeV, is used. It is labelled `EF_e20_medium`. The loss in efficiency owing to the higher  $p_T$  threshold can be recovered partially by looking for muon signatures as well. Hence, events triggered by an event filter searching for muon candidates with transverse momenta  $p_T \geq 18$  GeV (`EF_mu18_MG`) are also accepted. Due to a misconfiguration in the muon trigger menu, low  $p_T$  muon triggers exhibit significant efficiency losses for high  $p_T$  muons ( $\gtrsim 200$  GeV). Therefore, it is recommended to complement the low threshold muon trigger by a second muon trigger which is not affected by the misconfiguration. An event filter which looks for muon signatures with  $p_T \geq 40$  GeV only in the muon spectrometer and in the barrel region, is chosen to perform this task. It is labelled `EF_mu40_MOnly_barrel`. The final trigger decision is based on the logic

$$\text{EF\_e20\_medium} \quad \text{OR} \quad \text{EF\_mu18\_MG} \quad \text{OR} \quad \text{EF\_mu40\_MOnly\_barrel}. \quad (6.1)$$

### 6.2.2 Readout Problems in the Calorimeter System

Due to a power glitch on 29<sup>th</sup> of April 2011, the readout electronics for a part of the barrel electromagnetic calorimeter broke down and were not back to operation until the end of data-taking period H. The affected region spans  $0.1 < \eta < 1.48$  and  $-0.88 < \phi < -0.45$  corresponding to  $\approx 0.8\%$  of the full coverage of the calorimeter. In this region the performance of reconstruction and identification algorithms for electrons and jets is deteriorated as well as their energy measurement. Additionally, information for the trigger system are lost and the  $\vec{E}_{T,\text{miss}}$  measurement is biased towards the dead calorimeter region. This effect must be taken into account by removing events in which a reconstructed electron or jet candidate points to the problematic region. The exact details on how events are rejected are given in Appendix D.2. Simulated samples do not contain this detector defect and, thus, must be corrected for it according to the prescription given in Section 6.4.4.

---

<sup>1</sup>The definition and actual meaning of `medium` identification criteria evolves over time as the reconstruction and identification algorithms are improved continuously. However, it is intended that the corresponding identification efficiencies and background rejections remain at approximately the same level.

## 6.3 Object Definitions

The investigated final state of the signal process involves electrons, muons and neutrinos. In addition, hadronic showers arising from initial state radiation may occur. Some background processes are characterised by the presence of hadronic showers as well. Therefore, it is essential to specify the criteria for the reconstruction and identification of lepton candidates, jets and the missing transverse energy. The object definitions used for this analysis are summarised in Table D.2. They are very similar to the object definitions given in Section 5.3 for the cross section measurement. In the following paragraphs, these criteria are reviewed briefly and differences are highlighted.

**Electron Candidates** Electron candidates are considered within the range  $|\eta| \leq 2.4$  but outside  $1.37 \leq |\eta| \leq 1.52$ . They have to be reconstructed with either the standard or the soft- $p_T$  electron reconstruction algorithm. Electron candidates affected by problematic calorimeter regions are discarded.

A transverse momentum of  $p_T \geq 15$  GeV is required as a pre-selection. If an event is triggered by the electron trigger, the  $p_T$  threshold for the selected electron candidate is raised to 22 GeV to be in a regime where the trigger performance is well understood.

Since this analysis is a search for new phenomena, the neutral MSSM Higgs bosons, it is even more important to understand precisely the background processes for this search. The theoretical description of hadronic showers and their evolution is the focus of extensive research but still related to comparably large uncertainties. Hence, in order to reduce possible background contributions originating from mis-interpreted jets, only electron candidates passing the **tight** identification criteria are considered.

**Muon Candidates** Muon candidates, which meet the **tight** identification requirements, are selected with a transverse momentum above 10 GeV. Since the category of **tight** muon candidates comprises segment tagged muons with a high track quality in addition to combined muon candidates, the acceptance is extended to  $|\eta| \leq 2.5$  and the overall reconstruction/identification efficiencies are slightly improved compared to only considering combined muon candidates.

The associated track, when extrapolated back to the beam pipe, has to match the primary vertex within 10 mm. Further criteria on the number of hits in the different components of the inner detector are imposed to ensure a good track quality.

Analogously to the electron candidates, the  $p_T$  threshold for the selected muon candidate is raised to 20 GeV if the event is triggered by the muon trigger.

**Jet Candidates,  $\vec{E}_{T,\text{miss}}$  and Resolving Ambiguities** The definitions for reconstructed jet candidates and the missing transverse energy are the same as for the  $\gamma^*/Z \rightarrow \tau^+\tau^-$  cross section measurement. Moreover, the procedure for resolving ambiguities between different reconstructed objects remains unchanged. Details can be found in the corresponding paragraphs of Section 5.3.

## 6.4 Corrections to the Simulated Samples

Similarly to  $pp \rightarrow \gamma^*/Z \rightarrow \tau^+\tau^-$  cross section measurement, the simulated samples have to be corrected in order to reproduce the actual detector performance. The necessary corrections are already explained in Section 5.4. Due to the different data set and updated simulated samples, the corrections have to be modified. In the following paragraphs changes in the corrections are outlined. Tables with the updated correction factors are given in Appendix D.4.

### 6.4.1 Trigger Efficiency Correction

Trigger efficiencies for the combination of the two muon triggers are derived by studies of the process  $Z \rightarrow \mu^+\mu^-$  [84]. Due to the geometry of the muon trigger system, the correction factors  $w_{\text{trig},\mu}$  are calculated separately for the barrel region  $|\eta| < 1.05$ , where they depend on  $\eta$  and  $\phi$  of the selected muon candidate, and for the end-cap region  $|\eta| \geq 1.05$ , where the correction depends only on the transverse momentum of the muon candidate which triggered the event. The applied correction factors as a function of the  $\eta$  and  $\phi$  in the barrel region are shown in Figure D.2 while Table D.3 summarises the corrections in the end-cap region. Their relative uncertainties are of the order of  $\lesssim 3\%$ .

The correction factors for the electron trigger  $w_{\text{trig},e}$  are provided by other analyses which perform studies of the process  $Z \rightarrow e^+e^-$ . They are displayed in Figure D.1 and depend on the  $\eta$  and  $\phi$  position of the energy cluster associated to the selected electron which caused the trigger. The uncertainties on the correction factors are  $\leq 1.5\%$ .

The final correction factor, which is applied to the simulated samples, depends on the trigger selection. If the event is triggered by the electron trigger, then the correction factor  $w_{\text{trig},e}$  is applied. The decision of the combined muon trigger is only checked if the event is not accepted by the electron trigger. In case of a positive muon trigger decision, the simulated events are weighted with the correction factor for the combined muon trigger  $w_{\text{trig},\mu}$ .

### 6.4.2 Corrections Related to Lepton Candidates

Reconstruction, identification and isolation efficiencies for lepton candidates are investigated by studying the well-known SM processes  $Z \rightarrow e^+e^-$  and  $Z \rightarrow \mu^+\mu^-$  in data. The results are compared with predictions from simulations.

**Efficiency Corrections** In contrast to the 2010 data set, the reconstruction efficiency of electron candidates measured in data differs slightly from the expectation. Therefore, the simulated events are weighted with  $\eta$  dependent scale factors  $w_{e,\text{reco}}$  which are summarised in Table D.4 and have relative uncertainties up to 2%. Owing to the larger amount of statistics in the 2011 data set, the correction factors for the electron identification efficiencies are derived in a finer binning as given in Table D.5. The  $p_T$  dependent corrections exhibit relative uncertainties up to 10% in the low  $p_T$  range.

Contrary to the findings for the 2010 data, the isolation efficiencies for electron and muon candidates agree very well between the simulation and the 2011 data set. The correction accounting for electron related efficiencies is given by

$$w_e(\eta_e, p_{T,e}) = w_{e,\text{reco}}(\eta_e) \times w_{e,\text{ID}}(p_{T,e}) \times w_{e,\text{ID}}(\eta_e). \quad (6.2)$$

The uncertainties on the individual terms are added in quadrature to yield the total uncertainty.

Correction factors  $w_\mu$  for the muon reconstruction and identification efficiencies are provided in a  $\eta \times \phi$  binning which reflects the geometry of the muon spectrometer. They are of the order of 0.95 – 1.01 with relative uncertainties of  $\lesssim 0.5\%$ .

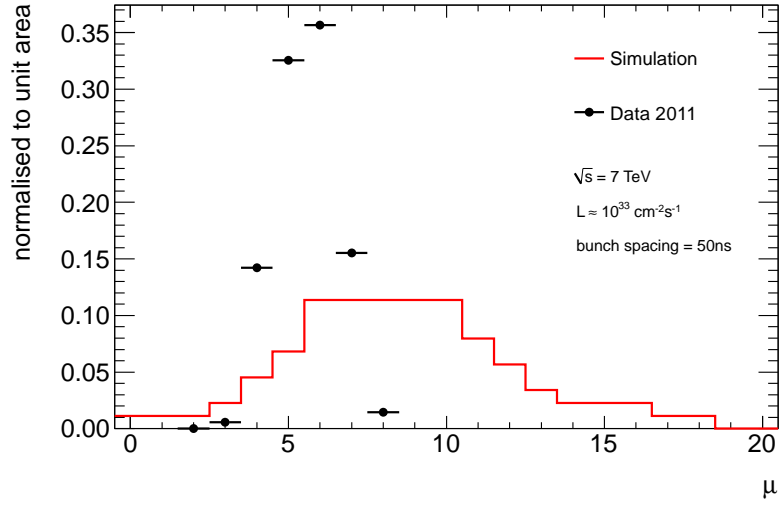
**Energy and Momentum Corrections** The prescription given in the corresponding paragraph of Section 5.4.2 also applies for this study. Updated tools, provided by other groups, are used to smear the transverse momenta of reconstructed muon candidates and to vary the energies of reconstructed electron candidates in order to reproduce the invariant mass spectra  $m_{\ell\ell}$  obtained from  $Z \rightarrow e^+e^-/\mu^+\mu^-$  studies with the 2011 data. The changes are propagated back to the missing transverse energy such that Equation (5.5) is fulfilled. This correction is applied to all lepton candidates before the object selection is performed.

### 6.4.3 Pile-up Related Corrections

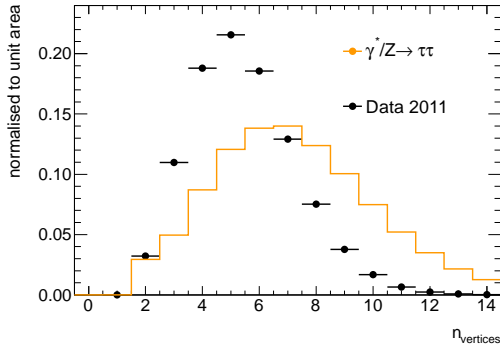
The pile-up conditions in the simulated samples do not reflect correctly the pile-up conditions observed in the 2011 data set. Owing to the reduced bunch spacing, out-of-time pile-up effects become important. Due to the latency of the calorimeter readout electronics, signals from proton-proton interactions, occurring in subsequent bunch crossings, can be overlaid and have to be disentangled correctly. Thus, the number of reconstructed vertices is not an appropriate indicator for the total pile-up conditions because it is only sensitive to multiple proton-proton interactions taking place during the same bunch crossing. Instead, the average number of interactions per bunch crossing, labelled  $\mu$ , is considered adequate to quantify the total pile-up conditions. The distributions of  $\mu$  as it is used for the simulation and how it is observed in the 2011 data set are shown in Figure 6.1(a). Scale factors  $w_{\text{pu}}$  are derived for the simulations to match the distribution of  $\mu$  in data. Figure 6.1 illustrates the effect of this pile-up correction on the distribution of the number of vertices. From this figure, one can infer that the description of in-time pile-up effects is significantly improved.

### 6.4.4 Correction for Problematic Calorimeter Regions

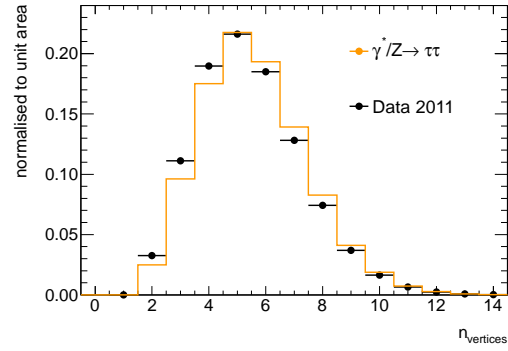
A large fraction of the 2011 data set is affected by dead readout electronics for the EM calorimeter in the barrel region as mentioned in Section 6.2.2. In order to reflect this problem correctly in the simulated samples, the following procedure is applied. If a



(a) Distribution of the average number of interactions per bunch crossing  $\mu$  as it is observed in data (black dots) and as it used during the simulation (red line).



(b) Without pile-up correction.



(c) With pile-up correction.

**Figure 6.1:** Pile-up conditions in data (top) and the effect of the pile-up correction on the  $n_{\text{vertex}}$  distribution (bottom).

simulated event is considered as affected by the dead readout channels (the details of this definition are explained in Appendix D.2), it is weighted with a scale factor

$$w_{\text{LAr}} = \frac{L_{\text{good}}}{L_{\text{total}}} = 0.152 \quad (6.3)$$

which is the fraction of the recorded integrated luminosity not affected by this problem.

## 6.5 Baseline Selection

Before the optimisation of the final event selection is explained, the basic selection motivated by the requirement of a high quality data sample and the event topology is outlined.

### 6.5.1 Event Preselection

The event selection starts with the preselection cuts explained in Section 6.2 to remove events which are affected by detector problems or do not originate from proton-proton collisions. The pile-up correction weight  $w_{\text{pu}}$  is applied at the very beginning. After the trigger requirement simulated events are weighted with the corresponding correction factor which depend on the trigger decision (cf. Section 6.4.1).

### 6.5.2 Selection of the $e\mu$ Final State

Analogously to the  $\gamma^*/Z \rightarrow \tau^+\tau^-$  cross section measurement, the presence of exactly one selected electron candidate and exactly one selected muon candidate is required. The considered lepton candidates are defined by the object selection criteria given in Section 6.3. Moreover, the two selected lepton candidates have to carry opposite electric charges. At this point, simulated events are weighted with the correction factors for the electron and muon reconstruction/identification efficiencies.

### 6.5.3 Raised $p_{\text{T}}$ Threshold for the Trigger Candidate

As already mentioned in Section 6.3, the  $p_{\text{T}}$  requirement on the selected lepton candidates may be raised depending on the trigger decision. If the event is accepted by the electron trigger EF\_e20\_medium, the selected electron candidate has to obey  $p_{\text{T}} \geq 22$  GeV. If an event is not accepted by the electron trigger, the combined muon trigger is checked. In that case the muon candidate has to fulfil  $p_{\text{T}} \geq 20$  GeV.

### 6.5.4 Lepton Isolation

The motivation for isolation requirements and the choice of different cone sizes are discussed in Sections 4.4 and 5.5.3. Since the increased pile-up effects influence mainly

process	expectation
$\gamma^*/Z \rightarrow \tau^+\tau^-$	$2073 \pm 23$
$t\bar{t}$	$1388 \pm 4$
di-boson production	$421 \pm 3$
multijet events	$213 \pm 30$
single top processes	$139 \pm 2$
other <sup>2</sup>	$90 \pm 16$
total background	$4324 \pm 41$
$\phi(120, 20) \rightarrow \tau^+\tau^-$	$153 \pm 3$
$S/\sqrt{B}$	2.33

**Table 6.1:** Expected event yields after the baseline selection. The simulations are normalised to an integrated luminosity of  $L = 1.06 \text{ fb}^{-1}$ . The multijet contribution is estimated from data. The signal yield is shown for the parameter point  $M_A = 120 \text{ GeV}$  and  $\tan\beta = 20$  in the  $m_h^{\text{max}}$  scenario. Only statistical uncertainties are given.

the energy measurement, calorimeter-based isolation variables with smaller cone size are employed in this study. An electron candidate is considered isolated if it fulfils

$$\text{ptcone40}/p_T < 0.06, \quad (6.4)$$

$$\text{and etcone20}/p_T < 0.08. \quad (6.5)$$

Muon candidates are defined as isolated if they pass

$$\text{ptcone40}/p_T < 0.06, \quad (6.6)$$

$$\text{and etcone20}/p_T < 0.04. \quad (6.7)$$

These isolation criteria are taken from official ATLAS analyses searching for the Higgs boson in channels with a similar event topology [85]. An optimisation of these criteria is not performed in the scope of this thesis. However, future analysis may consider an optimisation of the isolation criteria since it turns out that the background arising from multijet events is still sizeable after the full selection.

### 6.5.5 Summary of the Baseline Selection

Table 6.1 summarises the expectations for the different background processes after the baseline selection. All background contributions are estimated by using simulated samples except for the multijet background which is estimated from data as described in Section 6.7.1. For comparison the signal expectation for the parameter point  $M_A = 120 \text{ GeV}$  and  $\tan\beta = 20$  is shown as well as the statistical significance.

<sup>2</sup>Minor background contributions from  $W \rightarrow \ell\nu_\ell$  and  $\gamma^*/Z \rightarrow e^+e^-/\mu^+\mu^-$  processes are collected under the term “other” for the remainder of this chapter.



## 6.6 Optimisation of the Event Selection

As it can be seen from Table 6.1, a possible signal contribution is small compared to the total expected background yield. In order to enhance the sensitivity for the signal process, further selection criteria are imposed to improve the signal to background ratio. Therefore, it is essential to define a signal process as reference. Even though it is desirable to optimise the analysis for different parameter points in the  $M_A \times \tan \beta$  plane, only one reference point is used for this study. The choice of this parameter point is driven by the fact that the fully leptonic final state suffers from a small branching ratio and, thus, is only competitive in regions with comparably large cross sections. This requirement asks for small values of  $M_A$  and large values of  $\tan \beta$ . A lower bound on  $M_A$  is given by the exclusion limit derived at LEP while  $\tan \beta$  is bounded from above by already observed exclusion limit by ATLAS [85]. Therefore, the parameter point  $M_A = 120$  GeV and  $\tan \beta = 20$  is chosen as reference for the remainder of this chapter which results in the following masses for the other two neutral MSSM Higgs bosons:

$$M_h = 118.2 \text{ GeV}, \quad (6.8)$$

$$M_H = 132.0 \text{ GeV}. \quad (6.9)$$

Taking into account the typical experimental mass resolution of the order of 15 GeV, all three bosons can be considered as mass degenerated for this study. The total cross section including the contributions from all three Higgs bosons and both production mechanisms is

$$\sigma(pp \rightarrow h/H/A \rightarrow \tau^+\tau^- \rightarrow \ell^+\ell^- + 4\nu) = 3.3 \text{ pb}. \quad (6.10)$$

Since  $\gamma^*/Z \rightarrow \tau^+\tau^-$  is an irreducible background for the signal process, it is impossible to discriminate against this background without sacrificing a large fraction of the signal events. Therefore, this background contribution is not considered during the optimisation of the event selection. Moreover, the multijet component is omitted as well since these events can be suppressed by tighter isolation cuts which is not studied in the scope of this work.

Among the remaining background processes the production of top-quark pairs ( $t\bar{t}$ ), di-boson processes and single top production play an important role. Hence, the different selection strategies considered aim for a reduction of these three background components while retaining a maximum of the signal events. For this purpose, powerful discriminating variables are discussed in Section 6.6.1. The usage of simulated samples for the optimisation is justified in Section 6.6.2. Possible classification algorithms are reviewed in Section 6.6.3 and their performance is compared in Section 6.6.4.

### 6.6.1 Definition of Discriminating Variables

In this section, variables are investigated which provide a reasonable separation power between the signal and the considered background processes. A list of all discriminating variables considered together with a short motivation is given below. Figure 6.2

exemplifies the distributions of a few discriminating variables for the signal and the considered background processes. The distributions of remaining variables can be found in Appendix D.5.

**Number of Reconstructed Jet Candidates** The background contributions which involve one or more top quark decays are characterised by at least one  $b$  quark in the final state while for the signal process no partons are produced at tree-level. Thus, single top production and  $t\bar{t}$  processes are characterised by a larger number of reconstructed jet candidates (cf. Figure 6.2(a)). The fact, that some of these jets originate from a  $b$  quark, contains some additional discrimination power which is not employed in this study but may be studied by future analyses.

**Scalar  $p_T$  Sum of Reconstructed Objects** Similarly to the cross section measurement, the variable

$$\text{SumPtMETJets} = p_{T,e} + p_{T,\mu} + E_{T,\text{miss}} + \sum_j p_{T,\text{jet}} \quad (\text{cf. Figure D.3(c)}) \quad (6.11)$$

is examined. It provides a good discrimination power against the  $t\bar{t}$  background as already discussed in Section 5.5.5. In addition, the variable

$$\text{SumPtMET} = p_{T,e} + p_{T,\mu} + E_{T,\text{miss}} \quad (\text{cf. Figure 6.2(b)}) \quad (6.12)$$

is defined which has a slightly smaller rejection power as it ignores the contributions from jet candidates. In return, it is less affected by systematic uncertainties on the jet energy calibration.

**Angular Correlation between Lepton Candidates and  $\vec{E}_{T,\text{miss}}$**  The variable

$$\text{SumCosDPhi} = \cos(\phi_e - \phi_{\text{MET}}) + \cos(\phi_\mu - \phi_{\text{MET}}) \quad (\text{cf. Figure 6.2(c)}) \quad (6.13)$$

is defined analogously to the cross section measurement to suppress backgrounds containing decays of  $W$  bosons (cf. Section 5.5.4). Therefore, it is a useful variable to discriminate against  $t\bar{t}$ , single top,  $W \rightarrow \ell\nu_\ell$  and di-boson processes with at least one produced  $W$  boson. Additionally, the two variables

$$\text{DeltaPhiL1MET} = |\phi_{\ell_1} - \phi_{\text{MET}}| \quad (\text{cf. Figure D.3(a)}), \quad (6.14)$$

$$\text{DeltaPhiL2MET} = |\phi_{\ell_2} - \phi_{\text{MET}}| \quad (\text{cf. Figure D.3(b)}) \quad (6.15)$$

are investigated with  $\ell_{1/2}$  being the lepton candidate with the larger/smaller  $p_T$ . For the signal process, both lepton candidates are expected to be back-to-back in the transverse plane and the  $\vec{E}_{T,\text{miss}}$  vector is aligned along the same direction assuming that the  $\vec{E}_{T,\text{miss}}$  arises only from neutrinos produced by the tau lepton decays. Determined by the conservation of transverse momenta, the  $\vec{E}_{T,\text{miss}}$  vector should point in the direction of the lepton candidate with the smaller  $p_T$ . Thus,  $|\phi_{\ell_1} - \phi_{\text{MET}}| \approx \pi$  and  $|\phi_{\ell_2} - \phi_{\text{MET}}| \approx 0$  is expected for signal events.

Another variable connecting the  $\vec{E}_{T,\text{miss}}$  measurement with the kinematics of the lepton candidates is the projection of the  $\vec{E}_{T,\text{miss}}$  vector on the axis of the lepton candidate closest in  $\phi$ . It is defined as

$$\text{EtMissRel} = \begin{cases} E_{T,\text{miss}} \cdot \sin \Delta\phi_{\min} & , \Delta\phi_{\min} \leq \frac{\pi}{2} \\ E_{T,\text{miss}} & , \Delta\phi_{\min} > \frac{\pi}{2} \end{cases} \quad (\text{cf. Figure 6.2(e)}) \quad (6.16)$$

with  $\Delta\phi_{\min} = \min(|\phi_e - \phi_{\text{MET}}|, |\phi_\mu - \phi_{\text{MET}}|)$ .

**Angular Correlations of the Lepton Candidates** Inspired by the event topology the variable

$$\text{DeltaPhiLL} = |\phi_e - \phi_\mu| \quad (\text{cf. Figure 6.2(d)}) \quad (6.17)$$

is examined as well. The distribution is expected to peak at  $\pi$  for signal events while the background process exhibits large tails towards smaller values. Additionally, the absolute value of the difference in  $\eta$  is examined,

$$\text{DeltaEtaLL} = |\eta_e - \eta_\mu| \quad (\text{cf. Figure D.3(d)}). \quad (6.18)$$

**Transverse Masses** The definition of the transverse mass is given in Equation (5.27) and is calculated for the electron candidate  $m_{T,e}$  (cf. Figure D.3(f)) and the muon candidate  $m_{T,\mu}$  (cf. Figure D.3(f)). This variable is again useful for rejecting events which contain leptonic decays of  $W$  bosons.

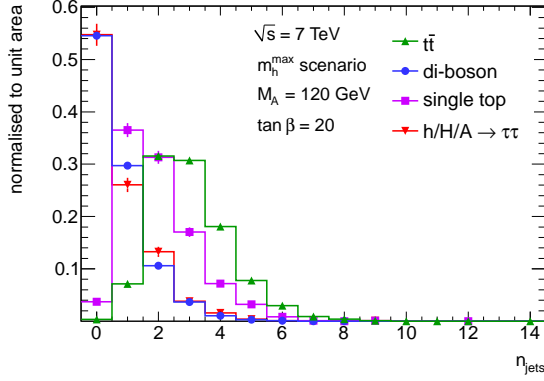
**Asymmetry in  $p_T$  of the Lepton Candidates** The asymmetry in  $p_T$  of both lepton candidates is given by

$$\text{PtAsymmetry} = \frac{p_{T,e} - p_{T,\mu}}{p_{T,e} + p_{T,\mu}} \quad (\text{cf. Figure D.3(e)}). \quad (6.19)$$

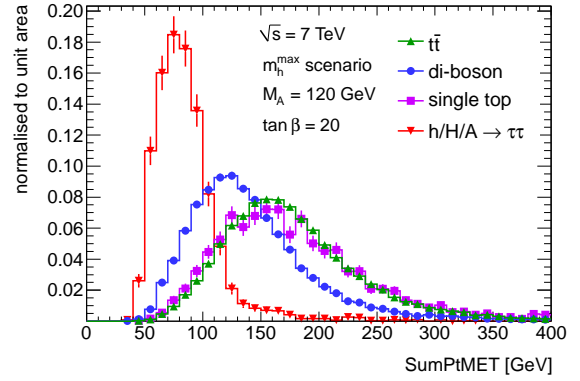
This variable is intended to discriminate against  $ZZ$  processes where one  $Z$  boson decays into a pair of electrons and the other into a pair of muons. If in each case one lepton is outside the detector acceptance or fails the reconstruction, this process is a direct background to the signal topology. However, the remaining two lepton candidates are expected to have transverse momenta of about half of the  $Z$  mass and the asymmetry is expected to be very small. In contrast, the signal process involves four neutrinos whose momenta contribute to the  $p_T$  conservation. Therefore, the transverse momenta of the lepton candidates can exhibit a larger asymmetry.

## 6.6.2 Validation of Simulated Samples

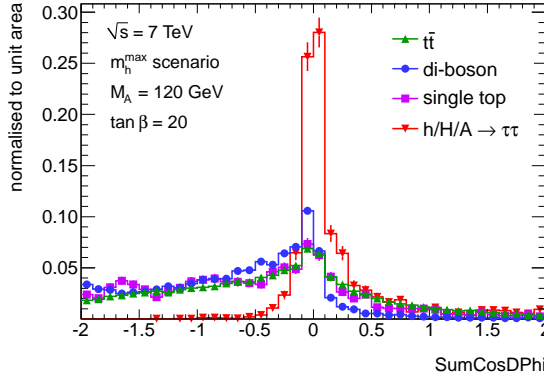
Before the proposed variables are employed in the optimisation of the event selection, the usage of simulated samples is justified. For this purpose, control regions for the two major background components,  $t\bar{t}$  and di-boson processes, are defined where distributions of important variables are validated.



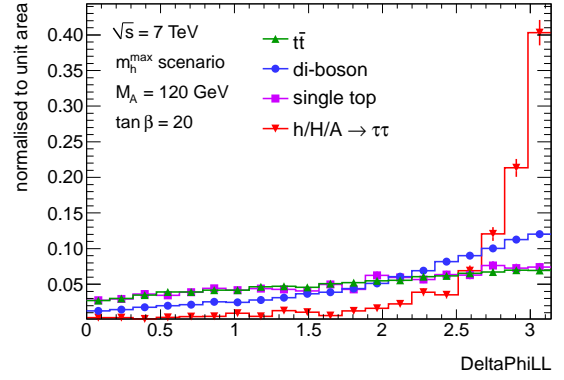
(a) Number of reconstructed jet candidates.



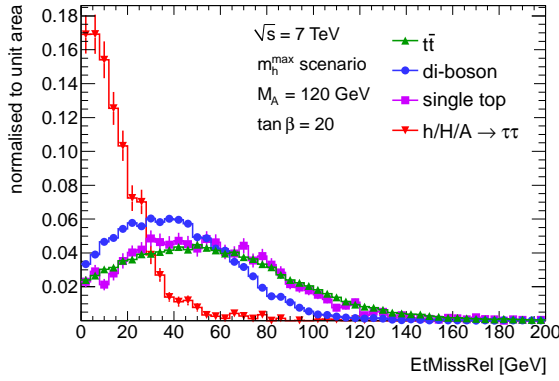
(b) Shape of SumPtMET distribution.



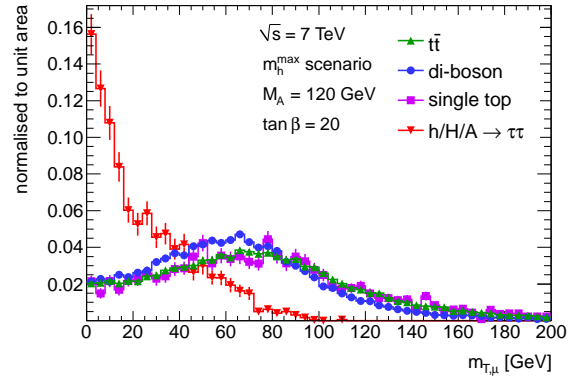
(c) Shape of SumCosDPhi distribution.



(d) Shape of DeltaPhiLL distribution.



(e) Shape of EtMissRel distribution.



(f) Shape of the transverse mass distribution with respect to the muon candidate.

**Figure 6.2:** Distributions of several discriminating variables for the background processes  $t\bar{t}$  (green triangles), di-boson production (blue dots) and single top production (violet squares) and the signal process (red reversed triangles) for the parameter point  $M_A = 120$  GeV and  $\tan \beta = 20$  in the  $m_h^{\max}$  scenario. All distributions are taken from simulated samples. The definitions of the individual variables are given in the text.

process	$t\bar{t}$	di-boson
$\gamma^*/Z \rightarrow \tau^+\tau^-$	$34 \pm 3$	$50 \pm 4$
$t\bar{t}$	$771 \pm 3$	$74 \pm 1$
di-boson production	$39 \pm 1$	$220 \pm 2$
multijet events	$14 \pm 11$	$23 \pm 12$
single top processes	$51 \pm 1$	$38 \pm 1$
other	$4 \pm 1$	$18 \pm 7$
total background	$913 \pm 12$	$423 \pm 14$
$\phi(120, 20) \rightarrow \tau^+\tau^-$	$7 \pm 1$	$12 \pm 1$
data 2011	927	407
ratio	$1.02 \pm 0.04$	$0.96 \pm 0.06$

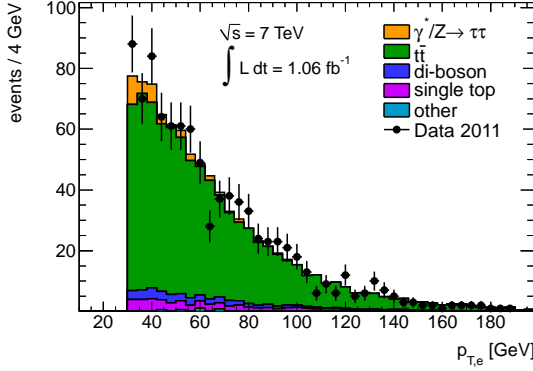
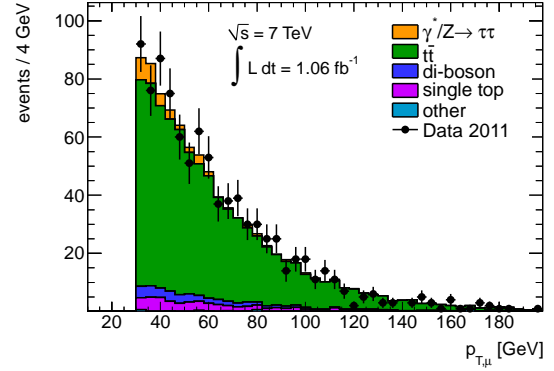
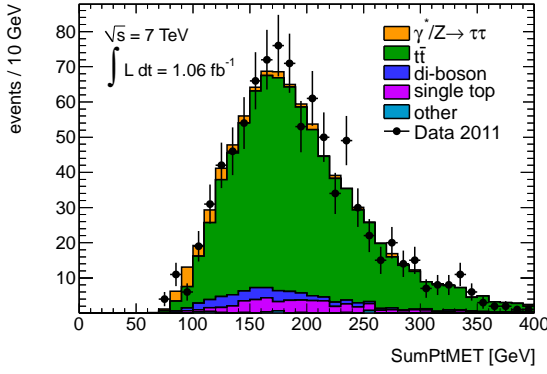
**Table 6.2:** Expected event yields in the two control regions are compared to the observed number of data events. The simulations are normalised to an integrated luminosity of  $L = 1.06 \text{ fb}^{-1}$ . The multijet contribution is estimated from data. The signal yield is shown for the parameter point  $M_A = 120 \text{ GeV}$  and  $\tan\beta = 20$  in the  $m_h^{\text{max}}$  scenario. Only statistical uncertainties are given. The ratio is calculated as data/total background.

### Control Region for the $t\bar{t}$ Process

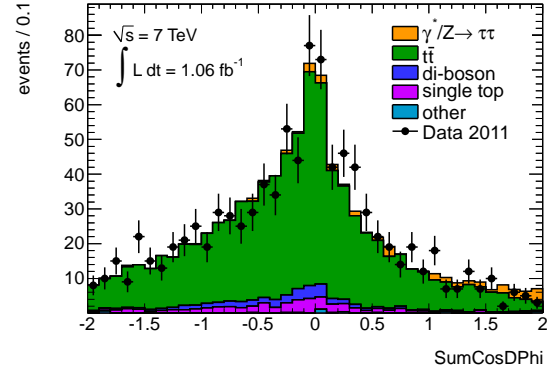
The control region for top-quark pair production is defined by the baseline selection criteria which are completed by the requirement of at least 2 reconstructed jet candidates. Additionally, the  $p_T$  thresholds for the two selected lepton candidates are raised to 30 GeV. The expected yields for this selection are given in Table 6.2 and compared to the observed number of data events. This control region is dominated by  $t\bar{t}$  events ( $\approx 84\%$ ) and the signal contamination is negligible ( $\leq 1\%$ ). From the observed agreement between the number of data events and the total expectation it is concluded that the normalisation of the  $t\bar{t}$  simulation is adequate. The distributions of different variables as predicted by simulations are compared to the distributions observed in data. Figure 6.3 shows the results which are in a good agreement considering the limited statistics.

### Control Region for Di-boson Production Processes

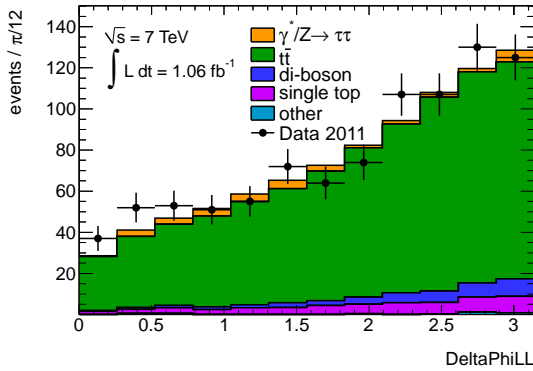
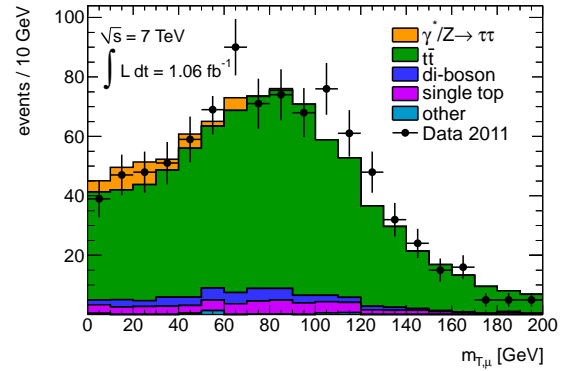
A control region for di-boson production processes is defined by the baseline selection steps with the  $p_T$  thresholds for the lepton candidates raised to 26 GeV. In addition, the requirements  $p_{T,e} + p_{T,\mu} + E_{T,\text{miss}} \geq 100 \text{ GeV}$  (against  $\gamma^*/Z \rightarrow \tau^+\tau^-$  events) and  $n_{\text{jets}} \leq 1$  (against  $t\bar{t}$  events) are imposed to enhance the purity of the control region. The resulting expectations for the different processes are shown in Table 6.2 and compared to the observed number of data events. The contribution from di-boson production processes is only 52% and the signal contamination of about 3% is in a regime where it becomes non-negligible. Albeit these drawbacks, this control region is used for


 (a) Electron  $p_T$  spectrum.

 (b) Muon  $p_T$  spectrum.


(c) SumPtMET distribution.



(d) SumCosDPhi distribution.


 (e)  $\Delta\text{PhiLL}$  distribution.


(f) Spectrum of the transverse mass with respect to the muon candidate.

**Figure 6.3:** Several distributions in the  $t\bar{t}$  control region. The expectations of the individual components are scaled to the stated integrated luminosity and stacked. The definition of the various variables are given in the text.

a rough cross check due to the difficulty of finding a more pure control region with sufficient statistics. Moreover, the second largest contribution arises from  $t\bar{t}$  events ( $\approx 18\%$ ) which is already validated. The observed agreement suggests that the normalisation for the simulation of di-boson processes is appropriate. Also, the distributions of important variables, which are depicted in Figure 6.4, do not exhibit severe deviations.

### 6.6.3 Description of Investigated Methods

Classification algorithms combine the information of discriminating variables in order to assign events to different categories. These strategies differ in implementation, requirements on the input variables, assumptions and performance in terms of the achieved signal to background ratio. The TMVA [86] framework provides a variety of different classifiers and is used for this study. Before the investigated methods are described, the definition of a figure-of-merit for the optimisation process is discussed shortly.

In the following  $\{x_i\}, i = 1 \dots N$ , denotes the set of  $N$  discriminating variables under investigation. The number of expected signal events is labelled  $S$  while  $B$  represents the total background expectation.

#### Figure-of-Merit for Optimisation

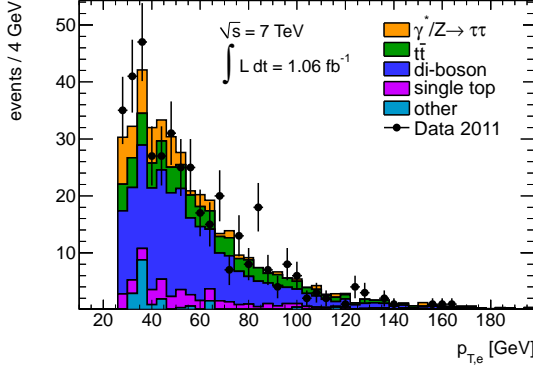
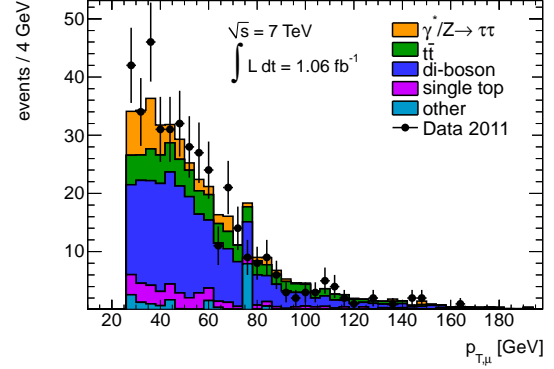
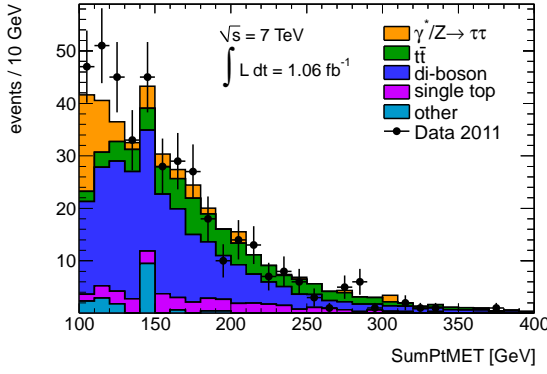
The goal of the optimisation of the event selection is to enhance the sensitivity of the analysis for the signal process. A measure for the sensitivity is the *significance*  $Z$  which is in the case for the search of new phenomena approximately given by  $Z = S/\sqrt{B}$ . The calculation of the significance always involves the expected signal and background yields which depend on external parameters like the integrated luminosity. However, the procedure of separating signal and background events should not depend on the collected amount of data. To disentangle both questions, the optimisation is done in terms of the signal efficiency<sup>3</sup>  $\varepsilon_S$  and background rejection  $r_B = 1 - \varepsilon_B$ . The methods described below maximises the background rejection for a given signal efficiency. The result is a function of  $r_B$  versus  $\varepsilon_S$  which is called *Receiver Operating Characteristic* (ROC). For a given expectation of  $S$  and  $B$ , the optimal working point corresponding to the largest significance lies on the obtained ROC curve and can be derived easily.

#### Rectangular Cuts

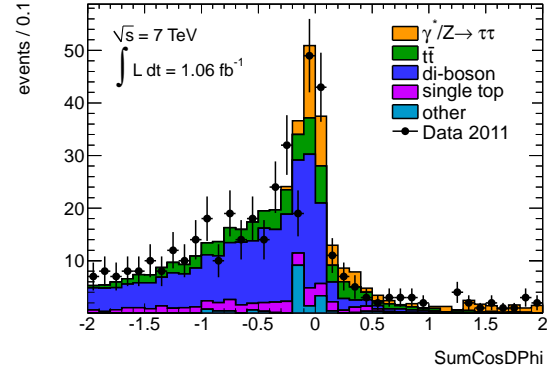
Rectangular cuts is the simplest method to define a phase space region. Simple requirements of the form  $c_i^l \leq x_i \leq c_i^u$  with lower/upper limits  $c_i^{l/u}$  are imposed on the discriminating variables<sup>4</sup>. Thereby, it is assumed that the signal is localised in the phase space in a way that one minimum and one maximum requirement on each variable is sufficient to optimally separate signal from background events. In order to meet this requirement, a

<sup>3</sup>The efficiencies for signal and background are defined as the fraction of events which are classified as signal-like.

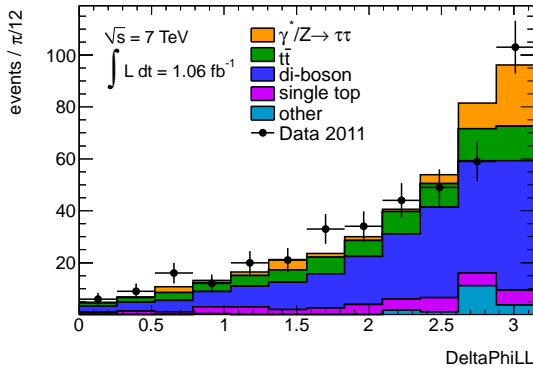
<sup>4</sup>It is possible that some variables are only bounded from one side or not used at all.


 (a) Electron  $p_T$  spectrum.

 (b) Muon  $p_T$  spectrum.


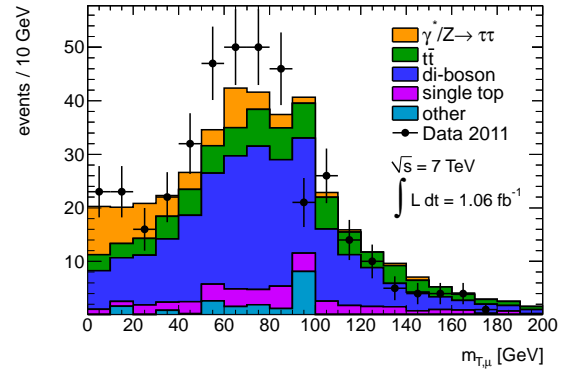
(c) SumPtMET distribution.



(d) SumCosDPhi distribution.



(e) DeltaPhiLL distribution.



(f) Spectrum of the transverse mass with respect to the muon candidate.

**Figure 6.4:** Several distributions in the di-boson control region. The expectations of the individual components are scaled to the stated integrated luminosity and stacked. The definition of the various variables are given in the text.



transformation of the input variables may be necessary. The signal efficiency and background rejection are estimated from simulations by counting the respective number of events passing the ensemble of cuts under investigation.

This method is not sensitive to non-linear correlations among the input variables and, thus, can not benefit from different correlations for the signal and background processes. Furthermore, the performance deteriorates quickly when using many variables with small discrimination power.

### Fisher Discriminant

The FISHER discriminant analysis renders optimal separation power in the case of Gaussian distributed input variables with linear correlations. It condenses the information of all input variables by projecting the  $N$ -dimensional variable space on one axis according to

$$y_F = F_0 + \sum_{i=1 \dots N} F_i x_i. \quad (6.20)$$

The projection axis is defined by the coefficients  $F_i$  which are determined such that the projection of signal and background events are well separated while events from the same category are confined in close vicinity. The metric used to define “well separated” and “in close vicinity” is the covariance matrix of the discriminating variables. The constant offset  $F_0$  is chosen such that the total sample mean of signal and background samples is  $\bar{y}_F = 0$ .

Despite of its simplicity, this method is competitive to more complicated strategies in the case of strong linear correlations. A disadvantage of this method is the fact that shape information is omitted. It is only sensitive to the difference between the means of individual distributions for background and signal processes. Therefore, it is not possible to distinguish between background and signal events if the distributions for both classes have the same mean value, even if their shapes are very different.

### Projective Likelihood Approach

The likelihood approach builds a model for the signal and background hypothesis by using probability density functions (PDFs). The projective likelihood approach assumes that all input variables are statistically independent which leads to the likelihood function

$$\mathcal{L}_a(\{x_i\}) = \prod_{i=1 \dots N} p_{a,k}(x_k), \quad a = S, B, \quad (6.21)$$

with  $p_{a,k}$  being the normalised PDFs for the variables  $x_i$  for the signal and background hypothesis, respectively. These PDFs are determined empirically from the simulations by non-parametric functions because their exact functional dependence is unknown in most of the cases.

The normalised signal likelihood

$$y_{\mathcal{L}} = \frac{\mathcal{L}_S}{\mathcal{L}_S + \mathcal{L}_B} \quad (6.22)$$

provides the best separation power and is used as the final test statistic.

The projective likelihood approach is suitable for a large number of input variables as its operation is very fast. However, the assumption of independent input variables is fulfilled seldom leading to a decreased performance compared to other, more complicated classifiers. Linear correlations can be corrected for by applying a de-correlation transformation on the input variables. The accuracy of the obtained PDFs is crucial for a good performance and depends on algorithm parameters as well as on the available statistics in the simulations. The exact options used in this study are given in Appendix D.5 and follow general guidelines.

The statistics in the simulated samples is not sufficient to investigate multidimensional likelihood estimators which overcome the problem of omitted correlations and provide an intrinsically more accurate description of the signal and background model.

### Boosted Decision Trees

A decision tree is a collection of binary decisions. Each node splits the sample into two sub-samples by a cut on one variable. The procedure is repeated until an abort condition is fulfilled (e.g. height of the tree, minimum number of events in leaf node). The leaf nodes are considered as signal- or background-like depending on the category the majority of events belongs to. In contrast to the rectangular cuts, not only one hypercube is selected in the variable space but rather many of them are defined and classified. This leads to a better performance as signal events failing one selection criterion can still be recycled in further steps. Individual decision trees are strongly affected by statistical fluctuations in the training sample. In order to reduce this effect, multiple trees are built from the same training sample resulting in a *forest* of decision trees. Events which are mis-classified by an individual tree are re-weighted before the next tree is built. The final response of the boosted decision tree (BDT) is the weighted average of all trees in the forest.

In general, BDTs outperform other classifiers as they can deal with very complicated correlations. In addition, the training and evaluation of BDTs is comparably easy since each splitting step involves the optimisation of a one-dimensional cut. However, for limited statistics one has to consider that the performance obtained on the training sample is overestimated due to statistical fluctuations (*over-training*).

#### 6.6.4 Performance Evaluation of Multivariate Analysis Tools

The performance of the different methods is evaluated using the TMVA toolkit with the exact steering options used to train the different algorithms given in Appendix D.5. For this purpose, simulated samples are split into a training and a test sample. The former is used to set up and initialise the multivariate methods (e.g. create PDFs, build decision trees etc.) while the latter is used to validate the results obtained on the training sample. All methods are trained with the  $\phi(M_A = 120 \text{ GeV}, \tan \beta = 20) \rightarrow \tau^+ \tau^-$  process as signal (including both production mechanisms) while  $t\bar{t}$  events, di-boson production and single top processes constitute the background under investigation. The individual

samples are weighted according to Equation (3.7) to account for different cross sections and sample sizes.

Before looking for a good set of discriminating variables, the effect of possible transformations of the input variables on the performance of the individual methods is evaluated with a reference set. The following transformations are examined:

**Normalisation:** All variables are scaled such that their range is  $[-1, 1]$ .

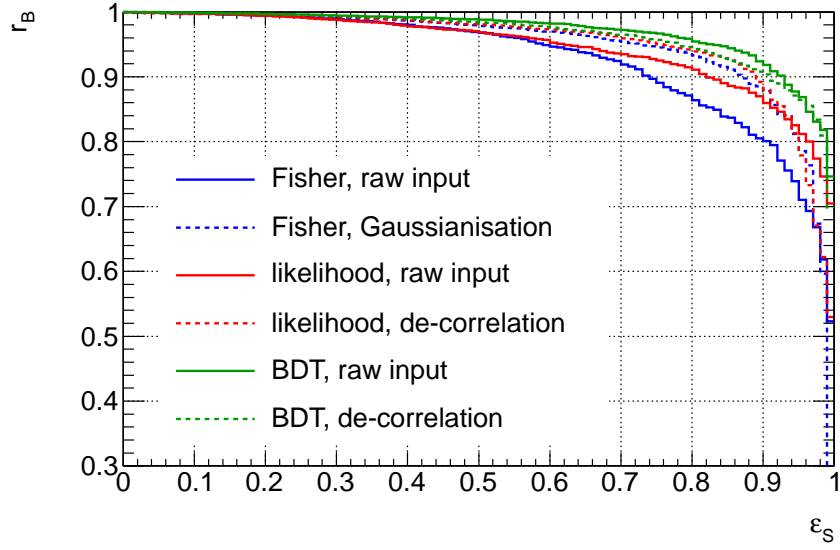
**“Gaussianisation”:** Every PDF can be transformed in an uniform distribution by using its cumulative distribution function. Afterwards, the uniform distribution can be transformed into a Gaussian PDF by using the inverse error function.

**De-correlation:** The vector of input variables is rotated by the square root of the covariance matrix. The de-correlation is complete only for linear correlations and normal distributed input variables.

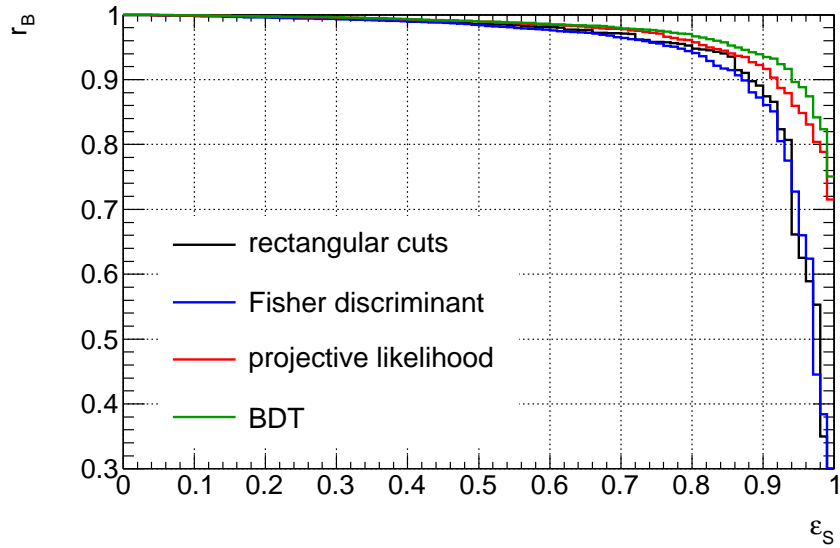
It turns out that neither method is influenced by a prior normalisation of the input variables. The projective likelihood method benefits slightly from a de-correlation transformation while the performance of the FISHER discriminant is improved considerably by a “Gaussianisation” transformation. The BDT shows even a drop in performance if a de-correlation is applied. These findings are in agreement with the properties of the individual methods discussed in Section 6.6.3. Consequently, the results presented below always contain a de-correlation transformation for the projective likelihood method and a “Gaussianisation” for the FISHER discriminant analysis while the BDT uses the raw input variables. Figure 6.5 shows the gain/loss in performance for some variable transformations and multivariate methods.

In general, the optimal set of discriminating variables depends on the applied method as these have different assumptions and cope differently with correlations. Starting from a reference set inspired from earlier analyses, the performance is improved by substituting/adding further variables. In order to compare the performances of two variable sets the integrals of the ROC curves are considered. The optimal value of the ROC integral is 1 corresponding to a background rejection of  $r_B = 1$  independently of the signal efficiency. The resulting variable sets, which are found to perform best for the individual methods, are defined in Table 6.3. Their performances are summarised in Table 6.4 and the corresponding ROC curves are displayed in Figure 6.6. Further variable combinations and the corresponding performances can be found in Appendix D.5. Cross checks on the validity of the performance of the individual methods are performed and can be found in Appendix D.5.

It can be concluded that using a boosted decision tree as classifier gives the best performance. The projective likelihood method yields comparable results while the performance of the FISHER discriminant analysis is slightly worse. Nevertheless, the differences between the individual methods are small and simple rectangular cuts on only four variables provide a very good background rejection as well. Moreover, one has to notice that the studied methods are trained to discriminate against the background processes  $t\bar{t}$ , di-boson and single top production while the largest background arises from  $\gamma^*/Z \rightarrow \tau^+\tau^-$



**Figure 6.5:** Effect of transformation of input variables on the performance of the FISHER discriminant analysis (blue), the projective likelihood method (red) and the BDT (green).



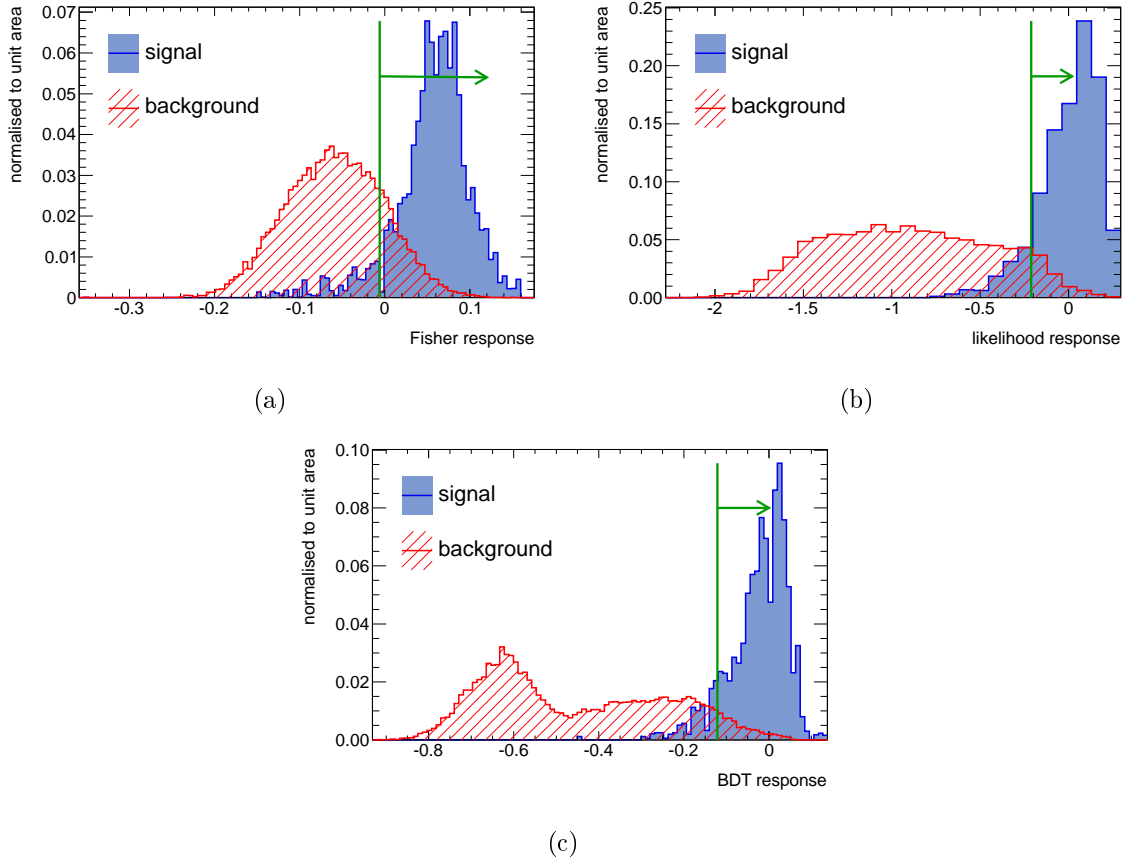
**Figure 6.6:** ROC curves for the best performing variable sets as defined in Table 6.3 for rectangular cuts (black), the FISHER discriminant analysis (blue), the projective likelihood method (red) and the BDT (green).

rectangular cuts	FISHER discriminant	projective likelihood	BDT
SumPtMET	SumPtMETJets	SumPtMET	SumPtMET
SumCosDPhi	SumCosDPhi	SumCosDPhi	SumCosDPhi
DeltaPhiLL	$m_{T,e}$	DeltaPhiLL	DeltaPhiLL
	$m_{T,\mu}$	DeltaEtaLL	DeltaEtaLL
		$m_{T,e} + m_{T,\mu}$	$m_{T,e} + m_{T,\mu}$
		EtMissRel	EtMissRel
			DeltaPhiL2MET
			PtAsymmetry
			$n_{\text{jets}}$

**Table 6.3:** Optimal sets of variables for the individual methods.

variable set	background rejection in %			ROC integral
	$\varepsilon_S = 1\%$	$\varepsilon_S = 10\%$	$\varepsilon_S = 30\%$	
rectangular cuts	40.1%	88.3%	94.3%	0.945
FISHER discriminant	39.4%	87.4%	94.9%	0.942
projective likelihood	49.4%	91.7%	99.7%	0.970
BDT	49.9%	94.3%	$\geq 99.9\%$	0.976

**Table 6.4:** The performances for the different variable sets defined in Table 6.3 for the corresponding methods. The background rejection  $r_B$  is given for three fixed signal efficiencies  $\varepsilon_S$  as well as the integral of the ROC curve.



**Figure 6.7:** Normalised classifier response distributions for signal (blue) and background (red) events for the FISHER discriminant analysis (top left), the projective likelihood method (top right) and the BDT (bottom). The green lines represent the cut values corresponding to a signal efficiency of  $\varepsilon_S = 90\%$ .

events. As the event kinematics of the latter are very similar to those of the signal process, the rejection of  $\gamma^*/Z \rightarrow \tau^+\tau^-$  events by the investigated methods is expected to be small. As a consequence, the optimal working point can not be derived from the ROC curves in Figure 6.6 but one has to take into account the additional  $\gamma^*/Z \rightarrow \tau^+\tau^-$  and multijet background components when calculating the total significance. The large amount of  $\gamma^*/Z \rightarrow \tau^+\tau^-$  events after the baseline selection compared to the expected signal yield (cf. Table 6.1) asks for a working point with a large signal efficiency. In the context of this work, the signal efficiency is fixed to 90% but future analysis may optimise this point with respect to the total significance. Except for the rectangular cuts, all multivariate methods return a response value for each event. The distributions of these response values for signal and background events are determined from training samples and are shown in Figure 6.7. The fixed signal efficiency of  $\varepsilon_S = 90\%$  corresponds to cuts on these response values which are indicated by the green lines. Table 6.5 states all cut values together with the associated background rejections. Because the background rejection for the FISHER discriminant analysis is worse than the performance of

method	cut values	background expected	rejection obtained	$\varepsilon_S$ obtained
rectangular cuts	$\text{SumPtMET} \leq 120 \text{ GeV}$			
	$\text{SumCosDPhi} \geq -0.25$	87.4%	93.6%	87.6%
	$\text{DeltaPhiLL} \geq 1.75$			
FISHER discriminant	$\geq 0.006$	86.7%	–	–
projective likelihood	$\geq -0.21$	92.0%	93.1%	89.5%
BDT	$\geq -0.12$	93.6%	95.1%	94.1%

**Table 6.5:** Cut values on the response of the individual classifiers and the values for the rectangular cuts which correspond to a signal efficiency of  $\varepsilon_S = 90\%$  as derived from the training samples. The given background rejections consider only  $t\bar{t}$ , di-boson and single top processes as background. For comparison the actual obtained signal efficiencies and background rejections on the full simulated samples are shown.

simple rectangular cuts, it is not further investigated and dropped at this point. The actual observed background rejections and signal efficiencies differ slightly from those obtained with the training samples due to the limited statistics in the training samples. Additionally, the values for the rectangular cuts are rounded to a reasonable precision. The resulting event yields for the remaining three methods are given in Table 6.6 together with the improved statistical significances. One concludes that rectangular cuts are competitive with the projective likelihood approach. Due to the large remaining  $\gamma^*/Z \rightarrow \tau^+\tau^-$  background, the BDT results only in a mildly improved significance even though it clearly outperforms the other two methods (cf. Table 6.5).

The final decision on which method is used for the event selection does not only depend on the performance of the method but also on its robustness and the effect of systematic uncertainties. As the evaluation of the systematic uncertainties on all three methods does not fit into the scope of this thesis, it is assumed that the relative systematic uncertainty increases with the number of discriminating variables employed. Moreover, the more variables are used the more correlations have to be validated for the simulated samples. So far, only distributions themselves are checked but no correlations are investigated due to the limited statistics. Wrongly modelled correlations in the simulations are not a direct systematic uncertainty but rather lead to a diminished performance in data compared to the one obtained from simulated samples. Regarding these arguments, simple rectangular cuts are chosen for the final event selection.

In addition to the cuts in Table 6.5, the requirement of  $n_{\text{jets}} \leq 3$  is introduced by hand. This criterion does not improve the significance but reduces the amount of expected  $t\bar{t}$  events which is beneficial when considering systematic uncertainties.

As discussed in Section 2.2.2 the mass splitting of the three neutral MSSM Higgs bosons depends on  $M_A$  and  $\tan\beta$ . In order to use the total cross sections shown in Figure 4.5, one has to ensure that the analysis is sensitive to the contributions of all three Higgs bosons. Taking into account the experimental resolution the following mass window in

	$\gamma^*/Z \rightarrow \tau^+\tau^-$	QCD	$t\bar{t}$	di-boson	single top	other	$\sum$	signal	$\frac{S}{\sqrt{B}}$
baseline	2073	213	1388	421	139	90	4324	153	2.33
BDT	1926	55	37	52	6	25	2101	144	3.13
likelihood	1901	26	68	44	6	22	2067	137	3.02
SumPtMET	1998	195	202	161	24	69	2649	1424	2.76
SumCosDPhi	1905	77	108	62	11	25	2188	138	2.95
DeltaPhiLL	1843	57	59	58	7	22	2046	134	2.97

**Table 6.6:** Expected signal and background yields for different selection strategies. The third to last column  $\sum$  is the sum of all background expectations. The background composition and signal expectation are given after the baseline selection (first row), after the application of the trained BDT (second row), after the usage of the projective likelihood method (third row). The last rows corresponds to the optimised rectangular cuts. All expectations are derived from simulation and normalised to  $L = 1.06 \text{ fb}^{-1}$  except for the multijet component which is estimated from data. The relative statistical uncertainties on the sum of all background components is  $\approx 2\%$ .

terms of the visible mass

$$30 \text{ GeV} \leq m_{e\mu} \leq 110 \text{ GeV} \quad (6.23)$$

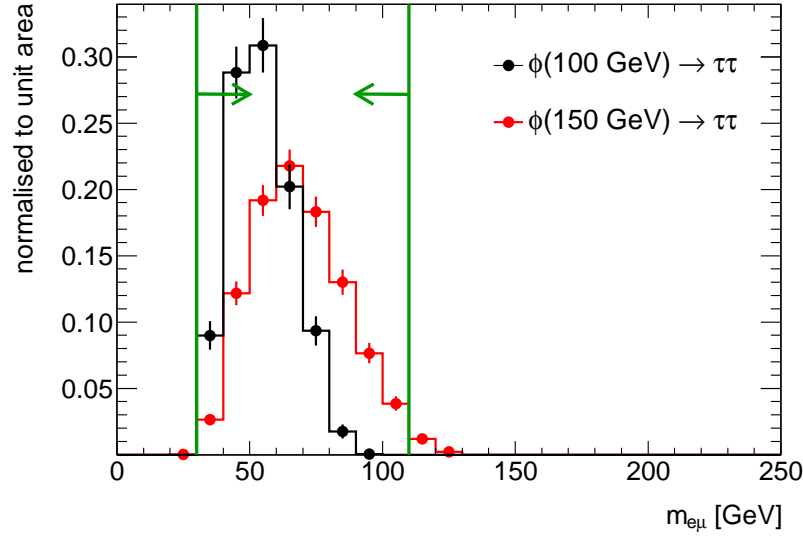
is suitable for accommodating sufficiently the contributions from all three MSSM Higgs bosons in the parameter space  $100 \text{ GeV} \leq M_A \leq 150 \text{ GeV}$  and  $\tan\beta \geq 5$ . Figure 6.8 compares the visible mass shapes for neutral Higgs boson of two different masses after the requirement  $n_{\text{jets}} \leq 3$ . One may tune the boundaries of the visible mass window depending on the Higgs boson mass under investigation in future analyses. This optimisation has to be done as a function of  $\tan\beta$  to correctly account for the mass splitting. A summary of all event yields and the observed number of data events for the final selection can be found in Table 6.7.

## 6.7 Background Estimation

For the background components  $\gamma^*/Z \rightarrow \ell^+\ell^-$  and  $W \rightarrow \ell\nu_\ell$  both the normalisation and the distribution of variables are taken from simulated samples. This approach is justified by the fact that the final contributions from  $W \rightarrow \ell\nu_\ell$  and  $\gamma^*/Z \rightarrow e^+e^-/\mu^+\mu^-$  processes in the signal region are small compared to other background components and the signal expectation. The usage of simulated samples for the  $\gamma^*/Z \rightarrow \tau^+\tau^-$  process is motivated by the good agreement with the data observed during the  $\gamma^*/Z \rightarrow \tau^+\tau^-$  cross section measurement. Simultaneously, the similarity in the event kinematics with the signal process impede the definition of a signal free control region. Nevertheless, there are methods which construct  $\gamma^*/Z \rightarrow \tau^+\tau^-$  from  $Z \rightarrow \mu^+\mu^-$  events measured in data using embedding techniques [87] which may be considered in future analyses.

The multijet background is estimated from data in an analogous manner as it is done for the cross section measurement. Additionally, the sum of the  $t\bar{t}$ , single top and di-boson





**Figure 6.8:** Normalised visible mass distributions before the application of the mass window cut for a neutral Higgs boson with a mass of 100 GeV (black) and 150 GeV (red). The green arrows indicate the visible mass window.

process	$n_{\text{jets}} \leq 3$	mass window
$\gamma^*/Z \rightarrow \tau^+\tau^-$	$1821.9 \pm 21.4$	$1819.6 \pm 21.4$
$t\bar{t}$	$43.1 \pm 0.7$	$37.2 \pm 0.7$
di-boson production	$57.5 \pm 1.0$	$45.7 \pm 0.8$
multijet events	$55.9 \pm 15.5$	$46.1 \pm 14.8$
single top processes	$6.6 \pm 0.5$	$5.8 \pm 0.4$
other	$17.9 \pm 2.3$	$16.9 \pm 2.2$
total background	$2002 \pm 26$	$1971 \pm 26$
data 2011	2155	2124
$\phi(120, 20) \rightarrow \tau^+\tau^-$	$132.6 \pm 3.0$	$132.6 \pm 3.0$

**Table 6.7:** Expected and observed number of events after the two final selection criteria. The simulated background components and the signal expectation are normalised to an integrated luminosity of  $L = 1.06 \text{ fb}^{-1}$ . The multijet background is estimated from data. The signal contribution is shown for the parameter point  $M_A = 120 \text{ GeV}$  and  $\tan\beta = 20$  in the  $m_h^{\text{max}}$  scenario. Only statistical uncertainties are given.

region	$N^{\text{signal}}$	$N^{\text{EW}}$	$N^{\text{data}}$
same sign, isolated ( $B$ )	$0.3 \pm 0.1$	$18.0 \pm 3.2$	41
opposite sign, anti-isolated ( $C$ )	$\leq 0.1$	$5.6 \pm 1.1$	8399
same sign, anti-isolated ( $D$ )	$\leq 0.1$	$2.6 \pm 0.4$	4146

**Table 6.8:** Expected and observed numbers of events in the three control regions. The simulations  $N_i^{\text{EW}}$  and  $N_i^{\text{signal}}$  are normalised to an integrated luminosity of  $L = 1.06 \text{ fb}^{-1}$ . The signal contribution is shown for the parameter point  $M_A = 120 \text{ GeV}$  and  $\tan\beta = 20$  in the  $m_h^{\text{max}}$  scenario. Only statistical uncertainties are given.

contributions is measured in a dedicated control region.

### 6.7.1 Estimation of the Multijet Background

Owing to the larger statistics in the 2011 data sample, the ABCD method described in Section 5.6.1 can be applied after the full selection. The numbers needed for the final calculation are summarised in Table 6.8. The anti-isolated regions are dominated by multijet events and the signal contribution is negligible. In the same-sign, isolated region, one has to correct for the electroweak contributions. The possible signal contribution is about 2% of the electroweak contributions and is treated as additional systematic uncertainty on  $N_B^{\text{EW}}$ . Finally, one obtains

$$R_{\text{OS/SS}} = \frac{N_C^{\text{data}}}{N_D^{\text{data}}} = 2.03 \pm 0.04 \text{ (stat.)}, \quad (6.24)$$

$$N_A^{\text{QCD}} = (N_B^{\text{data}} - N_B^{\text{EW}}) \cdot R_{\text{OS/SS}} = 46.6 \pm 14.5 \text{ (stat.)}. \quad (6.25)$$

### 6.7.2 Estimation of the Top Quark and Di-boson Background

A control region for the  $t\bar{t}$ , single top and di-boson processes is defined by the baseline selection steps and the following two requirements:

1.  $\text{SumPtMET} \geq 150 \text{ GeV}$ ,
2.  $\text{SumCosDPhi} \leq -0.25$ .

The event yields expected from simulated samples are given in Table 6.9. One concludes that this control region is dominated by  $t\bar{t}$ , single top and di-boson events while contribution from other processes are of the order of 0.7% and, therefore, can be neglected. In order to derive the expected number of  $t\bar{t}$ , single top and di-boson events in the signal region, one needs an extrapolation factor  $\tau$  which is derived from the simulated samples. Let  $n_{\text{top,db}}^{\text{control}}$  denote the expectation of all three background processes in the control region while  $n_{\text{top,db}}$  denotes the expectation from  $t\bar{t}$ , single top and di-boson processes in the

process	expectation
$\gamma^*/Z \rightarrow \tau^+\tau^-$	$\leq 0.1$
$t\bar{t}$	$479.6 \pm 2.4$
di-boson production	$94.9 \pm 1.2$
multijet events	$1.6 \pm 6.2$
single top processes	$52.0 \pm 1.3$
other	$2.3 \pm 1.0$
total background	$630.4 \pm 7.0$
data 2011	644
$\phi(120, 20) \rightarrow \tau^+\tau^-$	$0.2 \pm 0.2$

**Table 6.9:** Expected and observed event yields in the  $t\bar{t}$ , single top and di-boson control region. The simulated background components are normalised to an integrated luminosity of  $L = 1.06 \text{ fb}^{-1}$ . The multijet background is estimated from data. The signal contribution is shown for the parameter point  $M_A = 120 \text{ GeV}$  and  $\tan\beta = 20$  in the  $m_h^{\text{max}}$  scenario. Only statistical uncertainties are given.

signal region. According to the numbers in Tables 6.7 and 6.9 the extrapolation factor is given by

$$\tau = \frac{n_{\text{top,db}}}{n_{\text{top,db}}^{\text{control}}} = 0.1412 \pm 0.002 \text{ (stat.)}. \quad (6.26)$$

## 6.8 Statistical Procedure

The goal of this thesis is to make a statement on the existence of neutral resonances decaying into a pair of tau leptons in the context of the MSSM. For this purpose, the agreement between the SM prediction (*background only* model) and the observed data is checked. In the case, an incompatibility is found which exceeds a certain confidence level, a discovery of a new phenomenon is claimed. Contrarily, in the absence of a significant deviation upper limits on the cross section of hypothetical new processes are derived. The following statistical analysis relies on fundamental concepts of statistics like significance,  $p$ -values and hypothesis testing which are explained in standard text books (e.g. [88]).

After the event selection is fixed, there are several possibilities how one can extract information on the agreement between the SM prediction and the observed data. The most simple way is the comparison of the observed number of data events with the background yield expected. This procedure is referred to as *event counting* and is not sensitive to the distribution of individual variables. In order to increase the sensitivity, one can use information on the distributions of individual variables by fitting them to the SM expectations (*template fit*). Both approaches are investigated in this work by using the profile likelihood method which is reviewed briefly in the next section.

### 6.8.1 Review of the Profile Likelihood Method

The primary goal of statistical inference is the derivation of model parameters from experimental observations. The model is a function of one or more parameters and has to be flexible enough that it can be considered a true<sup>5</sup> description of nature for one point in the parameter space. The parameters can be classified into two categories: the parameter of interest<sup>6</sup>  $\mu$  and the set of *nuisance* parameters  $\vec{\theta}$  which comprise all parameters one is not directly interested in. Let  $\vec{x}$  denote the ensemble of experimental observations which can be described by the model. A key ingredient for the profile likelihood method [89] is the likelihood function  $\mathcal{L}(\vec{x}|\mu, \vec{\theta})$  which states the probability to observe the data  $\vec{x}$  under the assumption of the model parameters  $\mu$  and  $\vec{\theta}$ . One can then define the likelihood ratio

$$\lambda(\mu) = \frac{\mathcal{L}(\vec{x}|\mu, \hat{\vec{\theta}}(\mu))}{\mathcal{L}(\vec{x}|\hat{\mu}, \hat{\vec{\theta}})} \quad (6.27)$$

with

- $\vec{x}$  being the observed data,
- $\hat{\mu}$  and  $\hat{\vec{\theta}}$  being the maximum likelihood estimators (MLEs) which maximise the likelihood function with respect to the observed data,
- and  $\hat{\vec{\theta}}$  is the conditional MLE which maximises the likelihood function with respect to the observed data  $\vec{x}$  and the hypothesised value of  $\mu$ .

While the denominator is entirely fixed by the observed data, the nominator depends on the hypothesised value of  $\mu$ . The conditional MLE is a function of  $\mu$  and so is the likelihood ratio  $\lambda$  which can take values within  $0 \leq \lambda(\mu) \leq 1$ . A likelihood ratio close to unity represents a good agreement between the observed data and the hypothesised value of  $\mu$  whereas smaller values corresponds to increasing disagreement. It is convenient to define

$$t_\mu = -2 \ln \lambda(\mu) \quad (6.28)$$

which is again a function of the hypothesised value of  $\mu$ . Emerging from the properties of  $\lambda(\mu)$  it follows that  $0 \leq t_\mu$  and  $t_\mu$  close to zero represents a good agreement of the hypothesised parameter of interest with the observed data while larger values constitute increasing incompatibility. Given an observation  $t_\mu$  for an hypothesised value of  $\mu$  the corresponding  $p$ -value is defined as the cumulative probability of all possible observations whose compatibility is worse. Since a worse compatibility is expressed by larger values

---

<sup>5</sup>True in the sense that it describes the problem under investigation with sufficient precision.

<sup>6</sup>The parameters of interest can, of course, be a set of parameters. In this case,  $\mu$  should be replaced by  $\vec{\mu}$ .

of  $t'_\mu > t_\mu$  the  $p$ -value for the value of  $\mu$  under consideration is given by<sup>7</sup>

$$p_\mu = \int_{t_\mu}^{\infty} f(t'_\mu | \mu, \hat{\hat{\theta}}(\mu)) dt'_\mu \quad (6.29)$$

with  $f(t'_\mu | \mu', \hat{\hat{\theta}}(\mu')) \equiv f(t'_\mu | \mu')$  (*sampling distribution*) being the probability to observe the value  $t'_\mu$  assuming the true model parameters are  $\mu'$  and  $\hat{\hat{\theta}}(\mu')$ . According to WILKS' theorem [90] the sampling distribution  $f(t'_\mu | \mu')$  becomes a  $\chi^2$  distribution with one degree of freedom for the special case  $\mu = \mu'$  under certain regularity conditions. For the following, the validity of WILKS' theorem is assumed and the usage of asymptotic formulae is justified by the comparison to sampling distributions generated in toy experiments (cf. Figure 6.12).

### Definition of Appropriate Test Statistics

As it is explained below,  $\mu$  is interpreted as a *signal strength* parameter with  $\mu = 0$  representing the background-only model and  $\mu = 1$  corresponds to the nominal signal model. Since the contributions of new physics processes are assumed to be non-negative,  $\mu$  is bounded from below by physical arguments. Therefore, a modified version of Equation (6.28) is used to define a test statistic for a positive signal according to

$$\tilde{\lambda}(\mu) = \begin{cases} \frac{\mathcal{L}(\vec{x} | \mu, \hat{\hat{\theta}}(\mu))}{\mathcal{L}(\vec{x} | \hat{\mu}, \hat{\hat{\theta}})} & , \hat{\mu} > 0 \\ \frac{\mathcal{L}(\vec{x} | \mu, \hat{\hat{\theta}}(\mu))}{\mathcal{L}(\vec{x} | 0, \hat{\hat{\theta}}(0))} & , \hat{\mu} \leq 0 \end{cases} , \quad (6.30)$$

$$\tilde{t}_\mu = -2 \ln \tilde{\lambda}(\mu) . \quad (6.31)$$

A special case is the test of the background-only hypothesis which is

$$q_0 \equiv \tilde{t}_0 = \begin{cases} -2 \ln \lambda(0) & , \hat{\mu} > 0 \\ 0 & , \hat{\mu} \leq 0 \end{cases} \quad (6.32)$$

The sampling distribution  $f(q_0 | 0)$  is found to be half the  $\chi^2$  distribution with one degree of freedom for  $q_0 > 0$  [89]. Hence, the following two relations hold true

$$p_0 = 1 - \Phi(\sqrt{q_0}) , \quad (6.33)$$

$$Z_0 = \Phi^{-1}(1 - p_0) = \sqrt{q_0} \quad (6.34)$$

with  $\Phi(x)$  being the cumulative distribution function of the normal distribution. The value  $Z_0$  is referred to as *discovery significance* expressing the (in)compatibility of the background-only model with the observed data.

<sup>7</sup>As Equation (6.29) condenses a lot of information, it should be highlighted that both  $t_\mu$  and the conditional MLE  $\hat{\hat{\theta}}(\mu)$  depend on the hypothesised value of  $\mu$  as well as on the observed data. Additionally, all  $\mu$ 's appearing in this equation always take the same value.

For the purpose of upper limit setting, yet another test statistic is defined as

$$q_\mu = \begin{cases} -2 \ln \lambda(\mu) & , \mu > \hat{\mu} \\ 0 & , \mu \leq \hat{\mu} \end{cases} . \quad (6.35)$$

Hypothesised values of  $\mu \leq \hat{\mu}$  are not considered as representing less compatibility with the observed data when setting an upper limit on  $\mu$ . Hence, these values are not part of the rejection region of the hypothesis test and  $q_\mu$  is set to zero for  $\mu \leq \hat{\mu}$ . Again, it can be shown that  $f(q_\mu|\mu)$  is half the  $\chi^2$  distribution [89] which leads to

$$p_\mu = 1 - \Phi(\sqrt{q_\mu}) . \quad (6.36)$$

An upper limit  $\mu_{\text{up}}$  on  $\mu$  with a confidence level  $\alpha$  is then found by solving

$$1 - \alpha = 1 - \Phi(\sqrt{q_{\mu_{\text{up}}}}) \quad (6.37)$$

$$\Rightarrow q_{\mu_{\text{up}}} = (\Phi^{-1}(\alpha))^2 . \quad (6.38)$$

### Expected Discovery Significance

In order to estimate the median discovery significance for a hypothesised signal strength  $\mu$ , one needs the sampling distribution  $f(q_0|\mu)$  from which one obtains the median value  $\text{med}[q_0|\mu]$ . The median discovery significance is then given by  $\text{med}[Z_0|\mu] = \sqrt{\text{med}[q_0|\mu]}$ . As one is only interested in the median of the distribution  $f(q_0|\mu)$ , one does not need to generate the whole distribution using MC techniques. Instead one can use the ASIMOV data set  $\vec{x}_A$  [89], that is the set of observables which maximises the likelihood function  $\mathcal{L}(\vec{x}|\mu, \vec{\theta})$  for the given value of  $\mu$ . In practice,  $\vec{x}_A = \vec{x}_A(\mu)$  are the expectation values for the observables and can be estimated using simulated samples. The median value of  $q_0$  is then found by evaluating Equation (6.32) with the ASIMOV data set which leads to<sup>8</sup>

$$\text{med}[q_0|\mu] = q_{0,A} , \quad (6.39)$$

$$\text{med}[Z_0|\mu] = \sqrt{q_{0,A}} . \quad (6.40)$$

### Expected Exclusion Limit

For stating an expected upper limit, one needs the distributions  $f(q_\mu|0)$ . At a confidence level  $\alpha$  all values of  $\mu$  with

$$\text{med}[p_\mu|0] \leq 1 - \alpha \quad (6.41)$$

are excluded and the upper limit is given by

$$\mu_{\text{up}} = \min \{ \mu | \text{med}[p_\mu|0] \leq 1 - \alpha \} . \quad (6.42)$$

As one is also interested in the  $\pm 1\sigma$  and  $\pm 2\sigma$  error bands on the expected upper limit, one can not rely on the ASIMOV data set but rather needs to generate toy data for

---

<sup>8</sup>It is important to notice that the right hand sides depend on the hypothesised value of  $\mu$  to the extent that the ASIMOV data set is a function of  $\mu$ .

the background-only model. From these simulations one can construct the distribution for  $\mu_{\text{up}}$  from which one can read off the median expected upper limit as well as the  $\pm 1\sigma$  and  $\pm 2\sigma$  error bands. A technical subtlety is the treatment of the nuisance parameters during the toy data generation. It is recommended to allow these parameters to float in order to ensure the validity of the asymptotic formula given above.

### 6.8.2 Event Counting Analysis

For the event counting analysis the number<sup>9</sup> of data events  $N_{\text{signal}}^{\text{data}}$  observed in the signal region is assumed to be Poisson distributed with a mean value given by the total number of expected events  $n_{\text{exp}}$ ,

$$P(N_{\text{signal}}^{\text{data}}|n_{\text{exp}}) = \frac{n_{\text{exp}}^{N_{\text{signal}}^{\text{data}}}}{N_{\text{signal}}^{\text{data}}!} e^{-n_{\text{exp}}} . \quad (6.43)$$

The total expectation is the sum of all background and the signal contribution:

$$n_{\text{exp}} = n_{\text{sig}} + n_{Z\tau\tau} + n_{Z\mu\mu} + n_{\text{QCD}} + n_{\text{top,db}} \quad (6.44)$$

with the expected number of signal events  $n_{\text{sig}}$ ,  $\gamma^*/Z \rightarrow \tau^+\tau^-$  events  $n_{Z\tau\tau}$ , multijet events  $n_{\text{QCD}}$ , the sum of  $t\bar{t}$ , single top and di-boson events  $n_{\text{top,db}}$  and  $\gamma^*/Z \rightarrow \mu^+\mu^-$  events  $n_{Z\mu\mu}$ . Contributions from the remaining processes  $W \rightarrow \ell\nu_\ell$  and  $\gamma^*/Z \rightarrow e^+e^-$  are found to be negligible ( $\leq 1$ ). The expected event yields for the individual terms are either derived from simulated samples or inferred from an auxiliary measurement with data. In order to account correctly for correlation among different systematic uncertainties, the event yields estimated from MC simulation are written as

$$n_{Z\tau\tau} = n_{Z\tau\tau}^{\text{MC}} \cdot (1 + \delta L) \cdot (1 + \delta\sigma_Z) \cdot (1 + \delta_{Z\tau\tau}) \quad (6.45)$$

$$n_{Z\mu\mu} = n_{Z\mu\mu}^{\text{MC}} \cdot (1 + \delta L) \cdot (1 + \delta\sigma_Z) \cdot (1 + \delta_{Z\mu\mu}) \quad (6.46)$$

$$n_{\text{sig}} = \mu \cdot n_{\text{sig}}^{\text{MC}} \cdot (1 + \delta L) \cdot (1 + \delta\sigma_\phi) \cdot (1 + \delta_{\text{sig}}) \quad (6.47)$$

with ( $i = Z\tau\tau, Z\mu\mu, \text{sig}$ ):

- $n_i^{\text{MC}}$  is the expected number of events for process  $i$  in the signal region. These values are fixed from the simulated samples. For the signal process this number depends on the parameter  $M_A$  under investigation.
- $\delta L$  is the relative change in the integrated luminosity due to systematic effects which is correlated across all expectations derived from MC simulations.
- $\delta\sigma_Z$  is the relative change in the production cross section for the  $\gamma^*/Z \rightarrow \ell^+\ell^-$  processes due to systematic effects and, therefore, correlated for  $n_{Z\tau\tau}$  and  $n_{Z\mu\mu}$ .

---

<sup>9</sup>In order to better distinguish between parameters of the model and measured numbers of events, the latter are denoted by a capital  $N$ .

- $\delta_\phi$  is the relative change in the production cross section for the signal process due to systematic effects.
- $\delta_i$  is the relative change in the expected event yield for process  $i$  due to systematic effects and is assumed to be uncorrelated to all other contributions.
- $\mu$  is the signal strength parameter and is the parameter of interest in this model. The value  $\mu = 0$  corresponds to the background-only model while  $\mu = 1$  corresponds to the nominal signal model with the parameter  $M_A$  under investigation and  $\tan\beta = 20$ .

The contribution from multijet events is estimated according to the method described in Section 6.7.1. Therefore,  $n_{\text{QCD}}$  is given by

$$n_{\text{QCD}} = (n_{\text{SS}} - n_{\text{SS,EW}}) \cdot R_{\text{OS/SS}} \quad (6.48)$$

with  $n_{\text{SS}}$  being the *true* number of events in the same-sign isolated control region<sup>10</sup> while  $n_{\text{SS,EW}}$  is the contribution from electroweak processes in this control region. The latter is estimated from simulated samples and also affected by the cross section and luminosity uncertainties. However, these uncertainties are smaller than the statistical uncertainty arising from the limited number of simulated events in the control region (cf. Table 6.10). For this reason, correlations are not taken into account for this term.

The total contribution arising from  $t\bar{t}$ , single top and di-boson events is constrained by an auxiliary measurement as explained in Section 6.7.2. Hence, one finds

$$n_{\text{top,db}} = n_{\text{top,db}}^{\text{control}} \cdot \tau \quad (6.49)$$

with  $\tau$  being obtained from simulated samples.

The nuisance parameters in the model have to be constrained by additional auxiliary measurements or by adding a prior probability distribution for these parameters. The parameter  $n_{\text{SS}}$  is constrained by measurement of the number of data events in the same sign, isolated control region while  $n_{\text{top,db}}^{\text{control}}$  is constrained by the observed number of data events in the  $t\bar{t}$ , single top and di-boson control region. In both cases the observed number of data events is assumed to be Poisson distributed leading to the following two constraints:

$$P(N_{\text{SS}}^{\text{data}} | n_{\text{SS}}) = \frac{n_{\text{SS}}^{N_{\text{SS}}^{\text{data}}}}{N_{\text{SS}}^{\text{data}}!} e^{-n_{\text{SS}}}, \quad (6.50)$$

$$P(N_{\text{top,db}}^{\text{data}} | n_{\text{top,db}}^{\text{control}}) = \frac{(n_{\text{top,db}}^{\text{control}})^{N_{\text{top,db}}^{\text{data}}}}{N_{\text{top,db}}^{\text{data}}!} e^{-n_{\text{top,db}}^{\text{control}}}. \quad (6.51)$$

The nuisance parameters related to systematic effects  $\delta y$  are constrained by prior probability distributions which are assumed to be Gaussian<sup>11</sup>

$$P(\delta y) = G(\delta y; 0, \Delta y) \quad (6.52)$$

<sup>10</sup> $n_{\text{SS}}$  is not the observed number of data events in this control region.

<sup>11</sup> $G(y; a, b)$  represents a normal distribution of  $y$  with a mean  $a$  and a standard deviation  $b$ .



with  $\Delta y$  being the relative systematic uncertainties related to the quantity  $y$ . The prior probability distribution of the remaining free parameters are modelled by normal distributions with a mean value which is the central value determined from the simulated samples and a variance which includes statistical and systematic uncertainties on the central value:

$$P(n_{\text{SS},\text{EW}}) = G(n_{\text{SS},\text{EW}}; \bar{n}_{\text{SS},\text{EW}}, \Delta n_{\text{SS},\text{EW}}), \quad (6.53)$$

$$P(R_{\text{OS}/\text{SS}}) = G(R_{\text{OS}/\text{SS}}; \bar{R}_{\text{OS}/\text{SS}}, \Delta R_{\text{OS}/\text{SS}}), \quad (6.54)$$

$$P(\tau) = G(\tau; \bar{\tau}, \Delta\tau). \quad (6.55)$$

$$(6.56)$$

Finally, the likelihood function for the event counting approach is given by

$$\begin{aligned} \mathcal{L}(\vec{x}|\mu, \vec{\theta}) &= P(N_{\text{signal}}^{\text{data}}|n_{\text{exp}}) \times P(N_{\text{SS}}^{\text{data}}|n_{\text{SS}}) \times P(N_{\text{top,db}}^{\text{data}}|n_{\text{top,db}}^{\text{control}}) \\ &\times G(n_{\text{SS},\text{EW}}; \bar{n}_{\text{SS},\text{EW}}, \Delta n_{\text{SS},\text{EW}}) \times G(R_{\text{OS}/\text{SS}}; \bar{R}_{\text{OS}/\text{SS}}, \Delta R_{\text{OS}/\text{SS}}) \\ &\times G(\tau; \bar{\tau}, \Delta\tau) \times G(\delta L; 0, \Delta L) \times G(\delta\sigma_Z; 0, \Delta\sigma_Z) \\ &\times G(\delta\sigma_\phi; 0, \Delta\sigma_\phi) \times G(\delta_{Z\tau\tau}; 0, \Delta_{Z\tau\tau}) \times G(\delta_{Z\mu\mu}; 0, \Delta_{Z\mu\mu}) \\ &\times G(\delta_{\text{sig}}; 0, \Delta_{\text{sig}}) \end{aligned} \quad (6.57)$$

with the experimental observations

$$\vec{x} = \{N_{\text{signal}}^{\text{data}}, N_{\text{SS}}^{\text{data}}, N_{\text{top,db}}^{\text{data}}\} \quad (6.58)$$

and the set of nuisance parameters

$$\vec{\theta} = \{n_{\text{SS}}, n_{\text{top,db}}^{\text{control}}, n_{\text{SS},\text{EW}}, R_{\text{OS}/\text{SS}}, \tau, \delta L, \delta\sigma_Z, \delta\sigma_\phi, \delta_{Z\tau\tau}, \delta_{Z\mu\mu}, \delta_{\text{sig}}\}. \quad (6.59)$$

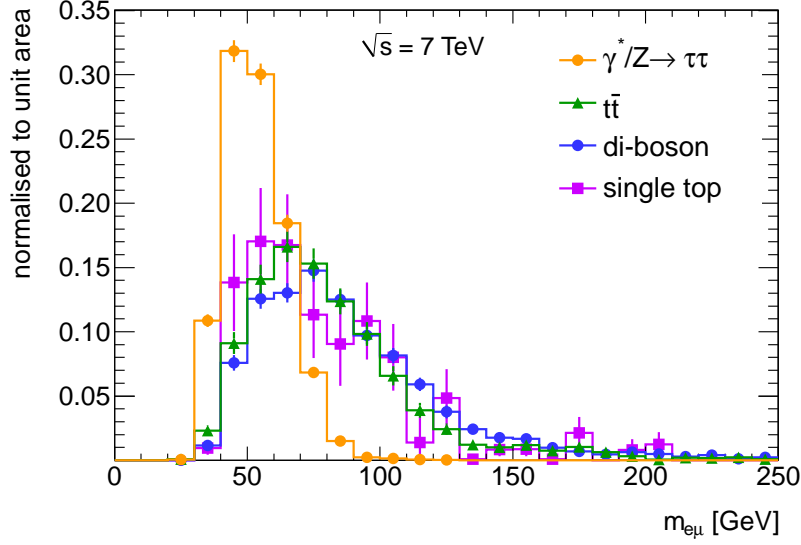
### 6.8.3 Template Fit of the Visible Mass Spectrum

Instead of restricting the analysis to the comparison of event yields, one can benefit from more information by using the distribution of variables which are sensitive to the signal process. A variable is considered sensitive if the shape expected for the signal process differs from those of the background processes. As already mentioned in Section 4.6, the most prominent difference between the signal process and the dominant  $\gamma^*/Z \rightarrow \tau^+\tau^-$  background is the invariant mass of the di-tau system. Therefore, a template fit to a mass distribution observed in data can be used to derive information on the signal cross section.

The mass definitions given in Section 4.6 are compared with regard to their feasibility in a template fit. Since the dominant background arises from  $\gamma^+/Z \rightarrow \tau^+\tau^-$  events, the separation between these events and signal<sup>12</sup> events is examined for the different mass definitions. For this purpose, a figure-of-merit is chosen as the difference in the mean values  $\mu_{Z/\phi}$  of the mass distributions normalised to their variances  $\sigma_{Z/\phi}^2$ ,

$$\text{sep} = \frac{\mu_\phi - \mu_Z}{\sqrt{\sigma_\phi^2 + \sigma_Z^2}}. \quad (6.60)$$

<sup>12</sup>Here, the reference signal process for  $M_A = 120$  GeV and  $\tan\beta = 20$  is used.



**Figure 6.9:** Normalised visible mass distribution for  $\gamma^*/Z \rightarrow \tau^+\tau^-$  (orange circles),  $t\bar{t}$  (green triangles), di-boson (blue circles) and single top (violet squares) events after the requirement of  $n_{\text{jets}} \leq 3$ .

One finds that the collinear approximation performs worst with  $\text{sep} = 0.06$ , the effective mass definition results in a separation of 0.35 while the visible mass yields the best result with  $\text{sep} = 0.63$ . Hence, an un-binned, extended maximum likelihood fit of the visible mass distribution is investigated.

The fit is performed after the requirement of  $n_{\text{jets}} \leq 3$  and the last criterion on the visible mass window is dropped. The remaining background contributions and the signal expectation at this point in the selection are summarised in Table 6.7.

The shapes of the visible mass distribution for the  $\gamma^*/Z \rightarrow \tau^+\tau^-$ ,  $t\bar{t}$ , single top, di-boson and signal processes are taken from simulated samples while the shape for the multijet background is derived from the opposite-sign, anti-isolated control region. The contribution of the remaining background processes arises mainly from  $\gamma^*/Z \rightarrow \mu^+\mu^-$  events and its shape is taken from simulated samples as well.

In order to reduce the number of free parameters, components with similar shapes are combined. Figure 6.9 shows the normalised visible mass distribution for important background components. One observes that the shapes for the  $t\bar{t}$ , single top and di-boson process are very similar and, thus, are merged into one template. Due to the limited statistics the contribution from  $\gamma^*/Z \rightarrow \mu^+\mu^-$  is fitted with a Gaussian. The visible mass shape for multijet events is fitted with a LANDAU distribution which has two parameters: a mode  $m$  and a width  $\sigma$ . For the remaining processes a log-normal distribution which has two shape parameters and takes the general form

$$\text{LogNormal}(x; \alpha, \beta) = \frac{1}{\sqrt{2\pi} \cdot \ln \beta \cdot x} \cdot \exp\left(-\frac{\ln^2 \frac{x}{\alpha}}{2 \ln^2 \beta}\right) \quad (6.61)$$

is used to fit the visible mass distribution. In Figure 6.10 the resulting templates for the

different background components and the signal with two different mass hypotheses are displayed. Templates for the signal process with other mass hypotheses can be found in Appendix D.6. The resulting visible mass distribution is given by

$$F(m_{e\mu}; \{n_i, \vec{\alpha}_i\}) = \sum_i n_i \cdot f_i(m_{e\mu}; \vec{\alpha}_i) \quad (6.62)$$

with  $n_i$  being the number of events of the component  $i$  and  $f_i(m_{e\mu}; \vec{\alpha}_i)$  being the visible mass shape of the component  $i$  which may depend on a set of shape parameters  $\vec{\alpha}_i$ . The functions  $f_i(m_{e\mu}; \vec{\alpha}_i)$  have to be normalised to unity. Therefore,  $F(m_{e\mu}; \{n_i, \vec{\alpha}_i\})$  is normalised to

$$n_{\text{total}} = \sum_i n_i \equiv \mu \cdot n_{\text{sig}} + n_{Z\tau\tau} + n_{\text{top,db}} + n_{\text{QCD}} + n_{Z\mu\mu} \quad (6.63)$$

where the signal strength parameter  $\mu$  is introduced. In an extended maximum likelihood fit, this normalisation is not fixed to the number of observed events but it is allowed to float. The number of observed events is assumed to be Poisson distributed around the expectation value  $n_{\text{total}}$  and a corresponding constraint is added to the likelihood function. Assuming the observation of  $k$  data events in the signal region with visible mass values  $\{m_j\}, j = 1 \dots k$  the likelihood function takes the form

$$\mathcal{L}(\text{data}|\mu, \{n_i, \vec{\alpha}_i\}) = \frac{n_{\text{total}}^k}{k!} e^{-n_{\text{total}}} \times \prod_{j=1 \dots k} \left( \frac{F(m_j; \{n_i, \vec{\alpha}_i\})}{n_{\text{total}}} \right). \quad (6.64)$$

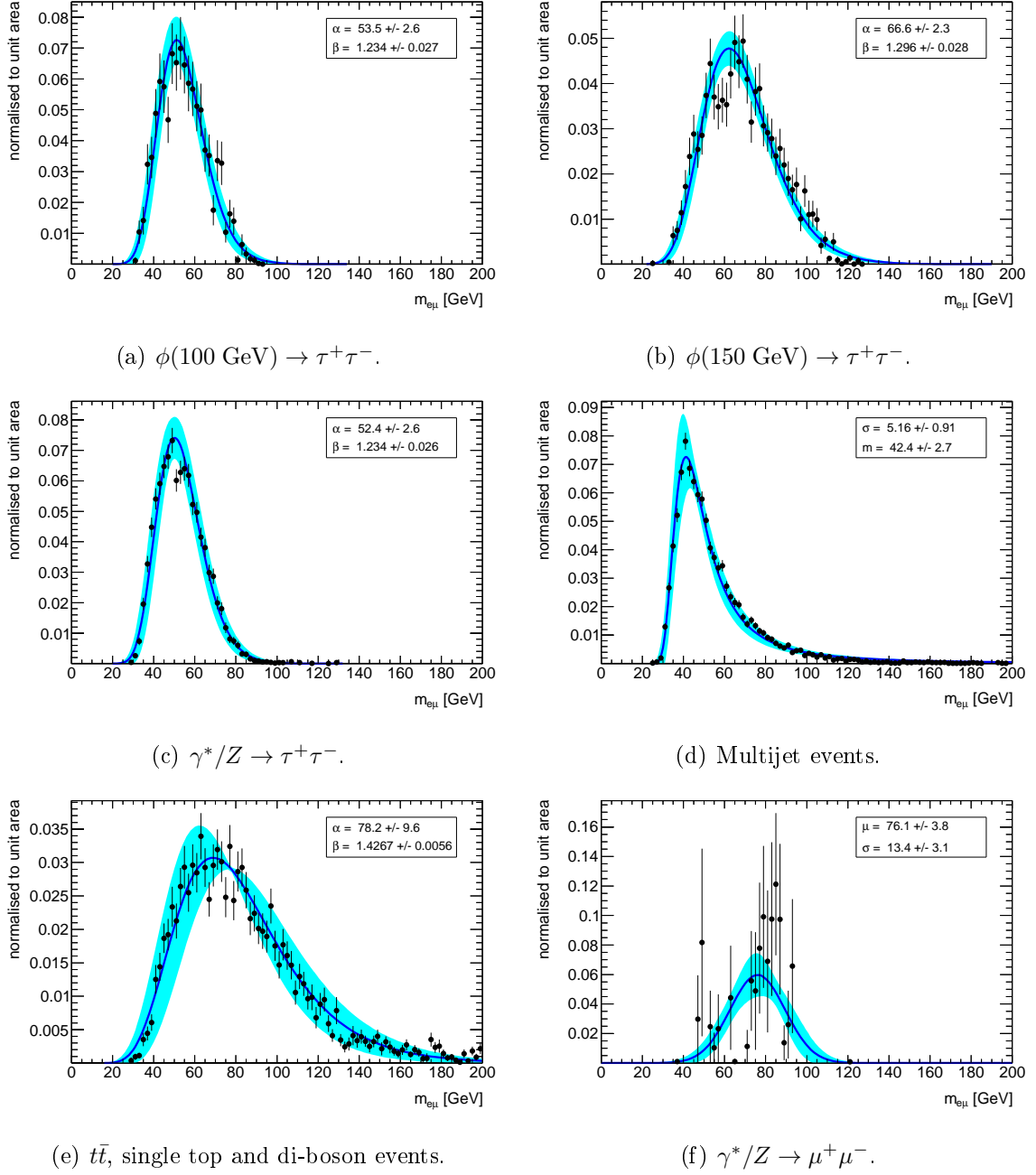
Because the shape parameters and the normalisations are allowed to float during the fit, a template fit is less affected by a possible mis-modelling<sup>13</sup> in the simulation. Unfortunately, strong negative correlation between the normalisation of different components may occur if these components have similar shapes. As a consequence, the fit becomes unstable and the obtained results are not reliable. The templates shown in Figure 6.10 suggests such correlations between the number of  $\gamma^*/Z \rightarrow \tau^+\tau^-$  and signal events, especially for small hypothesised Higgs boson masses.

The stability of the fit is tested by generating toy data using Equation (6.64), with the normalisations set to the values given in Table 6.7 and the shape parameters fixed. Afterwards, the pseudo-data is fitted and the pull for the number of signal events is plotted. For a fitted value  $y_{\text{fit}}$  the pull  $u$  is defined as

$$u = \frac{y_{\text{true}} - y_{\text{fit}}}{\sigma_{\text{fit}}} \quad (6.65)$$

with  $y_{\text{true}}$  being the parameter used during the generation process and  $\sigma_{\text{fit}}$  being the uncertainty on the fitted value. The distribution of the pulls is expected to be a normal distribution centred at zero with unit variance.

<sup>13</sup>The correction is, of course, limited to the case that at least the functional dependence is correctly modelled.



**Figure 6.10:** Templates for the visible mass distribution for signal process with two different mass hypotheses (top) and the background components. The black dots represent the values obtained from simulated samples or control regions. The blue lines correspond to the extracted shapes with their uncertainty indicated by the cyan area.

Toy data is generated for the reference signal process and  $\mu = 1$  and the resulting pull distribution for the number of fitted signal events is shown in Figure 6.11(a). The correlation between the number of fitted signal and  $\gamma^*/Z \rightarrow \tau^+\tau^-$  events is displayed in Figure 6.11(b). The similar shapes between the dominant background and the signal process with  $m_\phi = 120$  GeV causes most of the signal events being mistakenly assigned to the  $\gamma^*/Z \rightarrow \tau^+\tau^-$  background. Moreover, the strong correlation results in a very large uncertainty on the fitted value which leads to the peak at zero in the pull distribution. In order to increase the stability of the fit, the shape parameters are fixed and the normalisations of the background components are constrained by additional Gaussian terms in the likelihood function. The mean for the Gaussian constraints is set to the expectation derived from the simulation and the width is set to the total uncertainty. With this modified likelihood function, the whole procedure is repeated yielding the pull distribution in Figure 6.11(c) and the remaining correlation is shown in Figure 6.11(d). One observes that the behaviour of the fit is greatly improved by adding the constraints. Admittedly, the constraint template fit lost its flexibility and is only allowed to vary the normalisations of the background templates within a limited range. Hence, the template fit becomes almost equivalent to the event counting approach. Due to the fact that still  $\approx 5\%$  of the generated toy data lead to unstable fit results, the template fit is not applied in this work.

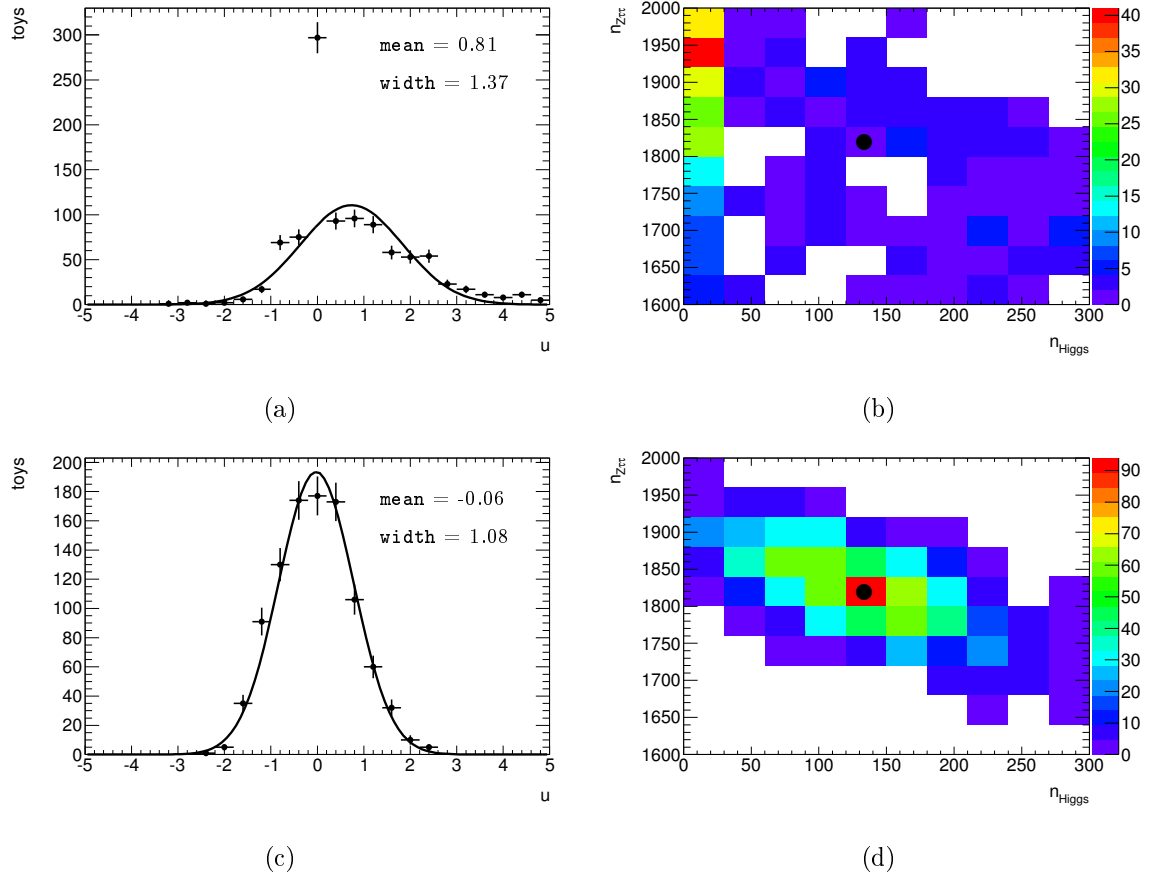
## 6.9 Evaluation of Systematic Uncertainties

For the event counting analysis, one needs the systematic uncertainties on the expectation of the individual background components and the signal process as well as the systematic uncertainties on the extrapolation factors  $R_{\text{OS/SS}}$  and  $\tau$ . Additionally, systematic uncertainties on the luminosity measurement and on the theoretical cross sections used for the normalisation of the simulated samples are required. Different sources of systematic uncertainties are discussed in the remainder of this section. In order to quantify the systematic uncertainties arising from the individual effects, the prescription outlined in Section 5.8 is applied unless otherwise stated. The resulting systematic uncertainties are summarised in Table 6.10.

### 6.9.1 Theoretical Uncertainties

The relative uncertainty on the  $\gamma^*/Z$  and  $W$  boson production cross sections is found to be 5% [54] including uncertainties on the strong coupling constant, the PDF set used and variations of the renormalisation and factorisation scales.

The relative theoretical uncertainty on the production cross section for neutral MSSM Higgs bosons in the  $m_h^{\text{max}}$  scenario are given by 25%-30% for the gluon-fusion process while they can reach up to 40% for the  $b$ -associated production [91]. In this thesis an overall uncertainty on the Higgs boson production cross section of 30% is used.



**Figure 6.11:** Pull distribution for the fitted number of signal events (left) and correlation between the fitted numbers of signal and  $\gamma^*/Z \rightarrow \tau^+\tau^-$  events (right) for the free (top) and constrained (bottom) template fit. The black dots in the two-dimensional correlation plots mark the values used for generating the toy data.

## 6.9.2 Experimental Uncertainties

### Luminosity Measurement

The relative uncertainty of the luminosity measurement is given by 3.4% [74] which is derived from the 2010 data set. An update for the 2011 data set was not available by the end of this work.

### Efficiency Corrections

The correction factors for the trigger, reconstruction and identification efficiencies are given in bins of the  $p_T$ ,  $\eta$  and/or  $\phi$  of the lepton candidates. The uncertainty on these correction factors arises mainly from the limited statistics in the data samples which are used to compare the observed performance with the expectation obtained from simulation. Since statistical uncertainties are uncorrelated across different bins, the correction factors are varied independently of each other. The following procedure is applied to derive the systematic uncertainty related to the correction factors:

1. In each bin the correction factor is drawn from a Gaussian with the mean value being the central value and the width being the total uncertainty on the correction factor in this bin.
2. The analysis is performed with these modified correction factors and all quantities of interest are saved.
3. Repeating steps 1) and 2) yields distributions for all quantities of interest. The variances divided by the means of these distributions are quoted as relative systematic uncertainties.

The procedure above is applied separately to the trigger efficiency correction and the electron related corrections. Since the uncertainties on the muon related efficiency corrections are  $\leq 0.5\%$ , these are negligible compared to the other corrections.

### Energy/Momentum Corrections

As explained in Section 6.4.2 the energy/momentum of the reconstructed lepton candidates is varied and the resulting shift is propagated back to the reconstructed  $\vec{E}_{T,\text{miss}}$  as well. Since the variation itself is a statistical procedure, an iteration of the analysis will yield varying results. The analysis is performed  $\mathcal{O}(100)$  times to obtain the distribution of the quantities of interest. The variances of the distributions obtained divided by their mean values is taken as relative systematic uncertainty.

### Jet Energy Scale Uncertainty

The uncertainty on the jet energy calibration affects the  $\vec{E}_{T,\text{miss}}$  measurement and, consequently, the result of this analysis. Additionally, the number of reconstructed jets

source	$n_{Z\tau\tau}^{\text{MC}}$	$n_{Z\mu\mu}^{\text{MC}}$	$n_{\text{sig}}^{\text{MC}}$	$n_{\text{SS,EW}}$	$\tau$
trigger efficiency	0.1	0.2	$\leq 0.1$	0.2	$\leq 0.1$
electron related efficiencies	0.6	4.7	0.5	4.9	0.3
electron energy resolution	0.2	2.7	0.4	2.3	0.3
muon momentum resolution	0.1	1.8	0.3	1.1	0.2
jet energy scale	0.2	9.3	0.6	11.5	1.4
total	0.5	10.9	0.9	12.8	1.5
MC statistic	1.2	13.0	2.3	17.8	1.4
theory	5.0	5.0	30.0	5.0	–
luminosity	3.4	3.4	3.4	3.4	–

**Table 6.10:** Relative systematic uncertainties (in percent) on the quantities needed for the event counting analysis. The uncertainties on the signal expectation are given for the parameter point  $M_A = 120$  GeV and  $\tan\beta = 20$ .

depends on the jet momenta and is also subject to mis-calibrated jet energy measurements. From the study of  $Z$  boson production in association with one jet, uncertainties on the jet energy scale calibration are derived which are found to be of the order of 2-3% [92].

The energy of reconstructed jet candidates is varied according to the found uncertainties and the effect on this analysis is derived by looking at the relative change in the quantities of interest.

### Multijet Background Estimation

The multijet background estimation relies on the assumption that the ratio  $R_{\text{OS/SS}}$  is independent of the isolation of the two lepton candidates. This assumption is validated by plotting  $R_{\text{OS/SS}}$  as a function of the calorimeter-based and track-based isolation variables used to classify lepton candidates as isolated. The result is shown in Figure D.7. As no dependence is observed, no systematic uncertainty is assigned to  $R_{\text{OS/SS}}$ .

### 6.9.3 Summary of Systematic Uncertainties

A summary of all systematic uncertainties on all quantities needed for the event counting analysis is shown in Table 6.10. The uncertainty for the signal expectation is given for the parameter point  $M_A = 120$  GeV and  $\tan\beta = 20$ . A slight dependence on the value of  $M_A$  is observed: the total experimental uncertainty (excluding the luminosity uncertainty) decreases from 1.1% for  $M_A = 100$  GeV to 0.8% for  $M_A = 150$  GeV. However, this difference is dwarfed by the theoretical uncertainty and, therefore, a total experimental uncertainty of 1% is applied across the full parameter space. For comparison, the uncertainty arising from the limited statistics in the simulated samples is also shown.



parameter	value	parameter	value	parameter	value
$\bar{n}_{\text{SS,EW}} \pm \Delta n_{\text{SS,EW}} = 18.0 \pm 3.9$		$n_{Z\tau\tau}^{\text{MC}} = 1819.6$		$n_{\text{sig},100}^{\text{MC}} = 166.9$	
$\bar{R}_{\text{OS/SS}} \pm \Delta R_{\text{OS/SS}} = 2.03 \pm 0.04$		$n_{Z\mu\mu}^{\text{MC}} = 15.3$		$n_{\text{sig},110}^{\text{MC}} = 148.2$	
$\bar{\tau} \pm \Delta\tau = 0.141 \pm 0.003$		$\Delta_{Z\tau\tau} = 0.013$		$n_{\text{sig},120}^{\text{MC}} = 132.6$	
$\Delta L = 0.034$		$\Delta_{Z\mu\mu} = 0.17$		$n_{\text{sig},130}^{\text{MC}} = 108.4$	
$\Delta\sigma_Z = 0.05$		$\Delta_{\text{sig}} = 0.025$		$n_{\text{sig},140}^{\text{MC}} = 93.3$	
$\Delta\sigma_\phi = 0.3$				$n_{\text{sig},150}^{\text{MC}} = 75.5$	

**Table 6.11:** Summary of all parameters needed for the event counting analysis.

The comparably large systematic uncertainties on the expectation of  $n_{Z\mu\mu}^{\text{MC}}$  and  $n_{\text{SS,EW}}$  contain significant contributions from limited statistics.

## 6.10 Summary

### 6.10.1 Results

In Table 6.11, the values of all parameters needed for the event counting analysis are summarised. The observed numbers of data events can be read off Tables 6.7, 6.8 and 6.9 which yield:

$$N_{\text{signal}}^{\text{data}} = 2124, \quad (6.66)$$

$$N_{\text{SS}}^{\text{data}} = 41, \quad (6.67)$$

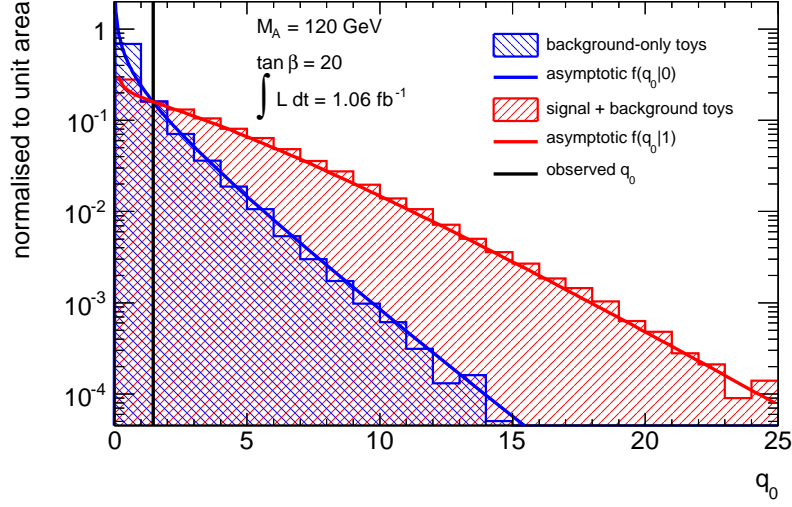
$$N_{\text{top,db}}^{\text{data}} = 644. \quad (6.68)$$

The expected discovery significance is calculated on a grid in the  $M_A \times \tan\beta$  plane for the values  $M_A = 100 - 150$  GeV in steps of 10 GeV and for  $\tan\beta = 5 - 50$  in steps of 5. For this purpose the observed number of data events in the signal region is replaced by the expected number of events including the signal expectation. The signal expectations given in Table 6.11 correspond to  $\tan\beta = 20$ . In order to obtain predictions for other values of  $\tan\beta$ , these numbers are scaled by the ratio of the cross sections:

$$n_{\text{sig}}^{\text{MC}}(M_A, \tan\beta') = n_{\text{sig}}^{\text{MC}}(M_A, 20) \cdot \frac{\sigma_\phi(M_A, \tan\beta')}{\sigma_\phi(M_A, 20)}. \quad (6.69)$$

The expected discovery significance including systematic uncertainties for the neutral MSSM Higgs boson in the  $m_h^{\text{max}}$  scenario with  $L = 1.06 \text{ fb}^{-1}$  as function of  $M_A$  and  $\tan\beta$  is shown in Figure 6.13(a).

In the signal region 2124 data events are found whereas only 1971 background events are expected. This corresponds to a discovery significance of  $Z_0 = 1.21$ . Figure 6.12 shows the sampling distribution for the background-only hypothesis and the nominal signal hypothesis for  $M_A = 120$  GeV and  $\tan\beta = 20$  obtained from generated toy data



**Figure 6.12:** Sampling distributions  $f(q_0|0)$  (blue) and  $f(q_0|1)$  (red) from generated toy data (histograms) and asymptotic formula (lines) for  $L = 1.06 \text{ fb}^{-1}$  and the signal parameters  $M_A = 120 \text{ GeV}$  and  $\tan \beta = 20$ . The black line indicates the observed value of  $q_0 = 1.466$ .

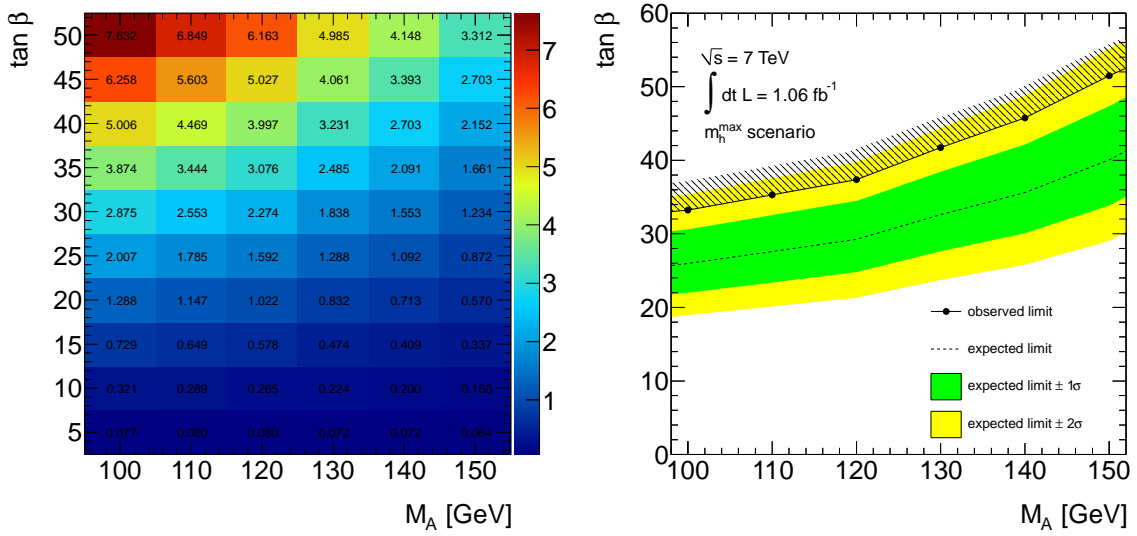
along with the distributions derived from the asymptotic formula. The usage of the latter is justified by the good agreement observed. As no significant deviation from the background-only hypothesis is observed, upper limits on the signal strength parameter  $\mu$  are derived for different mass hypotheses  $M_A$ . Since the parameter  $\tan \beta$  is assumed to affect only the cross section, the upper limits  $\mu_{\text{up}}(M_A)$  can be translated in an exclusion limit in the  $M_A \times \tan \beta$  plane according to

$$\sigma_{\text{up}}(M_A, \tan \beta_{\text{up}}) = \mu_{\text{up}}(M_A) \cdot \sigma(M_A, 20) \Rightarrow \tan \beta_{\text{up}}(M_A). \quad (6.70)$$

All values  $\tan \beta'(M_A) > \tan \beta_{\text{up}}(M_A)$  yield larger cross sections and, therefore, are excluded. The observed exclusion limit in the  $M_A \times \tan \beta$  plane at a 95% confidence level is displayed in Figure 6.13(b) and compared to the expected exclusion limit which is derived from simulations. Due to an excess of events observed in data, the exclusion limit is not as stringent as expected. Figure 6.14 shows the visible mass distribution for the expected background and how it is observed in data. One can clearly see the excess in the regions  $40 \text{ GeV} \leq m_{e\mu} \leq 50 \text{ GeV}$  and  $65 \text{ GeV} \leq m_{e\mu} \leq 75 \text{ GeV}$ . For comparison the contribution of the reference signal process is shown as well.

### 6.10.2 Discussion and Outlook

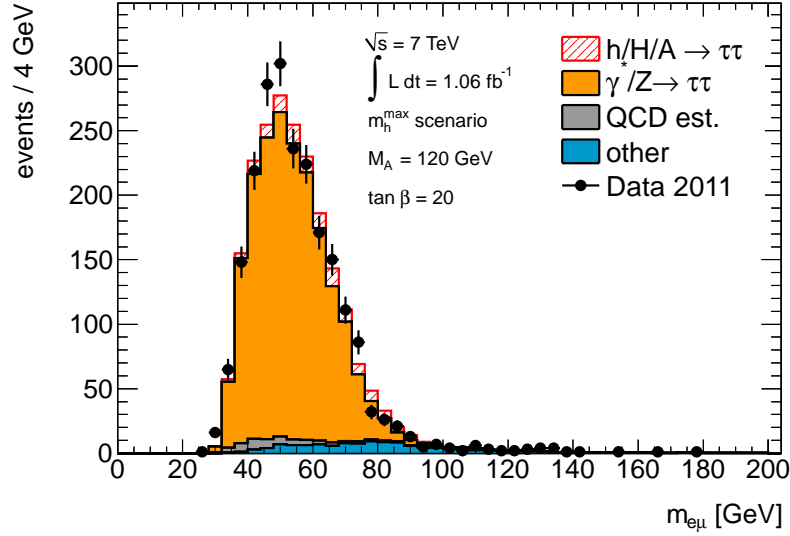
The results obtained differ slightly from those of the official ATLAS analysis searching for neutral MSSM Higgs bosons with the same data set [93]. The difference arises from different selection strategies and statistical methods for the limit extraction. The official ATLAS analysis performs a template fit to the effective mass distribution and uses the



(a) Expected discovery significance.

(b) Observed exclusion limit.

**Figure 6.13:** Results of the search for neutral MSSM Higgs bosons in the  $m_h^{\text{max}}$  scenario with  $L = 1.06 \text{ fb}^{-1}$ . The expected discovery significance (left) is calculated as a function of  $M_A$  and  $\tan \beta$  including systematic effects. The exclusion limit (right) in the  $M_A \times \tan \beta$  plane is derived from the observed data in the low mass regime  $M_A = 100 - 150 \text{ GeV}$ . The black dots and the solid line represent the observed exclusion limit while the dashed line is the median expected exclusion limit with its  $\pm 1\sigma$  (green) and  $\pm 2\sigma$  (yellow) error bands. The hatching indicates the region which is excluded at a 95% confidence level.



**Figure 6.14:** Visible mass distribution for the background expectation (stacked) and the observed data (black dots). The signal expectation is added on top of the stack (red, hatched). The simulation based background contributions and the signal expectation are normalised to the stated integrated luminosity. The multijet background component (grey) is estimated from data. The signal process is shown for the parameter point  $M_A = 120 \text{ GeV}$  and  $\tan \beta = 20$  in the  $m_h^{\text{max}}$  scenario.

$\text{CL}_S$  test statistic [19] to derive the exclusion limit. Considering the uncertainty on the expected median exclusion limit, both results are compatible.

Since the selection in this analysis does not depend on the mass hypothesis under investigation, the observed excess in data propagates coherently to all mass points  $M_A$  tested always leading to an exclusion limit which is less stringent than the median expected one. The excess observed in data corresponding to  $Z = 1.21$ , which gives a  $p$ -value of  $p_0 = 11.3\%$ , needs to be validated with more data in order to decide whether this is a statistical fluctuation or an indication of New Physics.

This analysis is performed on a data set corresponding to an integrated luminosity of  $L = 1.06 \text{ fb}^{-1}$ . By the end of this work the ATLAS detector had recorded  $L = 5.25 \text{ fb}^{-1}$  of data. However, the increased statistics of the data sample will only lead to a minor enhancement of the sensitivity since the analysis is already dominated by systematic uncertainties. The total expected background is 1971 events yielding a relative expected statistical uncertainty of 2.3% while the systematic uncertainties on the theoretical cross section for the background samples are of the order of 5% and the luminosity measurement is only accurate to a relative precision of 3.4%. Thus, data driven methods for the background estimation are essential to further reduce the systematic uncertainties and to improve the sensitivity of the analysis.

# Chapter 7

## Conclusion

In this thesis, the cross section for the process  $pp \rightarrow \gamma^*/Z \rightarrow \tau^+\tau^-$  at  $\sqrt{s} = 7$  TeV with  $66 \text{ GeV} \leq m_{\tau\tau} \leq 116 \text{ GeV}$  is measured to

$$\sigma(pp \rightarrow \gamma^*/Z \rightarrow \tau^+\tau^-) = 1.05 \pm 0.13(\text{stat.}) \pm 0.10(\text{syst.}) \pm 0.04(\text{lumi.}) \text{ nb}. \quad (7.1)$$

Its agreement with the theoretical prediction and other measurements is discussed in Section 5.9.

A data-driven method, the so-called ABCD method, for the estimation of the background component arising from QCD processes is presented. It is shown that this method yields robust results even in cases with very low statistics. Additionally, the validity of the assumptions for this method are tested and considered as sources of systematic uncertainties. Owing to the low statistics, a conservative systematic uncertainty of 31.5% is assigned to the method itself. These tests may be revisited in future analyses, which benefit from larger statistics, in order to reduce the systematic uncertainty on the measurement of the cross section.

From the insights gained during this cross section measurement, it is concluded that the simulated samples provide an adequate description of the process  $pp \rightarrow \gamma^*/Z \rightarrow \tau^+\tau^-$ . This statements applies to the normalisation of different distributions as well as to their shapes. Hence, the usage of simulated samples for this process in further studies is justified.

In the second part of this thesis, a search for neutral MSSM Higgs bosons in the channel  $h/H/A \rightarrow \tau^+\tau^- \rightarrow e\mu + 4\nu$  in the low mass regime  $M_A = 100 - 150 \text{ GeV}$  is performed. An optimisation of the event selection by using more complex classification algorithms is investigated. The multivariate methods studied for an efficient signal selection and background discrimination show a performance which is compatible or even better to the performance obtained by optimised rectangular cuts. Even though it is decided to use the latter for this study, multivariate tools will become important in future analysis. The increasing statistics of the recorded data sample will lead to an increasingly better understanding of the detector and its performance. Therefore, the combination of many and complex variables in multivariate methods will become feasible. Additionally, the performance of most classification algorithms can still be enhanced moderately by a thorough tuning of their parameters while the performance of rectangular cuts is expected to be at its limit. As a result of this study, one concludes that the usage of boosted decision trees as classifier is a promising alternative to simple rectangular cuts for rejecting reducible background components.

---

However, the main challenge for the search of light neutral MSSM Higgs bosons in the  $\tau^+\tau^-$  channel remains the irreducible background arising from  $\gamma^*/Z \rightarrow \tau^+\tau^-$  events. At this point, it should be emphasised that the sensitivity for the signal processes benefits most from a good discrimination against this background. Hence, future analysis may study different mass definitions with respect to their resolution and separation between the signal process and the  $\gamma^*/Z \rightarrow \tau^+\tau^-$  background in more detail.

In order to interpret the data in the signal region it is found that a template fit of the visible mass distribution is subject to serious instabilities. Due to the similarity in the mass shapes of the signal process and the dominant background, large negative correlations occur which lead to unreliable fit results, especially in the low mass region. This situation is unlikely to change with increased data statistics. To overcome this problem, a fit to other mass distributions might be studied.

The event counting approach leads to robust results and is used in the context of this work. After the final selection, 2124 events are observed in data while only 1971 events from background processes are expected. Including systematic uncertainties on the background expectation, the excess observed corresponds to a discovery significance of  $Z = 1.21$  which represents a  $p$ -value of 11.3%. In the absence of a significant deviation from the background expectation, the result is interpreted as exclusion limit in the  $M_A \times \tan \beta$  parameter space of the MSSM. In the context of the  $m_h^{\max}$  scenario, values of  $\tan \beta \geq 32 - 51$  depending on the parameter  $M_A$  are excluded at a 95% confidence level.

The sensitivity of this analysis is already limited by the theoretical uncertainty on the normalisation of the background expectation and the systematic uncertainty on the luminosity measurement. Therefore, an analysis of the full 2011 data set corresponding to  $L = 5.25 \text{ fb}^{-1}$  will only moderately enhance the sensitivity. In the higher mass region  $M_A \geq 130 \text{ GeV}$ , an optimisation of the mass window cut could be beneficial while the low mass region would profit more from a data driven estimate of the  $\gamma^*/Z \rightarrow \tau^+\tau^-$  background component.

# Appendix A

## Theoretical Considerations

### A.1 Conventions

#### A.1.1 Units

In this thesis the *Heaviside-Lorentz* units defined in Equations (A.1) – (A.2) are used

$$\hbar = c = k_B = 1, \quad (\text{A.1})$$

$$\epsilon_0 = \mu_0 = 1. \quad (\text{A.2})$$

Therefore, all quantities have units in terms of (inverse) energy:

$$[p] = [m] = [E], \quad (\text{A.3})$$

$$[s] = [t] = [E]^{-1}, \quad (\text{A.4})$$

$$[v] = [c] = 1. \quad (\text{A.5})$$

The equations needed for conversion from SI units to *Heaviside-Lorentz* units are given as

$$1 \text{ J} = 1.6 \cdot 10^{19} \text{ eV}, \quad (\text{A.6})$$

$$\hbar \cdot c = 0.2 \text{ GeV} \cdot \text{fm} = 1, \quad (\text{A.7})$$

$$c = 2.998 \cdot 10^8 \text{ m/s} = 1. \quad (\text{A.8})$$

#### A.1.2 Four-vector Notation

A four-dimensional space-time point  $x^\mu, \mu = 0 \dots 3$  is defined as  $x \equiv x^\mu = (t, \vec{r})$ . The metric  $g_{\mu\nu} = \text{diag}(1, -1, -1, -1)$  is chosen. Therefore, the product between two four-vectors is defined as  $xy \equiv x^\mu y_\mu = g_{\mu\nu} x^\mu y^\nu = x_\mu y^\mu = t_x t_y - \vec{r}_x \vec{r}_y$ . Accordingly, the four-dimensional derivative  $\partial_\mu \equiv \frac{\partial}{\partial x^\mu}$  is given as  $\partial_\mu = \left( \frac{\partial}{\partial t}, \vec{\nabla} \right)$  with  $\vec{\nabla} = \frac{\partial}{\partial \vec{r}}$  being the Nabla operator.

#### A.1.3 Pauli and $\gamma$ Matrices

The following set of *Pauli* matrices is chosen to represent the SU(2) algebra:

$$\sigma_x = \begin{pmatrix} 0 & 1 \\ 1 & 0 \end{pmatrix}, \quad \sigma_y = \begin{pmatrix} 0 & -i \\ i & 0 \end{pmatrix}, \quad \sigma_z = \begin{pmatrix} 1 & 0 \\ 0 & -1 \end{pmatrix}. \quad (\text{A.9})$$

Their commutation relations and properties are

$$\text{Tr}^1(\sigma_i) = 0, \quad (\text{A.10})$$

$$\det(\sigma_i) = -1, \quad (\text{A.11})$$

$$[\sigma_a, \sigma_b] = 2i\varepsilon_{abc}\sigma_c, \quad (\text{A.12})$$

$$\{\sigma_a, \sigma_b\} = 2\delta_{ab}\mathbb{1}_2. \quad (\text{A.13})$$

The  $\gamma$  matrices are defined by the following anticommutation relation

$$\{\gamma_\mu, \gamma_\nu\} = 2g_{\mu\nu}\mathbb{1}_4. \quad (\text{A.14})$$

A possible choice is stated below, together with the definition of  $\gamma^5$ .

$$\gamma^0 = \begin{pmatrix} 0 & \mathbb{1}_2 \\ \mathbb{1}_2 & 0 \end{pmatrix}, \gamma^i = \begin{pmatrix} 0 & \sigma_i \\ -\sigma_i & 0 \end{pmatrix}, \gamma^5 \equiv i\gamma^0\gamma^1\gamma^2\gamma^3 = \begin{pmatrix} -\mathbb{1}_2 & 0 \\ 0 & \mathbb{1}_2 \end{pmatrix}. \quad (\text{A.15})$$

Some useful properties are summarised in the following lines,

$$\gamma^{\mu\dagger} = \gamma^0\gamma^\mu\gamma^0, \quad (\text{A.16})$$

$$\{\gamma^\mu, \gamma^5\} = 0, \quad (\text{A.17})$$

$$\gamma^{5\dagger} = \gamma^5, \quad (\text{A.18})$$

$$(\gamma^5)^2 = \mathbb{1}_4. \quad (\text{A.19})$$

The product of  $\gamma$  matrices with a four-vector  $p_\mu$  is denoted as  $\gamma^\mu p_\mu = \not{p}$  and fulfils  $\not{p}^2 = p^2\mathbb{1}_4$ . Therefore,  $\not{p}$  is invertible if  $p^2 \neq 0$  with  $\not{p}^{-1} = \frac{1}{p^2}\not{p}$  and has the eigenvalues  $\pm\sqrt{p^2}$ .

## A.2 Lagrange Formalism and Dirac equation

One of the most fundamental concepts in physics is the principle of stationary action. Given the Lagrange density  $\mathcal{L}$  of a system as a function of the physical fields  $\phi_i$  and their derivatives  $\partial_\mu\phi_i$ , the action  $S$  for the evolution between two states is given by

$$S = \int_{\text{state1}}^{\text{state2}} dt d\vec{r} \mathcal{L}(\phi_i(t, \vec{r}), \partial_\mu\phi_i(t, \vec{r})). \quad (\text{A.20})$$

Applying the variational principle and requiring the action to be extremal leads to the EULER-LAGRANGE equations which correspond to the equation of motion for the individual fields,

$$\delta S = 0 \quad \Rightarrow \quad \partial_\mu \frac{\partial \mathcal{L}}{\partial(\partial_\mu\phi_i)} - \frac{\partial \mathcal{L}}{\partial\phi_i} = 0 \quad \forall i. \quad (\text{A.21})$$

The Lagrangian

$$\mathcal{L} = \bar{\psi}i\gamma^\mu\partial_\mu\psi - m\bar{\psi}\psi \quad (\text{A.22})$$

---

<sup>1</sup> $\text{Tr}(A) \equiv \sum_i A_{ii}$  denotes the trace of the matrix  $A$ .



leads to the DIRAC equation

$$0 = (i\gamma^\mu \partial_\mu - m) \psi \quad (\text{A.23})$$

and, therefore, is appropriate for describing relativistic fermionic particles of mass  $m$ . Hereby, the adjoint spinor  $\bar{\psi}$  is defined as  $\bar{\psi} = \psi^\dagger \gamma^0$ .

The DIRAC equation can be solved by making the ansatz

$$\psi_1 = u(p) e^{ipx}, \quad (\text{A.24})$$

$$\psi_2 = v(p) e^{-ipx}. \quad (\text{A.25})$$

Both ansatzes are valid solutions if the spinors  $u(p)$  and  $v(p)$  obey the following equations

$$(\not{p} - m\mathbb{1}_4) u(p) = 0, \quad (\text{A.26})$$

$$(\not{p} + m\mathbb{1}_4) v(p) = 0. \quad (\text{A.27})$$

The spinor  $\psi$  can be decomposed in its left and right chiral component using the projection operators

$$\hat{P}_L = \frac{1}{2} (\mathbb{1}_4 - \gamma^5), \quad (\text{A.28})$$

$$\hat{P}_R = \frac{1}{2} (\mathbb{1}_4 + \gamma^5). \quad (\text{A.29})$$

The resulting components are eigenstates to the  $\gamma^5$  matrix with eigenvalues  $\pm 1$ . In the limit of  $E \gg m$  the chirality and helicity of the particle coincide,

$$\gamma^5 \psi_L = \gamma^5 \hat{P}_L \psi = -\psi_L, \quad (\text{A.30})$$

$$\gamma^5 \psi_R = \gamma^5 \hat{P}_R \psi = +\psi_R. \quad (\text{A.31})$$

## A.3 Yang–Mills Theory

Suppose one has a theory describing  $N$  fermionic fields  $\psi_\alpha, \alpha = 1 \dots N$ , with masses  $m_\alpha$ , the Lagrangian can be written as

$$\mathcal{L}_{\text{YM}} = i\bar{\Psi} \gamma^\mu \partial_\mu \Psi - \bar{\Psi} M \Psi, \quad (\text{A.32})$$

with<sup>2</sup>

$$\Psi = \begin{pmatrix} \psi_1 \\ \vdots \\ \psi_N \end{pmatrix}, \quad (\text{A.33})$$

$$M_{\alpha\beta} = m_\alpha \delta_{\alpha\beta} \quad (\text{A.34})$$

---

<sup>2</sup>One might notice here that  $\Psi$  can be written in index notation as  $\psi_{\alpha,i}$  with  $\alpha = 1 \dots N$ , as particle index and  $i = 1 \dots 4$  labelling the spinor component. Possible symmetry transformation act only on the particle indices while the  $\gamma$  matrices, of course, act on the spinor indices.

and each field  $\psi_\alpha$  being a DIRAC spinor and solving the related DIRAC equation,

$$(i\gamma^\mu \partial_\mu - m_\alpha) \psi_\alpha = 0. \quad (\text{A.35})$$

When the mass term in (A.32) is neglected<sup>3</sup>, the remaining part  $\mathcal{L}_{\text{YM,kin}} = i\bar{\Psi}\gamma^\mu \partial_\mu \Psi$  of the Lagrange density is obviously invariant under a global symmetry transformation<sup>4</sup>  $U$  with

$$\Psi \rightarrow \Psi' = U\Psi, \quad (\text{A.36})$$

$$\bar{\Psi} \rightarrow \bar{\Psi}' = \bar{\Psi}U^\dagger. \quad (\text{A.37})$$

However, when applying a local<sup>5</sup> transformation,  $\mathcal{L}_{\text{YM,kin}}$  is not invariant anymore, i.e.

$$\mathcal{L}_{\text{YM,kin}} \rightarrow \mathcal{L}'_{\text{YM,kin}} \neq \mathcal{L}_{\text{YM,kin}}. \quad (\text{A.38})$$

To restore the invariance, one can replace  $\partial_\mu \Psi$  by the *covariant derivative*  $D_\mu \Psi$  and has to ensure that the following condition

$$D_\mu \Psi \rightarrow (D_\mu \Psi)' = U(x) D_\mu \Psi \quad (\text{A.39})$$

is satisfied. A generic symmetry transformation can be written as

$$U(x) = \exp \left[ i \sum_a \vartheta_a(x) T_a \right] \quad (\text{A.40})$$

with  $\vartheta_a(x)$  being continuous, real parameters and  $T_a$  being the generators of the symmetry group.

The covariant derivative can then be defined as

$$D_\mu = \partial_\mu + igW_\mu \quad (\text{A.41})$$

with the transformation of  $W_\mu$  given by

$$W_\mu \rightarrow W'_\mu = U(x) W_\mu U^\dagger(x) - \frac{1}{ig} (\partial_\mu U(x)) U^\dagger(x), \quad (\text{A.42})$$

where  $W_\mu = W_\mu^a T_a$  and  $W_\mu^a$  being real valued fields, the *gauge boson* fields. It can be shown that condition (A.39) is then fulfilled. Hence, the requirement of local symmetry asks for new fields in order to ensure the invariance of the Lagrangian. The covariant derivative connects these gauge boson fields with the fermion fields which are charged under this symmetry group and establishes possible interactions with an interaction strength  $g$ , the *coupling constant*. Furthermore, a term  $\mathcal{L}_{\text{gauge}}$  can be added to the Lagrangian without violating the invariance of the theory. This part is given by the field strength

---

<sup>3</sup>In general, this statement holds true if  $m_\alpha \equiv m \forall \alpha$ . Mass terms for all fermions are introduced later using an alternative mechanism.

<sup>4</sup>Symmetry transformation can be represented by unitary matrices.

<sup>5</sup>Local means that the transformation  $U$  becomes a function of the space-time point  $x$ :  $U = U(x)$ .

tensor  $F^{\mu\nu}$  and contains, in addition to the kinematic terms for the gauge boson fields, possible self-couplings among those in the case of non-abelian symmetries,

$$\mathcal{L}_{\text{gauge}} = -\frac{1}{4} \text{Tr} (F^{\mu\nu} F_{\mu\nu}) , \quad (\text{A.43})$$

$$\text{with } F^{\mu\nu} = \frac{1}{ig} [D^\mu, D^\nu] . \quad (\text{A.44})$$

## A.4 Derivation of the Electroweak Lagrangian

Using the notation introduced in Section 2.1.1 the Lagrangian for the first fermion generation can be written as

$$\mathcal{L}_0 = \bar{L} i \gamma^\mu \partial_\mu L + \bar{Q} i \gamma^\mu \partial_\mu Q + \bar{e}_R i \gamma^\mu \partial_\mu e_R + \bar{u}_R i \gamma^\mu \partial_\mu u_R + \bar{d}_R i \gamma^\mu \partial_\mu d_R . \quad (\text{A.45})$$

By replacing the partial derivative by the covariant derivative of the  $U(1)_Y \otimes SU(2)_L$  symmetry group given in Equation (2.7), one obtains an extended Lagrangian.

$$\begin{aligned} \mathcal{L} = \mathcal{L}_0 &- \bar{L} \gamma^\mu [g_W W_\mu^a T_a + g_Y Y_L B_\mu] L - \bar{Q} \gamma^\mu [g_W W_\mu^a T_a + g_Y Y_L B_\mu] Q \\ &- g_Y \bar{e}_R \gamma^\mu B_\mu Y_L e_R - g_Y \bar{u}_R \gamma^\mu B_\mu Y_L u_R - g_Y \bar{d}_R \gamma^\mu B_\mu Y_L d_R \end{aligned} \quad (\text{A.46})$$

Let  $G$  denote the  $2 \times 2$  matrix  $G = [g_W W_\mu^a T_a + g_Y Y_L B_\mu]$  which is acting on the particle indices of  $L$ , then  $G$  takes the form

$$G_\mu = g_W [W_\mu^1 T_1 + W_\mu^2 T_2] + [g_W W_\mu^3 T_3 + g_Y Y_L B_\mu] \quad (\text{A.47})$$

$$= \begin{pmatrix} \frac{g_W}{2} W_\mu^3 + g_Y Y_L B_\mu & \frac{g_W}{2} (W_\mu^1 - i W_\mu^2) \\ \frac{g_W}{2} (W_\mu^1 + i W_\mu^2) & -\frac{g_W}{2} W_\mu^3 + g_Y Y_L B_\mu \end{pmatrix} . \quad (\text{A.48})$$

Using the linear combination given in Equation (2.21) and choosing the convention  $Y_L = -\frac{1}{2}$  for the lepton doublet, the matrix elements  $G_{11,\mu}$  and  $G_{22,\mu}$  can be written as

$$G_{11,\mu} = \frac{1}{2} [(g_W \sin \theta_W - g_Y \cos \theta_W) A_\mu + (g_W \cos \theta_W + g_Y \sin \theta_W) Z_\mu] , \quad (\text{A.49})$$

$$G_{22,\mu} = -\frac{1}{2} [(g_W \sin \theta_W + g_Y \cos \theta_W) A_\mu + (g_W \cos \theta_W - g_Y \sin \theta_W) Z_\mu] . \quad (\text{A.50})$$

Driven by the motivation of identifying  $A_\mu$  with the photon and the fact that neutrinos do not interact with photons as they are neutral particles, the coefficient of  $A_\mu$  in  $G_{11,\mu}$  must vanish. Similarly, the coefficient of  $A_\mu$  in  $G_{22,\mu}$  describes the coupling between the electron and photon which should take the form<sup>6</sup>  $Q_e e = -e$

$$0 = g_W \sin \theta_W - g_Y \cos \theta_W , \quad (\text{A.51})$$

$$-e = -\frac{1}{2} (g_W \sin \theta_W + g_Y \cos \theta_W) \quad (\text{A.52})$$

$$\Rightarrow e = g_W \sin \theta_W = g_Y \cos \theta_W . \quad (\text{A.53})$$

---

<sup>6</sup> $e$  denotes here the elementary charge and  $Q_e = -1$ .

Applying also the linear combination (2.20),  $G_\mu$  becomes

$$G_\mu = \frac{g_W}{\sqrt{2}} \begin{pmatrix} 0 & W_\mu^+ \\ W_\mu^- & 0 \end{pmatrix} + e (T_3 + Y_L) A_\mu + (g_W \cos \theta_W T_3 - g_Y \sin \theta_W Y_L) Z_\mu. \quad (\text{A.54})$$

From this point, the general identity  $Q = Y_L + T_3$  can be inferred. The terms of the right chiral components have the general structure

$$\mathcal{L}|_{\psi_R} = -g_Y Y_L \bar{\psi}_R \gamma^\mu (\cos \theta_W A_\mu - \sin \theta_W Z_\mu) \psi_R \quad (\text{A.55})$$

$$= -e Y_L \bar{\psi}_R \gamma^\mu A_\mu \psi_R + g_Y \sin \theta_W Y_L \bar{\psi}_R \gamma^\mu Z_\mu \psi_R. \quad (\text{A.56})$$

As for right chiral particles  $Q = Y_L$  and  $\psi_L + \psi_R = \psi$ , the electromagnetic part of the Lagrangian is given by

$$\mathcal{L}_{\text{EM}} = -e \sum_{i=e,u,d} Q_i \bar{\psi}_i \gamma^\mu \psi_i A_\mu. \quad (\text{A.57})$$

The gauge boson fields  $W_\mu^\pm$  couple only to left chiral particles and are therefore responsible for the parity violation. They can be identified with the off-diagonal elements of  $G_\mu$

$$\tilde{W}_\mu = \begin{pmatrix} 0 & W_\mu^+ \\ W_\mu^- & 0 \end{pmatrix} \quad (\text{A.58})$$

and introduce flavor changing charged currents. The corresponding Lagrangian is

$$\mathcal{L}_{\text{CC}} = -\frac{g_W}{\sqrt{2}} \bar{L} \gamma^\mu \tilde{W}_\mu L - \frac{g_W}{\sqrt{2}} \bar{Q} \gamma^\mu \tilde{W}_\mu Q \quad (\text{A.59})$$

$$\begin{aligned} &= -\frac{g_W}{2\sqrt{2}} \begin{pmatrix} \bar{\nu}_e & \bar{e} \end{pmatrix} \tilde{W}_\mu \gamma^\mu (\mathbb{1}_4 - \gamma^5) \begin{pmatrix} \nu_e \\ e \end{pmatrix} \\ &\quad - \frac{g_W}{2\sqrt{2}} \begin{pmatrix} \bar{u} & \bar{d} \end{pmatrix} \tilde{W}_\mu \gamma^\mu (\mathbb{1}_4 - \gamma^5) \begin{pmatrix} u \\ d \end{pmatrix}. \end{aligned} \quad (\text{A.60})$$

In Equation (A.60) the “V–A” coupling structure is explicitly shown. The couplings between fermion fields and the  $Z_\mu$  gauge field are more complicated as these differ for left and right-handed fermions. Equation (A.61) shows the general structure for left-handed fermions whereas in Equation (A.62) the corresponding term for right-handed fermions is given.

$$\mathcal{L}|_{Z_\mu, L} = -\frac{g_W}{\cos \theta_W} \bar{\psi}_L \gamma^\mu [T_3 - \sin^2 \theta_W Q] \psi_L Z_\mu \quad (\text{A.61})$$

$$\mathcal{L}|_{Z_\mu, R} = -\frac{g_W}{\cos \theta_W} \bar{\psi}_R \gamma^\mu (-\sin^2 \theta_W Q) \psi_R Z_\mu \quad (\text{A.62})$$

Hence, the generic coupling to the  $Z_\mu$  is of the form

$$\mathcal{L}_{\text{NC}} = -\frac{g_W}{\cos \theta_W} (\bar{\psi}_L \gamma^\mu c_L \psi_L Z_\mu + \bar{\psi}_R \gamma^\mu c_R \psi_R Z_\mu) \quad (\text{A.63})$$

$$= -\frac{g_W}{\cos \theta_W} \bar{\psi} \gamma^\mu (c_L \hat{P}_L + c_R \hat{P}_R) \psi Z_\mu \quad (\text{A.64})$$

with

$$c_L = T_3 - \sin^2 \theta_W Q, \quad (\text{A.65})$$

$$c_R = -\sin^2 \theta_W Q \quad (\text{A.66})$$

being the left and right handed coupling terms and  $\hat{P}_{L,R}$  denoting the projection operators. Evaluating the term  $c_L \hat{P}_L + c_R \hat{P}_R$  explicitly reveals the mixed “ $c_V V - c_A A$ ” coupling structure as shown in Equation (A.68).

$$c_L \hat{P}_L + c_R \hat{P}_R = \frac{1}{2} [(c_L + c_R) \mathbb{1}_4 - (c_L - c_R) \gamma^5] \quad (\text{A.67})$$

$$\Rightarrow \mathcal{L}_{\text{NC}} = -\frac{g_W}{2 \cos \theta_W} \bar{\psi} (c_V \gamma^\mu - c_A \gamma^\mu \gamma^5) \psi Z_\mu \quad (\text{A.68})$$

Hereby, the definition of the vector  $c_V$  and axial coupling  $c_A$  have been introduced as

$$c_V = c_L + c_R = T_3 - 2 \sin^2 \theta_W Q, \quad (\text{A.69})$$

$$c_A = c_L - c_R = T_3. \quad (\text{A.70})$$

The Lagrangian corresponding to (A.43) and describing the kinematic evolution and self-interactions between gauge fields is

$$\mathcal{L}_{\text{gauge}} = -\frac{1}{4} B^{\mu\nu} B_{\mu\nu} - \frac{1}{4} F_a^{\mu\nu} F_{a\mu\nu} \quad (\text{A.71})$$

$$\text{with } B^{\mu\nu} = \partial^\mu B^\nu - \partial^\nu B^\mu \quad (\text{A.72})$$

$$\text{and } F_a^{\mu\nu} = \partial^\mu W_a^\nu - \partial^\nu W_a^\mu - g_W \varepsilon_{bca} W_b^\mu W_c^\nu. \quad (\text{A.73})$$

The last term in Equation (A.73) arises from the non-vanishing commutator between the generators of the  $\text{SU}(2)$  symmetry group and gives rise to gauge boson self-couplings. This prediction is purely based on the chosen symmetry group of the Standard Model and can therefore be used to test the theory.

The complete electroweak Lagrangian for the first fermion generation is then given by

$$\mathcal{L}_{\text{EW}} = \mathcal{L}_0 + \mathcal{L}_{\text{EM}} + \mathcal{L}_{\text{CC}} + \mathcal{L}_{\text{NC}} + \mathcal{L}_{\text{gauge}} + \mathcal{L}_{\text{Higgs}} \quad (\text{A.74})$$

with  $\mathcal{L}_{\text{Higgs}}$  according to Equation (2.12). The extension to the second and third generation is straight forward by adding identical terms and replacing the fermion fields of the first generation by the fermion fields of the other generations.



# Appendix B

## Coordinate Transformations

The kinematics of a particle are described by the three variables  $p_T$ ,  $\eta$  and  $\phi$  with the definition of  $\eta$  given in Equation (3.3). Using the conventions of Section 3.2.1 the following relations hold

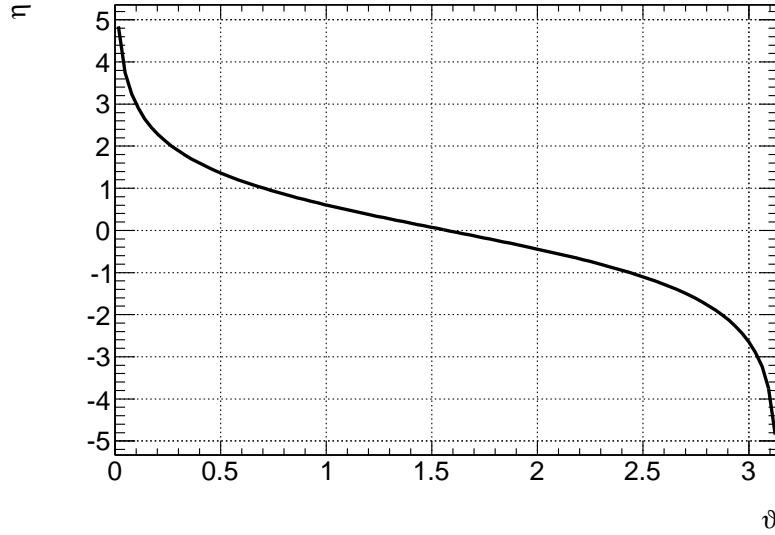
$$\tan \phi = \frac{p_y}{p_x} , \quad (B.1)$$

$$p_T = \sqrt{p_x^2 + p_y^2} = \frac{p}{\cosh \eta} , \quad (B.2)$$

$$p_z = p_T \cdot \sinh \eta , \quad (B.3)$$

$$\cot \vartheta = \sinh \eta , \quad (B.4)$$

$$\vartheta = 2 \tan^{-1} (e^{-\eta}) . \quad (B.5)$$



**Figure B.1:**  $\eta$  as function of  $\vartheta$  according to Equation (3.3).

---



# Appendix C

## Measurement of the Cross Section of the Process $pp \rightarrow \gamma^*/Z \rightarrow \tau^+\tau^-$ in the $e\mu + 4\nu$ Final State

### C.1 Simulated Data Sets

A list of the simulated samples used is given in Table C.1.

### C.2 Jet Cleaning Procedure

**Coherent Electronic Noise in the EM Calorimeter** Electronic noise in association with cross-talk between adjacent readout channels can mimic a localised energy deposition in the electromagnetic calorimeter. Depending on the amplitude of the noise, this signal can bias the jet reconstruction or even cause additional jet candidates. As those jets are reconstructed from noise induced signals in the EM calorimeter, the electromagnetic energy fraction  $f_{\text{EM}}$  is close to 1. In addition, the shape of the electronic pulse in the calorimeter cells is different for electronic noise and a physical energy deposition. The agreement between the measured shape and its expectation is expressed as a quality factor  $|Q_{\text{LAR}}|$  with  $|Q_{\text{LAR}}| \approx 0$  representing a good agreement.

**Energy Bursts in the Hadronic Endcap Calorimeter** Sporadic energy bursts in the Hadronic Endcap Calorimeter affects the jet reconstruction in a similar manner as the coherent electronic noise. The cause for these energy bursts in the liquid-argon calorimeters is not yet understood completely. However, a set of variables was found to identify reconstructed jets influenced by energy bursts in the HEC.

The energy fraction of the reconstructed jet in the HEC  $f_{\text{HEC}}$  is large because the dominant contribution comes from the energy burst. Similarly to  $|Q_{\text{LAR}}|$  a quality factor for the pulse shape comparison considering only energy cells in the HEC can be computed  $|Q_{\text{HEC}}|$ . Due to the fact that the jet is mainly reconstructed from a large energy deposition in one calorimeter cell, the associated cluster contains many cells without any real energy deposition (“empty” cells). The applied corrections on cell level, in order to correct for average pile-up and noise effects, yield actual energy contributions of these

“empty” cells which are negative. For a reconstructed jet arising from energy bursts in the HEC, the expected number of “empty” calorimeter cells is large leading to significant amount of negative energy contributions  $E_{\text{neg}}$  in the jet.

**Cosmic Rays and Beam Background** Fake energy depositions coming from cosmic rays can be reduced by requiring that the energy deposition occur at time compatible with a proton-proton collision. Therefore, a jet time  $t_{\text{jet}}$  which respect to the event time is defined as an energy weighted average of the timing information of all associated calorimeter cells.

In most of the cases, beam background effects manifest themselves as pions or muons travelling parallel to the beam pipe at larger radii. These charged particles, the ensemble of them also called *beam halo*, can be produced by interactions of the beam with the collimators upstream the ATLAS detector. Since the particles traverse the calorimeter parallel to the beam pipe, their energy depositions are concentrated in one calorimeter layer but over the whole length of the detector.

If the trajectory of the particle happens to pass only the hadronic calorimetry system, the electromagnetic energy fraction  $f_{\text{EM}}$  defined above, is very small. On the other hand, a trajectory passing the electromagnetic calorimeter parallel to the beam axis will deposit most of the energy in one compartment. Hence, the maximum jet energy fraction in one sampling layer  $f_{\text{samp}}$  is close to 1.

In addition, the beam halo particles create no tracks, which point from the collision point to the energy deposition. An assignment of track candidates to the reconstructed jet is purely accidentally. Thus, the charged fraction  $f_{\text{ch}}$  of the jet defined as the  $p_{\text{T}}$  sum of all associated tracks divided by the reconstructed jet  $p_{\text{T}}$  is expected to be small.

**Final Cuts** To suppress all possible source of disturbing energy depositions mentioned, the variables introduced above can be deployed in the geometrical regions where they are well-defined. An event is vetoed if at least one reconstructed jet candidate with  $p_{\text{T}} \geq 20$  GeV passes the cuts given in Table C.2 where conditions in different rows are connected with a logical OR. The jet cleaning is only applied on data events as the employed variables are not expected to be well-modelled in simulated samples. However, the jet cleaning has a minor impact on the event selection and is treated as systematic uncertainty for the simulated samples.

## C.3 Detailed Object Definitions

A detailed description of the object selection criteria is given in Table C.3.

## C.4 Correction Factors for the Simulated Samples

The correction factors for the electron identification efficiencies as a function of  $\eta$  and  $p_{\text{T}}$  are given in Table C.4. Table C.5 summarises the correction factors for isolation effi-

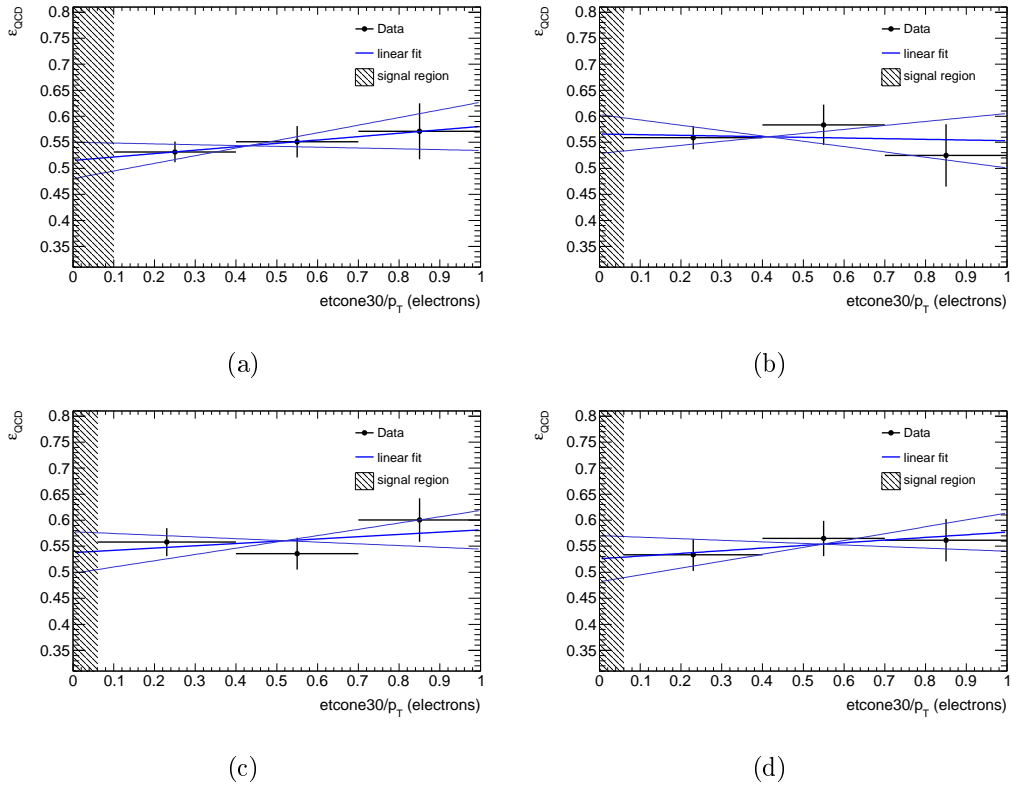
ciencies of the electron and muon candidates. In order to account for the varying pile-up conditions observed in data, the simulated samples are re-weighted with correction factors which depend on the number of reconstructed vertices with at least three associated tracks and are stated in Table C.6.

## C.5 Cutflows for the Individual Regions

Table C.7 summarises the cut flows for the individual regions.

## C.6 Systematic Uncertainty on the QCD Background Estimate

The dependence of the selection efficiency  $\varepsilon_{\text{QCD}}$  on the isolation variables is shown in Figure C.1. As the fitted slope parameter is always consistent with zero, no systematic uncertainty is assigned.



**Figure C.1:** Dependence of the selection efficiency  $\varepsilon_{\text{QCD}}$  on calorimeter-based (left) and track-based (right) isolation variables for electron (top) and muon (bottom) candidates. The linear fit with its uncertainty is displayed by the blue lines.

process	$\sigma$ in pb	filter efficiency	process id	generator	configuration tags
$\gamma^*/Z \rightarrow ee, m_{ee} > 60 \text{ GeV}$	990	1	106046	Pythia	e574_s933_s946_r1831_r2040
$\gamma^*/Z \rightarrow \mu\mu, m_{\mu\mu} > 60 \text{ GeV}$	990	1	106047	Pythia	e574_s933_s946_r1831_r2040
$\gamma^*/Z \rightarrow \tau\tau, m_{\tau\tau} > 60 \text{ GeV}$	990	1	106052	Pythia	e574_s934_s946_r1833_r2040
$\gamma^*/Z \rightarrow ee, 15 \text{ GeV} < m_{ee} < 60 \text{ GeV}$	1462	1	108320	Pythia	e574_s933_s946_r1831_r2040
$\gamma^*/Z \rightarrow \mu\mu, 15 \text{ GeV} < m_{\mu\mu} < 60 \text{ GeV}$	1462	1	108319	Pythia	e574_s933_s946_r1831_r2040
$\gamma^*/Z \rightarrow \tau\tau, 10 \text{ GeV} < m_{\tau\tau} < 60 \text{ GeV}$	3967	1	107055	Pythia	e574_s934_s946_r1833_r2040
$W \rightarrow e\nu$	10460	1	106043	Pythia	e574_s933_s946_r1831_r2040
$W \rightarrow \mu\nu$	10460	1	106044	Pythia	e574_s933_s946_r1831_r2040
$W \rightarrow \tau\nu$	10460	1	107054	Pythia	e574_s934_s946_r1833_r2040
$t\bar{t}$ , at least one lepton	164.6	0.561	105200	MC@NLO	e598_s933_s946_r1831_r2040
$WW$ , at least one lepton	44.9	0.388	105985	Herwig	e598_s933_s946_r1831_r2040
$ZZ$ , at least one lepton	5.64	0.214	105986	Herwig	e598_s933_s946_r1831_r2040
$WZ$ , at least one lepton	18.0	0.309	105987	Herwig	e598_s933_s946_r1831_r2040

**Table C.1:** Samples of simulated processes used for the  $pp \rightarrow \gamma^*/Z \rightarrow \tau^+\tau^- \rightarrow e\mu + 4\nu$  cross section measurement.

background source	cuts
EM coherent noise	$f_{\text{EM}} > 0.95$ AND $ Q_{\text{LAR}}  > 0.8$ AND $ \eta_{\text{jet}}  < 2.8$
HEC spikes	$f_{\text{HEC}} > 0.5$ AND $ Q_{\text{HEC}}  > 0.5$ $ E_{\text{neg}}  > 60$ GeV
Non-collision background	$ t_{\text{jet}}  > 25$ ns $f_{\text{EM}} < 0.05$ AND $ \eta_{\text{jet}}  \geq 2$ $f_{\text{EM}} < 0.05$ AND $f_{\text{ch}} < 0.05$ AND $ \eta_{\text{jet}}  < 2$ $f_{\text{samp}} > 0.99$ AND $ \eta_{\text{jet}}  < 2$

**Table C.2:** Jet cleaning cuts applied on reconstructed jet candidates (conditions of different rows are combined with a logical OR).

objects	selection criteria
electrons	$p_T \geq 16 \text{ GeV}$ $ \eta  < 2.47$ , but excluding $1.37 <  \eta  < 1.52$ electron Medium_WithTrackMatch electron author 1 or 3 not in bad object quality maps region (map for runs $\geq 167521$ )
muons	$p_T \geq 10 \text{ GeV}$ $ \eta  < 2.4$ combined STACO muon $ z_0  < 10 \text{ mm}$ no BlayerHit expected or nBLayerHits $> 0$ nPixHits + nDeadPixelSensors $> 1$ nSCTHits + nDeadSCTSensors $> 5$ nPixHoles + nSCTHoles $< 2$ $ \eta  < 1.9$ : $\frac{\text{nTRT Outliers}}{\text{nTRT Hits} + \text{nTRT Outliers}} < 0.9$ AND nTRT Hits + nTRT Outliers $> 5$ $ \eta  \geq 1.9$ : nTRT Hits + nTRT Outliers $\leq 5$ OR $\frac{\text{nTRT Outliers}}{\text{nTRT Hits} + \text{nTRT Outliers}} < 0.9$
jets	Anti- $k_T$ jets with $\Delta R = 0.4$ calibrated at EM scale with JES factor $p_T > 20 \text{ GeV}$ $ \eta  < 4.5$
overlap Removal	muon-muon ( $\Delta R < 0.2$ ) elec-elec and elec-muon ( $\Delta R < 0.2$ ) jet-jet, jet-elec and jet-muon ( $\Delta R < 0.4$ )
MET	MET(LocHadTopo) + MET(MuonBoy) - MET(RefMuonTrack)

**Table C.3:** Object definitions used for the  $pp \rightarrow \gamma^*/Z \rightarrow \tau^+\tau^- \rightarrow e\mu + 4\nu$  cross section measurement.

$\eta$ range	correction factor	$p_T$ range in GeV	correction factor
$-2.47 \leq \eta < -2.01$	$0.945 \pm 0.017$	$0 \leq p_T < 20$	$0.852 \pm 0.102$
$-2.01 \leq \eta < -1.52$	$0.988 \pm 0.016$	$20 \leq p_T < 25$	$0.928 \pm 0.044$
$-1.37 \leq \eta < -0.80$	$0.972 \pm 0.016$	$25 \leq p_T < 30$	$0.972 \pm 0.015$
$-0.80 \leq \eta < -0.00$	$0.974 \pm 0.015$	$30 \leq p_T < 35$	$0.998 \pm 0.007$
$0.00 \leq \eta < 0.80$	$0.972 \pm 0.015$	$35 \leq p_T < 40$	$1.002 \pm 0.006$
$0.80 \leq \eta < 1.37$	$0.967 \pm 0.015$	$40 \leq p_T < 45$	$1.003 \pm 0.007$
$1.52 \leq \eta < 2.01$	$0.995 \pm 0.029$	$45 \leq p_T < \infty$	$1.013 \pm 0.013$
$2.01 \leq \eta < 2.47$	$0.961 \pm 0.017$		

**Table C.4:** Correction factors for the electron identification efficiency with total uncertainty.

$\eta$ range	electron candidates			muon candidates	
	correction	$p_T$ in GeV	correction	$p_T$ in GeV	correction
$-2.47 \leq \eta < -2.01$	$0.90 \pm 0.02$	$16 \leq p_T < 25$	$0.88 \pm 0.03$	$10 \leq p_T < 15$	$1.03 \pm 0.05$
$-2.01 \leq \eta < -1.52$	$0.91 \pm 0.02$	$25 \leq p_T < 35$	$0.97 \pm 0.01$	$15 \leq p_T < 20$	$1.04 \pm 0.03$
$-1.52 \leq \eta < -0.80$	$0.92 \pm 0.01$	$35 \leq p_T < 45$	$1.01 \pm 0.01$	$20 \leq p_T < 25$	$1.00 \pm 0.02$
$-0.80 \leq \eta < -0.00$	$0.97 \pm 0.01$	$45 \leq p_T < 60$	$1.04 \pm 0.01$	$25 \leq p_T < 30$	$1.02 \pm 0.01$
$0.00 \leq \eta < 0.80$	$0.96 \pm 0.01$	$60 \leq p_T < \infty$	$1.05 \pm 0.01$	$30 \leq p_T < 35$	$1.02 \pm 0.01$
$0.80 \leq \eta < 1.52$	$0.91 \pm 0.01$			$35 \leq p_T < \infty$	$1.00 \pm 0.01$
$1.52 \leq \eta < 2.01$	$0.97 \pm 0.02$				
$2.01 \leq \eta < 2.47$	$0.88 \pm 0.02$				

**Table C.5:** Correction factors for the isolation efficiency of reconstructed lepton candidates with total uncertainty.

$n_{\text{vertices}}$	correction weight
1	$1.895 \pm 0.013$
2	$1.235 \pm 0.006$
3	$0.861 \pm 0.004$
4	$0.653 \pm 0.004$
5	$0.537 \pm 0.004$
6	$0.463 \pm 0.006$
7	$0.414 \pm 0.010$
8	$0.446 \pm 0.021$
9	$0.405 \pm 0.038$
$\geq 10$	$0.582 \pm 0.106$

**Table C.6:** Pile-up correction factors with total uncertainty.

cut	Multijets	$W \rightarrow e\nu_e$	$W \rightarrow \mu\nu_\mu$	$W \rightarrow \tau\nu_\tau$	$t\bar{t}$	$\gamma^*/Z \rightarrow e^+e^-$	$\gamma^*/Z \rightarrow \mu^+\mu^-$	di-boson	$\gamma^*/Z \rightarrow \tau^+\tau^-$	$\Sigma$	data
Dilepton cut	–	$94.5 \pm 2.4$	$103.7 \pm 2.2$	$19.2 \pm 1.8$	$166.2 \pm 0.9$	$13.2 \pm 0.5$	$25.6 \pm 0.5$	$14.7 \pm 0.2$	$176.0 \pm 1.7$	$613.1 \pm 4.1$	9855
Oppositely charged	–	$76.6 \pm 2.2$	$57.0 \pm 1.7$	$13.0 \pm 1.6$	$124.7 \pm 0.8$	$6.4 \pm 0.3$	$15.2 \pm 0.4$	$13.4 \pm 0.2$	$167.2 \pm 1.7$	$473.5 \pm 3.6$	5939
Lepton isolation	$12.4 \pm 7.3$	$0.2 \pm 0.1$	$9.2 \pm 0.6$	$1.0 \pm 0.4$	$48.7 \pm 0.5$	$\leq 0.1$	$5.5 \pm 0.2$	$9.1 \pm 0.1$	$86.9 \pm 1.2$	$173.0 \pm 7.5$	190
$\Sigma \cos \Delta\phi$	$9.4 \pm 5.5$	$\leq 0.1$	$1.6 \pm 0.3$	$0.3 \pm 0.3$	$21.1 \pm 0.3$	$\leq 0.1$	$3.8 \pm 0.2$	$2.6 \pm 0.1$	$81.8 \pm 1.1$	$120.7 \pm 5.6$	134
$\Sigma p_T + E_{T,\text{miss}}$	$8.1 \pm 4.8$	$\leq 0.1$	$1.0 \pm 0.2$	$0.3 \pm 0.3$	$0.2 \pm 0.1$	$\leq 0.1$	$3.5 \pm 0.2$	$1.1 \pm 0.1$	$74.6 \pm 1.1$	$89.0 \pm 4.9$	89
$m_{e\mu}$	$6.9 \pm 4.1$	$\leq 0.1$	$0.6 \pm 0.2$	$\leq 0.1$	$0.2 \pm 0.1$	$\leq 0.1$	$1.9 \pm 0.1$	$0.5 \pm 0.1$	$72.9 \pm 1.1$	$83.0 \pm 4.2$	85

cut	$W \rightarrow e\nu_e$	$W \rightarrow \mu\nu_\mu$	$W \rightarrow \tau\nu_\tau$	$t\bar{t}$	$\gamma^*/Z \rightarrow e^+e^-$	$\gamma^*/Z \rightarrow \mu^+\mu^-$	di-boson	$\gamma^*/Z \rightarrow \tau^+\tau^-$	$\Sigma$	data
Dilepton cut	$94.5 \pm 2.4$	$103.7 \pm 2.2$	$19.2 \pm 1.8$	$166.2 \pm 0.9$	$13.2 \pm 0.5$	$25.6 \pm 0.5$	$14.7 \pm 0.2$	$176.0 \pm 1.7$	$613.1 \pm 4.1$	9855
Equally charged	$17.9 \pm 1.1$	$46.8 \pm 1.5$	$6.1 \pm 1.0$	$41.5 \pm 0.5$	$6.8 \pm 0.3$	$10.4 \pm 0.3$	$1.3 \pm 0.1$	$8.9 \pm 0.4$	$139.7 \pm 1.0$	3916
Lepton isolation	$0.1 \pm 0.1$	$9.6 \pm 0.7$	$0.5 \pm 0.3$	$0.4 \pm 0.1$	$\leq 0.1$	$2.8 \pm 0.2$	$0.6 \pm 0.1$	$1.4 \pm 0.2$	$15.4 \pm 0.5$	22
$\Sigma \cos \Delta\phi$	$\leq 0.1$	$1.6 \pm 0.3$	$0.1 \pm 0.1$	$0.1 \pm 0.1$	$\leq 0.1$	$1.6 \pm 0.1$	$0.2 \pm 0.1$	$1.3 \pm 0.2$	$4.9 \pm 0.5$	9
$\Sigma p_T + E_{T,\text{miss}}$	$\leq 0.1$	$1.3 \pm 0.2$	$\leq 0.1$	$\leq 0.1$	$\leq 0.1$	$1.5 \pm 0.1$	$\leq 0.1$	$1.1 \pm 0.2$	$3.9 \pm 0.4$	6
$m_{e\mu}$	$\leq 0.1$	$0.8 \pm 0.2$	$\leq 0.1$	$\leq 0.1$	$\leq 0.1$	$0.8 \pm 0.1$	$\leq 0.1$	$1.1 \pm 0.2$	$2.7 \pm 0.4$	3

cut	$W \rightarrow e\nu_e$	$W \rightarrow \mu\nu_\mu$	$W \rightarrow \tau\nu_\tau$	$t\bar{t}$	$\gamma^*/Z \rightarrow e^+e^-$	$\gamma^*/Z \rightarrow \mu^+\mu^-$	di-boson	$\gamma^*/Z \rightarrow \tau^+\tau^-$	$\Sigma$	data
Dilepton cut	$94.5 \pm 2.4$	$103.7 \pm 2.2$	$19.2 \pm 1.8$	$166.2 \pm 0.9$	$13.2 \pm 0.5$	$25.6 \pm 0.5$	$14.7 \pm 0.2$	$176.0 \pm 1.7$	$613.1 \pm 4.1$	9855
Oppositely charged	$76.6 \pm 2.2$	$57.0 \pm 1.7$	$13.0 \pm 1.6$	$124.7 \pm 0.8$	$6.4 \pm 0.3$	$15.2 \pm 0.4$	$13.4 \pm 0.2$	$167.2 \pm 1.7$	$473.5 \pm 3.6$	5939
Lepton anti-isolation	$1.7 \pm 0.3$	$4.1 \pm 0.4$	$0.8 \pm 0.4$	$4.6 \pm 0.2$	$0.3 \pm 0.1$	$0.3 \pm 0.1$	$\leq 0.1$	$0.6 \pm 0.1$	$12.6 \pm 0.7$	3771
$\Sigma \cos \Delta\phi$	$0.2 \pm 0.1$	$\leq 0.1$	$\leq 0.1$	$2.0 \pm 0.1$	$0.2 \pm 0.1$	$\leq 0.1$	$\leq 0.1$	$0.5 \pm 0.1$	$2.9 \pm 0.2$	2841
$\Sigma p_T + E_{T,\text{miss}}$	$\leq 0.1$	$\leq 0.1$	$\leq 0.1$	$\leq 0.1$	$\leq 0.1$	$\leq 0.1$	$\leq 0.1$	$0.5 \pm 0.1$	$\leq 1$	2475
$m_{e\mu}$	$\leq 0.1$	$\leq 0.1$	$\leq 0.1$	$\leq 0.1$	$\leq 0.1$	$\leq 0.1$	$\leq 0.1$	$0.5 \pm 0.1$	$\leq 1$	2101

cut	$W \rightarrow e\nu_e$	$W \rightarrow \mu\nu_\mu$	$W \rightarrow \tau\nu_\tau$	$t\bar{t}$	$\gamma^*/Z \rightarrow e^+e^-$	$\gamma^*/Z \rightarrow \mu^+\mu^-$	di-boson	$\gamma^*/Z \rightarrow \tau^+\tau^-$	$\Sigma$	data
Dilepton cut	$94.5 \pm 2.4$	$103.7 \pm 2.2$	$19.2 \pm 1.8$	$166.2 \pm 0.9$	$13.2 \pm 0.5$	$25.6 \pm 0.5$	$14.7 \pm 0.2$	$176.0 \pm 1.7$	$613.1 \pm 4.1$	9855
Equally charged	$17.9 \pm 1.1$	$46.8 \pm 1.5$	$6.1 \pm 1.0$	$41.5 \pm 0.5$	$6.8 \pm 0.3$	$10.4 \pm 0.3$	$1.3 \pm 0.1$	$8.9 \pm 0.4$	$139.7 \pm 1.0$	3916
Lepton anti-isolation	$0.4 \pm 0.2$	$3.5 \pm 0.4$	$0.7 \pm 0.4$	$3.2 \pm 0.1$	$0.9 \pm 0.1$	$0.3 \pm 0.1$	$\leq 0.1$	$0.5 \pm 0.1$	$9.5 \pm 0.6$	2432
$\Sigma \cos \Delta\phi$	$0.2 \pm 0.1$	$0.4 \pm 0.1$	$0.1 \pm 0.1$	$1.6 \pm 0.1$	$0.1 \pm 0.1$	$0.1 \pm 0.1$	$\leq 0.1$	$0.4 \pm 0.1$	$2.9 \pm 0.3$	1835
$\Sigma p_T + E_{T,\text{miss}}$	$\leq 0.1$	$0.2 \pm 0.1$	$\leq 0.1$	$\leq 0.1$	$\leq 0.1$	$\leq 0.1$	$\leq 0.1$	$0.3 \pm 0.1$	$\leq 1$	1583
$m_{e\mu}$	$\leq 0.1$	$\leq 0.1$	$\leq 0.1$	$\leq 0.1$	$\leq 0.1$	$\leq 0.1$	$\leq 0.1$	$0.2 \pm 0.1$	$\leq 1$	1367

**Table C.7:** Number of data and MC events and their statistical uncertainties for the cutflow after the event preselection in the signal region (top) and the three control regions: region  $B$ , same-sign, isolated (second), region  $C$ , opposite-sign, anti-isolated (third), region  $D$ , same-sign, anti-isolated (fourth). The simulations are normalised to an integrated luminosity of  $35.5 \text{ pb}^{-1}$ . The second to last column contains the sum of all simulations. The multijet component is estimated from data only for the signal region and after the lepton isolation requirement.



# Appendix D

## A Search for Neutral MSSM Higgs Bosons in the $\tau^+\tau^-$ Channel

### D.1 Simulated Data Sets

A list of the simulated samples used for the MSSM Higgs boson search is given in Table [D.1](#).

### D.2 Readout Problems in the EM Calorimeter

In this section, the procedure for removing events, which suffer from dead readout channels in part of the EM barrel calorimeter, is described. The reconstruction of jet, electron and photon candidates is affected by the problem as well as the  $\vec{E}_{T,\text{miss}}$  measurement. The basic idea is to reject events where an energetic object lies within the problematic region because the energy of this object is not reconstructed correctly resulting in a bias of the missing transverse energy. In events, where no energetic object is in the dead calorimeter region, the  $\vec{E}_{T,\text{miss}}$  measurement is only distorted by contributions from low energy deposits or noise signals which are missed in the affected region. However, these effects can be corrected on average as the average density of energy deposits is known from measurements without colliding beams. For the prescription given below, all reconstructed electron and jet candidates are considered. They do not have to pass the object definitions given in Section [6.3](#) since the distorted energy cluster reconstruction may lead to a bad quality of the reconstructed object. As a consequence, high energetic objects could be missed which is undesired.

Owing to the dimension of reconstructed energy clusters, the definition for the problematic region is slightly larger than the actual affected region and given by

$$-0.1 < \eta < 1.55 \text{ and } -0.9 < \phi < -0.5 \text{ for electron candidates ,} \quad (\text{D.1})$$

$$-0.2 < \eta < 1.65 \text{ and } -1.0 < \phi < -0.4 \text{ for jet candidates .} \quad (\text{D.2})$$

Photons are not treated separately since they show a signature similar to the one for jet candidates and, therefore, are reconstructed as jet candidates as well. An event is affected if any of the following two statements is true.

- At least one reconstructed electron candidate with  $p_T \geq 15$  GeV is within the problematic region.
- At least one reconstructed jet candidate with a corrected transverse momentum of  $p_T \geq 20$  GeV is within the problematic region.

Affected data events are rejected while simulated events are weighted with a correction factor (cf. Section 6.4.4).

## D.3 Detailed Object Definitions

A detailed description of the object selection criteria is given in Table D.2.

## D.4 Corrections for the Simulated MC Samples

The trigger efficiency correction factors for the electron trigger EF\_e20\_medium are given as a function of  $\eta$  and  $\phi$  of the electron candidate as shown in Figure D.1.

The correction factors for the combined muon trigger

$$\text{EF\_mu18\_MG OR EF\_mu40\_MSonly\_barrel}$$

in the barrel region are shown in Figure D.2. In this region, the correction factors do not exhibit a dependence on the transverse momentum of the muon candidate. Hence, they are given by a two-dimensional map in  $\eta \times \phi$ . In contrast, the dependence on  $\eta$  and  $\phi$  is negligible in the end-cap regions  $|\eta| \geq 1.05$ . Thus, the muon trigger efficiency corrections in these regions are given for different  $p_T$  bins and are summarised in Table D.3.

The  $p_T$  dependent correction factors for the electron reconstruction efficiency are stated in Table D.4 while Table D.5 summarises the identification efficiency corrections.

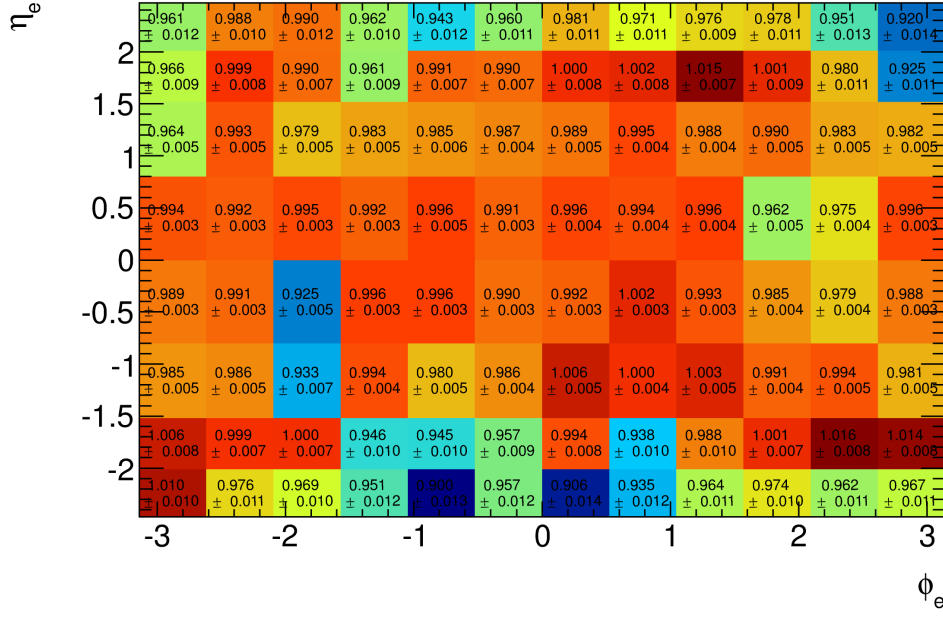
## D.5 Optimisation of the Event Selection

### Definition of Discriminating Variables

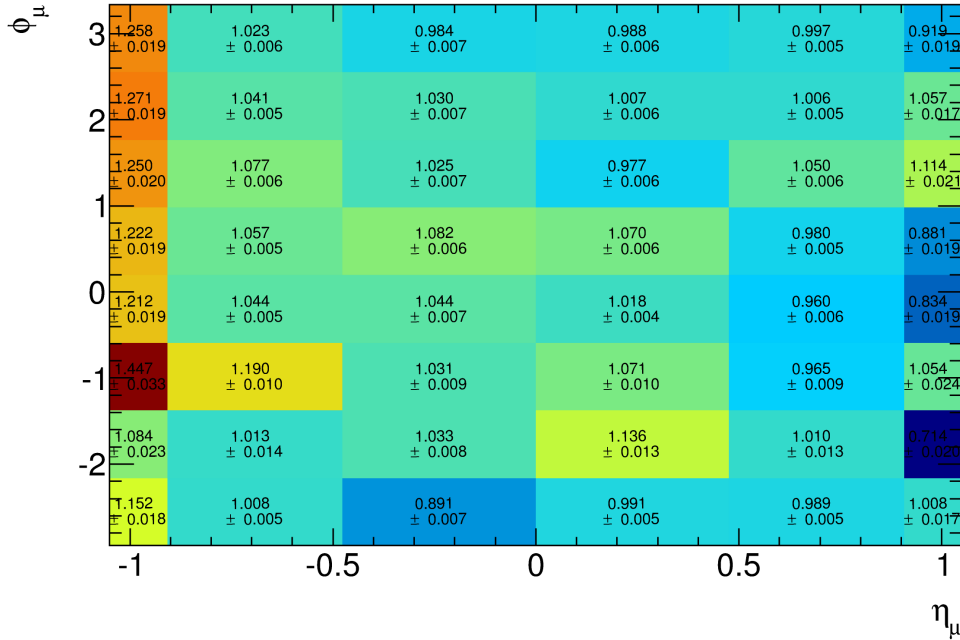
The distributions of the discriminating variables, which are not shown in Figure 6.2, can be found in Figure D.3.

### Steering Options for TMVA Algorithms

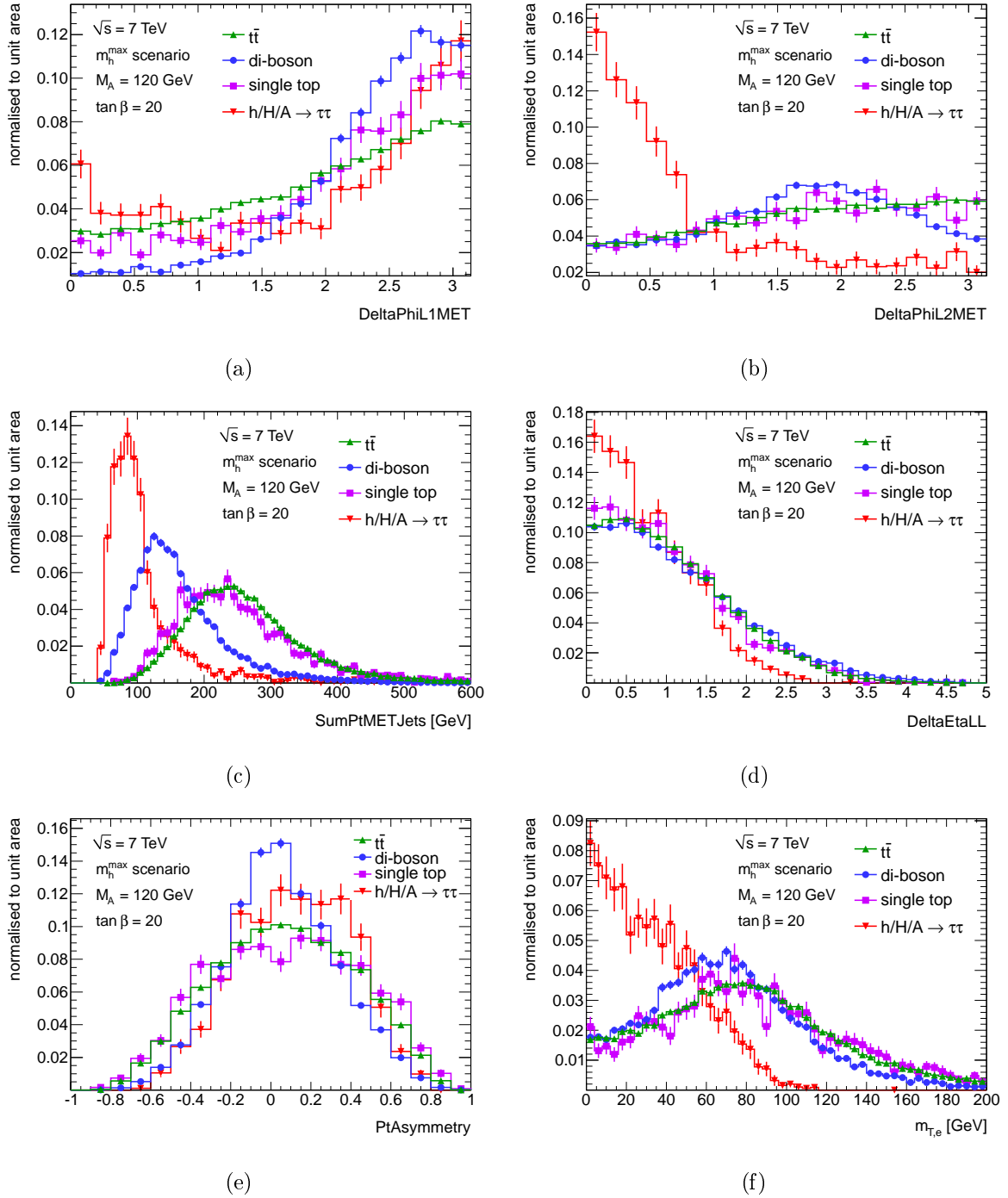
The options used for the training of the individual methods are summarised in Table D.6.



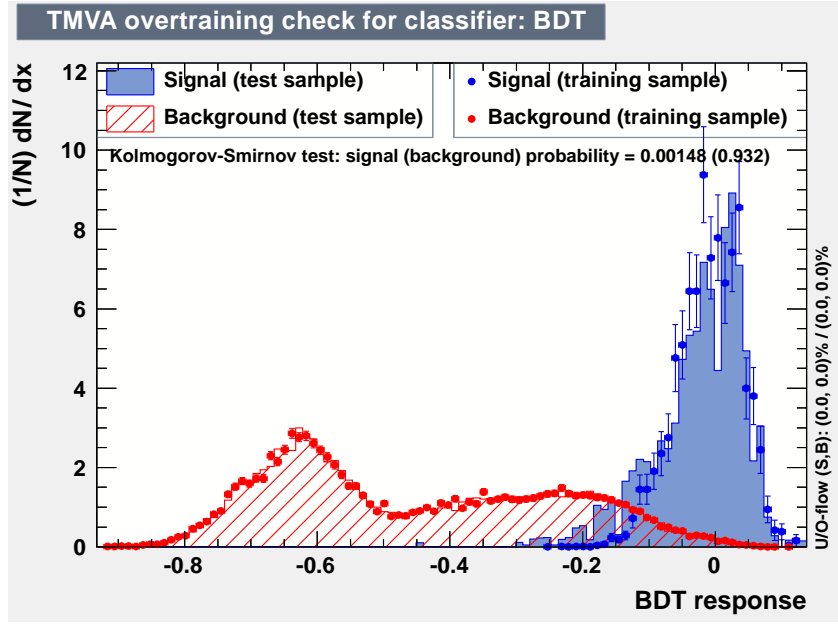
**Figure D.1:** Trigger efficiency correction factors with total uncertainties for the electron trigger `EF_e20_medium` as a function of  $\eta$  and  $\phi$  of the electron candidate which caused the trigger.



**Figure D.2:** Trigger efficiency correction factors with total uncertainties for the combined muon trigger `EF_mu18_MG OR EF_mu40_MOnly_barrel` in the barrel region as a function of  $\eta$  and  $\phi$  of the muon candidate which caused the trigger.



**Figure D.3:** Distributions of several discriminating variables for the background processes  $t\bar{t}$  (green triangles), di-boson production (blue dots) and single top production (violet squares) and the signal process (red reversed triangles) for the parameter point  $M_A = 120$  GeV and  $\tan \beta = 20$  in the  $m_h^{\max}$  scenario. All distributions are taken from simulated samples. The definitions of the individual variables are given in the text.



**Figure D.4:** Distribution of the BDT response values for the background (red) and the signal (red) processes obtained on the training (dots) and test (histogram) samples.

## Sets of Discriminating Variables

Additional sets of discriminating variables investigated during the optimisation of the event selection can be found in Table D.7 with their performances summarised in Table D.8.

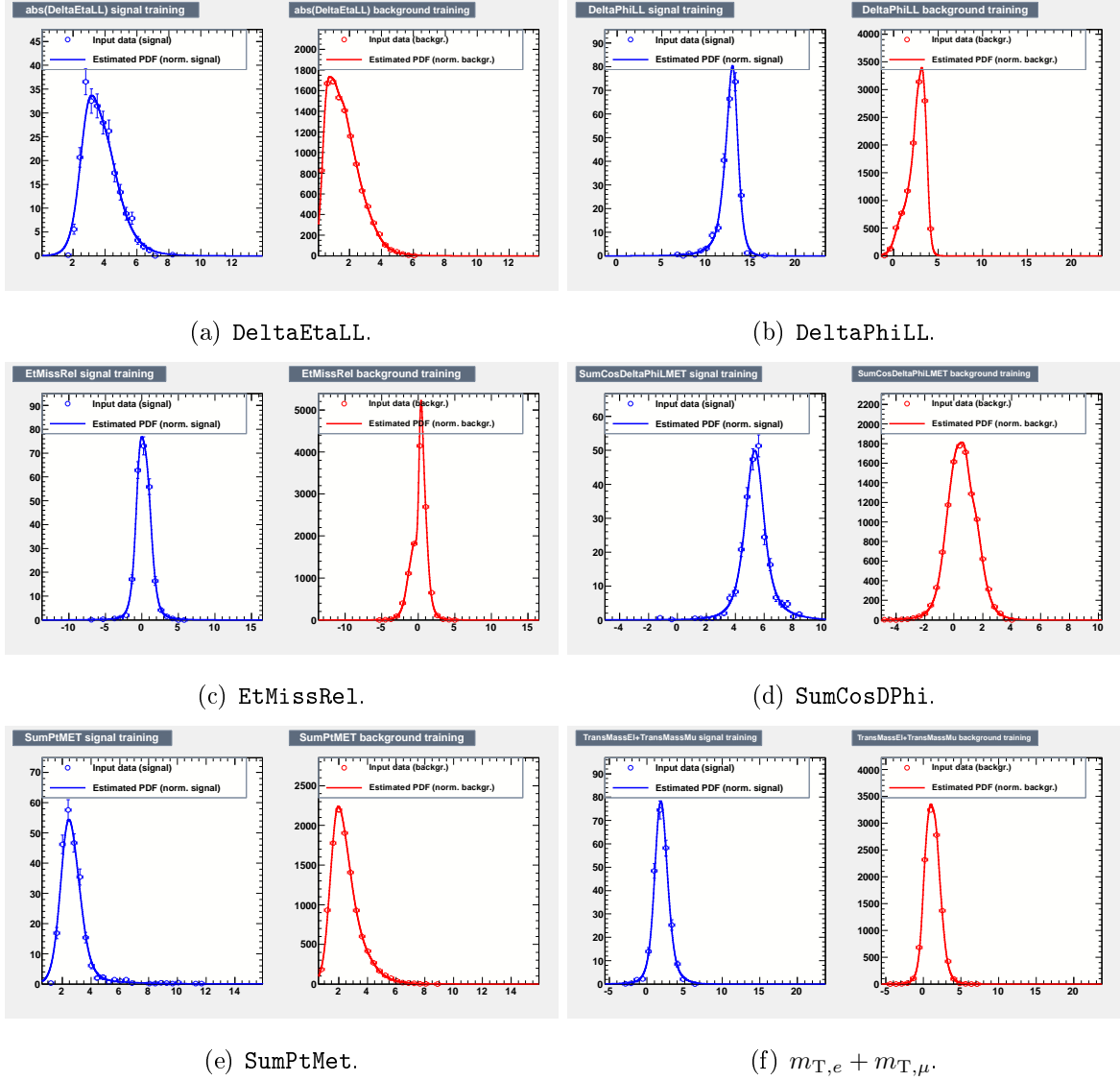
## Cross Checks for MVA Methods

Figure D.4 shows the obtained distributions of the BDT response value for the training and the test sample. One observes a mismatch of both samples for the signal distribution around  $\approx -0.2$ . This is an indication that the limited statistics in the training sample leads to an overestimation of the performance.

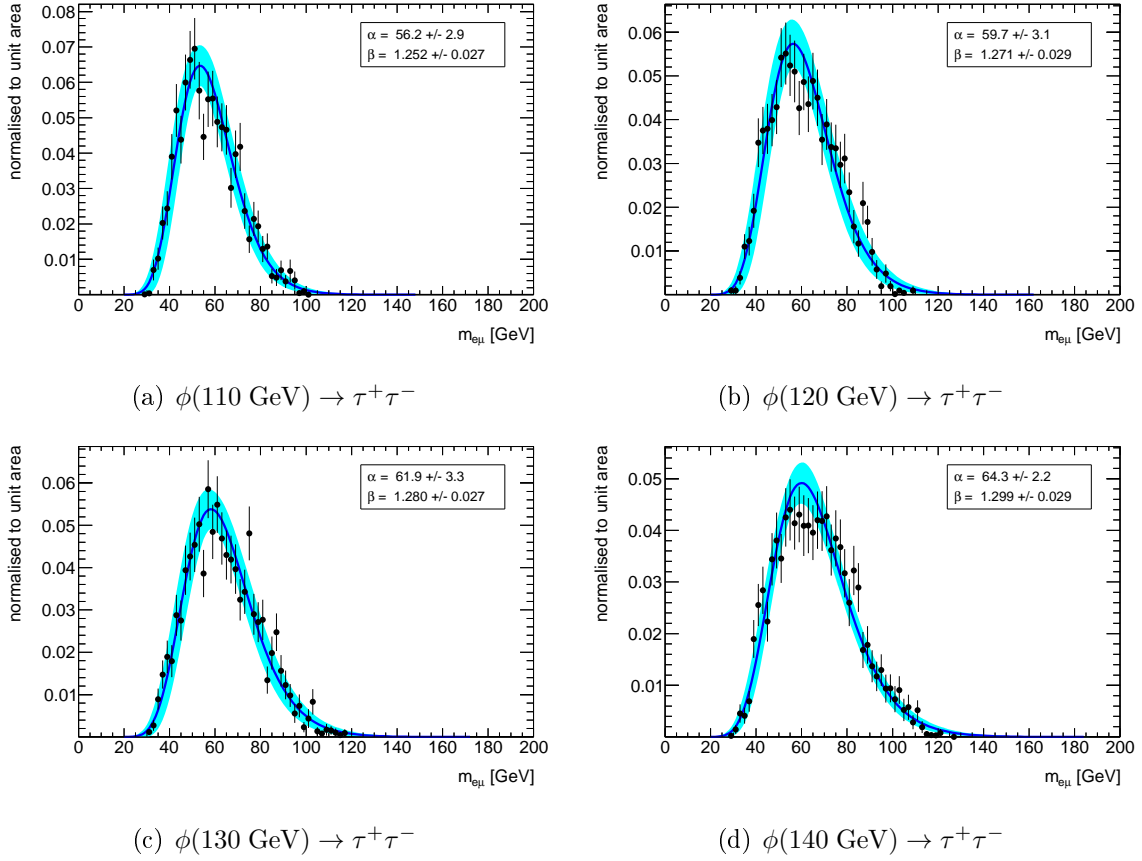
Figure D.5 shows the normalised distributions of the discriminating variables used for the projective likelihood approach. The derived PDFs provide a good description of the individual variables for both the signal and the background processes.

## D.6 Template Fit of the Visible Mass Spectrum

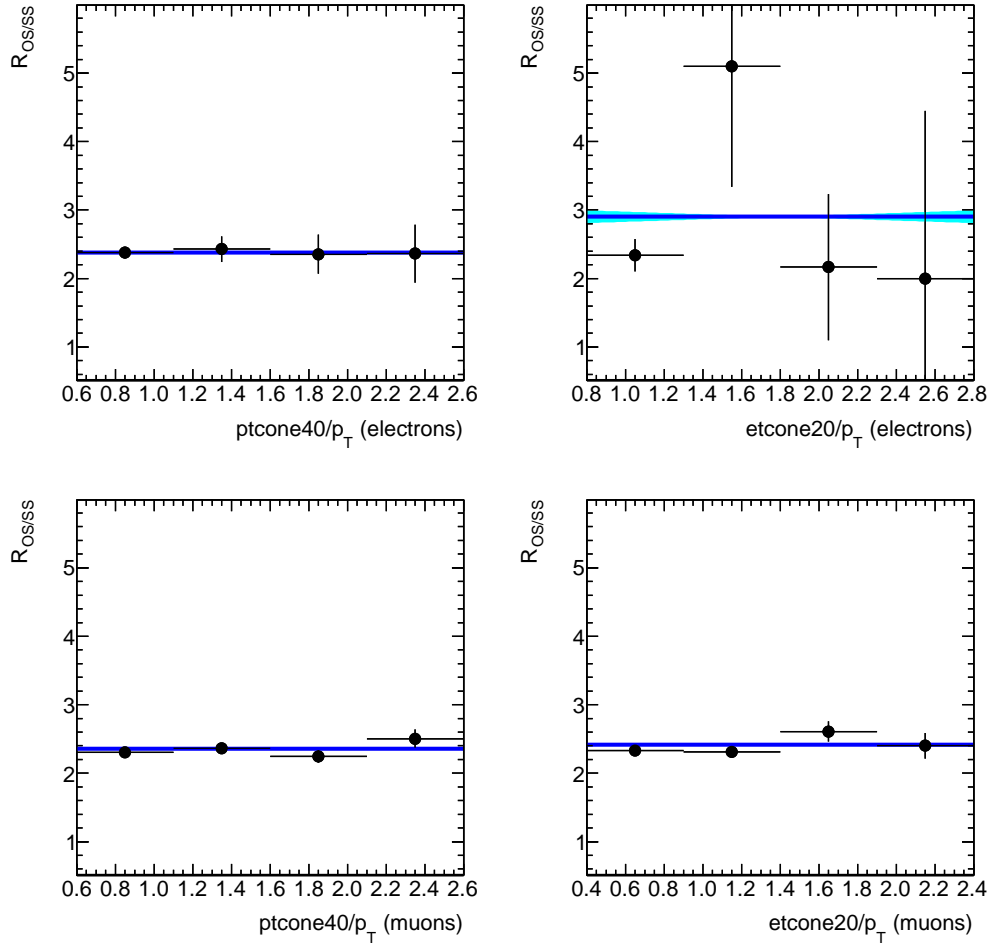
Figure D.6 displays the templates for the visible mass distribution of signal processes with different mass hypothesis.



**Figure D.5:** Normalised distribution of variables used in the projective likelihood approach for the signal process (blue) and background processes (red). The dots represent the distributions obtained from simulated samples and the functions represent the derived PDFs. For the definition of the individual variables, please refer the Section 6.6.1.



**Figure D.6:** Templates for the visible mass distribution for signal processes with different mass hypotheses taken from simulated samples. The black dots represent the values obtained from simulated samples. The blue lines correspond to the extracted shapes with their uncertainty indicated by the cyan area.



**Figure D.7:** Dependence of  $R_{OS/SS}$  on the calorimeter-based (left) and track-based (right) isolation variables for electron (top) and muon (bottom) candidates. The linear fit with its uncertainty on the slope parameter is displayed as blue lines.

## D.7 Systematic Uncertainty on the QCD Estimate

The dependence of the ratio  $R_{OS/SS}$  on the isolation variables used for the definition of isolated lepton candidates in the MSSM Higgs search is shown in Figure D.7. The observed values are fitted with a linear function. In all cases, the slope parameter is found to be compatible with 0 within its uncertainty. Hence, no systematic uncertainty on the ratio  $R_{OS/SS}$  is assigned.



process	process id	generator	configuration tags
$\gamma^*/Z \rightarrow ee, m_{ee} > 40 \text{ GeV}$	10765[0-5]	Alpgen	e737_s933_s946_r2302_r2300
$\gamma^*/Z \rightarrow \mu\mu, m_{\mu\mu} > 40 \text{ GeV}$	10766[0-5]	Alpgen	e737_s933_s946_r2302_r2300
$\gamma^*/Z \rightarrow \tau\tau, m_{\tau\tau} > 40 \text{ GeV}$	10767[0-5]	Alpgen	e844_s933_s946_r2302_r2300
$\gamma^*/Z \rightarrow ee, 10 \text{ GeV} < m_{ee} < 40 \text{ GeV}$	11625[0-5]	Alpgen	e660_s933_s946_r2302_r2300
$\gamma^*/Z \rightarrow \mu\mu, 10 \text{ GeV} < m_{\mu\mu} < 40 \text{ GeV}$	11626[0-5]	Alpgen	e660_s933_s946_r2302_r2300
$\gamma^*/Z \rightarrow \tau\tau, 10 \text{ GeV} < m_{\tau\tau} < 40 \text{ GeV}$	11627[0-5]	Alpgen	e844_s933_s946_r2302_r2300
$W \rightarrow e\nu$	10768[0-5]	Alpgen	e600_s933_s946_r2302_r2300
$W \rightarrow \mu\nu$	10769[0-5]	Alpgen	e600_s933_s946_r2302_r2300
$W \rightarrow \tau\nu$	10770[0-5]	Alpgen	e844_s933_s946_r2302_r2300
$t\bar{t}$ , at least one lepton	105200	MC@NLO	e598_s933_s946_r2302_r2300
$WW$ , at least one lepton	105985	Herwig	e598_s933_s946_r2302_r2300
$ZZ$ , at least one lepton	105986	Herwig	e598_s933_s946_r2302_r2300
$WZ$ , at least one lepton	105987	Herwig	e598_s933_s946_r2302_r2300
single top, t-channel, $e\nu$	108340	MC@NLO	e598_s933_s946_r2302_r2300
single top, t-channel, $\mu\nu$	108341	MC@NLO	e598_s933_s946_r2302_r2300
single top, t-channel, $\tau\nu$	108342	MC@NLO	e598_s933_s946_r2302_r2300
single top, s-channel, $e\nu$	108343	MC@NLO	e598_s933_s946_r2302_r2300
single top, s-channel, $\mu\nu$	108344	MC@NLO	e598_s933_s946_r2302_r2300
single top, s-channel, $\tau\nu$	108345	MC@NLO	e598_s933_s946_r2302_r2300
single top, Wt-channel	108346	MC@NLO	e598_s933_s946_r2302_r2300
gluon-fusion, $\phi \rightarrow \tau^+\tau^- \rightarrow \ell^+\ell^- + 4\nu$	11688[1-5]	PowHeg	e773_s933_s946_r2302_r2300
$b$ -associated production, $\phi \rightarrow \tau^+\tau^- \rightarrow \ell^+\ell^- + 4\nu$	12555[0-5]	Sherpa	e769_s933_s946_r2302_r2300

Table D.1: Samples of simulated processes used for the MSSM Higgs boson search.

objects	selection criteria
electrons	$p_T \geq 15 \text{ GeV}$ $ \eta  < 2.47$ , but excluding $1.37 <  \eta  < 1.52$ electron <b>tight</b> electron author 1 or 3 object quality bit & 1446 == 0
muons	$p_T \geq 10 \text{ GeV}$ $ \eta  < 2.5$ <b>tight</b> STACO muon $ z_0  < 10 \text{ mm}$ no BlayerHit expected or nBLayerHits > 0 nPixHits + nDeadPixelSensors > 1 nSCTHits + nDeadSCTSensors > 5 nPixHoles + nSCTHoles < 3 $ \eta  < 1.9$ : $\frac{\text{nTRT Outliers}}{\text{nTRT Hits} + \text{nTRT Outliers}} < 0.9$ AND nTRT Hits + nTRT Outliers > 5 $ \eta  \geq 1.9$ : nTRT Hits + nTRT Outliers $\leq 5$ OR $\frac{\text{nTRT Outliers}}{\text{nTRT Hits} + \text{nTRT Outliers}} < 0.9$
jets	Anti- $k_T$ jets with $\Delta R = 0.4$ calibrated at EM scale with JES factor $p_T > 20 \text{ GeV}$ $ \eta  < 4.5$
overlap Removal	muon-muon ( $\Delta R < 0.2$ ) elec-elec and elec-muon ( $\Delta R < 0.2$ ) jet-jet, jet-elec and jet-muon ( $\Delta R < 0.4$ )
MET	MET(LocHadTopo) + MET(MuonBoy) - MET(RefMuonTrack)

**Table D.2:** Object definitions used for the MSSM Higgs boson search.

$p_T$ range in GeV	correction factor
$15 \leq p_T \leq 18$	$1.035 \pm 0.034$
$18 \leq p_T \leq 20$	$1.028 \pm 0.007$
$20 \leq p_T \leq 30$	$1.023 \pm 0.002$
$30 \leq p_T \leq 40$	$1.030 \pm 0.002$
$40 \leq p_T \leq 50$	$1.037 \pm 0.001$
$50 \leq p_T \leq 70$	$1.043 \pm 0.003$
$70 \leq p_T \leq 100$	$1.025 \pm 0.008$
$100 \leq p_T$	$1.047 \pm 0.027$

**Table D.3:** Trigger efficiency correction factors with total uncertainties for the combined muon trigger `EF_mu18_MG OR EF_mu40_MOnly_barrel` in the end-cap region.

$ \eta $ range	correction factor
$0.00 \leq \eta < 0.80$	$0.998 \pm 0.018$
$0.80 \leq \eta < 2.01$	$1.009 \pm 0.007$
$2.01 \leq \eta < 2.47$	$0.976 \pm 0.006$

**Table D.4:** Correction factors for the electron reconstruction efficiency with total uncertainty.

$\eta$ range	correction factor	$p_T$ range in GeV	correction factor
$-2.47 \leq \eta < -2.37$	$1.000 \pm 0.028$	$0 \leq p_T < 7$	–
$-2.37 \leq \eta < -2.01$	$0.992 \pm 0.015$	$7 \leq p_T < 10$	$1.094 \pm 0.106$
$-2.01 \leq \eta < -1.81$	$1.034 \pm 0.026$	$10 \leq p_T < 15$	$1.021 \pm 0.107$
$-1.81 \leq \eta < -1.52$	$1.027 \pm 0.007$	$15 \leq p_T < 20$	$0.843 \pm 0.102$
$-1.37 \leq \eta < -1.15$	$1.130 \pm 0.020$	$20 \leq p_T < 25$	$0.894 \pm 0.028$
$-1.15 \leq \eta < -0.80$	$1.111 \pm 0.010$	$25 \leq p_T < 30$	$0.972 \pm 0.016$
$-0.80 \leq \eta < -0.60$	$1.035 \pm 0.007$	$30 \leq p_T < 35$	$1.003 \pm 0.013$
$-0.60 \leq \eta < -0.10$	$0.996 \pm 0.008$	$35 \leq p_T < 40$	$1.013 \pm 0.004$
$-0.10 \leq \eta < 0.00$	$0.984 \pm 0.007$	$40 \leq p_T < 45$	$1.012 \pm 0.004$
$0.00 \leq \eta < 0.10$	$1.008 \pm 0.015$	$45 \leq p_T < \infty$	$1.015 \pm 0.011$
$0.10 \leq \eta < 0.60$	$0.992 \pm 0.010$		
$0.60 \leq \eta < 0.80$	$0.981 \pm 0.010$		
$0.80 \leq \eta < 1.15$	$1.005 \pm 0.007$		
$1.15 \leq \eta < 1.37$	$1.028 \pm 0.008$		
$1.52 \leq \eta < 1.81$	$1.138 \pm 0.007$		
$1.81 \leq \eta < 2.01$	$1.035 \pm 0.018$		
$2.01 \leq \eta < 2.37$	$0.984 \pm 0.011$		
$2.37 \leq \eta < 2.47$	$1.022 \pm 0.023$		

**Table D.5:** Correction factors for the electron identification efficiency with total uncertainty.

method	TMVA type	TMVA configuration string
rectangular cuts	kCuts	FitMethod=MC:EffSel VarProp=FSmart
FISHER discriminant	kFisher	CreateMVAPdfs VarTransform=G
projective likelihood	kLikelihood	CreateMVAPdfs VarTransform=D TransformOutput NAvEvtPerBin=30 MinNSmooth=1 MaxNSmooth=3 PDFInterpol=Spline2
BDT	kBDT	CreateMVAPdfs IgnoreNegWeightsInTraining

**Table D.6:** TMVA configuration options. For an explanation of these options, please refer to [86].

set 1	set 2	set 3	set 4
SumPtMET	SumPtMET	SumPtMETJets	SumPtMET
$m_{T,e}$	$m_{T,e}$	$m_{T,e}$	$m_{T,e}$
$m_{T,\mu}$	$m_{T,\mu}$	$m_{T,\mu}$	$m_{T,\mu}$
SumCosDPhi	DeltaPhiL1MET	SumCosDPhi	SumCosDPhi
	DeltaPhiL2MET		DeltaPhiLL
set 5	set 6	set 7	
SumPtMET	SumPtMET	SumPtMET	
$m_{T,e}$	$m_{T,e} + m_{T,\mu}$	$m_{T,e}$	
$m_{T,\mu}$	SumCosDPhi	$m_{T,\mu}$	
SumCosDPhi		SumCosDPhi	
DeltaEtaLL		PtAsymmetry	

**Table D.7:** Different sets of discriminating variables which are investigated with regard to their performance.

variables	ROC integral			
	rectangular cuts	FISHER discriminant	projective likelihood	BDT
set 1	0.910	0.940	0.940	0.959
set 2	0.901	0.938	0.950	0.957
set 3	0.898	0.947	0.940	0.961
set 4	0.909	0.938	0.958	0.966
set 5	0.900	0.940	0.930	0.964
set 6	0.950	0.937	0.947	0.957
set 7	0.907	0.940	0.941	0.959

**Table D.8:** Performance of variable sets defined in Table D.7 in terms of the ROC integral for different methods. The input variables are de-correlated for the projective likelihood method and transformed into normal distributed variables for the FISHER discriminant analysis.



# Bibliography

- [1] J. J. Thomson, *Cathode rays*, Philosophical Magazine **44** (1897) 293.
- [2] E. Fermi, *Versuch einer Theorie der  $\beta$ -Strahlen. I*, Zeitschrift für Physik A Hadrons and Nuclei **88** (1934) 161–177.
- [3] S. L. Glashow, *Partial Symmetries of Weak Interactions*, Nucl. Phys. **22** (1961) 579–588.
- [4] A. Salam, *Renormalizability of Gauge Theories*, Phys. Rev. **127** (Jul., 1962) 331–334.
- [5] S. Weinberg, *A Model of Leptons*, Phys. Rev. Lett. **19** (Nov, 1967) 1264–1266.
- [6] UA1 Collaboration, G. Arnison et al., *Experimental observation of isolated large transverse energy electrons with associated missing energy at  $\sqrt{s} = 540$  GeV*, Physics Letters B **122** (1983) no. 1, 103 – 116.
- [7] UA2 Collaboration, M. Banner et al., *Observation of single isolated electrons of high transverse momentum in events with missing transverse energy at the CERN pp collider*, Physics Letters B **122** (1983) no. 5-6, 476 – 485.
- [8] UA1 Collaboration, G. Arnison et al., *Experimental observation of lepton pairs of invariant mass around 95 GeV at the CERN SPS collider*, Physics Letters B **126** (1983) no. 5, 398 – 410.
- [9] UA2 Collaboration, P. Bagnaia et al., *Evidence for  $Z^0 \rightarrow e^+e^-$  at the CERN pp collider*, Physics Letters B **129** (1983) no. 1-2, 130 – 140.
- [10] R. B. et al., *Evidence for planar events in  $e^+e^-$  annihilation at high energies*, Physics Letters B **86** (1979) no. 2, 243 – 249.
- [11] P. W. Higgs, *Broken Symmetries and the Masses of Gauge Bosons*, Phys. Rev. Lett. **13** (Oct, 1964) 508–509.
- [12] F. Englert and R. Brout, *Broken Symmetry and the Mass of Gauge Vector Mesons*, Phys. Rev. Lett. **13** (Aug, 1964) 321–323.
- [13] K. Nakamura et al., *Review of Particle Physics*, J. Phys. G: Nucl. Part. Phys. **37** (2010) no. 7A, 075021.

- [14] C. N. Yang and R. L. Mills, *Conservation of Isotopic Spin and Isotopic Gauge Invariance*, *Phys. Rev.* **96** (Oct, 1954) 191–195.
- [15] P. W. Higgs, *Spontaneous Symmetry Breakdown without Massless Bosons*, *Phys. Rev.* **145** (May, 1966) 1156–1163.
- [16] M. S. et. al., *Concepts of Electroweak Symmetry Breaking and Higgs Physics*, [arXiv:0712.2419 \[hep-ph\]](#).
- [17] R. Barate et al., *Search for the standard model Higgs boson at LEP*, *Phys. Lett. B* **565** (2003) 61–75, [arXiv:hep-ex/0306033 \[hep-ex\]](#).
- [18] ATLAS Collaboration, G. Aad et al., *Combination of Higgs Boson Searches with up to  $4.9\text{ fb}^{-1}$  of  $pp$  Collisions Data Taken at a center-of-mass energy of 7 TeV with the ATLAS Experiment at the LHC*, [ATLAS-CONF-2011-163](#), CERN, Dec, 2011.
- [19] A. L. Read, *Presentation of search results: the  $CL_S$  technique*, *J. Phys. G: Nucl. Part. Phys.* **28** (2002) no. 10, 2693.
- [20] P. B. Renton, *Precision electroweak tests of the standard model*, *Rept. Prog. Phys.* **65** (2002) 1271–1330, [arXiv:hep-ph/0206231 \[hep-ph\]](#).
- [21] J. R. Ellis, S. Kelley, and D. V. Nanopoulos, *Constraints from gauge coupling unification on the scale of supersymmetry breaking*, *Phys.Lett. B* **287** (1992) 95–100, [arXiv:hep-ph/9206203 \[hep-ph\]](#).
- [22] J. Casas, J. Espinosa, and I. Hidalgo, *Implications for new physics from fine-tuning arguments. 1. Application to SUSY and seesaw cases*, *JHEP* **0411** (2004) 057, [arXiv:hep-ph/0410298 \[hep-ph\]](#).
- [23] S. P. Martin, *A Supersymmetry primer*, [arXiv:hep-ph/9709356 \[hep-ph\]](#).
- [24] M. S. Carena, S. Heinemeyer, C. Wagner, and G. Weiglein, *Suggestions for benchmark scenarios for MSSM Higgs boson searches at hadron colliders*, *Eur.Phys.J. C* **26** (2003) 601–607, [arXiv:hep-ph/0202167 \[hep-ph\]](#).
- [25] L. Evans and P. Bryant, *LHC Machine*, *JINST* **3** (2008) no. 08, S08001.
- [26] M. Benedikt, P. Collier, V. Mertens, J. Poole, and K. Schindl, *LHC Design Report*, vol. 3. CERN, Geneva, 2004. <https://cdsweb.cern.ch/record/823808>.
- [27] ATLAS Collaboration, G. Aad et al., *The ATLAS Experiment at the CERN Large Hadron Collider*, *JINST* **3** (2008) S08003.
- [28] CMS Collaboration, S. Chatrchyan et al., *The CMS experiment at the CERN LHC*, *JINST* **3** (2008) S08004.
- [29] ALICE Collaboration, K. Aamodt et al., *The ALICE experiment at the CERN LHC*, *JINST* **3** (2008) S08002.



- [30] LHCb Collaboration, A. A. Alves et al., *The LHCb Detector at the LHC*, **JINST** **3** (2008) S08005.
- [31] R. Garoby, *Upgrade Issues for the CERN Accelerator Complex.*, **LHC-PROJECT-Report-1110**, Sep, 2008.
- [32] ATLAS Collaboration, G. Aad et al., *Expected Performance of the ATLAS Experiment - Detector, Trigger and Physics*, **arXiv:0901.0512 [hep-ex]**.
- [33] GEANT4 Collaboration, S. Agostinelli et al., *GEANT4: A simulation toolkit*, **Nucl. Instrum. Meth.** **A506** (2003) 250–303.
- [34] T. Sjostrand, S. Mrenna, and P. Z. Skands, *PYTHIA 6.4 Physics and Manual*, **JHEP** **0605** (2006) 026, **arXiv:hep-ph/0603175 [hep-ph]**.
- [35] M. L. Mangano, M. Moretti, F. Piccinini, R. Pittau, and A. D. Polosa, *ALPGEN, a generator for hard multiparton processes in hadronic collisions*, **JHEP** **0307** (2003) 001, **arXiv:hep-ph/0206293 [hep-ph]**.
- [36] S. Frixione and B. R. Webber, *The MC@NLO 3.3 Event Generator*, **arXiv:hep-ph/0612272 [hep-ph]**.
- [37] S. Frixione and B. R. Webber, *Matching NLO QCD computations and parton shower simulations*, **JHEP** **0206** (2002) 029, **arXiv:hep-ph/0204244 [hep-ph]**.
- [38] G. Corcella, I. Knowles, G. Marchesini, S. Moretti, K. Odagiri, et al., *HERWIG 6: An Event generator for hadron emission reactions with interfering gluons (including supersymmetric processes)*, **JHEP** **0101** (2001) 010, **arXiv:hep-ph/0011363 [hep-ph]**.
- [39] P. Nason, *A New method for combining NLO QCD with shower Monte Carlo algorithms*, **JHEP** **0411** (2004) 040, **arXiv:hep-ph/0409146 [hep-ph]**.
- [40] T. Gleisberg, S. Hoeche, F. Krauss, M. Schonherr, S. Schumann, et al., *Event generation with SHERPA 1.1*, **JHEP** **0902** (2009) 007, **arXiv:0811.4622 [hep-ph]**.
- [41] J. M. Butterworth, J. R. Forshaw, and M. H. Seymour, *Multiparton interactions in photoproduction at HERA*, **Z. Phys.** **C72** (1996) 637–646, **arXiv:hep-ph/9601371 [hep-ph]**.
- [42] J. Pumplin et al., *New generation of parton distributions with uncertainties from global QCD analysis*, **JHEP** **07** (2002) 012, **arXiv:hep-ph/0201195 [hep-ph]**.
- [43] P. M. Nadolsky et al., *Implications of CTEQ global analysis for collider observables*, **Phys. Rev.** **D78** (2008) 013004, **arXiv:0802.0007 [hep-ph]**.
- [44] A. Martin, W. Stirling, R. Thorne, and G. Watt, *Parton distributions for the LHC*, **Eur.Phys.J.** **C63** (2009) 189–285, **arXiv:0901.0002 [hep-ph]**.

- [45] ATLAS Collaboration, G. Aad et al., *First tuning of HERWIG/JIMMY to ATLAS data*, [ATL-PHYS-PUB-2010-014](#), CERN, Oct, 2010.
- [46] ATLAS Collaboration, G. Aad et al., *Charged particle multiplicities in  $pp$  interactions at  $\sqrt{s} = 0.9$  and 7 TeV in a diffractive limited phase-space measured with the ATLAS detector at the LHC and new PYTHIA6 tune*, [ATLAS-CONF-2010-031](#), CERN, Jul, 2010.
- [47] N. Davidson, G. Nanava, T. Przedzinski, E. Richter-Was, and Z. Was, *Universal Interface of TAUOLA Technical and Physics Documentation*, [arXiv:1002.0543 \[hep-ph\]](#).
- [48] W. Lampl, S. Laplace, D. Lelas, P. Loch, H. Ma, S. Menke, S. Rajagopalan, D. Rousseau, S. Snyder, and G. Unal, *Calorimeter Clustering Algorithms: Description and Performance*, [ATL-LARG-PUB-2008-002](#), CERN, Apr, 2008.
- [49] ATLAS Collaboration, G. Aad et al., *Expected electron performance in the ATLAS experiment*, [ATL-PHYS-PUB-2011-006](#), CERN, Apr, 2011.
- [50] ATLAS Collaboration, G. Aad et al., *Muon reconstruction efficiency in reprocessed 2010 LHC proton-proton collision data recorded with the ATLAS detector*, [ATLAS-CONF-2011-063](#), CERN, Apr, 2011.
- [51] ATLAS Collaboration, G. Aad et al., *Muon Momentum Resolution in First Pass Reconstruction of  $pp$  Collision Data Recorded by ATLAS in 2010*, [ATLAS-CONF-2011-046](#), CERN, Mar, 2011.
- [52] M. Cacciari, G. P. Salam, and G. Soyez, *The anti- $k_t$  jet clustering algorithm*, [JHEP 04 \(2008\) 063](#), [arXiv:0802.1189 \[hep-ph\]](#).
- [53] M. Cacciari and G. P. Salam, *Dispelling the  $N^3$  myth for the  $k_t$  jet-finder*, [Phys.Lett. B641 \(2006\) 57–61](#), [arXiv:hep-ph/0512210 \[hep-ph\]](#).
- [54] ATLAS Collaboration, J. Butterworth et al., *Single Boson and Diboson Production Cross Sections in  $pp$  Collisions at  $\sqrt{s} = 7$  TeV*, [ATL-COM-PHYS-2010-695](#), CERN, Aug, 2010. (access restricted to ATLAS).
- [55] R. Gavin, Y. Li, F. Petriello, and S. Quackenbush, *FEWZ 2.0: A code for hadronic  $Z$  production at next-to-next-to-leading order*, [Comput.Phys.Commun. 182 \(2011\) 2388–2403](#), [arXiv:1011.3540 \[hep-ph\]](#).
- [56] S. Dawson, A. Djouadi, and M. Spira, *QCD corrections to SUSY Higgs production: The Role of squark loops*, [Phys.Rev.Lett. 77 \(1996\) 16–19](#), [arXiv:hep-ph/9603423 \[hep-ph\]](#).
- [57] S. Heinemeyer, W. Hollik, and G. Weiglein, *FeynHiggs: A Program for the calculation of the masses of the neutral CP even Higgs bosons in the MSSM*, [Comput.Phys.Commun. 124 \(2000\) 76–89](#), [arXiv:hep-ph/9812320 \[hep-ph\]](#).

- [58] S. Heinemeyer, W. Hollik, and G. Weiglein, *The Masses of the neutral CP - even Higgs bosons in the MSSM: Accurate analysis at the two loop level*, *Eur.Phys.J.* **C9** (1999) 343–366, [arXiv:hep-ph/9812472 \[hep-ph\]](#).
- [59] G. Degrandi, S. Heinemeyer, W. Hollik, P. Slavich, and G. Weiglein, *Towards high precision predictions for the MSSM Higgs sector*, *Eur.Phys.J.* **C28** (2003) 133–143, [arXiv:hep-ph/0212020 \[hep-ph\]](#).
- [60] M. Frank, T. Hahn, S. Heinemeyer, W. Hollik, H. Rzehak, et al., *The Higgs Boson Masses and Mixings of the Complex MSSM in the Feynman-Diagrammatic Approach*, *JHEP* **0702** (2007) 047, [arXiv:hep-ph/0611326 \[hep-ph\]](#).
- [61] M. Spira, *HIGLU: A program for the calculation of the total Higgs production cross-section at hadron colliders via gluon fusion including QCD corrections*, [arXiv:hep-ph/9510347 \[hep-ph\]](#).
- [62] R. V. Harlander and W. B. Kilgore, *Next-to-next-to-leading order Higgs production at hadron colliders*, *Phys.Rev.Lett.* **88** (2002) 201801, [arXiv:hep-ph/0201206 \[hep-ph\]](#).
- [63] R. V. Harlander and W. B. Kilgore, *Production of a pseudoscalar Higgs boson at hadron colliders at next-to-next-to leading order*, *JHEP* **0210** (2002) 017, [arXiv:hep-ph/0208096 \[hep-ph\]](#).
- [64] R. Harlander, M. Krämer, and M. Schuhmacher, *Bottom-quark associated Higgs-boson production: reconciling the four- and five-flavour scheme approach*, <https://twiki.cern.ch/twiki/pub/LHCPhysics/MSSMNeutral/santandermatching-hks.pdf>. (visited on 14.12.2011).
- [65] R. V. Harlander and W. B. Kilgore, *Higgs boson production in bottom quark fusion at next-to-next-to leading order*, *Phys.Rev.* **D68** (2003) 013001, [arXiv:hep-ph/0304035 \[hep-ph\]](#).
- [66] S. Dittmaier, M. Kramer, and M. Spira, *Higgs radiation off bottom quarks at the Tevatron and the CERN LHC*, *Phys.Rev.* **D70** (2004) 074010, [arXiv:hep-ph/0309204 \[hep-ph\]](#).
- [67] ATLAS Collaboration, G. Aad et al., *Performance of the Reconstruction and Identification of Hadronic Tau Decays with ATLAS*, **ATLAS-CONF-2011-152**, CERN, Nov, 2011.
- [68] M. Beneke, P. Falgari, S. Klein, and C. Schwinn, *Hadronic top-quark pair production with NNLL threshold resummation*, *Nucl.Phys.* **B855** (2011) 695–741, [arXiv:1109.1536 \[hep-ph\]](#).
- [69] N. Kidonakis, *Next-to-next-to-leading-order collinear and soft gluon corrections for t-channel single top quark production*, *Phys.Rev.* **D83** (2011) 091503, [arXiv:1103.2792 \[hep-ph\]](#).

- [70] N. Kidonakis, *NNLL resummation for s-channel single top quark production*, *Phys.Rev.* **D81** (2010) 054028, [arXiv:1001.5034 \[hep-ph\]](#).
- [71] N. Kidonakis, *Two-loop soft anomalous dimensions for single top quark associated production with a  $W^-$  or  $H^-$* , *Phys.Rev.* **D82** (2010) 054018, [arXiv:1005.4451 \[hep-ph\]](#).
- [72] R. K. Ellis, I. Hinchliffe, M. Soldate, and J. J. van der Bij, *Higgs Decay to  $\tau^+\tau^-$ : A Possible Signature of Intermediate Mass Higgs Bosons at the SSC*, *Nucl. Phys.* **B297** (1988) 221.
- [73] ATLAS Collaboration, G. Aad et al., *Measurement of the  $Z \rightarrow \tau^+\tau^-$  Cross Section with the ATLAS Detector*, [arXiv:hep-ex/1108.2016 \[hep-ex\]](#).
- [74] ATLAS Collaboration, G. Aad et al., *Updated Luminosity Determination in pp Collisions at  $\sqrt{s} = 7$  TeV using the ATLAS Detector*, [ATLAS-CONF-2011-011](#), CERN, Mar, 2011.
- [75] ATLAS Collaboration, G. Aad et al., *Electron performance measurements with the ATLAS detector using the 2010 LHC proton-proton collision data*, [arXiv:1110.3174 \[hep-ex\]](#).
- [76] ATLAS Collaboration, G. Aad et al., *Determination of the muon reconstruction efficiency in ATLAS at the Z resonance in proton-proton collisions at  $\sqrt{s} = 7$  TeV*, [ATLAS-CONF-2011-008](#), CERN, Feb, 2011.
- [77] ATLAS Collaboration, E. Barberio et al., *Measurement of the cross section  $\sigma \times \mathcal{BR}(Z \rightarrow \tau^+\tau^-)$  in the dilepton channel with the ATLAS detector*, [ATL-COM-PHYS-2011-418](#), CERN, Apr, 2011. (access restricted to ATLAS).
- [78] ATLAS Collaboration, G. Aad et al., *A measurement of the total  $W^\pm$  and  $Z/\gamma^*$  cross sections in the e and  $\mu$  decay channels and of their ratios in pp collisions at  $\sqrt{s} = 7$  TeV with the ATLAS detector*, [ATLAS-CONF-2011-041](#), CERN, Mar, 2011.
- [79] ATLAS Collaboration, G. Aad et al., *A combined measurement of the top quark pair production cross-section using dilepton and single-lepton final states*, [ATLAS-CONF-2011-040](#), CERN, Mar, 2011.
- [80] ATLAS Collaboration, G. Aad et al., *Jet energy scale and its systematic uncertainty in proton-proton collisions at  $\sqrt{s} = 7$  TeV in ATLAS 2010 data*, [ATLAS-CONF-2011-032](#), CERN, Mar, 2011.
- [81] ATLAS Collaboration, G. Aad et al., *Performance of Missing Transverse Momentum Reconstruction in Proton-Proton Collisions at 7 TeV with ATLAS*, [arXiv:1108.5602 \[hep-ex\]](#).

- [82] H1 and ZEUS Collaboration Collaboration, F. Aaron et al., *Combined Measurement and QCD Analysis of the Inclusive  $e^+ - p$  Scattering Cross Sections at HERA*, **JHEP** **1001** (2010) 109, [arXiv:0911.0884 \[hep-ex\]](#).
- [83] Atlas Collaboration Collaboration, G. Aad et al., *Measurement of the  $W \rightarrow \ell\nu$  and  $Z/\gamma^* \rightarrow \ell\ell$  production cross sections in proton-proton collisions at  $\sqrt{s} = 7$  TeV with the ATLAS detector*, **JHEP** **1012** (2010) 060, [arXiv:1010.2130 \[hep-ex\]](#).
- [84] M. C. P. group, *Muon trigger recommendations*, <https://twiki.cern.ch/twiki/pub/Atlas/MuonTriggerPhysicsTriggerRecommendations2011/trigger.pdf>. (visited on 02.12.2011, access restricted to ATLAS).
- [85] ATLAS Collaboration, G. Aad et al., *Search for the Standard Model Higgs boson in the decay mode  $H \rightarrow \tau^+\tau^- \rightarrow \ell^+\ell^- + 4\nu$  in Association with jets in Proton-Proton Collisions at  $\sqrt{s} = 7$  TeV with the ATLAS detector*, **ATLAS-CONF-2011-133**, CERN, Sep, 2011.
- [86] A. Hoecker, P. Speckmayer, J. Stelzer, J. Therhaag, E. von Toerne, and H. Voss, *TMVA: Toolkit for Multivariate Data Analysis*, PoS **ACAT** (2007) 040, [arXiv:physics/0703039](#).
- [87] N. Möser, M. Schmitz, J. Kroseberg, M. Schumacher, and N. Wermes, *Estimation of  $Z \rightarrow \tau^+\tau^-$  Background in VBF  $H \rightarrow \tau^+\tau^-$  Searches from  $Z \rightarrow \mu^+\mu^-$  Data using an Embedding Technique*, **ATL-PHYS-INT-2009-109**, CERN, Dec, 2009. (access restricted to ATLAS).
- [88] F. James, *Statistical Methods in Experimental Physics*. World Scientific, 2 ed., 2006.
- [89] G. Cowan, K. Cranmer, E. Gross, and O. Vitells, *Asymptotic formulae for likelihood-based tests of new physics*, **European Physical Journal C** **71** (Feb., 2011) 1554, [arXiv:1007.1727 \[physics.data-an\]](#).
- [90] S. S. Wilks, *The large-sample distribution of the likelihood ratio for testing composite hypotheses*, **Ann. Math. Statist.** **9** (1938) 60–62.
- [91] LHC Higgs Cross Section Working Group Collaboration, S. Dittmaier et al., *Handbook of LHC Higgs Cross Sections: 1. Inclusive Observables*, [arXiv:1101.0593 \[hep-ph\]](#).
- [92] ATLAS Collaboration, G. Aad et al., *Validating the measurement of jet energies with the ATLAS detector using  $Z + \text{jet}$  events from proton-proton collisions at  $\sqrt{s} = 7$  TeV*, **ATLAS-CONF-2011-159**, CERN, Dec, 2011.
- [93] ATLAS Collaboration, G. Aad et al., *Search for neutral MSSM Higgs bosons decaying to  $\tau^+\tau^-$  pairs in proton-proton collisions at  $\sqrt{s} = 7$  TeV with the ATLAS detector*, **ATLAS-CONF-2011-132**, CERN, Sep, 2011.



# Danksagung

An dieser Stelle möchte ich mich bei meinen Betreuern Prof. M. Kobel und Dr. W. Mader für die Herausgabe und Betreuung dieser interessanten und ambitionierten Diplomarbeit bedanken. Weiterhin möchte ich mich bei meinen Kollegen der ATLAS Gruppe für das angenehme und kollegiale Arbeitsumfeld bedanken, so dass bei all dem Termindruck nie der Spass an der Arbeit verloren ging. Im Besonderen danke ich Peter Steinbach, Marcus Morgenstern und Felix Friedrich für die anregenden Diskussionen über fortgeschrittene Programmiertechniken in C++. Alexander Voigt stand mir immer hilfreich bei theoretischen Fragen zur Seite und überzeugte mich von der Stärke konsolenbasierter Anwendungen. Einen herzlichen Dank möchte ich auch an die Korrekturleser Felix Thomas, Xavier Prudent, Sebastian Wahrmund, Marcus und Wolfgang aussprechen, welche innerhalb kürzester Zeit mit konstruktiven Kommentaren zum Gelingen dieser Arbeit beigetragen haben.

An dieser Stelle möchte ich auch meinen Eltern danken, die mir mit ihrer finanziellen und moralischen Unterstützung das Studium ermöglicht haben. Neben den vielen schönen Erinnerungen an eine tolle Kindheit danke ich ihnen besonders für die Entscheidung, mich an dem Heinrich-Hertz-Gymnasium in Berlin anzumelden, wo ich mein Interesse für die Naturwissenschaften entdeckte.

Spezieller Dank geht an meine Freundin Andrea Lißner, die mich in den vier Wochen des Aufschreibens meiner Diplomarbeit mit Kuchen, Keksen und viel Verständnis unterstützte und dafür leider auf eine besinnliche Adventszeit verzichten musste.





# Erklärung

Hiermit versichere ich, dass ich die vorliegende Arbeit ohne unzulässige Hilfe Dritter und ohne Benutzung anderer als der angegebenen Hilfsmittel angefertigt habe. Die aus fremden Quellen direkt oder indirekt übernommenen Gedanken sind als solche kenntlich gemacht. Die Arbeit wurde bisher weder im Inland noch im Ausland in gleicher oder ähnlicher Form einer anderen Prüfungsbehörde vorgelegt.

Christian Gumpert  
Dresden, 16. Dezember 2011